



**Michigan
Technological
University**

Michigan Technological University
Digital Commons @ Michigan Tech

Dissertations, Master's Theses and Master's Reports

2019

Development of a 2D SCR Catalyst on a Diesel Particulate Filter Model for Design and Control Applications to a Ultra Low NOx Aftertreatment System

Venkata Chundru
Michigan Technological University, vrchundr@mtu.edu

Copyright 2019 Venkata Chundru

Recommended Citation

Chundru, Venkata, "Development of a 2D SCR Catalyst on a Diesel Particulate Filter Model for Design and Control Applications to a Ultra Low NOx Aftertreatment System", Open Access Dissertation, Michigan Technological University, 2019.
<https://doi.org/10.37099/mtu.dc.etr/869>

Follow this and additional works at: <https://digitalcommons.mtu.edu/etr>



Part of the [Heat Transfer, Combustion Commons](#)

DEVELOPMENT OF A 2D SCR CATALYST ON A DIESEL PARTICULATE
FILTER MODEL FOR DESIGN AND CONTROL APPLICATIONS TO A
ULTRA LOW NO_x AFTERTREATMENT SYSTEM

By
Venkata Rajesh Chundru

A DISSERTATION
Submitted in partial fulfillment of the requirements for the degree of
DOCTOR OF PHILOSOPHY
In Mechanical Engineering - Engineering Mechanics

MICHIGAN TECHNOLOGICAL UNIVERSITY
2019

© 2019 Venkata Rajesh Chundru

This dissertation has been approved in partial fulfillment of the requirements for the Degree of DOCTOR OF PHILOSOPHY in Mechanical Engineering - Engineering Mechanics.

Department of Mechanical Engineering - Engineering Mechanics

Dissertation Co-advisor: *Dr. Gordon G. Parker*

Dissertation Co-advisor: *Dr. John H. Johnson*

Committee Member: *Dr. Jeffrey D. Naber*

Committee Member: *Dr. Sunil S. Mehendale*

Department Chair: *Dr. William W. Predebon*

Contents

List of Figures	viii
List of Tables	xvii
Preface	xix
Acknowledgments	xxi
Nomenclature	xxii
Abstract	xxxii
1 Introduction	1
1.1 Motivation	4
1.2 Diesel Aftertreatment System Experimental Data	5
1.3 Research Objectives	8
1.4 Overview of the Thesis	9
2 Background and Literature Review	10
2.1 SCR-F Models	11
2.2 SCR-F Experimental Studies	19
2.3 1D and Multi Dimensional CPF Models	22
2.4 Pressure Drop Modeling	24
2.5 SCR and CPF State Estimator Studies	24
2.6 Ultra-Low NO _x Aftertreatment Systems	27
2.7 Summary	29
3 SCR-F Model Development	31
3.1 Overview of the Model	32
3.2 Model Architecture	33
3.3 Submodels	36
3.3.1 Mesh Development	36
3.3.2 Calculation of Physical Properties	38

3.3.3	Exhaust Gas Velocity	41
3.3.4	Temperature Sub Model	42
3.3.5	Species Model	44
3.3.6	PM Mass Retained Model	49
3.3.7	Filtration Model	52
3.3.8	Pressure Drop Model	53
4	Experimental Data and Model Calibration Procedure	56
4.1	SCRF [®] Configuration 1 Data PO With and Without Urea	58
4.2	SCRF [®] Configuration 1 AR Data	61
4.3	SCRF [®] Configuration 2 Data With and Without PM Loading	62
4.4	SCRF [®] Configuration 3 Data	65
4.5	Experimental Data Uncertainties	68
4.5.1	Exhaust Mass Flow Rate	68
4.5.2	Temperature	68
4.5.3	Pressure Drop	69
4.5.4	Gaseous Emissions	70
4.5.5	Particulate Matter concentration and mass retained	71
4.6	Procedure for the Model Calibration	71
4.6.1	SCRF [®] Configuration 1 PO Tests Without Urea	72
4.6.1.1	PM Oxidation Kinetics	74
4.6.1.2	Temperature Distribution and Thermal Response	74
4.6.1.3	Filtration Efficiency and Pressure Drop	75
4.6.1.4	Cake Permeability	77
4.6.2	SCRF [®] Configuration 1 PO Tests With Urea Injection	78
4.6.3	SCRF [®] Configuration 1 AR Tests	79
4.6.3.1	Active Regeneration PM Oxidation Kinetics	80
4.6.3.2	HC Oxidation Kinetics	80
4.6.4	SCRF [®] Configuration 2 Tests With and Without PM	81
5	Results and Discussion	84
5.1	SCRF [®] Configuration 1 Passive Oxidation With and Without Urea Data	85
5.1.1	Impact of SCR Reactions on PM Oxidation Rate	85
5.1.2	Change in Temperature, NO ₂ concentration and PM Mass Dis- tribution for Cases With and Without Urea Injection	89
5.1.3	Filtration Efficiency With and Without Urea injection	91
5.1.4	Impact of Urea Injection on PM Mass Retained	92

5.1.5	Impact of Urea Injection on Wall and Cake Pressure Drop Characteristics	94
5.1.6	Change in Cake Permeability Due to Forward Diffusion	95
5.2	SCR ^F ® Configuration 1 Active Regeneration Data	96
5.2.1	Energy Release by HC Oxidation	97
5.2.2	Contribution of Thermal and NO ₂ Assisted PM Oxidation	98
5.3	Summary of Configuration 1 Results	99
5.4	SCR ^F ® Configuration 2 With and Without PM Loading Data	100
5.4.1	Change in Local NO ₂ /NO _x Ratio Inside the Substrate Wall	103
5.4.2	Contribution of Each SCR Reaction on NO _x Reduction Performance	104
5.4.3	Inhibition of SCR Reactions Due to PM Loading	105
5.4.4	SCR-F Temperature as a Function of Inlet ANR	106
5.4.5	NO _x Reduction Efficiency	109
5.5	Summary of Configuration 2 Results	111
5.6	SCR ^F ® Configuration 3 Data	111
5.6.1	SCR ^F ®+SCR system NO _x Reduction Efficiency	112
5.6.2	NH ₃ Characteristics of SCR ^F ® and SCR	115
5.6.3	Contribution of Individual SCR Reactions in SCR ^F ® and SCR	118
5.6.4	Impact of local NO ₂ /NO _x Ratio on System Performance	120
5.7	Summary of Configuration 3 Results	125
6	SCR-F State Estimator	126
6.1	SCR-F Estimator Model	127
6.1.1	SCR-F Estimator Model Governing Equations	127
6.1.2	SCR-F Estimator Model Results	128
6.2	SCR-F State Estimator	135
6.2.1	Outlet value calculations	139
6.2.2	Jacobian calculations	140
6.2.3	State Estimator Results	140
6.2.4	Temperatures States	141
6.2.5	PM Mass Retained States and Pressure Drop	146
6.2.6	NH ₃ Coverage Fraction States (θ_1, θ_2) and Outlet NO, NO ₂ , NH ₃ Concentrations	148
6.3	DOC+SCR-F State Estimator	152
6.3.1	DOC+SCR-F State Estimator Results	153
7	Ultra Low NOx Aftertreatment System	156

7.1	Aftertreatment Systems	156
7.1.1	Production System	157
7.1.2	Proposed - Ultra Low NO _x Aftertreatment System Configurations	158
7.2	Parametric Studies and Results	162
7.3	Control System Design	178
7.3.1	Summary of the Ultra Low NO _x Control System Design and Performance	182
7.4	Further Improvements to the Ultra Low NO _x System	186
8	Summary and Conclusions	188
8.1	Summary of SCR-F Model Development	188
8.2	Summary of the Results from SCR ^F ® Configuration 1 and 2 Data	189
8.3	Summary of the Results from SCR ^F ® Configuration 3 Data	191
8.4	Summary of the Results from SCR ^F ® Ultra Low NO _x Aftertreatment System Modeling	192
8.5	Summary of the Results from SCR ^F ® State Estimator	193
8.6	Summary of Major Findings from the Research	194
8.7	Major Conclusions from the Research	196
	References	198
	A Development of SCR-F Model Mesh Equations	206
	B Development of Temperature Model and SCR Energy Release Terms	209
	C Development of Effectiveness Factor for the SCR Reactions	213
	D Development of Cake Permeability, Pressure Drop and Filtration Models	216
	D.0.1 Wall and Cake Pressure drop	218
	D.0.2 Total Pressure drop	218
	D.0.3 Filtration Efficiency	218
	E SCR^F® Species Model Development	220
	E.0.1 Oxidation Reactions	221
	E.0.2 SCR Reactions	222
	F SCR^F® Configuration 1, 2 and 3 Experimental Data Test Points	224

G	SCRF® Calibration Parameters	247
G.1	Parameters from Model Calibration	247
G.1.1	Filtration Parameters	247
G.1.2	Thermal Parameters	249
G.1.3	Catalyst Parameters	249
G.1.4	Catalytic Reactions and PM Oxidation Kinetics	250
G.1.5	SCR Kinetics	253
G.1.6	Diffusion Parameters	254
G.1.7	Cake Permeability Parameters	255
H	Ultra Low NOx Parametric Study Results	256
H.1	Test1	257
H.2	TestA	260
H.3	TestD	263
H.4	TestE	266
I	Letters of Permission	270

List of Figures

1.1	Time vs BSPM and BSNO _x	1
1.2	Cummins ISB 2013 Production Aftertreatment System Schematic .	3
1.3	Configurations 1 and 2 with PM loading Aftertreatment System Schematic	6
1.4	Configurations 2 without PM Aftertreatment System Schematic . .	7
1.5	Configurations 3 Aftertreatment System Schematic	7
2.1	Inhibition of NH ₃ transport to active site due to PM in the substrate wall	12
2.2	Radial NO/NO ₂ profiles (PM cake and substrate wall) with and without NH ₃	13
2.3	NH ₃ storage and NO ₂ consumption in PM cake and wall with and without PM	14
2.4	NH ₃ adsorption and desorption for PM free filter with 250 ppm inlet NH ₃	16
2.5	Change in NO ₂ concentration in radial and axial direction	17
2.6	Competition for NO ₂ between PM oxidation and SCR reactions . .	17
2.7	PM oxidation rate CSF vs SCRF®	20
2.8	NH ₃ inlet and outlet concentrations	22
2.9	SCR estimator setup	26
2.10	Two brick SCR system	27
2.11	CPF estimator system	28
3.1	SCR-F model flowchart	34
3.2	SCR-F model schematic	36
3.3	SCR-F discretization illustrating 12 annular zones where $N = 3$ and $M = 4$	37
3.4	SCR-F model mesh - temperature and filtration	38
3.5	Schematic of temperature solver mesh for SCR-F/CPF model . . .	42
3.6	Schematic of SCRF® thermocouple arrangement	44
3.7	Schematic of cake and wall filtration and PM oxidation	46

3.8	NH ₃ storage inside substrate wall for the SCR-F model	48
3.9	PM mass balance in SCR-F	50
3.10	Schematic of the streamlines (shown a dashed lines) used for calculating the pressure drop across CPF/SCR-F for 3x1 zone model (4 axial and 1 radial discretization).	54
4.1	Configuration 1 with and without PM loading	58
4.2	Pressure drop for passive oxidation experiments configuration 1 without and with urea stages S1 - Stage 1, S2 - Stage 2, RU - Ramp up, PO - Passive oxidation, S3 - Stage 3, S4 - Stage 4	59
	(a) Without urea Test C	59
	(b) With urea Test C	59
4.3	Pressure drop active regeneration experiment for configuration 1 (AR-1) without urea	61
4.4	Configuration 2 without PM loading	63
4.5	Configuration 2 with PM loading	63
4.6	Pressure drop for configuration 2 experiment stages	64
4.7	Configuration 3 test setup	66
4.8	Pressure drop for Configuration 3 test cycle PO-C	67
4.9	Schematic of SCR-F calibration with configuration 1 data without urea injection	73
4.10	Schematic of SCR-F calibration with configuration 1 data with urea injection	79
4.11	Schematic of SCR-F calibration with configuration 2 data SCR reaction kinetics	82
5.1	Outlet NO ₂ emissions from PO-C experiment (with and without urea injection) inlet temperature = 349/347°C, NO ₂ = 301/228 ppm, NO = 387/321 ppm	86
5.2	NO ₂ in the PM cake for PO-C experiment (with and without urea injection) inlet temperature = 349/347°C, NO ₂ = 301/228 ppm, NO = 387/321 ppm for Test C	87
5.3	Change in NO ₂ concentration through the PM cake and substrate wall for PO-C (with/without urea) inlet temperature = 349/347°C, NO ₂ = 301/228 ppm, NO = 387/321 ppm with (t = 6.7 hrs, 47 minutes after start of PM oxidation) and without (t = 6.7 hrs, 52 minutes after start of PM oxidation) urea injection for Test C.	88
	(a) NO ₂ concentration through PM cake + substrate wall with urea injection	88

(b)	NO ₂ concentration through PM cake + substrate wall without urea injection	88
5.4	Experimental and model NO ₂ assisted PM oxidation rates for all 7 SCRF® configuration 1 experiments	89
5.5	2D temperature distribution for Test C (with/without urea) inlet temperature = 349/347°C, NO ₂ = 301/228 ppm, NO = 387/321 ppm with (t = 6.7 hrs, 5 minutes after start of PM oxidation) and without (t = 6.7 hrs, 5 minutes after start of PM oxidation) urea injection.	90
(a)	2D temperature distribution PO-C with urea injection	90
(b)	2D temperature distribution PO-C without urea injection	90
5.6	Change in NO ₂ concentration and NO ₂ /NO _x ratio through the PM cake and substrate wall for PO-C inlet temperature = 347°C, NO ₂ = 301 ppm, NO = 387 ppm with urea injection (t = 6.7 hrs, 47 minutes after start of PM oxidation) for Test C	91
(a)	NO ₂ concentration	91
(b)	Change in NO ₂ /NO _x ratio	91
5.7	2D PM mass distribution for Test C (with/without urea) inlet temperature = 349/347°C, NO ₂ = 301/228 ppm, NO = 387/321 ppm with (t = 6.7 hrs, 47 minutes after start of PM oxidation) and without (t = 6.7 hrs, 52 minutes after start of PM oxidation) urea injection.	92
(a)	2D PM mass distribution with urea injection	92
(b)	2D PM mass distribution without urea injection	92
5.8	Filtration efficiency PO-C with/without urea injection vs time.	93
(a)	Filtration efficiency with urea injection	93
(b)	Filtration efficiency without urea injection	93
5.9	PM mass retained vs time for Test C with and without urea injection	93
(a)	PM mass retained vs time for with urea injection	93
(b)	PM mass retained vs time for without urea injection	93
5.10	Pressure drop vs time for Test C with urea injection inlet temperature = 347 °C, NO ₂ = 228 ppm, NO = 321 ppm	95
5.11	Pressure drop vs time for Test C with urea injection inlet temperature = 349 °C, NO ₂ = 301 ppm, NO = 387 ppm	95
5.12	PM cake permeability vs time for Test C experiment (with and without urea injection) inlet temperature = 349/347 °C, NO ₂ = 301/228 ppm, NO = 387/321 ppm	96
5.13	Contribution of HC, NO ₂ assisted PM and thermal PM oxidation rate to the total energy release during AR stage	97

5.14	Percent of total PM oxidation rate for Thermal and NO ₂ assisted vs exhaust gas temperature during active regeneration	98
5.15	Inlet and outlet NO, NO ₂ , NH ₃ concentrations Test 1 inlet temperature = 206°C, NO ₂ = 203 ppm, NO = 403 ppm, 2 g/l PM loading configuration 2	101
5.16	Inlet and outlet NO, NO ₂ , NH ₃ concentrations Test 8 inlet temperature = 438°C, NO ₂ = 125 ppm, NO = 424 ppm, 2 g/l PM loading configuration 2	103
5.17	Change in local NO ₂ /NO _x ratio across PM cake and substrate wall slabs configuration 2 with PM loading experiments	104
5.18	SCR reaction rates for configuration 2 vs time - Test 6 with 2 g/l .	105
5.19	Change in Effectiveness factor for the three SCR reactions and adsorption reactions on site 1 and 2 vs PM mass retained in the wall . . .	106
5.20	2D Temperature distribution experimental and model for Test 6 with 2g/l PM loading, ANR = 0.8, 1 and 1.2	108
	(a) 2D experimental temperature distribution at ANR = 0.8, 5 min. after PO start	108
	(b) 2D model temperature distribution at ANR = 0.8, 5 min. after PO start	108
	(c) 2D experimental temperature distribution at ANR = 1.0, 10 min. after PO start	108
	(d) 2D model temperature distribution at ANR = 1.0, 10 min. after PO start	108
	(e) 2D experimental temperature distribution at ANR = 1.2, 15 min. after PO start	108
	(f) 2D model temperature distribution at ANR = 1.2, 15 min. after PO start	108
5.21	NO _x conversion efficiency experimental and model vs ANR for Configuration 2 data with and without urea injection	110
5.22	2D SCR-F + 1D SCR model - Configuration 3	112
5.23	SCR-F® and SCR NO _x conversion efficiency vs exhaust gas temperature for the SCR-F®+SCR	113
5.24	Simulated NO ₂ /NO _x ratio and NO _x conversion efficiency vs time for Test C inlet data for PM loading 2g/l and inlet temperature 339°C.	114
5.25	SCR-F® NO ₂ /NO _x ratio vs outlet NO, NO ₂ and NH ₃ concentrations for Test C at ANR = 1.0	115
5.26	NH ₃ slip SCR model vs inlet NO ₂ /NO _x ratio at ANR = 1.2 for test 5	116

5.27	Coverage fraction of SCR NH ₃ storage sites 1 and 2 vs SCR inlet temperature	117
5.28	NH ₃ slip for SCR-F model and experimental data at ANR = 1.0 vs SCR inlet temperature	117
5.29	NH ₃ slip for SCR model and experimental data at ANR = 1.0 vs SCR inlet temperature	118
5.30	Contribution of the three SCR reactions in the NO _x reduction performance of the SCR from the model at ANR = 1.0	119
5.31	NO _x conversion efficiency vs SCR inlet NO ₂ /NO _x ratio from the model at ANR = 1.0	120
5.32	NO ₂ /NO _x ratio vs percent NO _x conversion SCRF® and SCR at ANR = 1.0 from the models	121
5.33	SCR NO _x conversion efficiency vs exhaust gas temperature for the SCRF®+SCR system with NO ₂ /NO _x ratio = 0 (Experimental and 2D SCR-F Model data)	122
5.34	SCR NO _x conversion efficiency vs exhaust gas temperature for the SCRF®+SCR system with NO ₂ /NO _x ratio = 0.5 (2D SCR-F Model data)	123
6.1	SCR-F estimator model 5X5 mesh	127
6.2	SCR-F estimator model pressure drop vs time PO - C with urea injection	129
6.3	SCR-F estimator model filtration efficiency vs time PO - C with urea injection	130
6.4	SCR-F estimator model PM mass retained vs time PO - C with urea injection	131
6.5	SCR-F estimator model outlet temperature vs time PO - C with urea injection	131
6.6	SCR-F estimator model outlet NO concentration vs time PO - C with urea injection	132
6.7	SCR-F estimator model outlet NO ₂ concentration vs time PO - C with urea injection	133
6.8	SCR-F estimator model outlet NH ₃ concentration vs time PO - C with urea injection	133
6.9	Experimental 2D temperature distribution - PO - C with urea injection	134
6.10	SCR-F estimator model 2D temperature distribution PO - C with urea injection	134

6.11 SCR-F estimator model 2D PM mass distribution PO - C with urea injection	135
6.12 SCR-F State estimator outlet temperature vs time (estimator off and on case) Test 6 with 2g/l PM loading	142
6.13 SCRF® experimental temperature distribution 5 minutes after start of Passive oxidation in Test 6 with 2g/l PM loading	143
6.14 2D SCR-F model temperature distribution 5 minutes after start of Passive oxidation in Test 6 with 2g/l PM loading	144
6.15 SCR-F state estimator temperature distribution 5 minutes after start of Passive oxidation in Test 6 with 2g/l PM loading with open loop estimator	145
6.16 SCR-F state estimator temperature distribution 5 minutes after start of Passive oxidation in Test 6 with 2g/l PM loading with closed loop estimator	145
6.17 SCR-F PM mass retained vs time (Experimental, 2D SCR-F model, SCR-F state estimator) Test 6 with 2g/l PM loading	146
6.18 SCR-F pressure drop vs time (Experimental, 2D SCR-F model, SCR-F state estimator) Test 6 with 2g/l PM loading	147
6.19 SCR-F state estimator 2D PM mass distribution Test 6 with 2g/l PM loading	148
6.20 SCR-F NH ₃ coverage fraction site 1 vs time (Experimental, 2D SCR-F model, SCR-F state estimator) Test 6 with 2g/l PM loading	149
6.21 SCR-F NH ₃ coverage fraction site 2 vs time (Experimental, 2D SCR-F model, SCR-F state estimator) Test 6 with 2g/l PM loading	149
6.22 SCR-F outlet NO vs time (Experimental, 2D SCR-F model, SCR-F state estimator) Test 6 with 2g/l PM loading	150
6.23 SCR-F outlet NO ₂ vs time (Experimental, 2D SCR-F model, SCR-F state estimator) Test 6 with 2g/l PM loading	150
6.24 SCR-F outlet NH ₃ vs time (Experimental, 2D SCR-F model, SCR-F state estimator) Test 6 with 2g/l PM loading	151
6.25 DOC+SCRF® system	152
6.26 DOC-SCRF® outlet NO concentration experimental and estimator vs time Test 6 0g/l PM loading	153
6.27 DOC-SCRF® outlet NO ₂ concentration experimental and estimator vs time Test 6 0g/l PM loading	154
6.28 DOC-SCRF® outlet NH ₃ concentration experimental and estimator vs time Test 6 0g/l PM loading	154

6.29	DOC-SCR [®] outlet exhaust gas temperature experimental and estimator vs time Test 6 0g/1 PM loading	155
7.1	Aftertreatment system with SCR-F with 1 injector	158
7.2	Aftertreatment system with SCR-F+SCR with 1 injector	158
7.3	Aftertreatment system with SCR-F, SCR and two urea injectors	159
7.4	A new, ultra low outlet NO _x aftertreatment system with a SCR-F, a downstream DOC ₂ and a SCR with two injectors	160
7.5	Aftertreatment system with dCSC TM , SCR-F, downstream DOC ₂ and SCR with two injectors	161
7.6	Outlet concentrations and SCR [®] outlet NO ₂ /NO _x ratio vs inlet ANR values at engine condition C (SCR [®] with 1 injector)	165
7.7	NO _x conversion efficiency, urea flow rate and PM oxidation rate vs SCR [®] Inlet ANR at engine condition C (SCR [®] with 1 injector)	166
7.8	NO _x conversion efficiency, urea flow rate and outlet concentrations vs SCR [®] inlet ANR at engine condition C (SCR [®] +SCR with 1 urea injector)	167
7.9	NO _x conversion efficiency, ANR ₂ , PM oxidation rate, SCR [®] outlet NO ₂ and SCR outlet NH ₃ concentration vs ANR ₁ at engine condition C (SCR [®] +DOC ₂ +SCR with 2 urea injectors)	168
7.10	NO ₂ /NO _x ratio vs ANR ₁ at engine condition C (SCR [®] +DOC ₂ +SCR with 2 urea injectors)	169
7.11	NO _x conversion efficiency, urea flow rate and outlet concentrations vs SCR [®] Inlet ANR ₂ at engine condition C and for ANR ₁ 0.6 and 0.7 (SCR [®] +SCR with 2 urea injectors)	171
7.12	NO _x conversion efficiency, urea flow rate and outlet concentration vs SCR [®] inlet ANR at engine condition C (SCR [®] +DOC ₂ +SCR with 2 urea injectors)	172
7.13	NO _x conversion efficiency, urea flow rate and PM oxidation rate vs system Inlet ANR at engine condition C	173
7.14	DOC+SCR [®] +DOC ₂ +SCR control system flowchart	185
A.1	2D SCR-F model mesh	206
B.1	Schematic of the 2D SCR-F model temperature solver mesh	209
C.1	Inhibition of NH ₃ transport to active site due to PM in the substrate wall	213

D.1	Schematic of the streamlines (shown a dashed lines) used for calculating the pressure drop across CPF/SCR-F for 3x1 zone model (4 axial and 1 radial discretization).	217
F.1	Test 1 with 2g/l PM loading outlet emissions vs time	239
F.2	Test 1 with 4 g/l PM loading outlet emissions vs time	239
F.3	Test 3 with 2 g/l PM loading outlet emissions vs time	240
F.4	Test 3 with 4 g/l PM loading outlet emissions vs time	240
F.5	Test 6 with 2 g/l PM loading outlet emissions vs time	241
F.6	Test 6 with 4 g/l PM loading outlet emissions vs time	241
F.7	Test 8 with 2 g/l PM loading outlet emissions vs time	242
F.8	Test 8 with 4 g/l PM loading outlet emissions vs time	242
F.9	Test 1 with 2 and 4 g/l PM loading experimental and model temperature distribution at ANR = 1.2	243
	(a) Test 1 2 g/l	243
	(b) Test 1 4 g/l	243
F.10	Test 3 with 2 and 4 g/l PM loading experimental and model temperature distribution at ANR = 1.2	244
	(a) Test 3 2 g/l	244
	(b) Test 3 4 g/l	244
F.11	Test 6 with 2 and 4 g/l PM loading experimental and model temperature distribution at ANR = 1.2	245
	(a) Test 6 2 g/l	245
	(b) Test 6 4 g/l	245
F.12	Test 8 with 2 and 4 g/l PM loading experimental and model temperature distribution at ANR = 1.2	246
	(a) Test 8 2 g/l	246
	(b) Test 8 4 g/l	246
G.1	Temperature distribution during NO _x reduction at ANR 1 - Test 6 with 2 g/l PM loading configuration 2	250
G.2	Different catalyst loading zones in the SCR [®]	251
H.1	NO _x conversion efficiency, ANR ₂ , PM oxidation rate, SCR [®] outlet NO ₂ and SCR outlet NH ₃ concentration vs ANR ₁ at engine condition 1 (SCR [®] +DOC ₂ +SCR with 2 urea injectors)	257
H.2	Outlet concentrations and SCR [®] outlet NO ₂ /NO _x ratio vs inlet ANR values at engine condition 1 (SCR [®] with 1 injector)	258
H.3	NO ₂ /NO _x ratio vs ANR ₁ at engine condition 1 (SCR [®] +DOC ₂ +SCR with 2 urea injectors)	258

H.4	NO _x conversion efficiency, urea flow rate and PM oxidation rate vs SCRF® Inlet ANR at engine condition 1 (SCRF® with 1 injector)	259
H.5	NO _x conversion efficiency, ANR ₂ , PM oxidation rate, SCRF® outlet NO ₂ and SCR outlet NH ₃ concentration vs ANR ₁ at engine condition A (SCRF®+DOC ₂ +SCR with 2 urea injectors)	260
H.6	Outlet concentrations and SCRF® outlet NO ₂ /NO _x ratio vs inlet ANR values at engine condition A (SCRF® with 1 injector)	261
H.7	NO ₂ /NO _x ratio vs ANR ₁ at engine condition A (SCRF®+DOC ₂ +SCR with 2 urea injectors)	261
H.8	NO _x conversion efficiency, urea flow rate and PM oxidation rate vs SCRF® Inlet ANR at engine condition A (SCRF® with 1 injector)	262
H.9	NO _x conversion efficiency, ANR ₂ , PM oxidation rate, SCRF® outlet NO ₂ and SCR outlet NH ₃ concentration vs ANR ₁ at engine condition D (SCRF®+DOC ₂ +SCR with 2 urea injectors)	263
H.10	Outlet concentrations and SCRF® outlet NO ₂ /NO _x ratio vs inlet ANR values at engine condition D (SCRF® with 1 injector)	264
H.11	NO ₂ /NO _x ratio vs ANR ₁ at engine condition D (SCRF®+DOC ₂ +SCR with 2 urea injectors)	264
H.12	NO _x conversion efficiency, urea flow rate and PM oxidation rate vs SCRF® Inlet ANR at engine condition D (SCRF® with 1 injector)	265
H.13	NO _x conversion efficiency, ANR ₂ , PM oxidation rate, SCRF® outlet NO ₂ and SCR outlet NH ₃ concentration vs ANR ₁ at engine condition E (SCRF®+DOC ₂ +SCR with 2 urea injectors)	266
H.14	Outlet concentrations and SCRF® outlet NO ₂ /NO _x ratio vs inlet ANR values at engine condition E (SCRF® with 1 injector)	267
H.15	NO ₂ /NO _x ratio vs ANR ₁ at engine condition E (SCRF®+DOC ₂ +SCR with 2 urea injectors)	267
H.16	NO _x conversion efficiency, urea flow rate and PM oxidation rate vs SCRF® inlet ANR at engine condition E (SCRF® with 1 injector)	268
H.17	NO conversion efficiency vs DOC ₂ temperature for all the five engine conditions	269

List of Tables

3.1	Reactions in the SCR-F model	48
4.1	Aftertreatment system specification	57
4.2	Passive oxidation SCR-F® inlet conditions for PO experiments without urea in configuration 1	60
4.3	Passive oxidation conditions for PO experiments with urea in configuration 1	61
4.4	Active regeneration conditions for AR experiments in configuration 1 without urea injection	62
4.5	Configuration 2 with and without PM engine and exhaust conditions	65
4.6	Configuration 3 engine and exhaust conditions	67
4.7	Coriolis meter specifications	68
4.8	Specifications of the thermocouples used in the aftertreatment system	69
4.9	Specifications of pressure transducers	69
4.10	Specifications of IMR-MS and calibration gases	70
4.11	Specification NO _x and NH ₃ sensor on production aftertreatment system	70
4.12	Specifications of the weighing balance used to weigh the SCR-F® .	71
4.13	Pressure drop parameters during PM loading for the SCR-F model	76
4.14	Pressure drop parameters during PM loading SCR-F model	77
4.15	Pressure drop parameters during PM loading SCR-F model	78
5.1	NO ₂ /NO _x at SCR-F® inlet, SCR-F® wall inlet and SCR inlet.	113
7.1	Engine conditions	163
7.2	Aftertreatment components specifications	164
7.3	Performance of the four systems at system ANR = 1.04	174
7.4	SCR-F®+DOC ₂ +SCR system performance for maximum NO _x conversion efficiency	175
7.5	SCR-F®+DOC ₂ +SCR system performance for maximum PM oxidation rate at ANR ₁ = 0	175

7.6	SCR-F®+DOC ₂ +SCR System Performance for Maximum PM Oxidation Rate at ANR ₁ = 0	176
F.1	Outlet NH ₃ (experimental vs model) configuration 1 data	225
F.2	Outlet temperature (experimental vs model) configuration 1 data	225
F.3	Filtration efficiency (experimental vs model) configuration 1 data	226
F.4	Pressure drop (experimental vs model) configuration 1 data	227
F.5	PM mass retained (experimental vs model) configuration 1 data	228
F.6	Outlet NO ₂ (experimental vs model) configuration 1 data	229
F.7	Outlet NO (experimental vs model) configuration 1 data	230
F.8	Outlet temperature (experimental vs model) configuration 2 data	231
F.9	Filtration efficiency (experimental vs model) configuration 2 data	231
F.10	Pressure drop (experimental vs model) configuration 2 data	232
F.11	PM mass retained (experimental vs model) configuration 2 data	232
F.12	Outlet NO ₂ (experimental vs model) configuration 2 data	233
F.13	Outlet NO (experimental vs model) configuration 2 data	234
F.14	Outlet NH ₃ (experimental vs model) configuration 2 data	235
F.15	Outlet temperature (experimental vs model) configuration 3 data	236
F.16	Filtration efficiency (experimental vs model) configuration 3 data	236
F.17	Pressure drop (experimental vs model) configuration 3 data	237
F.18	PM mass retained (experimental vs model) configuration 3 data	237
F.19	Outlet NO ₂ (experimental vs model) configuration 3 data	238
F.20	Outlet NO (experimental vs model) configuration 3 data	238
F.21	Outlet NH ₃ (experimental vs model) configuration 3 data	238
G.1	SCR-F model pressure drop parameters	248
G.2	SCR-F model thermal parameters	249
G.3	PM oxidation kinetics - PM cake	251
G.4	PM oxidation kinetics - PM in the wall	252
G.5	Gaseous species kinetics	252
G.6	SCR kinetics	253
G.7	Diffusivity parameters	254
G.8	Chemical species diffusivity values	254
G.9	Cake permeability parameters	255

Preface

The work presented in this PhD dissertation has resulted in four publications and one patent disclosure. The first journal paper has been published in the Emissions Control Science and Technology Journal, the second paper has been published in the SAE Fuels and Lubricants Journal, the third paper based on ultra low NO_x aftertreatment system has been submitted to the SAE Fuels and Lubricants Journal and a fourth paper on the SCR-F state estimator development is in draft phase and will be submitted to the International Journal of Engine Research. A technology disclosure on Ultra Low NO_x was submitted to Michigan Technological University to evaluate the possibility of applying a patent based on this technology.

The first paper titled “Development of a 2D SCR-F Model” has been used for development of Chapters 1 to 5 in the dissertation. The authors of this publication are Venkata Rajesh Chundru, Dr.Boopathi S. Mahadevan, Dr.Gordon G. Parker, Dr.John H. Johnson and Dr.Mahdi Shahbakthi from Michigan Technological University. Venkata Rajesh Chundru was responsible for development of the 2D SCR-F model. Dr.Boopathi S. Mahadaven and Dr.Gordon G. Parker developed the framework for the model development. Dr.John H. Johnson provided the technical guidance regarding the experimental data and modeling aspects.

The second paper titled “The Effect of NO_2/NO_x Ratio on the Performance of a SCR Downstream of a SCR Catalyst on a DPF” deals with development of a system model consisting of 2D SCR-F and 1D SCR models developed at Michigan Technological University. The aim of the paper is to develop a model that can simulate the experimental data collected on a SCR-F® + SCR system at Michigan Technological University and determine the NO_x conversion efficiency of the individual components present in the system. This paper was used for Chapter 5 of the dissertation. The authors of this publication are Venkata Rajesh Chundru, Dr.Gordon G. Parker and Dr. John H. Johnson of Michigan Technological University. Venkata Rajesh Chundru was responsible for the model development and calibration. Dr.John H. Johnson and Dr.Gordon G. Parker provided the technical guidance for the experimental data and modeling aspects.

The third paper titled “A Modeling Study of an Advanced Ultra-Low NO_x Aftertreatment System” based on the ultra low NO_x aftertreatment system disclosure with

Venkata Rajesh Chundru, Dr.Gordon G. Parker and Dr.John H. Johnson as the authors has been submitted to the SAE Fuels and Lubricants Journal.

The fourth paper titled “Development of a Extended Kalman Filter Based State Estimator for a SCR Catalyst on a DPF” deals with development of a simplified SCR-F model and EKF based state estimator to estimate the unknown internal states of 2D temperature, PM mass retained and NH₃ coverage fraction of the two storage sites in a SCR Catalyst on a DPF. The authors of this paper are Venkata Rajesh Chundru, Dr.Gordon G. Parker and Dr.John H. Johnson. Venkata Rajesh Chundru was responsible for development of the SCR-F state estimator code. Dr.Gordon G. Parker and Dr.John H. Johnson provided the technical guidance for development of the state estimator. This paper is in draft phase and will be submitted to International Journal of Engine Research. Parts of this paper were used to develop Chapter 6 of the dissertation.

The Ultra Low NO_x technology disclosure was submitted to Michigan Technological University to evaluate the possibility of applying a patent based on this technology. The authors of this work are Venkata Rajesh Chundru, Dr.Gordon G.Parker and Dr.John H. Johnson. The work for this invention was conceived to overcome the limitations of a SCR-F+SCR system. Venkata Rajesh Chundru was responsible for all the simulation results presented in this work. Dr.Gordon G. Parker and Dr.John H. Johnson provided the technical guidance for the project. Parts of the disclosure were used to develop Chapter 7 of the dissertation.

The citations of the two published journals and the third journal under review are :

1. Chundru, V.R., Mahadevan, B.S., Johnson, J.H., Parker, G.G., Shahbakhti, M.: “Development of a 2D Model of a SCR Catalyst on a DPF”, Journal of Emiss. Control. Sci Technol., (2019). doi: 10.1007/s40825-019099115-4.
2. Chundru, V., Parker, G., and Johnson, J., “The Effect of NO₂/NO_x Ratio on the Performance of a SCR Downstream of a SCR Catalyst on a DPF,” SAE Int. J. Fuels Lubr. 12(2):2019, doi:10.4271/04-12-02-0008.
3. Chundru, V., Parker, G., and Johnson, J., “A Modeling Study of an Advanced Ultra-Low NO_x Aftertreatment System,” SAE Int. J. Fuels Lubr. (2019, under review)

Acknowledgments

I would like to thank my advisors Dr.Gordon G. Parker and Dr.John H. Johnson whose constant support and encouragement has helped me to pursue this research. I would also like to thank Dr.Jeffery D. Naber and Dr.Sunil S. Mehendale for spending time on my committee and reviewing my research. I would also like to thank all the graduate students in my research group including Vaibhav Kadam, Krishnan Ragahavan, Erik Gustafson, Saksham Gupta, Abhishek Jadav and Sagar Sharma who collected the experimental data that has been used for this research work. Also I would like to thank Dr.Boopathi S. Mahadevan who helped me immensely in development of the SCR-F model framework.

I would like to thank MTU Diesel Engine Aftertreatment Consortium (Cummins, John Deere, Isuzu, Daimler, Johnson Matthey, Tenneco and Corning) and the Michigan Technological University graduate school for supporting this project and providing financial support for the duration of this study.

I would like to thank my parents Ch.Surya Narayana Murthy and Ch.Sai Sudha without whom all of this effort wouldn't have been possible. Last but not the least, I would also like to thank my friends including Jaya, Yash, Sri Ram, Hemanth, Nelima, Nandu, Bhargav, Dasika and Niranjan among others who have supported me during the course of this study.

Nomenclature

List of symbols

$1D$	1Dimensional
$2D$	2Dimensional
$3D$	3Dimensional
$0D$	0Dimensional
a	Width of the clean inlet and outlet channel [m]
a^*	Effective width of the clean inlet channel loaded with PM [m]
A	Heat transfer area normal to the gas flow [m ²]
A_{amb}	Surface area of outer surface [m ²]
\bar{A}	Average cross-sectional area [m ²]
A_f	Cross-sectional area perpendicular to direction of heat transfer [m ²]
A_r	Area normal to direction of heat transfer in the radial direction [m ²]
A_{CO}	Pre-exponential for CO oxidation reaction [m K ⁻¹ s ⁻¹]
A_{HC}	Pre-exponential for HC oxidation reaction [m K ⁻¹ s ⁻¹]
A_{NO}	Pre-exponential for NO oxidation reaction [m K ⁻¹ s ⁻¹]
A_{NO_2}	Pre-exponential for NO ₂ assisted PM oxidation [m K ⁻¹ s ⁻¹]
$A_{NO_2, cake}$	Pre-exponential for NO ₂ -assisted PM oxidation used in filtration and pressure drop models [m K ⁻¹ s ⁻¹]
$A_{NO_2, wall}$	Pre-exponential for NO ₂ -assisted PM oxidation used in filtration and pressure drop models [m K ⁻¹ s ⁻¹]
A_{O_2}	Pre-exponential for thermal (O ₂) PM oxidation [m K ⁻¹ s ⁻¹]
$A_{O_2, cake}$	Pre-exponential for thermal (O ₂) PM oxidation used in the temperature model [m K ⁻¹ s ⁻¹]
$A_{s_{i,j}}$	Combined surface area of both Inlet and outlet channels [m ²]
$A_{s_{i,i,j}}$	Surface area of Inlet channels [m ²]
$A_{s_{o,i,j}}$	Surface area of outlet channels [m ²]
ANR	Ammonia to NO _x ratio
ANR_1	Ammonia to NO _x ratio at urea injector 1 for ultra low NO _x system [-]
ANR_2	Ammonia to NO _x ratio at urea injector 2 for ultra low NO _x system [-]
AMOX	Ammonia oxidation catalyst

ASC	Ammonia slip catalyst
AR	Active Regeneration experiment
b	Wall unit cell diameter [-]
BSPM	Brake specific PM
BSNO _x	Brake specific NO _x
C	Constant notation used for temperature factor [-]
c_f	Specific heat of filter material [J kg ⁻¹ K ⁻¹]
c_{NO_2}	CPF inlet NO ₂ concentration [mg m ⁻³]
c_{O_2}	CPF inlet O ₂ concentration [mg m ⁻³]
c_{HC}	HC concentration [mg m ⁻³]
c_i	Concentration of chemical species i [mg m ⁻³]
c_p	Constant pressure specific heat [J kg ⁻¹ K ⁻¹]
c_v	Constant volume specific heat [J kg ⁻¹ K ⁻¹]
C_{PM}	CPF and SCR-F inlet PM concentration [mg m ⁻³]
c_s	Specific heat of PM cake [J kg ⁻¹ K ⁻¹]
C3	Reference pressure for wall permeability correction factor [kPa]
C4	Wall permeability correction factor [-]
C5	Cake permeability correction factor [-]
C6	Reference pressure for lambda correction [kPa]
C7	Reference temperature for lambda correction [°C]
C_{8NO_2}	Slope of the delta mass offset equation for NO ₂ assisted PM oxidation [s-g]
C_{8th}	Slope of the delta mass offset equation for thermal (O ₂) PM oxidation [s-g]
C_{9NO_2}	Constant of the delta mass offset equation for NO ₂ -assisted PM oxidation [-]
C_{9th}	Constant of the delta mass offset equation for thermal (O ₂) PM oxidation [-]
C10	Slope of the post loading permeability equation [g ⁻¹]
C11	Constant for post loading permeability equation [-]
CPF	Catalyzed Particulate Filter
CO	Carbon Monoxide
CO ₂	Carbon Dioxide
CDPF	Catalyzed DPF
Cu-Ze	Copper Zeolite
CuO	Copper oxide
CSF	Catalyzed soot filter
d	Side length of square channels [m]

D	Overall diameter of the CPF [m]
d	Damage variable [-]
DOC	Diesel Oxidation Catalyst
DPF	Diesel Particulate Filter
$d_{C,s_i,j}$	Instantaneous wall collector diameter at each zone [m]
$d_{C0,s}$	Initial wall collector diameter [m]
D_I	Effective diffusivity of species [-]
$D_{kn,l}$	Knudsen diffusivity of species [-]
$D_{mol,l}$	Molecular diffusivity of species [-]
DDOC	Downstream of DOC
DSCR _F	Downstream of SCR-F
DSCR	Downstream of SCR
$d_{pore,wall}$	Diameter of pore in the substrate wall [m]
E_{CO}	Activation energy for CO oxidation [J gmol ⁻¹]
E_{HC}	Activation energy for HC oxidation [J gmol ⁻¹]
E_{NO}	Activation energy for NO oxidation [J gmol ⁻¹]
E_{NO_2}	Activation energy for NO ₂ assisted PM oxidation [J gmol ⁻¹]
E_{O_2}	Activation energy for O ₂ assisted PM oxidation [J gmol ⁻¹]
EKF	Extended Kalman Filter
ECU	Electronic control unit
F	Friction factor in the inlet and outlet channel of the particulate filter [-]
F3-1	Radiation view factor between inlet of the channel to filter wall [-]
F3-2	Radiation view factor between outlet of the channel to filter wall [-]
FE-Ze	Iron zeolite
FTP75	Federal Test Procedure 75
h_{amb}	Ambient convective heat transfer coefficient [W m ⁻² K ⁻¹]
h_g	Convective heat transfer coefficient [W m ⁻² K ⁻¹]
HC	Hydrocarbons
ΔH_{reac}	Heat of reaction for carbon oxidation via O ₂ [J kg ⁻¹]
J1	Radiosity of channel inlet surface [W m ⁻²]

J2	Radiosity of filter wall surface [W m^{-2}]
J3	Radiosity of channel outlet surface [W m^{-2}]
k_d	Permeability of the damaged porous media [m^2]
k_g	Thermal conductivity of channel gas [$\text{W m}^{-1} \text{K}^{-1}$]
k_{NO_2}	Rate constant for NO_2 assisted PM oxidation [m s^{-1}]
$k_{NO_2,i,j}$	Rate constant for NO_2 assisted PM oxidation at each zone [m s^{-1}]
k_{O_2}	Rate constant for O_2 assisted PM oxidation [m s^{-1}]
$k_{O_2,i,j}$	Rate constant for O_2 assisted PM oxidation at each zone [m s^{-1}]
$k_{P,i,j}$	Permeability of PM cake layer accounting for the change in gas mean free path length [m^2]
$k_{s,i,j}$	Permeability of substrate wall due to change in wall collector diameter at each zone [m^2]
$k_{wall,i,j}$	Wall permeability at each zone [m^2]
k_0	Permeability of the undamaged porous media [m^2]
K_{sub}	Thermal conductivity of substrate wall [W/m.K]
K_{PM}	Thermal conductivity of PM cake [W/m.K]
K_k	Kalman gain at time step k
L	Axial length [m]
L_t	Total length of CPF or SCR-F [m]
\dot{m}	Instantaneous exhaust mass flow rate [kg s^{-1}]
M	Number of radial zones [-]
$m_{cake,initial}$	Initial mass of the undamaged PM cake [g]
$m_{cake,corr}$	Mass of the PM cake after applying delta mass offset value at current time step [g]
$m_{Cim,j}$	Mass of cake PM in each zone [kg]
$m_i n$	Inlet PM mass in each zone [kg]
$\dot{m}_{i,j}$	Mass flow rate at each zone [kg s^{-1}]
$m_{s,i,j}$	Mass of PM retained in each zone [kg]
m_{s_t}	Mass of total PM inlet to the CPF or SCR-F [kg]
\dot{m}_{total}	Total mass flow rate into CPF or SCR-F [kg s^{-1}]
$\dot{m}_{i,j}$	Mass flow rate into a given zone [kg s^{-1}]
$[mw_{i,j}]_n$	Mass of PM in each zone for slab n [kg]
$(MW)_{exh}$	Molecular weight of exhaust gas [kg/kmol]

\dot{m}_{in}	PM mass flow rate into a zone [kg/s]
\dot{m}_{out}	PM mass flow rate out of a zone [kg/s]
\dot{m}_{ret}	Rate of PM retained in a zone [kg/s]
\dot{m}_{ox}	Rate of PM oxidation in a zone [kg/s]
M	Number of radial zones
n	Wall slab index [-]
N	Number of axial zones [-]
NEDC	New European drive cycle
NO	Nitrogen Monoxide
NO ₂	Nitrogen Dioxide
NO _x	Oxides of Nitrogen
N ₂ O	Nitrous Oxide
NH ₃	Ammonia
N ₂	Nitrogen
NH ₄ NO ₃	Ammonium Nitrate
n_{max}	Maximum number of wall slabs [-]
N_{c_i}	Number of cells in each radial zone [-]
N_{ct}	Total number of cells [-]
$Np_{i,j}$	Number of pores at each zone [-]
n_{sp}	Number of chemical species [-]
Nu	Nusselt number [-]
N	Number of axial zones
OBD	On board diagnostics
ODE15s	Variable time step ODE solver
P_{in}	CPF or SCR-F inlet gas pressure [kPa]
$P_1 _{i,j}$	Absolute pressure at the inlet channel of each zone [kPa]
$P_2 _{i,j}$	Absolute pressure at the outlet channel of each zone [kPa]
p	Number of slabs in the substrate wall [-]
PM	Particulate Matter
PO	Passive oxidation experiment
POU	Passive oxidation experiment with urea injection
P_m	Absolute pressure of exhaust gas [kPa]
$\dot{Q}_{cond,axial}$	Axial conduction [W]
\dot{Q}_{conv}	Convection between channels gases and filter wall [W]
$\dot{Q}_{cond,radial}$	Radial conduction [W]
\dot{Q}_{rad}	Radiation between channel surfaces [W]
$\dot{Q}_{reac,HC}$	Energy released during oxidation of

	HC in the inlet gas [W]
$\dot{Q}_{reac,SCR}$	Energy released during SCR reactions [W]
$\dot{Q}_{reac,PM}$	Energy released during oxidation of PM [W]
Δr	Effective zone radius [m]
RR_{CO}	Reaction rate of carbon monoxide [s ⁻¹]
RR_{HC}	Reaction rate of hydrocarbons [s ⁻¹]
RR_{ov}	Overall reaction rate [s ⁻¹]
RR_H	Universal gas constant [J mol ⁻¹ K ⁻¹]
R	Radius of SCR-F [m]
\bar{R}	Universal gas constant [kJ/kmol K]
R_j	Reaction rate of reaction j [kmol/m ^s s]
R_k	Covariance matrix of state estimator
\dot{S}_{CO_2}	Thermal (O ₂) assisted PM cake oxidation rate [kg C(s) m ⁻³ s ⁻¹]
\dot{S}_{CNO_2}	NO ₂ assisted PM cake oxidation rate [kg C(s) m ⁻³ s ⁻¹]
SCR	Selective Catalytic Reduction
SCR – A	Production SCR
SCR – B	Production SCR with AMOX coating at the end
SCR – F	SCR catalyst on a DPF
SCR _F	Johnson Matthey SCR-F
Smax	Number of ways of calculating the inlet pressure at each radial section [-]
S1 – S20	Thermocouple name [-]
S_p	Specific surface area of PM (5.5*10 ⁷) [m ⁻¹]
t	Time [s]
T_{amb}	Ambient temperature [K]
T_m	Temperature of the exhaust gas [K]
T_f	Temperature of combined filter and PM cake [K]
$T_{f,i,j}$	Temperature of combined filter and PM cake at each zone [K]
T_{in}	CPF or SCR-F inlet temperature [K]
T_1	Exhaust gas temperature in the inlet channel [K]
T_2	Exhaust gas temperature in the outlet channel [K]
T_W	Temperature of the substrate wall [K]
$[T_{i,j}]_k$	Temperature of substrate wall in zone i,j at time step k [K]
$T_{inlet,i,j}$	Temperature of the gas at the inlet channel at each zone [K]
$t_{ins+can}$	Thickness of insulation and can [-]
$ts_{i,j}$	PM cake thickness at each zone [m]

$u_{inlet,i,j}$	Inlet channel velocity at each zone [$m s^{-1}$]
$u_{outlet,i,j}$	Outlet channel velocity at each zone [$m s^{-1}$]
u_k	Input at time step k
$UDOC$	Upstream of DOC
$USCRF$	Upstream of SCR-F
$USCR$	Upstream of SCR
$v_{s,i,j}$	Velocity of gas through PM cake layer at each zone [$m s^{-1}$]
$v_{w,i,j}$	Velocity of gas through substrate wall at each zone [$m s^{-1}$]
$V_{i,j}$	Total volume of a zone [m^3]
$V_{es,i,j}$	Empty volume in each zone while accounting for average PM cake layer thickness [m^3]
$V_{eo,i,j}$	Empty volume of the substrate wall [m^3]
$V_{fi,j}$	Volume of filter in each zone [m^3]
VF_i	Volume fraction at each axial section of the CPF or SCR-F [-]
V_{inlet}	Volume of inlet channels [m^3]
V_{outlet}	Volume of outlet channels [m^3]
$V_{s,i,j}$	PM cake volume in each zone [m^3]
V_t	Total volume of CPF or SCR-F [m^3]
V_w	Volume of substrate wall [m^3]
V_{PM}	Volume of PM cake [m^3]
v_1	Exhaust gas velocity in inlet channel [m/s]
v_2	Exhaust gas velocity in outlet channel [m/s]
v_w	Exhaust gas velocity in PM cake + Substrate wall [m/s]
W	Exhaust gas molecular weight [$kg kmol^{-1}$]
W_C	Molecular weight of carbon [$kg kmol^{-1}$]
W_{NO_2}	Molecular weight of nitrogen dioxide [$kg kmol^{-1}$]
W_{O_2}	Molecular weight of oxygen [$kg kmol^{-1}$]
$w_{p,i,j}$	PM cake layer thickness at each zone [m]
w_p	Average PM cake layer thickness of the CPF or SCR-F [m]
w_s	Substrate wall thickness [m]
w_k	State estimator process noise matrix
WHTC	World harmonized transient cycle
x	Diameter ratio of CPF or SCR-F [-]
x_k	State estimate at time step k
x_{model}	Model value of variable x
x_{exp}	Experimental value of variable x

Y_l	Concentration of species l [mg L ⁻¹]
Y_{i,jNO_2}	Mass fraction of inlet NO ₂ at each zone [-]
Y_{i,jO_2}	Mass fraction of inlet O ₂ at each zone [-]

Subscripts and Superscripts

i	Radial direction
j	Axial direction
l	Species index
m	Reactions index
p	Wall slab index
s	Stream line index

Greek Symbols

α_{NO_2}	NO ₂ oxidation partial factor [-]
α_{k,NO_2}	Multiplicative constant for cake permeability model of NO ₂ assisted PM oxidation [-]
α_{O_2}	O ₂ oxidation partial factor [-]
α_{k,O_2}	Multiplicative constant for cake permeability model of thermal (O ₂) PM oxidation [-]
β_{k,NO_2}	Power constant for cake permeability model of NO ₂ assisted PM oxidation [-]
β_{k,O_2}	Power constant for cake permeability model of thermal (O ₂) PM oxidation [-]
$\Delta P_{CPF/SCR-F}$	Total pressure drop across CPF or SCR-F [kPa]
$\Delta P_{cake_{i,j}}$	PM cake pressure drop at each zone [kPa]
ΔL	Effective zone length [m]
Δr	Effective zone radius [m]
$\Delta P_{wall_{i,j}}$	Wall pressure drop at each zone [kPa]
Δt	Solver time step [s]
Δx	Discretization length in axial direction [m]
$\epsilon_{s_{i,j}}$	Porosity of the substrate wall [-]
$\epsilon_{0,s}$	Clean wall porosity [-]

$\rho_{i,j}$	Exhaust gas density at each zone [kg m ⁻³]
ρ_f	Filter substrate density [kg m ⁻³]
ρ_s	PM cake density [kg m ⁻³]
σ	Stefan-Boltzmann constant [W m ⁻² K ⁻⁴]
μ	Dynamic viscosity of exhaust gas [Ns m ⁻²]
$\mu_{avg,gas}$	Average dynamic viscosity of exhaust gas in the CPF or SCR-F [Ns m ⁻²]
$\mu_{i,j}$	Dynamic viscosity of exhaust gas at each zone [Ns m ⁻²]
η_{cake}	PM cake layer filtration efficiency [-]
$\eta_{cake,loaded}$	Loaded PM cake layer filtration efficiency [-]
$\eta_{wall,n}$	Wall filtration efficiency for each slab [-]
$\eta_{wall,i,j,slab,n}$	Wall filtration efficiency for each slab [-]
$\eta_{D,i,j}$	Collection efficiency of a single unit collector due to Brownian diffusion mechanism [-]
$\eta_{R,i,j}$	Particle Collection efficiency of a single unit collector due to interception [-]
$\lambda k_{i,j}$	Effective thermal conductivity of PM cake and filter [W m ⁻¹ K ⁻¹]
λk_f	Thermal conductivity of filter [W m ⁻¹ K ⁻¹]
λk_s	Thermal conductivity of PM cake [W m ⁻¹ K ⁻¹]
η_{total}	Total filtration efficiency [-]
$\lambda_{i,j}$	Mean free path length of the gas [m]
λ_{ref}	Mean free path length of the gas at reference condition [m]
Φ	Partition coefficient [-]
Ψ	Percolation factor [-]
ξ	Stoichiometric coefficient of species l in reaction m [-]
Ω_1	Storage capacity of site 1 [-]
Ω_2	Storage capacity of site 2 [-]
θ_1	Coverage fraction of site 1 [-]
θ_2	Coverage fraction of site 2 [-]

Abstract

This research focuses on modeling and control of PM and NO_x in diesel engine exhaust using a SCR catalyst on a Diesel Particulate Filter (SCR-F). A 2D SCR-F model was developed that is capable of predicting internal states: 2D temperature, PM and NH₃ storage distributions and filtration efficiency, pressure drop, PM mass retained in the PM cake and substrate wall and outlet NO, NO₂ and NH₃ concentrations. The SCR-F model was used to simulate a DOC + SCR-F + DOC + SCR ultra-low NO_x system that can achieve > 99.5% NO_x conversion efficiency.

The model was calibrated with experimental data from a Johnson Matthey SCRF® with a Cummins 2013 ISB engine. The impact of SCR reactions on passive PM oxidation rate and PM loading on SCR reactions was determined. A comparison of the experimental and model data for different ammonia to NO_x ratios, PM loading and passive oxidation conditions is presented. A 2D SCR-F state estimator was developed by combining a simplified version of the 2D SCR-F model with pressure drop, outlet thermocouple and NO_x sensor measurements using an Extended Kalman Filter. The temperature, PM mass retained and NH₃ coverage fraction states were predicted which can be used to develop fuel and urea dosing strategies for the SCR-F.

A 2D SCR-F + 1D SCR system model was used to simulate the experimental data collected on a SCR-F + SCR system from a Cummins 2013 ISB engine. The NO₂/NO_x ratio at the SCR-F and SCR inlet was found to be limiting factor for NO_x conversion efficiency of this system. An ultra-low NO_x system was developed with a DOC downstream of the SCR-F that maintains an optimum NO₂/NO_x ratio of 0.5 at the downstream SCR inlet by using 2 urea injectors. This system was simulated with a combination of 1D DOC, 2D SCR-F and 1D SCR models and it was found to be capable of > 99.5% NO_x conversion efficiency, a 90% increase in PM oxidation rate compared to a SCR-F + SCR system with 1 injector for typical engine operating conditions.

Chapter 1

Introduction

Diesel engines are used in wide ranging applications including industrial, agricultural and transportation. They significantly reduce CO₂ emissions, but due to lean combustion they emit significant amounts of nitrogen oxides (NO_x) and particulate matter (PM) emissions which are harmful to human health. Environmental agencies around the world including the Environmental Protection Agency (EPA) and the California Air Resources Board (CARB) regulate the amount of emissions emitted by diesel engines including nitrogen oxides (NO_x), carbon monoxide (CO), total hydrocarbons (THC) and particulate matter (PM). Figure 1.1 shows the limits set for brake specific NO_x (BSNO_x) and brakes specific PM (BSPM) by EPA between 1985 and 2015.

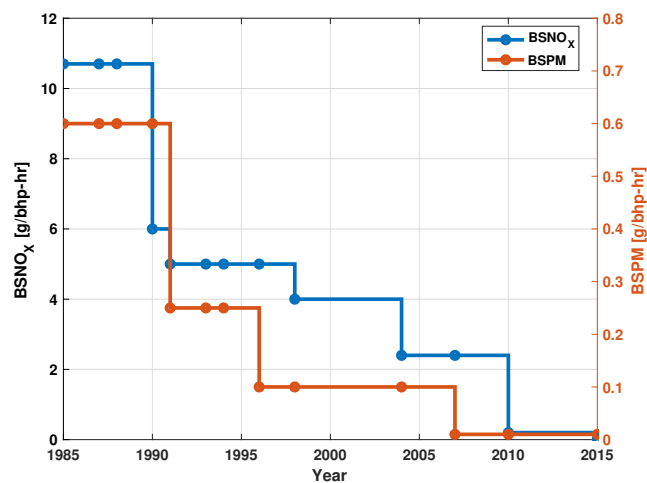


Figure 1.1: Time vs BSPM and BSNO_x [1]

In Figure 1.1 the x axis represents the years at which EPA standards were set and the y axes consist of brake specific NO_x and brake specific PM standards in grams/bhp-hr for on highway heavy duty Diesel engines [1]. The BSNO_x standard was started at 10.7 g/bhp-hr in 1985 followed by a revision to 6, 5 and 4 g/bhp-hr. in 1990, 1991, and 1998 respectively. A combined HC + NO_x standard of 2.4 g/bhp-hr. as standard in 2004. Some manufacturers supplied engines from 2002 that met this standard. The PM standard started at 0.6 g/bhp-hr. in 1987 which was lowered to 0.25, 0.1 and 0.01 g/bhp-hr. in 1991, 1994 and 2007. The 2007 standard required used of a Diesel Particulate Filter (DPF) in addition to a DOC to meet the PM standards. The BSNO_x was further reduced to 0.2 g/bhp-hr in 2010 as shown in Figure 1.1. From 2007 to 2009, the standards required as percent-of-sale basis: 50% compliance in 2007 to 2009 and 100 % in 2010. In practice during 2007 - 2009 most manufacturers opted for NO_x family emissions limit (FEL) of 1.2 g/bhp-hr. for most of their engines. This limit was achieved through a combination of Exhaust gas recirculation (EGR) and Diesel particulate filter (DPF). Engines in model year 2010 and later used a combination of DOC, DPF and selective catalytic reduction (SCR) to comply with the 0.2 g/bhp-hr. standard.

In order to meet the 2010 EPA standard emissions limits for PM and NO_x , aftertreatment systems consisting of a Diesel oxidation catalyst (DOC), Diesel particulate filter (DPF) and a Selective catalytic reduction (SCR) have been used by engine manufacturers. These aftertreatment systems are used in addition to the several in cylinder strategies including exhaust gas recirculation (EGR), multiple injections and turbocharging that are used for emissions reduction.

The existing production heavy-duty diesel aftertreatment system shown in Figure 1.2 primarily consists of a DOC, catalyzed particulate filter (CPF), SCR and an AMOX. This system has been used in production since 2010 to control CO, HC, NO_x and PM emissions for heavy duty on highway diesel engines.

The CPF is used to filter and oxidize the PM emissions. The DOC is used to oxidize CO, NO and the dosed fuel from the fuel doser is used to provide periodic active regeneration of the CPF to remove the excess PM retained in the CPF. Urea is injected into the exhaust gas using the injector and is mixed with exhaust gas using the mixer in a decomposition tube where the urea decomposes to form NH_3 , CO_2 and H_2O . The SCR reduces NO_x emissions into N_2 and H_2O by reduction reactions between NH_3 , NO and NO_2 . The AMOX oxidizes the NH_3 that slips out of the SCR.

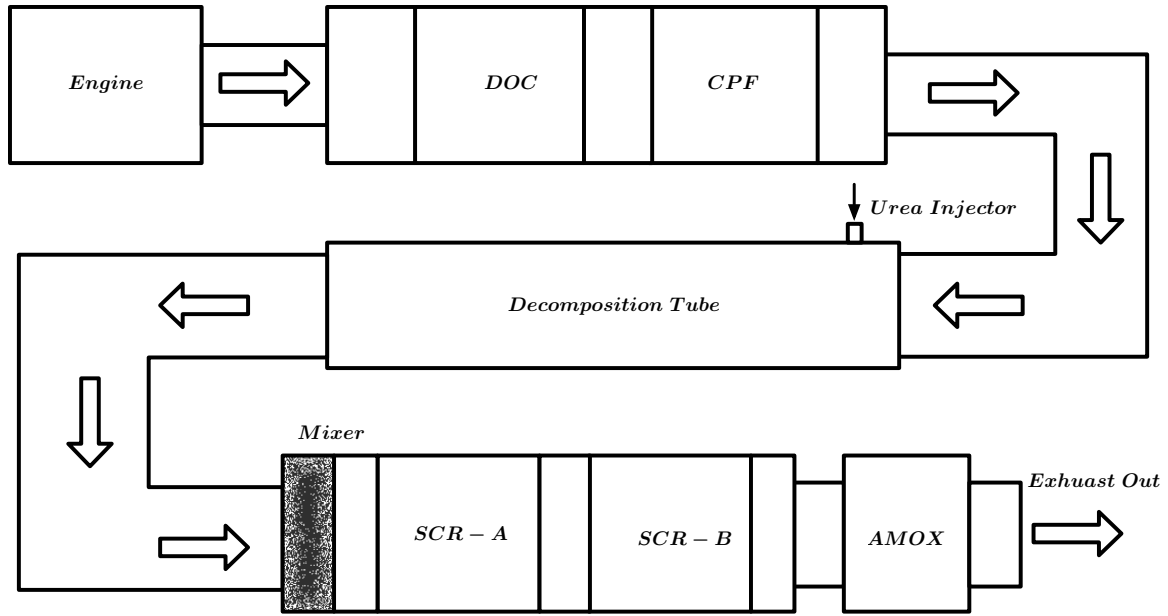


Figure 1.2: Cummins ISB 2013 Production Aftertreatment System Schematic

In both the CPF and SCR, a ratio of NO_2/NO_x from 0.5-0.6 is required for optimum passive PM oxidation and fast SCR reactions respectively to maximize the performance of these devices [2]. In order to achieve this ratio, the DOC is used to oxidize the NO to NO_2 and the oxidation catalyst in the CPF is used to oxidize NO to NO_2 leading to a higher PM oxidation rate by back diffusion of NO_2 in the CPF. In order to reduce the packaging volume and cost associated with the CPF and SCR, the selective catalytic reduction catalyst on a filter (SCR-F) has been in development over the past 17 years as reviewed by Song. et al. [3].

For the 2015 CARB optional standard, a further 90 % reduction in BSNO_x from 0.2 g/bhp-hr. to 0.02 g/bhp-hr. has been proposed. In order to meet this new ultra-low NO_x standard, engine manufacturers have been doing R and D on aftertreatment systems consisting of SCR catalyst on a DPF (SCR-F) a device capable of simultaneously removing NO_x and PM from the exhaust gas. The research in this thesis focuses on the application of a SCR-F in an ultra-low NO_x aftertreatment system and the development of a 2D numerical model of the SCR-F that simulates the major phenomena encountered in the device during typical engine operation. This is followed by development of a SCR-F state estimator and a system level model that can

simulate the performance of an ultra-Low NO_x aftertreatment system that consists of a SCR-F being the major component.

1.1 Motivation

Design and optimization of aftertreatment systems requires an understanding of the internal variables of all the devices used including the internal temperature distribution, change in concentration of chemical species within the CPF and SCR-F etc. In order to estimate these internal states for accurate control and design of aftertreatment systems, numerical models are required which can predict the unmeasurable quantities, enabling robust control system design and on board diagnostic (OBD) applications development.

The internal quantities to be estimated in the SCR-F in this research include 2D temperature, PM mass retained and NH_3 coverage fraction distribution. These quantities are functions of other internal quantities such as change in chemical species concentration of NO , NO_2 and NH_3 in the PM cake and substrate wall layers by convection, reaction and diffusion mechanisms. The numerical model developed is capable of simulating the chemical species concentrations in the PM cake and substrate wall using a reaction - diffusion scheme. The temperature distribution and in turn PM mass distribution are simulated using a 2D mesh for energy conservation equations in the inlet, outlet channel and substrate wall.

The development of a numerical model of the SCR-F enables estimation of internal states of the device which can be combined with measurable quantities such as outlet exhaust gas temperature, outlet NO_x concentration sensor data and pressure drop data. The predictions from such a state estimator enable the electronic control unit (ECU) in the vehicle to better control the urea injection rate and fuel injection rate into the exhaust gas thus ensuring efficient NO_x reduction, lower urea consumption and lower fuel consumption of fuel during active regeneration and lower pressure drop across the SCR-F. In order to meet these goals, the 2D SCR-F model was combined with thermocouple, NO_x sensor and pressure drop sensor data using extended Kalman filter equations to create the SCR-F state estimator.

The SCR-F numerical model also enables simulation of the interaction of the SCR-F with other after treatment devices in the system such as the DOC and SCR. Such a

simulation can enable design of an aftertreatment system with higher NO_x reduction performance and lower fuel consumption. In order to demonstrate this application, the 2D SCR-F model was combined with the 1D DOC and 1D SCR models to simulate an ultra-low NO_x aftertreatment system with potential to significantly reduce the NO_x emissions and enable efficient regeneration of the SCR-F.

1.2 Diesel Aftertreatment System Experimental Data

A SCR-F designed by Johnson Matthey referred to as a SCR-F® was used with a Cummins 2013 ISB engine to collect the experimental data for the 2D SCR-F model development in this work. The SCR-F® was used to replace the CPF. One configuration using both the CPF and SCR-F® to collect SCR-F® performance data with 0 g/l PM loading. These experimental configurations are described below.

In order to evaluate the performance of the SCR-F, the experimental data were collected in three different configurations as reported in references [4] and [5]. The three configurations consist of the following combinations of aftertreatment devices:

1. Configuration 1 with and without urea injection consisting of a DOC + SCR-F® (Figure 1.3)
2. Configuration 2 without PM loading consisting of a DOC + CPF + SCR-F® (Figure 1.4)
3. Configuration 2 with PM loading consisting of a DOC + SCR-F® (Figure 1.3)
4. Configuration 3 consisting of a DOC + SCR-F® + SCR (Figure 1.5)

Figures 1.3 to 1.5 show the different configurations used for the experimental data. The experimental setup in Figure 1.3 was used for configuration 1 and configuration 2 experiments with PM loading. In configuration 1 the exhaust passes through the DOC to oxidize the NO to NO_2 and the PM is collected and oxidized along with the NO_x reduction in the SCR-F®. There are four active regeneration experiments with inlet exhaust gas temperature 500 - 600 °C, seven passive oxidation experiments

with no urea injection and seven passive oxidation experiments with urea injection at inlet ammonia to NO_x target ratio (ANR) of 1.0 conducted with the configuration 1. There are four test conditions with 2 and 4 g/l PM loading in experiments with configuration 2. A urea cycle with inlet ANR of 0.8, 1 and 1.2 was used after loading the filter with the required amount of PM.

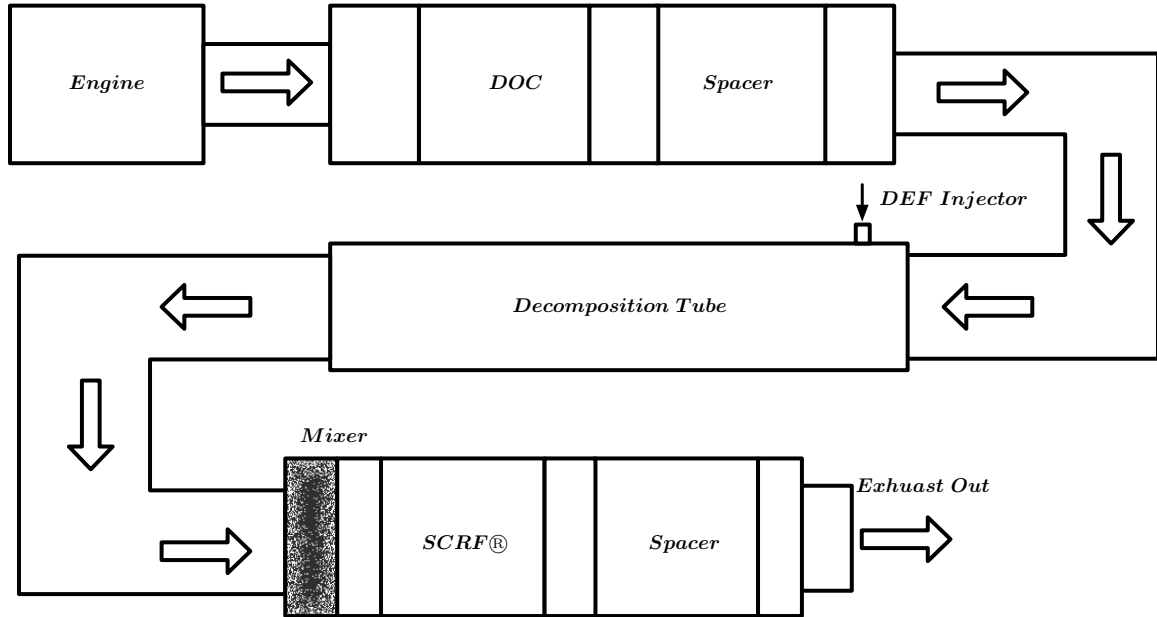


Figure 1.3: Configurations 1 and 2 with PM loading Aftertreatment System Schematic

The experimental setup shown in Figure 1.4 is used in configuration tests with no PM loading. For these experiments, a CPF is placed upstream of the SCR® to remove all the PM in the exhaust and a urea injection cycle with inlet ANR of 0.8, 1.0 and 1.2 was used.

Experimental setup in Figure 1.5 was used for Configuration 3 experiments. The test cycle used in this configuration is similar to configuration 1 passive oxidation experiments with urea injection, with a target inlet ANR of 1.1 and a downstream SCR.

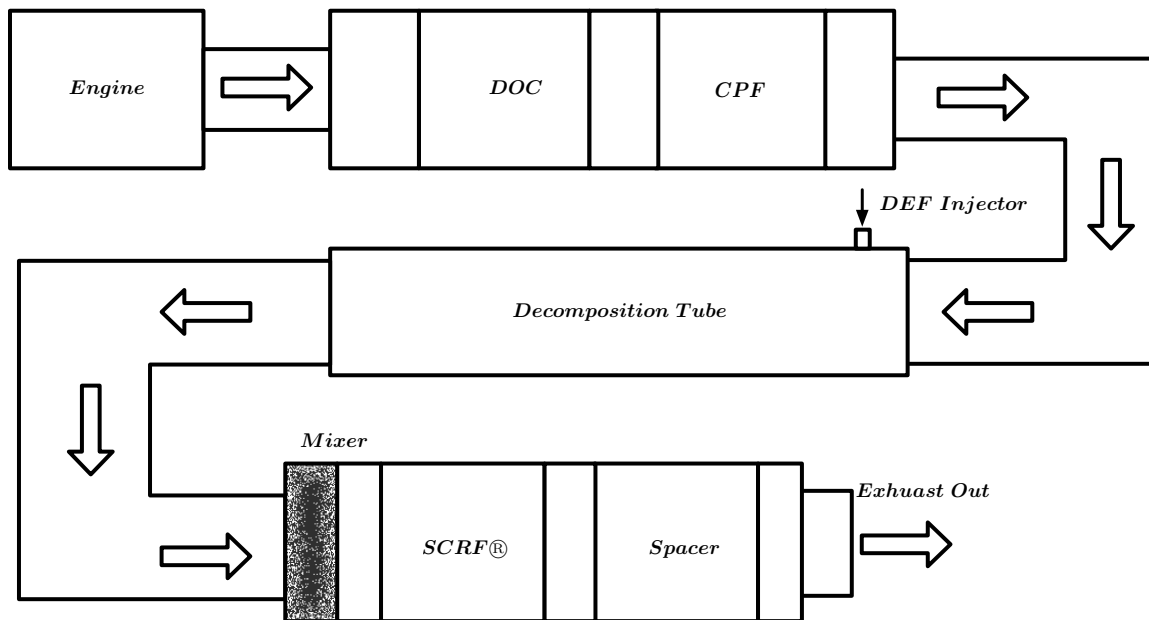


Figure 1.4: Configurations 2 without PM Aftertreatment System Schematic

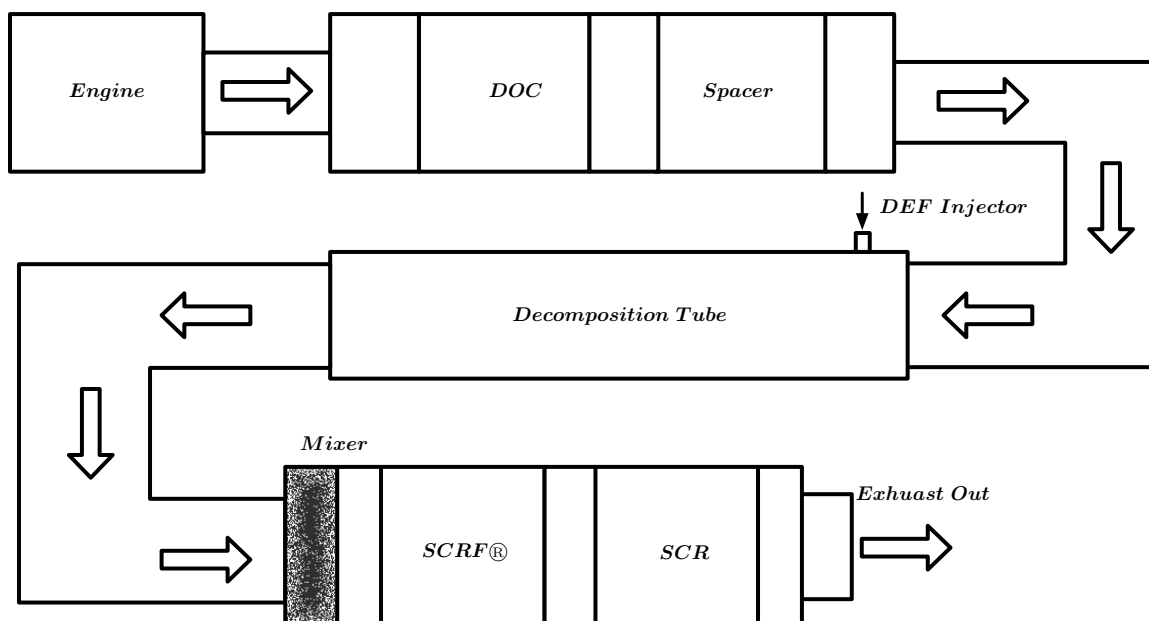


Figure 1.5: Configurations 3 Aftertreatment System Schematic

1.3 Research Objectives

The specific objectives of the research work are as follows:

1. Develop a 2D numerical model of a SCR catalyst on a DPF (SCR-F) capable of simulating the 2D temperature, PM mass retained and NH_3 coverage fraction. The model should also predict pressure drop across the SCR-F, filtration efficiency and outlet concentrations of NO, NO_2 and NH_3 .
2. Develop a calibration process using a numerical optimization scheme comparing experimental and model output data to determine the optimized PM oxidation and SCR kinetics for the 2D SCR-F model using the data collected on Johnson Matthey SCR-F® on a 2013 Cummins ISB 6.7 L engine. The experimental data consists of data from the three configurations.
3. Determine the impact of the local NO_2/NO_x ratio at the SCR-F outlet on NO_x conversion efficiency and NH_3 slip of the SCR-F + SCR system.
4. Develop an ultra-low NO_x aftertreatment system consisting of $\text{DOC}_1+\text{SCR-F}+\text{DOC}_2+\text{SCR}$ using models to determine if the system can achieve $> 99\%$ NO_x conversion and a 90% increase in PM oxidation rate compared to a $\text{DOC}_1+\text{SCR-F} + \text{SCR}$ system while minimizing the NH_3 slip.
5. Develop a simplified 2D SCR-F model with a reduced mesh and quasi steady state chemical species and channel temperature equations along with a solution which will be used for the 2D SCR-F state estimator development. The 2D SCR-F state estimator needs to predict the unknown states consisting of 2D temperature, PM mass retained and NH_3 coverage fraction distributions.

1.4 Overview of the Thesis

The development of the 2D SCR-F model (v2.3) and the calibration of the model with experimental data using a Johnson Matthey SCR-F® with a Cummins 2013 6.7L ISB engine is described. The development of the 2D SCR-F + 1D SCR model, simplified 2D SCR-F model, 2D SCR-F state estimator and an ultra-low NO_x aftertreatment system is also presented.

Chapter 1 gives an introduction to the research work and states the goals and objectives of the research. Chapter 2 describes the literature related to the SCR-F modeling, experimental work, pressure drop, multi-dimensional CPF modeling, SCR/CPF state estimator development and ultra-low NO_x aftertreatment system development.

Chapter 3 consists of the 2D SCR-F model description with all the governing equations and model architecture. Chapter 4 presents the experimental data from configurations 1, 2 and 3 that was used to calibrate the 2D SCR-F model. This chapter also deals with the calibration procedure used to determine all the calibration parameters for the 2D SCR-F and 1D SCR model including all the PM oxidation and SCR reaction kinetics. Chapter 5 consists of results from the 2D SCR-F and 2D SCR-F + 1D SCR model with an analysis of all the internal variables and phenomenon that were found as part of the model development and calibration process using all the thirty-eight experiments.

Chapter 6 describes the procedure used for the development of the simplified 2D SCR-F model and the 2D SCR-F state estimator. The results from the DOC+SCR-F+SCR state estimator using configuration 3 data is also described. Chapter 7 describes the ultra-low NO_x aftertreatment system consisting of a DOC₁+SCR-F+DOC₂+SCR+AMOX and two urea injectors, along with the results of the parametric study that was carried out using configuration 3 data and a description of a control system that can be used for such a system. Chapter 8 summarizes the results from this research work and the conclusions from the 2D SCR-F model, 2D SCR-F state estimator development and Ultra Low NO_x aftertreatment system.

Chapter 2

Background and Literature Review

The major goal of this research is to develop a 2D SCR-F model for ECU application to a state estimator and for the design of an aftertreatment system that can meet the ultra low NO_x standard of 0.02 g/bhp-hr. Existing literature was reviewed to develop the 2D SCR-F model that can simulate the 2D temperature, PM mass retained and NH_3 coverage fraction distributions and outlet concentrations of NO , NO_2 and NH_3 along with pressure drop and filtration efficiency of a SCR-F. The review literature consisted of work related to SCR-F modeling, experimental studies along with CPF pressure drop and multidimensional modeling. This was followed by a literature review on the SCR and SCR-F estimator development. Also, literature on after treatment systems designed to potentially meet the ultra low NO_x standard have been reviewed as part of the work.

Xiaobo Song et al. [3] conducted a literature review of papers involved with a SCR catalyst on DPF's related to catalyst design, performance characterization and modeling which was carried out as part of the MTU Diesel Engine Aftertreatment Consortium. The main conclusions from this paper are :

- The SCR-F leads to lower substrate volume leading to easier light off at lower temperatures.
- The catalyst that is embedded inside the substrate wall is more effective than layer type catalyst
- That the effect of PM on NO_2 diffusion needs to be modeled

- The competition for NO_2 between SCR and PM oxidation reactions needs to be modeled.
- Multiple NH_3 storage sites were modeled in literature.

The present literature review is an extension of this work with a focus on modeling, experimental data and estimator development aspects of the SCR catalyst on DPF's and ultra low NO_x systems.

2.1 SCR-F Models

SCR-F models reviewed in the literature all have a focus on the interaction of the SCR reactions with the PM oxidation reactions. The major focus of the modelling includes

- Effect of SCR reactions on PM oxidation rate
- Impact of PM loading on SCR reactions and de NO_x performance of the SCR catalyst on a DPF
- Low temperature NO_x reduction performance and inhibition due to nitrate formation
- Change in local NO_2/NO_x ratio in the substrate wall and its impact on the SCR reactions
- Inhibition in active sites by PM deposited in the wall
- Change in NH_3 storage capacity with PM loading
- Incomplete conversion of urea to NH_3 at low temperatures ($T < 250$ °C)

Park et al. [6][7] developed a one-dimensional two way DPF/SCR model by combining the 1D physical model of a DPF with chemical reactions and kinetics from a SCR model with a focus on evaluating PM NO_x interactions. This model found a correlation between PM loading and local NO_2/NO_x ratio in the wall PM which

impacts the NO_x reduction activity by controlling the types of SCR reactions taking place in the substrate wall. The study also found the inhibition of SCR reactions due to deep bed PM in the substrate wall. The decrease in the mass transfer of NH_3 to the catalyst sites and the resultant reduction NO_x reduction performance was modeled. The model assumed that the SCR catalyst coating was present inside the substrate wall and considered forward diffusion of the chemical species between the PM cake and the substrate wall. Figure 2.1 shows the PM deposited on the substrate wall which blocks the active sites involved in NH_3 storage.

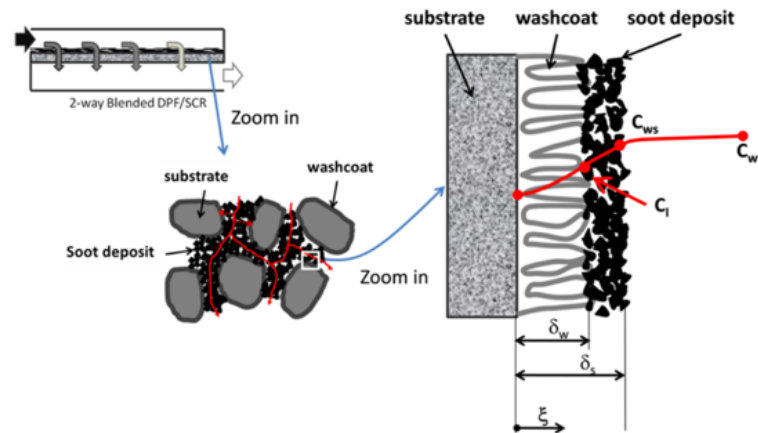


Figure 2.1: Inhibition of NH_3 transport to active site due to PM in the substrate wall [7]

Colombo et al. [8] developed a SCR catalyst on a DPF model based on Axisuite[®] software that focuses on coupling the diffusion and reaction mechanisms which affect the interaction between the PM oxidation and the SCR reactions. The study found a significant change in local NO_2/NO_x ratio in the substrate wall due to the presence of PM which altered the NO_x reduction performance either in the positive direction when NO_2/NO_x ratio is greater than 0.5 or decreased NO_x reduction in the case of NO_2/NO_x ratio less than or equal to 0.5. Figure 2.2 shows the decrease in NO_2 concentration through the PM cake layer that was observed in this work in the case with urea injection.

Tan et al. [9] developed a 2-way SCR catalyst on a DPF model for a Cu-Ze based SCR on a DPF for heavy duty diesel systems. This study found that up to 30% reduction in overall SCR volume can be achieved using a SCR catalyst on a DPF+SCR system compared to a CDPF + SCR system while obtaining similar deNO_x and PM filtration

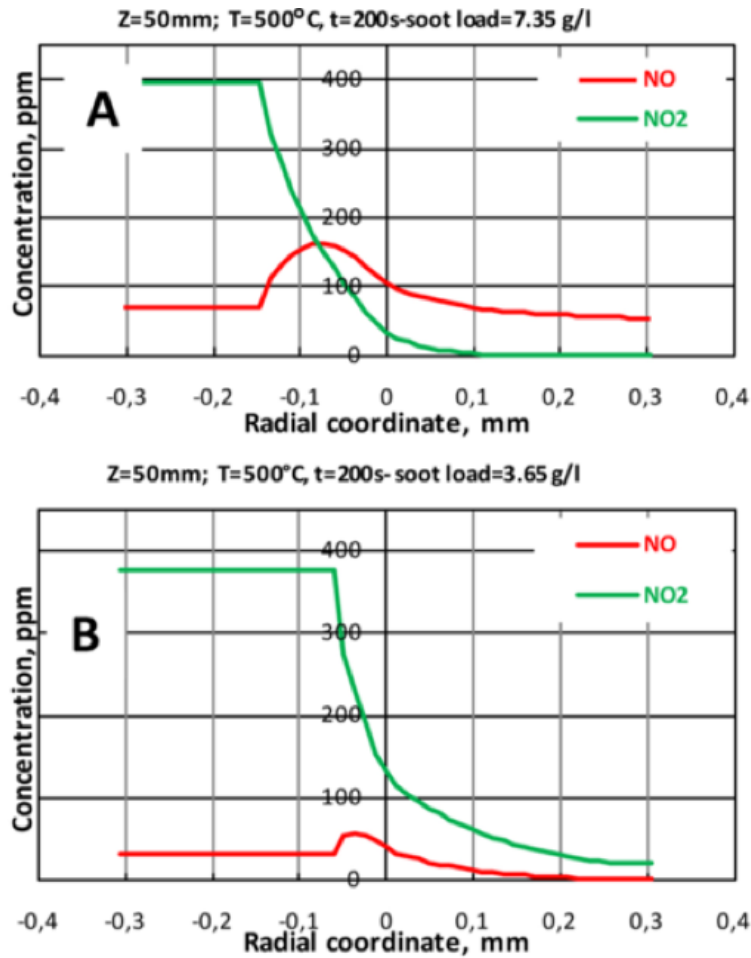


Figure 2.2: Radial NO/NO₂ profiles (PM cake and substrate wall) with and without NH₃ [8]

efficiency performance. It was observed that a degreened SCR catalyst on a DPF showed a 30% decrease in NH₃ storage with PM loading but an aged SCR catalyst on a DPF showed no change in storage of NH₃ with PM. Also, it was concluded that with a 20 - 30°C increase in the temperature profile, the PM oxidation rate can be increased to the levels observed in a CDPF.

Yang et al. [10] developed a 1D model for Cu-Ze SCR on a DPF. This study focused on the effects of space velocity, temperature and local NO₂/NO_x ratio on clean and PM loaded filters. The variation in space velocity was found to have a 2% change in the NO_x reduction performance. PM in the substrate wall on the other hand played an important role in decreasing NO_x reduction performance. Unlike previous studies,

the effect of PM in the substrate wall and PM cake was studied separately in this work and it was found that wall PM is the main reason for blocking the active NH_3 storage sites. The inhibition of NH_3 storage caused by wall PM was simulated. Also, energy release by the SCR reactions and their impact on wall PM oxidation rate were simulated. Figure 2.3 shows the variation of NH_3 storage and NO_2 consumption rate through the PM cake and substrate wall observed in this study.

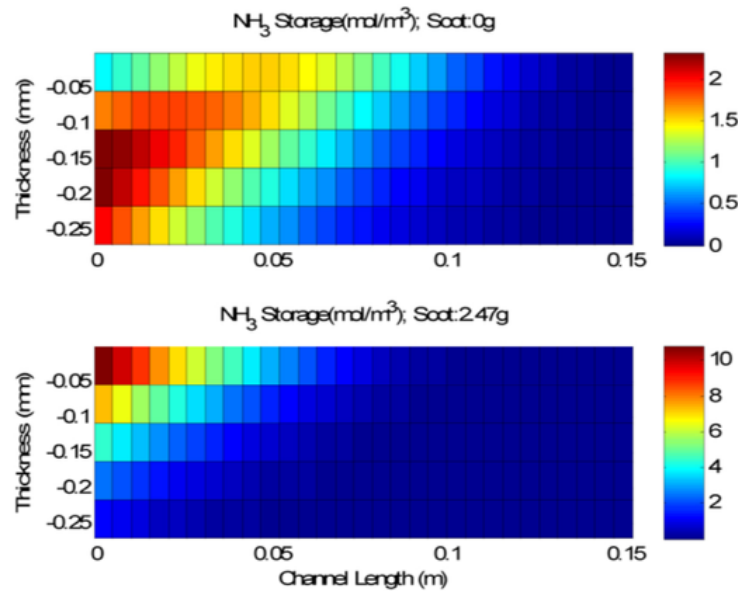
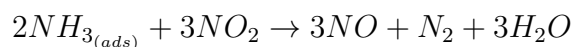


Figure 2.3: NH_3 storage and NO_2 consumption in PM cake and wall with and without PM [10]

Watling al. [11] developed a 1D model of a SCR catalyst on a DPF using kinetics from lab reactor experiments. The model was able to predict outlet concentrations of NO , NO_2 and NH_3 slip as well as N_2O formation and NH_3 storage. It was found that PM had minimal impact on SCR activity but had significant impact on PM oxidation rate by NO_2 oxidation. An additional global reaction used in this model is the decomposition of NO_2 to NO by adsorbed NH_3 to simulate the excess NO which could not be explained by the reversible NO_2 decomposition reaction.



Also, an exotherm of 5°C was observed due to SCR reactions which has a beneficial

effect on PM oxidation at temperatures above 500°C where thermal PM oxidation is dominant.

Konstandopoulos, et al. [12] developed a two-layer SCR catalyst on a DPF model that studied the impact of thin coatings and variable porosity in the filter substrate wall on the pressure drop as well as deNO_x performance of the SCR on a DPF. This model takes into account variation of PM oxidation rate based on the PM contact variation. The effect of PM catalyst dynamics on the oxidation rate and SCR reaction rate as well as pressure drop across the filter were studied which is useful in developing efficient filter designs to find a proper tradeoff between pressure drop and filtration efficiency.

Schrade et.al [13] developed a physico-chemical model of the SCR on DPF based on fundamental principles for control strategies of a SCR catalyst on a DPF using AxiSuite ® software. This model was calibrated with transient data from the NEDC cycle and from reactor data. The reactor data showed bimodal adsorption and desorption of NH₃ which led to a two-site model development. The two sites represent weakly bonded NH₃ at Lewis acid sites and strongly bonded NH₃ by chemisorption at Bronstedt sites. Figure 2.4 shows the desorption pattern of a clean filter in this study which shows two distinct peaks for desorption which correspond to two different storage sites.

A significant change in the amount of NH₃ storage in the presence of the PM cake was found in this study which could lead to a third storage site present in the PM cake. Although the third site was neglected in the model as the change in NH₃ storage was less than 5 %. The light off temperature for the SCR on a DPF was found to be above 200°C. NH₄NO₃ formation and the inhibition caused by these deposits was simulated for temperatures less than 250°C and high NO₂/NO_x ratios using a third site for nitrates deposition. Water adsorption on zeolites was also considered in this model along with inhibition of active sites by wall PM.

Tronconi et.al [14] developed a multiscale SCR catalyst on a DPF model using AxiSuite ® software with NH₃ kinetics collected from fixed bed reactor based tests which were used for creating a physicochemical model. A decoupled calibration procedure was used for the calibration of the SCR reactions and NO₂ assisted PM oxidation kinetics. The validity of kinetics found was then tested on a model of a medium and heavy duty engine SCR catalyst on a DPF. Higher CO/CO₂ was found for cases with NO₂ presence due to NO₂ assisted PM oxidation till 400°C. Studies on the filtration

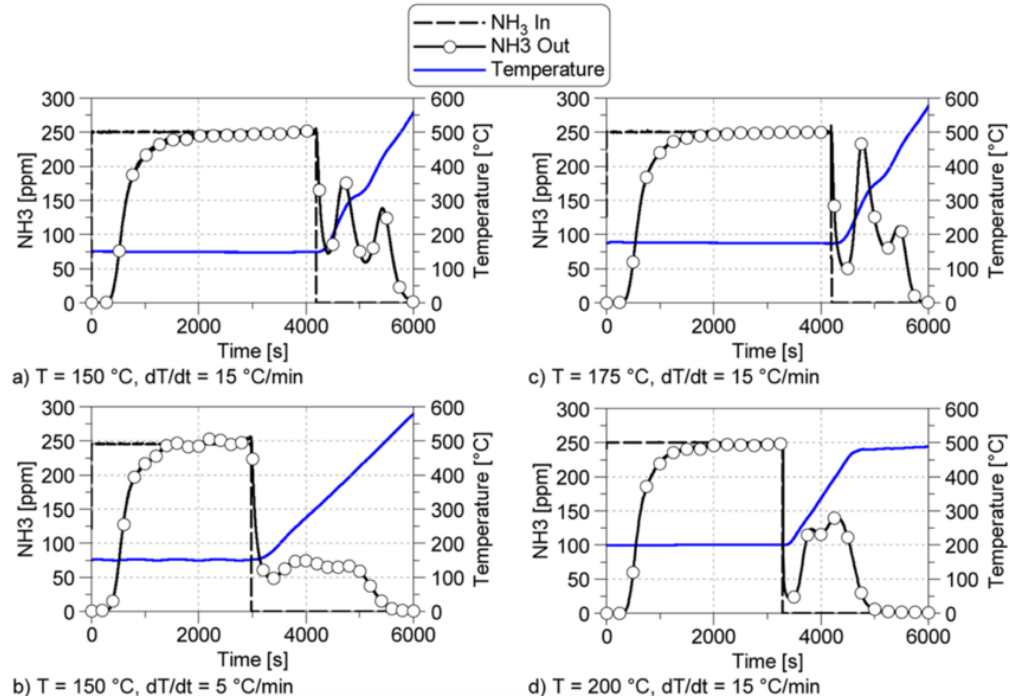


Figure 2.4: NH_3 adsorption and desorption for PM free filter with 250 ppm inlet NH_3 [13]

and pressure drop characteristics of the SCR catalyst on a DPF for different PM loading values was also conducted. It was found that with the presence of the SCR reactions, the available NO_2 in the PM cake and thus PM oxidation rate was reduced due to forward diffusion phenomena between PM cake and the substrate wall. As shown in Figure 2.5, a significant decrease in the NO_2 concentration across the PM cake was observed in the case with urea injection.

Figure 2.6 shows the competition for NO_2 between SCR reactions and PM oxidation in the SCR catalyst on a DPF [14] which is responsible for the decrease in the NO_2 concentration in the PM cake.

Dosda et al. [15] developed a SCR catalyst on a DPF and SCR exhaust line model to simulate the SCR catalyst on a DPF with a downstream SCR. This model studied the deterioration of the catalyst due to thermal oxidation. The model found that CuO species aggregation in the Cu-Ze catalyst was the reason behind the decrease in the number of active sites in an aged SCR catalyst on a DPF. This model assumed

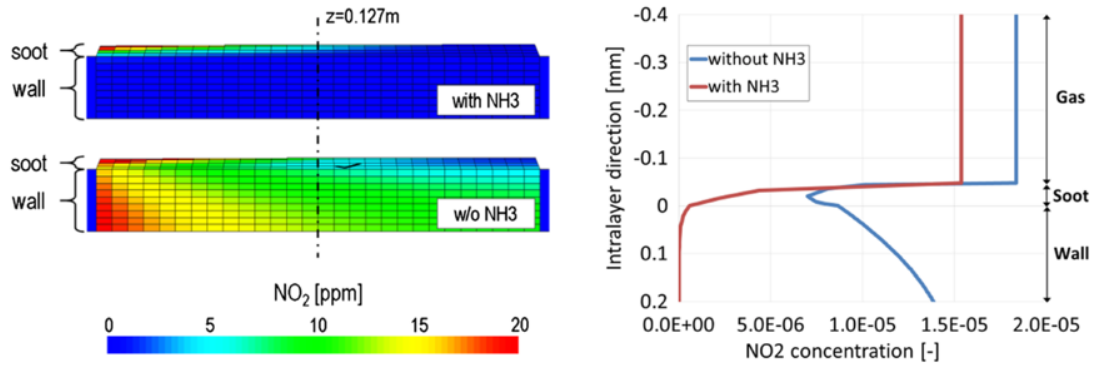


Figure 2.5: Change in NO_2 concentration in radial and axial direction [14]

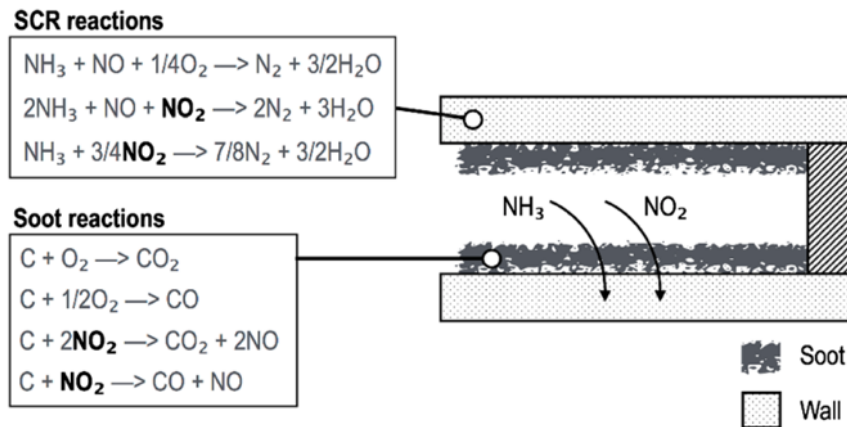


Figure 2.6: Competition for NO_2 between PM oxidation and SCR reactions [14]

one site for storage and consumption of NH_3 .

Lopez et. al [16] developed a Vanadium catalyst based SCR-F model. This study found that the fast SCR reaction did not affect the PM balance point. The maximum deNO_x was found to be between $180 - 300^\circ\text{C}$ with deNO_x efficiency of 90 %. Higher temperatures led to NH_3 oxidation which significantly decreased the deNO_x performance. This model assumed that the number of active sites is linearly proportional to the wash coat loading present on the SCR[®].

Strots et.al [17] performed a comparative study on a DOC+CDPF+SCR system and DOC+SCR-F+SCR system on a HDD engine with the WHTC cycle data and 1D SCR/DPF model using AxiSuite ® software. The SCR-F based system was found to have faster light off at 200°C.

Overall the major trends that were observed from the literature review of the SCR-F modeling are as follows

- PM loading does not significantly affect the SCR reactions
- PM in the substrate wall is responsible for a decrease in the SCR storage
- Significant change in local NO_2/NO_x ratio is observed across the PM cake and substrate wall for PM loaded filters which affects NO_x reduction performance
- Some studies found an increase in storage of the NH_3 with PM loading which needs to be studied further
- SCR reactions have significant impact on PM oxidation rate due to forward diffusion of NO_2 caused by competition for NO_2 between PM oxidation and SCR reactions
- Inhibition of SCR reactions by the presence of nitrate deposits in the substrate wall below 250°C was observed in some studies
- An exotherm of about 5°C caused by SCR reactions was reported in some of the studies but a quantitative modelling study of temperature change caused by the SCR reactions needs to be developed.

Some of the new trends that were observed in this literature review compared to earlier work by Xiaobo et al. [3] are as follows

- Forward diffusion phenomena governs the competition for NO_2 between SCR and PM oxidation reactions
- PM in the substrate is responsible for a decrease in the NH_3 storage
- Inhibition of the SCR reactions occurs due to the nitrate deposits at temperatures below 250°C

- There is an increase in NH_3 storage due to PM loading
- Exotherm of 5°C caused by the SCR reactions was observed in the experimental data

2.2 SCR-F Experimental Studies

Experimental studies of a SCR catalyst on a DPF have been performed by multiple groups to study the effect of PM loading on SCR activity and the effect of SCR reactions on PM oxidation rate. Studies on N_2O formation and NH_4NO_3 deposits at temperatures below 250°C have also been conducted. Comparison studies of production after-treatment systems consisting of a DOC+CDPF+SCR as compared to a DOC+SCR-F+SCR have been performed to determine the quantitative decrease in SCR catalyst volume, system level deNO_x performance and PM oxidation rate. The major classification of the catalysts used in the SCR on a DPF are Fe-Ze, Cu-Ze and Vandia with each having its advantages and disadvantages. The following paragraphs give a brief explanation of the experimental studies performed on SCR catalysts on DPF's.

Mihai et al. [18] [19] has conducted experimental studies on a Cu-Ze based SCR coated DPF which has been hydrothermally aged to 850°C for 12 hrs. The filter was loaded with PM and cut into sections which were then subjected to reactor tests. NO_x reduction performance decreased with increase in PM loading with the largest CO/ CO_2 formation at 540°C . The standard SCR reaction rate increased slightly when PM is removed. The presence of PM reduced the formation of NH_4NO_3 which increased the fast SCR reaction rate at 150°C . The authors proposed that PM reacts with NH_4NO_3 present on CuO species outside the zeolite leading to less number of blocked sites and higher standard SCR reaction rate at low temperatures ($< 250^\circ\text{C}$). Maximum NO_x reduction was observed between $250\text{-}400^\circ\text{C}$. Cu particles are susceptible to NO oxidation so less NO oxidation was observed with PM loading. NH_3 oxidation increases with an increase in PM loading at high temperature.

Lasitha et al. [20][21] conducted a comparative study on PM oxidation efficiency of a SCR-F® vs a CSF during active regeneration. It was found that for $T > 270^\circ\text{C}$, the CSF had a higher passive oxidation rate compared to the SCR-F®. For the same inlet temperature, the SCR-F® had 5 - 45 % lower PM oxidation rate compared to

the CSF. Also, a significant amount of NO_2 was formed in the CSF compared to the SCR $\text{F}^{\text{®}}$ during passive oxidation e.g. 6-12 % vs 1%. The location of PM was found to have minimal effect on PM oxidation rate. Also, for the CSF, it was found that PM oxidation rate increased with increase in Pt catalyst loading with 40 g/ft³ filter having higher PM oxidation rate than 10 g/ft³. Pt was found to not catalyze the NO_2 based PM oxidation but instead caused an increase in the NO_2 available in the PM cake by oxidizing NO to NO_2 unlike the catalyst Cu-Ze in the SCR $\text{F}^{\text{®}}$ which did not oxidize a significant amount of NO to NO_2 .

During active regeneration, the PM oxidation rate remained the same for the SCR $\text{F}^{\text{®}}$ with and without NH_3 . The CSF had higher PM oxidation rate during active regeneration compared to the SCR $\text{F}^{\text{®}}$ due to the higher NO_2 produced by the Pt catalyst which back diffused into the PM cake at the cake wall boundary. Figure 2.9 shows the comparison of the PM oxidation rate between the CSF and the SCR $\text{F}^{\text{®}}$ for temperatures greater than 550°C.

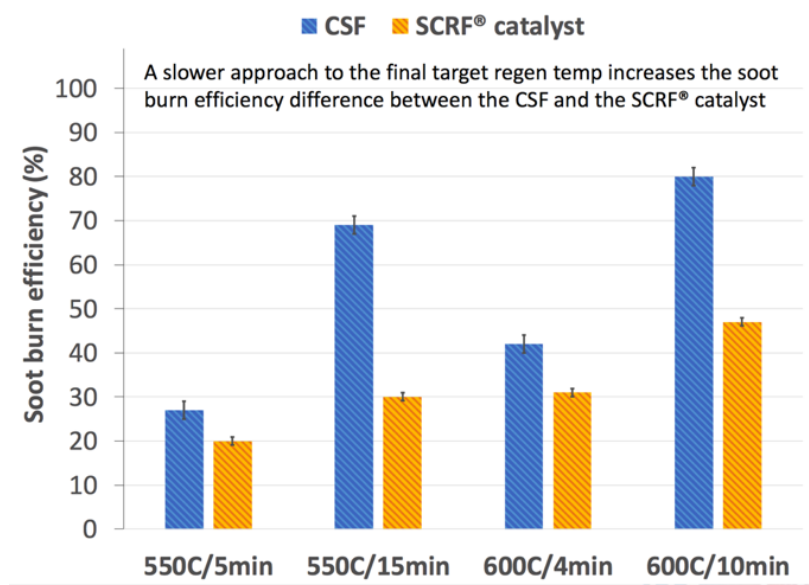


Figure 2.7: PM oxidation rate CSF vs SCR $\text{F}^{\text{®}}$ [20]

Lee et al. [22] conducted experiments on Cu-Ze SCR/DPF using US06 and cold FTP cycles to evaluate transient performance of the SCR/DPF. It was found that NO_x reduction performance of the SCR/DPF decreased from 84% to 82% with increase in mileage. Back pressure did not affect the NO_x reduction performance of the SCR/DPF.

The SCR/DPF was found to have 96% NO_x reduction efficiency for US06 cycle with PM loading up to 5 g/l having minimal impact on NO_x reduction performance. The NO_x reduction efficiency reduced to 53 % at temperatures above 400°C due to NH_3 oxidation. Also, oxidation of about 5 % of the NH_3 to NO_x in the mixer was observed at high temperatures. Catalyst deactivation was also studied and it was found that the number of active sites on the Cu-Ze catalyst and thus NH_3 storage capacity reduced after the filter was subjected to thermal regeneration above 550°C.

Tang et.al. [23] performed experiments on a Cu-Ze SCR on filters (SCRoF) to study DeNO_x and NH_3 slip characteristics for steady state and transient conditions. The study also focused on the effect of sulphur content in the fuel on the Cu-Ze catalyst. The SCRoF was exposed to fuel containing 395 ppm of sulphur which led to degradation of catalyst performance. The desulfication process was conducted at 500°C for 0.5 hrs which led to complete recovery of the NH_3 storage capacity and NO_x reducing performance of the SCRoF. SCR reaction rates were found to be significantly faster than the PM oxidation reactions leading to a decrease in the PM oxidation rate due to forward diffusion of NO_2 . A NO_2/NO_x ratio of 0.74 was found to be suitable for a loaded filter to achieve a NO_x reduction performance of 84 %.

Naseri et.al. [24] and Cavataio et.al. [25] performed SCR catalyst on a DPF experiments to compare the performance of the CSF to a SCR catalyst on a DPF. They found higher NO_x reduction performance in the SCR catalyst on a DPF compared to a CSF+SCR system for both transient and steady state conditions.

Mihani et al. [26] conducted experiments to study the effects of ammonia nitrate on the low temperature performance of a Cu-Ze SCR on a DPF. The study found that there is a significant increase in ammonia storage with PM loaded filters compared to a clean filter (493 mol for PM loaded filter vs 424 mol for filter without PM). Figure 2.8 shows the change in outlet NH_3 concentration between the filter with and without PM loading.

The study also found that PM reduced the formation of NH_4NO_3 at low temperatures which led to a decrease in N_2O formation at $T > 400^\circ\text{C}$ as well as increasing the NO_2 SCR reaction at low temperatures. In the case of a clean filter, the nitrate deposits block the active sites reducing the NH_3 storage and deNO_x performance but in the case of PM loaded filters, the PM reacts with nitrates keeping the active sites free, leading to higher NO_x reduction performance. Also, two types of nitrates were observed in the filter based on outlet N_2O values at high temperatures.

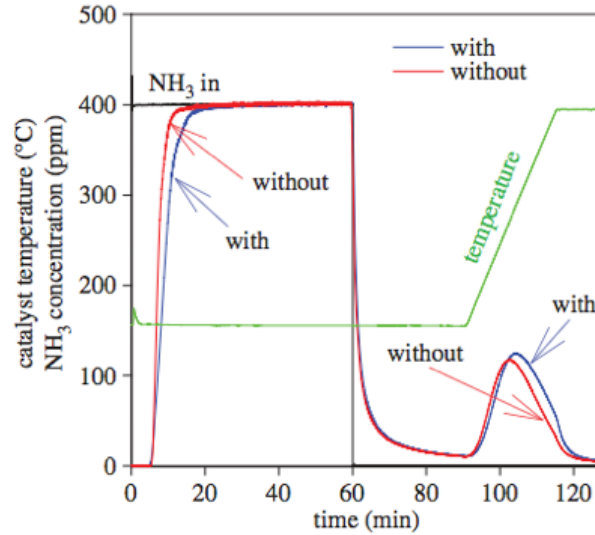


Figure 2.8: NH₃ inlet and outlet concentrations [26]

Upon analysis of the PM, the authors propose that the hydrothermal aging of filters leads to the formation of CuO species which are coated on top of zeolite particles. The PM reacts with NH₄NO₃ undergoing oxidation over these CuO species which reduces the nitrate deposits and thus keeps the active sites free for NH₃ storage.

2.3 1D and Multi Dimensional CPF Models

The CPF models in 0D and 1D can be used to implement model based control systems for fuel dosing during active regeneration events in the ECU. Several 0D, 1D models including the ones developed by Kladopoulou et al. [27] and Rose et al. [28] have been implemented which are faster than real time. These models assume a lumped approach to heat transfer to the ambient with heat conduction through the substrate wall. Nagar et al [29] implemented a 0-D model faster than real time with an temperature prediction which is within 25 °C of the experimental values. This model had difficulty predicting the pressure drop for initiating fuel injection. The reason for inaccuracies in this model arise because of a lack of the radial conduction term in the model for heat transfer to the ambient. Mulone et al. [30] implemented a model that was able to predict steady state and transient loading which are critical in the ability to accurately predict the pressure drop across the CPF.

In order to overcome some of the inaccuracies that arise due to lack of radial heat transfer in the filter, Depcik et al.[31] described a computationally efficient 2D CPF model. This model used a lumped approach to solve the temperature equation in each of the radial and axial zones that are part of the 2D mesh developed using resistance node methodology. This model was implemented in real time in an ECU and combined with the classical filtration model [32] with lumped PM in each of the zones. This approach was further extended by Boopathi et al. to develop a 2D high fidelity CPF model capable of simulating pressure drop, temperature and pressure drop distribution. This model was further used to create a 2D CPF state estimator. The approach used by Boopathi et al. is further extended in this work to simulate the 2D temperature in the SCR-F.

Konstandopoulos et al. [12] developed a multidimensional CPF model with multiphase approach to simulate non uniformity's in the filter. The model was based on several single channel descriptions involving a 3D mesh in which several partial differential equations were solved in a CFD framework. The 3D temperature equation considered heat transfer by conduction, convection and radiation to the ambient. This approach although accurate was computationally expensive leading to a model that's slower than real time.

Miyari et al. [33] developed a 2D thermal conduction model to simulate the 2D temperature profile during active regeneration events. The temperature equation considered conduction of heat through the substrate material in both the radial and axial direction. The mesh consisted of several 1D models that were arranged radially to simulate the overall temperature distribution. This model considered energy release into the gas stream using thermal PM oxidation reaction although energy release by hydrocarbon oxidation and NO_2 assisted PM oxidation were not considered.

Yi et al. [34] developed a 3D model to predict the PM distribution and temperature inside a CPF. This model used a lumped set of channels with similar inlet properties using a 1D approach to predict the 3D properties. This approach reduced the computational expense involved with a full 3D CFD model. This model neglected oxidation of PM and heat losses to the ambient.

2.4 Pressure Drop Modeling

Modelling of pressure drop across a CPF is an important aspect in predicting the fuel dosing strategy during regeneration. The pressure drop across the filter consists of three components 1) Frictional losses due to flow of exhaust gases through the inlet and outlet channel 2) Pressure drop due to flow through the PM cake 3) Pressure drop in the substrate wall. The original formulation for these 3 components was developed using packed bed filtration theory by Konstandopoulos and Johnson [35]. Haralampous et al. [36] further derived an analytic approach to calculate the pressure drop in a 1D pressure drop model. This new approach considered variation of permeability of the substrate wall due to PM deposited in the wall during filtration. Premchand et al. [37] further developed a 1D model for prediction of CPF pressure drop using axial momentum equations in the channels and the Darcy equation for cake and wall pressure drop. The filtration calculations in this case were performed using a packed bed filtration approach using the unit collector concept. The oxidation of PM in the cake and substrate wall was also accounted for this model along with a transition permeability concept to simulate the formation of the PM cake after the wall is filled with certain amount of PM. Mahadevan et al. further developed this approach to take into account the change in the permeability of cake during PM oxidation using the damage permeability concept.

2.5 SCR and CPF State Estimator Studies

A SCR catalyst on a DPF estimator can be used to estimate the outlet temperature, pressure drop across filter, PM mass retained and the outlet concentrations of NO, NO₂, NH₃ and the NH₃ storage. Since there are no SCR-F estimators in the open literature, this review will focus on recent work on both SCR and CPF state estimators.

The major trends in the research directions observed in the SCR literature are as follows:

1. Modeling of the cross-sensitivity of the outlet NO_x sensor with NH₃ to improve NO_x estimation.

2. Reducing the number of sensors used to reliably predict downstream NO/NO₂ and NH₃ concentrations
3. Estimating the inlet NH₃ for low temperature conditions
4. Estimating the coverage fraction of NH₃ stored inside the SCR
5. Estimating the concentrations of NO, NO₂ and NH₃

Upadhyay et al. [38] developed a model based SCR control law using a 3-state lumped model. In order to take into account the competing objectives of high NO_x conversion and low NH₃ slip, an alternate definition of conversion efficiency that combined these factors was used. The observability matrix was found to have the required rank of 3 for all the normal engine operating conditions. A FTP75 cycle based test was used to evaluate the estimator.

Devarkonda et al. [39] developed a model based linear estimator and nonlinear urea injection controller for a Fe-Ze SCR. The plant model used 4 states NO, NO₂, NH₃ and coverage fraction allowing NO, NO₂ to be controlled independently. The system was found to be observable and controllable for all the operating conditions. In order to quantify the accuracy of the 4 state model, a 3-state version of the plant model was developed and both of these models were compared in terms of accuracy of states predicted and stability. It was found that NO, NO₂ based 4 state approach was more accurate at predicting the states and controlling the system compared to a NO_x based 3 state approach. A full state feedback nonlinear control law was used for urea injection where the only measurement was a downstream NO_x sensor.

Hsieh et al. [40] developed a nonlinear Extended Kalman Filter (EKF) based SCR estimator to predict NO_x concentration using a NO_x sensor. The EKF simultaneously estimated a NO_x/NH₃ cross sensitivity factor to improve the NO_x and NH₃ slip estimates. In production systems, a manufacturer supplied, constant, cross sensitivity factor is used to extract a NO_x measurement from the NH₃ corrupted NO_x sensor output. However, cross sensitivity is a function of catalyst deterioration, sensor aging, temperature, etc.

Zhou et al. [41] a kalman filter based on 3 state linear state estimator and a extended kalman filter based non linear 4 state estimator. Both the estimators were used to predict the NH₃ storage and outlet NO_x concentrations. Feedback loop control was used for SCR control and the estimators were validated on a world harmonized

transient cycle (WHTC). The 4 state based EKF was found to be more accurate compared to 3 state based KF estimator.

Chen et al. [41] developed an SCR estimator to predict NO_x concentrations at low exhaust gas temperatures ($T < 250^\circ\text{C}$). Since low temperatures lead to incomplete conversion of urea to NH_3 and incomplete hydrolysis of isocyanic acid, estimation of inlet NH_3 is important. Two separate estimators were used - one to compute storage of ammonia in the SCR and the outlet NH_3 concentration and the other estimator to predict the inlet NH_3 concentration. The setup used is shown in Figure 2.9.

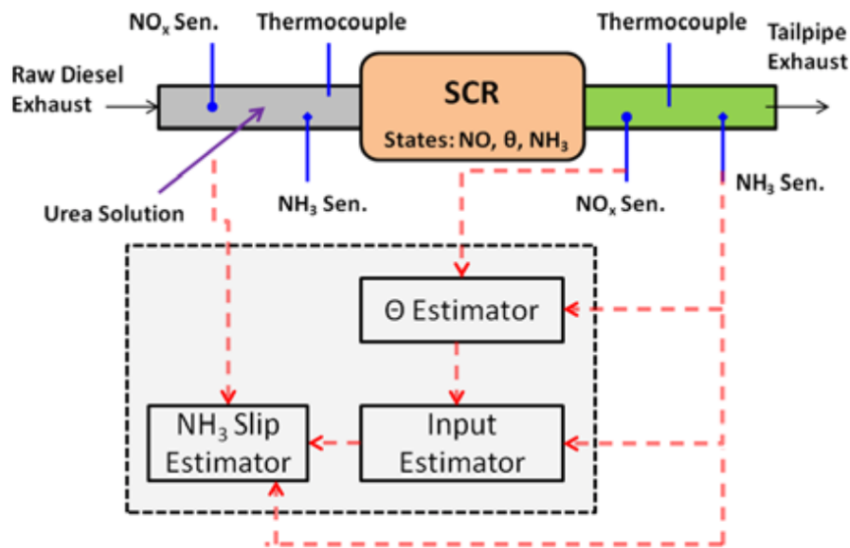


Figure 2.9: SCR estimator setup [41]

Surenhalli et.al [42] developed an EKF SCR estimator to predict NH_3 storage and outlet NO , NO_2 and NH_3 concentrations. Estimator performance was evaluated for three different sensor configurations : (1) NO_x , (2) NH_3 and (3) NO_x and NH_3 . The system with both NO_x and NH_3 sensors had the best performance followed by the NH_3 sensor configuration. The system with a single NO_x sensor had worst performance.

The plant model used a two-site NH_3 storage model along with the SCR reaction. The plant model was calibrated with engine steady state data to within ± 40 ppm for NO/NO_2 and ± 1 ppm for NH_3 concentrations.

These estimator results were validated with both steady state and transient data.

Zhang et al. [43] developed a SCR estimator to predict outlet NO_x concentrations in a two SCR motivated by exchanging sensors with estimated quantities. Figure 2.10 shows the arrangement of sensors in the original system consisting of 3 NH_3 sensors and three NO_x sensors:

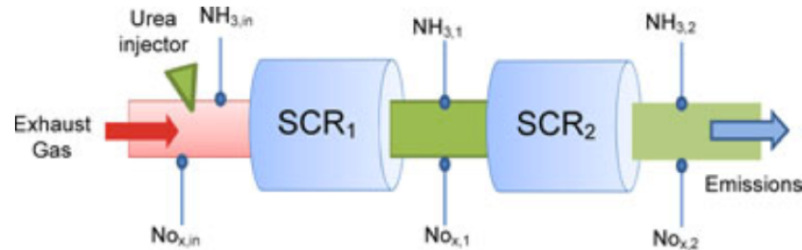


Figure 2.10: Two brick SCR system [43]

A two-estimator scheme was used. The first estimator predicted the inlet NH_3 and coverage fraction inside the first SCR thus replacing the NH_3 sensor at the inlet of the first SCR. The second estimator was a Luenberger observer [43] and estimated NO_x concentration and NH_3 coverage fraction in the second SCR.

Mahadevan et.al [44] developed a CPF estimator to predict the outlet temperature, pressure drop and the PM mass retained as shown in Figure 2.11. The strategy consisted of an EKF for estimation of temperature and PM loading distribution while a linear Kalman filter predicted the pressure drop.

A 2D CPF model was used in both estimators.. The pressure drop estimate was computed based on the pressure drop sensor reading along with the internal states of temperature and PM distribution at every time step. The estimator was able to predict outlet temperature to within 5°C and pressure drop to within 0.5 kPa of experimental values.

2.6 Ultra-Low NO_x Aftertreatment Systems

The modeling and experimental studies with a SCR-F indicate a reduction in NO_x conversion of the SCR-F due to low inlet exhaust gas temperature ($<250^\circ\text{C}$), increased

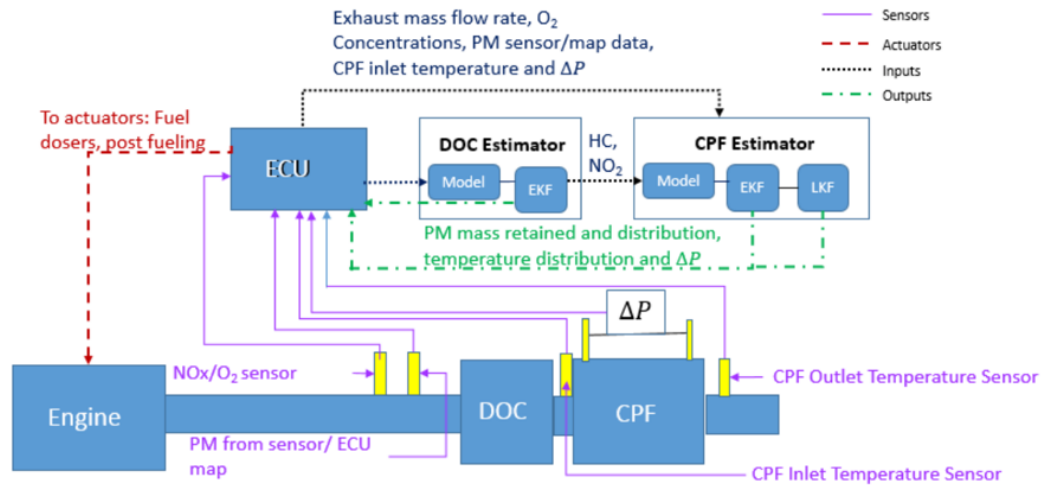


Figure 2.11: CPF estimator system [44]

PM loading, thermal aging, sulphur poisoning and unfavorable NO_2/NO_x ratio < 0.5 during engine operation. In order to ensure a NO_x reduction efficiency of greater than 99.0 % required to meet the 0.02g/bhp-hr standard, a combination of a SCR-F with a SCR is potentially required to mitigate the impact of reduced NO_x conversion of the SCR-F. Experimental studies on different combinations of SCR-F, SCR and passive NO_x adsorber (PNA) have been studied in the literature that have been designed to meet the cold start and hot cycle parts for the NO_x standards.

Strots et al. [17] developed a system model of the SCR-F with other catalysts and a urea dosing injector to determine the interaction of the SCR-F with a SCR in terms of NO_x reduction performance. A 1D SCR-F model was used along with 1D DOC and SCR models. WHTC cycle based on a 6-cylinder 255 kW Euro 5 engine simulation was used for the work. Two designs of a DOC+DPF+SCR+ammonia oxidation catalyst (AMOX) and DOC+DPF+SCR+SCR+AMOX were compared against a DOC+SCR-F+SCR+AMOX system. A faster light off of the SCR-F compared to the SCR in the DPF+SCR system was observed during cold startup due to the lower system thermal inertia caused by the upstream DPF in the DPF+SCR system. A higher operating temperature $> 8^\circ\text{C}$ compared to the SCR during the hot portion of the cycle was observed for the SCR-F. The importance of NO_2 concentration profile caused by reaction-diffusion interaction with the fast SCR reaction in the substrate

wall was identified for future work.

Sharp. et al. [45][46][47] studied different combinations of aftertreatment devices that can achieve the 0.02 g/bhp-hr NO_x emissions standard target. It was determined that in order to achieve this target for a cycle consisting of 1/7th cold start and 6/7th hot start, a composite of 99.4% NO_x reduction efficiency is required. A final configuration consisting of PNA + Mini Burner (MB) +SCR-F +SCR +ammonia slip catalyst (ASC) was identified as plausible system that can meet the 0.02 g/bhp-hr. NO_x standard. Significant cold start FTP emissions reduction is required to achieve the target. It was concluded that a combination of the addition of external heat, reduction of thermal mass of the system, the optimum positioning of catalyst is required to achieve the objective.

Georgiadis et al. [48] designed a system that can significantly reduce the non-uniformity of the NH_3 coverage fraction in the SCR-F leading to lower NH_3 slip. A control system that can reduce NH_3 slip by maximizing NH_3 utilization in the SCR-F during real world operation was developed in order to eliminate the need for an ASC downstream of the SCR-F.

In the system level studies consisting of a SCR-F the role of external heating, lower thermal mass along with placement of catalyst were explored. The impact of local NO_2/NO_x ratio and NH_3 adsorption rate in the SCR-F and SCR as a function of temperature and flow rate of exhaust need to be studied. The contribution of each of the SCR reactions at different temperatures and flow rate conditions in both the SCR-F and SCR is also an important parameter that determines the system performance. These aspects have been studied in this thesis while taking into account the impact of PM loading on NO_x reduction performance and the change in NO_2/NO_x ratio across the SCR-F during PM loading.

2.7 Summary

The literature on a SCR catalyst on DPF's by modeling, experimental data and the design of estimators, led to the following observations that needs to be studied as part of this research

1. The impact of the SCR reactions on PM oxidation rate and the amount of forward diffusion of NO_2 from cake to substrate wall
2. The requirement for one or two sites for storage of NH_3 in the substrate wall
3. The interaction of PM with NH_3 in terms of storage
4. The impact of PM in the wall on SCR reactions in terms of temperature and inhibition of active sites
5. The impact of PM loading on local NO_2/NO_x ratio in the substrate wall which affects the NO_x reduction performance of the Johnson Matthey SCR-F® used for the experimental data in this thesis.
6. The requirements for a state estimator that can estimate the 2D PM mass retained, temperature, NH_3 storage and the pressure drop as well as outlet chemical species concentrations of NO , NO_2 and NH_3

The literature review on ultra low NO_x aftertreatment systems focused on increasing the NO_x reduction efficiency during cold start conditions. This objective is achieved by the addition of external heat, use of a close coupled SCR and NO_x adsorber. Other factors such as local NO_2/NO_x ratio at the inlet of each device have been identified as important variables that need to be studied in order to optimize the system performance for a cycle NO_x conversion efficiency of $> 99.5\%$ required to meet the 0.02 g/bhp-hr. standard. This work will explore a possible system that achieves this system performance by a method in which the NO_2/NO_x ratio can be controlled within $\pm 5\%$ using a combination of a second DOC after the SCR-F with two urea injectors along with a control algorithm that adapts according to engine conditions.

Chapter 3

SCR-F Model Development ¹

The 2D SCR-F model was developed to compute the 2D temperature, PM and NH₃ distribution, SCR-F outlet concentration of NO, NO₂ and NH₃, filtration efficiency and pressure drop across the SCR-F and PM mass retained. The model was developed in MATLAB/Simulink with a variable time step ODE solver (ODE15s) with a capability to run at 60 times real time speed (1 hour experiment is simulated in 1 minute). The model architecture and the governing equations used are described in the following sections. The major outputs of the model are :

1. 2D temperature distribution of the exhaust gas in the inlet/outlet channel and substrate
2. Total PM mass retained and 2D PM mass distribution
3. Outlet NO, NO₂ and NH₃ concentrations
4. 2D distribution of the coverage fraction of the two NH₃ storage sites
5. Filtration efficiency across the SCR-F
6. Pressure drop across the SCR-F

¹Parts of this chapter are from reference [49]

3.1 Overview of the Model

The SCR-F is discretized into N axial and M radial zones, each comprised of hundreds of cells with inlet, outlet channels, PM cake and substrate wall. It is assumed that all cells within a zone have the same intensive properties such as pressure drop, substrate temperature, inlet and outlet channel gas temperatures, etc. and can be modeled using a single, representative cell. The extensive properties, such as total PM mass retained, NH_3 stored etc., are scaled up from those of the representative cell according to the number of actual cells in each zone. The SCR-F's exit variables, such as species concentration and temperature, are calculated from their volume averaged outlet properties of all zones at the exit end of the SCR-F. The SCR-F model assumptions are outlined as follows:

1. There is no inlet PM maldistribution. Thus, each zone's PM inlet rate is the product of the SCR-F's PM inlet rate and the ratio of the zone's volume to the SCR-F's total volume.
2. Each zone contains three temperature states: inlet, outlet channel gas and the zone's - the combined mass of the PM cake layer and the substrate wall.
3. A fully developed thermal boundary layer exists at the inlet of the SCR-F.
4. The exhaust gas is ideal whose properties are functions of temperature and pressure in the test cell. Its molecular weight is based on the concentration of the most prevalent inlet species: CO_2 , O_2 , N_2 and H_2O .

3.2 Model Architecture

The SCR-F model was developed in MATLAB/Simulink using an object oriented M-Coded S Function with a variable time step solver ODE15s. The M-coded S function used for the model computed the gradients at each time step for all the temperature, PM mass retained, species concentrations and NH_3 coverage fraction states. These gradients were supplied to the ODE solver which then integrated them over time based on the time step size computed by the solver using the magnitude of the gradients. Figure 3.1 shows the flowchart of the SCR-F model including the steps involved in the model's execution are shown in Figure 3.1 and as summarized below:

1. The initial conditions of the temperature, PM mass in cake and wall and chemical species concentrations including the NH_3 coverage fraction are computed at time $t = 0$.
2. The time step size is determined by the ODE solver based on the magnitude of the gradients
3. Temperature states are updated by the solver after integration over time based on temperature gradients obtained using heat transfer by conduction, convection, radiation, heat loss to ambient, energy release by chemical reactions
4. PM states are updated based on filtration efficiency and PM oxidation gradients.
5. Species states and NH_3 coverage fraction states are updated based on convection, diffusion transport and consumption of chemical species by reactions.
6. Filtration efficiency and pressure drop based on PM states is computed.
7. The solver checks for convergence based on gradients, relative, absolute tolerance values. If convergence is not reached, a sub iteration with changed time step size is performed. On reaching convergence, the simulation outputs quantities at the major time step and moves to the next time step.
8. If the simulation end time has not been reached, then steps 2-7 are repeated.

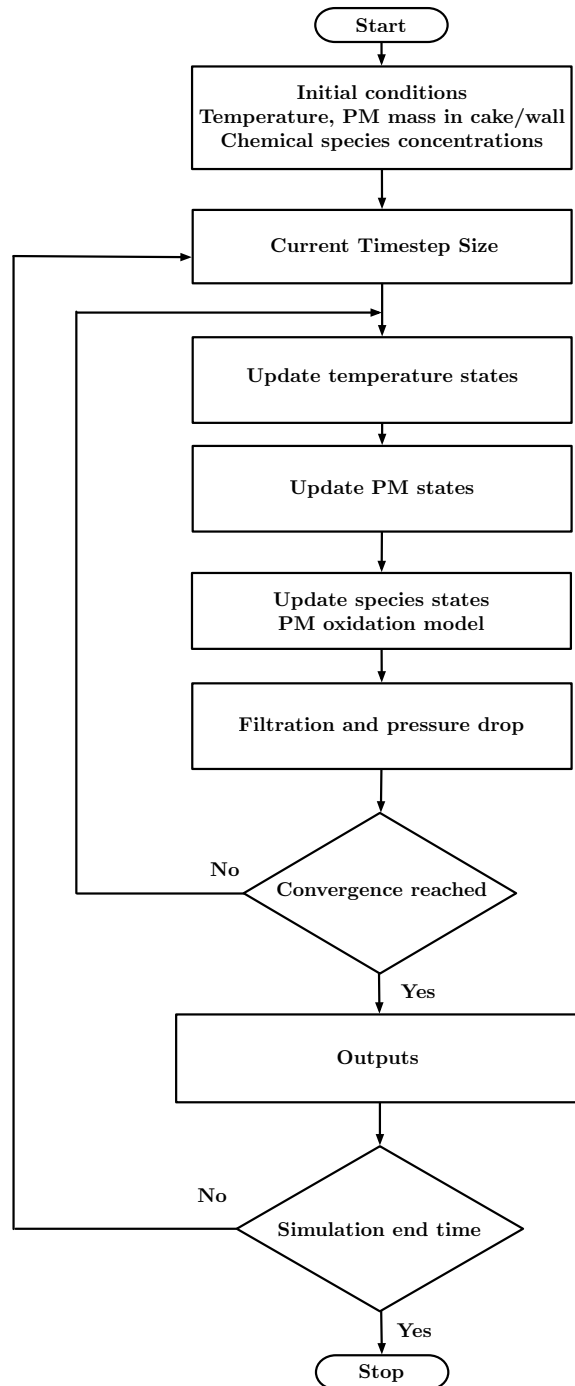


Figure 3.1: SCR-F model flowchart

MATLAB Classes were used to compute each of the physical properties used in the model with numerical integration being performed using the ODE solver. The main classes used in the model were :

1. classDelP - Calculates pressure drop and filtration efficiency.
2. classDOC - Computes the radial temperature profile at the inlet of the SCR-F
3. classGas - Handles calculation of all the physical properties of the gas along with the species sub model that tracks species concentration across the SCR-F
4. classMesh - Creates the mesh used for the model (determines number of axial and radial zones)
5. classPM - Tracks PM mass retained in the PM cake and wall using inputs from filtration and species models
6. classRxn - Calculates the rate constants of all the reactions and the PM oxidation rate
7. classThermal - Computes the temperature in the inlet, outlet channels and substrate + PM cake domains

The following scripts were used along with classes to compute the required outputs :

1. autoCheck - Main setup file that initializes the initial conditions of all the states and runs the Simulink model
2. Parameters - Contains all the user defined parameters
3. Constants - Defines all the physical quantities
4. Derived - Contains derived quantities based on physical constants
5. docFcn - Initializes the temperature states
6. Indices - Initializes variables used for indices in the model
7. cpfContSFcn - Main M coded S-function of the model

Figure 3.2 shows the schematic of the 2D SCR-F model.

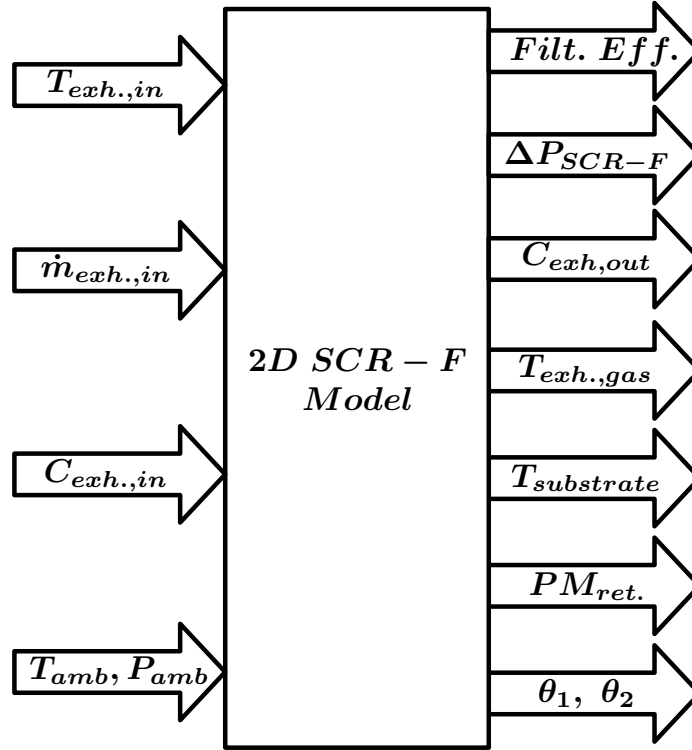


Figure 3.2: SCR-F model schematic

3.3 Submodels

The SCR-F model consists of several submodels that are used to calculate the important states and outputs of the model. Each of the submodels are run once per time step to evaluate the change in either the internal state or output. The major submodels in the SCR-F Model are temperature, exhaust gas velocity, chemical species, PM oxidation, filtration, pressure drop and cake permeability.

3.3.1 Mesh Development

Figure 3.3 shows an SCR-F with length L and radius R that has been discretized in the axial and radial directions creating NM annular regions. The model uses a 2D representation where the annular region properties, such as conduction and convection, are transformed into 2D equivalent values.

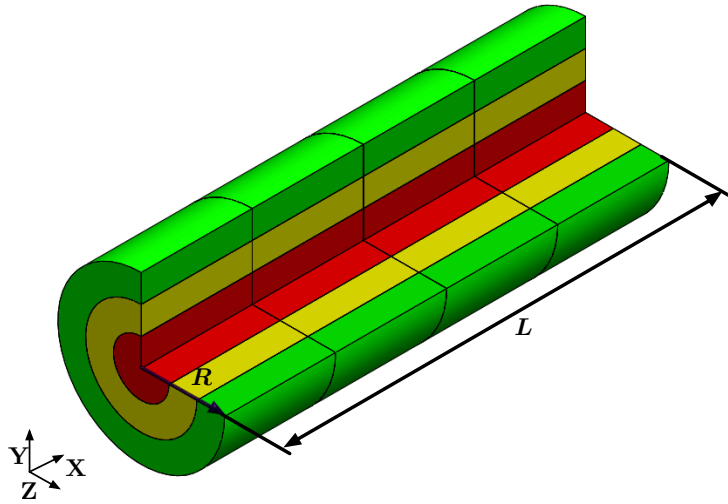


Figure 3.3: SCR-F discretization illustrating 12 annular zones where $N = 3$ and $M = 4$

Figure 3.4 illustrates the details of the discretization approach and how it is used for the thermal and filtration submodels. Figure 3.4a shows the rectangular 2D mesh using four axial and four radial zones. It should be noted that the model assumes symmetry about the SCR-F's centerline and thus only one half of the SCR-F is represented in the mesh. The properties of zones are not required to be uniform. For example, outer zones include the properties of the SCR-F's insulation and metal housing. Another example is that catalyst loading can vary from zone to zone.

Figure 3.4b shows a single representative cell with its inlet and outlet channels, PM cake and substrate wall. Figure 3.4c shows a single zone with quantities relevant to the filtration portion of the model including the PM cake and the substrate wall which is discretized into p slabs. From a differential equation modeling perspective, the cake has PM mass, seven concentration states NO, NO₂, O₂, HC (unburnt hydrocarbons), NH₃, CO and CO₂ concentration states while the wall slabs each have a single PM mass state, two stored NH₃ states and the seven concentration states. Figure 3.4d shows the three control volumes of a zone used for its thermal model. Each zone has three temperature states: the inlet channel, the outlet channel, and a single temperature for the PM cake and substrate wall.

In summary, each zone has four categories of states: three temperature states, $(p + 1)$ PM states in the cake and the wall slabs, $2p$ NH₃ storage states in the wall and $21 + 7p$

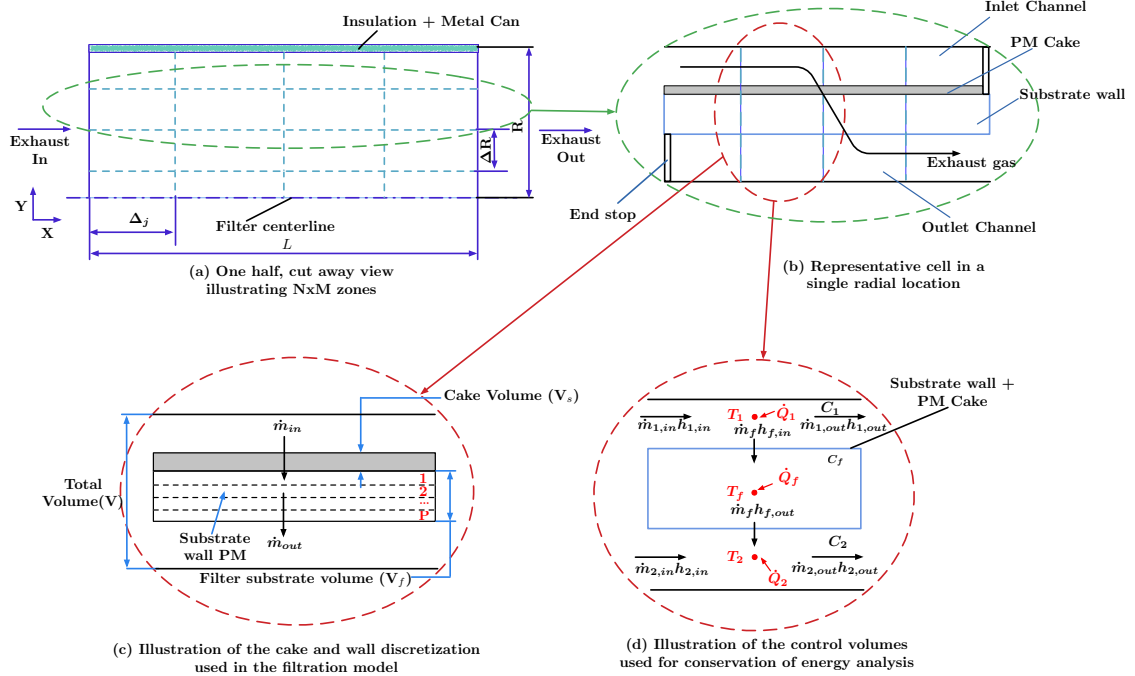


Figure 3.4: SCR-F model mesh - temperature and filtration

concentration states in the inlet and outlet channels, the PM cake and the substrate wall. A total of $25 + 10p$ states, and the same number of differential equations in the NM zones are solved at each time step. For all the cases considered in this work, the model ran about 50 times faster than real time with $p = 4$ and $N = M = 10$. detailed description of the equations used for mesh development are in Appendix A.

3.3.2 Calculation of Physical Properties

The physical properties of the exhaust gas are calculated on classGas.m class of the model. The following paragraphs describe the equations used for the calculation of the different properties.

Density

The ideal gas equation was used to calculate the density of the exhaust gas at every

time step as shown in Equation 3.1.

$$\rho_{exh,m} = \frac{P_m(MW)_{exh,m}}{\bar{R}T_m}, m = 1, 2, w \quad (3.1)$$

$\rho_{exh,m}$ is the density of exhaust gas, P_m is the absolute pressure, $(MW)_{exh,m}$ is the molecular weight of exhaust gas, T_m is the temperature of the exhaust gas and m is the index of the domain consisting of inlet channel, outlet channel and wall. \bar{R} is the universal gas constant with a value of 8.314 kJ/kmol-K .

Molecular weight

The exhaust gas molecular density was calculated using Equation 3.2 using the mole fractions of the dominant chemical species (CO_2 , O_2 , N_2 and H_2O) concentrations in the exhaust gas mixture. n

$$(MW)_{exh,m} = \sum_{i=1}^{n_{sp}} (Y_i)_m (MW)_i \quad (3.2)$$

n_{sp} is the number of chemical species used for calculation of exhaust gas molecular weight. $(Y)_i$ is the mole fraction of the chemical species i in the exhaust gas mixture. $(MW)_i$ is the molecular weight of individual species i . The molecular weight of species used in this calculation are $MW_{O_2} = 15.9 \text{ kg/kmol}$, $MW_{CO_2} = 44.0 \text{ kg/kmol}$, $MW_{N_2} = 28.0 \text{ kg/kmol}$ and $MW_{H_2O} = 18.0 \text{ kg/kmol}$

Dynamic viscosity

The dynamic viscosity of the exhaust gas is computed as a function of the temperature in the substrate wall T_w using Equation 3.3.

$$\mu_{exh} = -1.3126E - 11 * T_w^2 + 4.2194E - 08 * T_w + 1.7843E - 05 \quad (3.3)$$

Specific heat

The specific heat of the exhaust gas (assumed as air) is computed as a function of the temperature in the substrate wall T_w using Equation 3.4.

$$c_{p,exh} = 3.7835E - 05 * T_w^2 + 2.0196E - 01 * T_w + 9.8135E + 02 \quad (3.4)$$

Thermal Conductivity

The thermal conductivity of the filter (PM cake + substrate wall) is computed using Equation 3.5 based on the thermal conductivity of PM and substrate wall. Since the volume of the PM cake changes with time the thermal conductivity value is computed after updating the PM cake thickness value at every time step.

$$k_f = \frac{V_w * k_{sub} + V_{PM} * k_{PM}}{V_w + V_{PM}} \quad (3.5)$$

k_f is the conductivity of the filter (PM cake + Substrate wall). k_{sub} and k_{PM} are conductivities of the substrate wall and PM cake. V_w and V_{PM} are the volume of substrate wall and PM cake.

Convection Heat Transfer Coefficient

The convection heat transfer coefficient of exhaust gas in each zone i, j is computed using Equations 3.6.

$$h_{i,j} = \frac{Nu_{i,j} * k_{exh.}}{\frac{a-ts_i}{2}} \quad (3.6)$$

$Nu_{i,j}$ is the Nusselt number (2.975) for square channels. $k_{exh.}$ is the thermal conductivity of the exhaust gas. a and ts_i are channel width and PM cake thickness, L_t is the length of axial discretization.

The conductivity of the exhaust gas is given by :

$$k_{exh} = \sum_{i=1}^{n_{sp}} Y_i \frac{k_i}{e_i} \quad (3.7)$$

where:

$$k_i = \frac{A_i T^{B_i}}{1 + \frac{C_i}{T} + \frac{D_i}{T^2}} \quad (3.8)$$

The coefficients A_i , B_i , C_i and D_i are used for individual chemical species in the exhaust gas. These are described in detail in reference [37].

3.3.3 Exhaust Gas Velocity

The velocity of exhaust gas in the inlet, outlet channels and the substrate wall is computed using conservation of mass and momentum equations shown in Equations 3.9, 3.10, 3.11 and 3.12.

$$v_{s_i,k} = \frac{\dot{m}_{i,j}}{4\rho_{i,j}\frac{N_{c_i}}{2}(a - 2\bar{t}_{s_i})L_t} \quad (3.9)$$

$$v_{w_i,j} = \frac{v_{s_i,j}(a - 2\bar{t}_{s_i})}{a} \quad (3.10)$$

$$v_1|_{i,j} = v_1|_{j-1} - \frac{4v_{s_i,j}}{a - 2\bar{t}_{s_i}}\Delta L_{j-1} \quad (3.11)$$

$$v_2|_{i,j} = v_2|_{j-1} - \frac{4u_{w,i}}{a}\Delta L_{j-1} \quad (3.12)$$

Where $\dot{m}_{i,j}$ is the total exhaust mass flow rate into each zone. The density of exhaust gas and number of cells in each zone are represented by $\rho_{i,j}$ and N_{c_i} . v_1 , $v_{s_i,j}$, $v_{w_i,j}$ and v_2 are the exhaust gas velocity in the inlet channel, PM cake, substrate wall and outlet channel respectively. The PM cake thickness is represented by \bar{t}_{s_i} , a is the clean inlet/outlet channel width. ΔL is the length of axial discretization in each of the domain.

The boundary conditions for this system are given by Equations 3.13, 3.14 and 3.15.

$$v_1|_{i,j=0} = \frac{\dot{m}_{total,i,j}}{\rho_{i,j}\frac{N_{c_i}}{2}(a - 2\bar{t}_{s,i})^2} \quad (3.13)$$

$$v_1|_{i,j=L} = 0 \quad (3.14)$$

$$v_2|_{i,j=0} = 0 \quad (3.15)$$

Equation 3.13 is used to calculate the velocity of exhaust gas entering the inlet channel in each radial zone based on thermodynamic conditions including absolute pressure, temperature and density of the exhaust gas. The inlet channel velocity decreases as a function of the distance with the velocity at the end of channel equal to zero given by Equation 3.14. The exhaust gas velocity at the start of the inlet channel is zero and increases as a function of length given by boundary condition in Equation 3.15.

3.3.4 Temperature Sub Model

The assumed SCR-F inlet temperature distribution is a fully developed thermal boundary layer as explained in Appendix B. In each zone, conservation of energy is applied to three control volumes shown in Figure 3.4d, (1) the inlet channel, (2) the outlet channel and (3) the substrate wall and PM cake also called filter, resulting in Eq. 3.16 to 3.18 that are solved using the mesh the shown in Figure 3.5

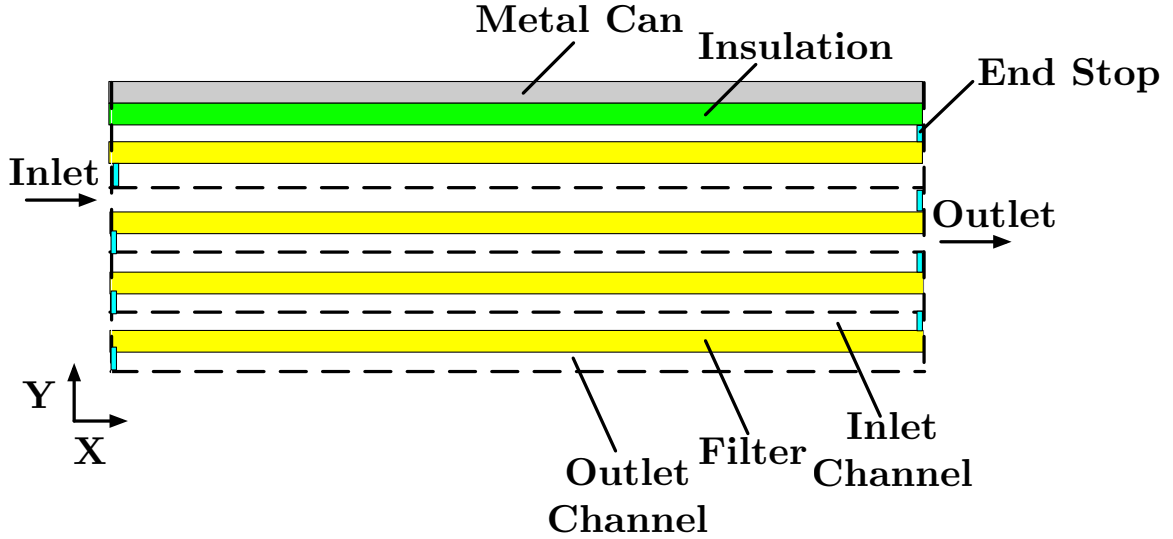


Figure 3.5: Schematic of temperature solver mesh for SCR-F/CPF model

$$\rho_g c_v V_1 \frac{dT_1}{dt} |_{i,j} = \rho_g c_p (a - \bar{t}_s l)^2 v_1 T_1 |_{i,j-1} - \rho_g c_p (a - \bar{t}_s l)^2 v_1 T_1 |_{i,j} - \rho_g c_p 4a \Delta L v_w T_1 |_{i,j} + \dot{Q}_1 |_{i,j} \quad (3.16)$$

$$(\rho_c c_c V_c + \rho_w c_w V_w) \frac{dT_f}{dt} |_{i,j} = \rho_g c_p 4a \Delta L v_w (T_1 - T_f) |_{i,j} + \dot{Q}_{cond,axial} |_{i,j} + \dot{Q}_{cond,radial} |_{i,j} + \dot{Q}_{conv} |_{i,j} + \dot{Q}_{reac,SCR} |_{i,j} + \dot{Q}_{reac,PM} |_{i,j} + \dot{Q}_{cond,HC} |_{i,j} + \dot{Q}_{amb} |_{i,j} \quad (3.17)$$

$$\rho_g c_v V_2 \frac{dT_2}{dt} |_{i,j} = \rho_g c_p a^2 v_2 T_2 |_{i,j-1} - \rho_g c_p a^2 v_2 T_2 |_{i,j} + \rho_g c_p 4a \Delta L v_w T_f |_{i,j} + \dot{Q}_2 |_{i,j} \quad (3.18)$$

The indices 1, 2, c , w and f are used to represent quantities such as temperature, volume etc., in the inlet channel, the outlet channel, PM cake, substrate wall and PM cake + substrate wall respectively. A zone's three temperature states are denoted T_i where i is 1, 2 or f .

ρ_g , ρ_c and ρ_w represent the density of the exhaust gas, PM cake and substrate wall. V_1 , V_2 , V_c and V_w represent the volume of inlet, outlet channel, PM cake and substrate wall. The constant volume and constant pressure specific heat capacities of the exhaust gas in the inlet, outlet channel are given by c_v and c_p . Specific heat of PM cake and substrate wall in the filter are given by c_c and c_w .

a is the width of clean inlet/outlet channel and \bar{t}_{s_i} is the thickness of PM cake. ΔL is the length of the axial division. The velocity of the exhaust gas in the inlet channel, outlet channel and filter are given by v_1 , v_2 and v_w .

The right hand side terms of Equations 3.16 and 3.18 represent the heat capacity of the exhaust gas in the inlet and outlet channels. The first terms on the right hand side represent the change in enthalpy of the exhaust gas in the given zones inlet and outlet channels. The last terms on the right hand side \dot{Q}_1 and \dot{Q}_2 represent the heat transfer by convection from the exhaust gas in the inlet channel to the filter and the filter to the outlet channel exhaust gas.

In Equation 3.17 the right hand side term represents the heat capacity of the system and rate of temperature change. The first term of the right hand arises from the conservation of enthalpy of the exhaust gas flowing through the filter. $\dot{Q}_{cond,axial}$ and $\dot{Q}_{cond,radial}$ represent the conduction of heat in axial and radial direction through the filter, insulation material and metal can at the SCR-F's outer edges. The heat transfer from the exhaust gas in the inlet channel to the filter and from the filter to the exhaust gas in the outlet channel by convection is represented by \dot{Q}_{conv} . $\dot{Q}_{reac,SCR}$, $\dot{Q}_{reac,PM}$ and $\dot{Q}_{reac,HC}$ represent the energy release by SCR reactions, PM oxidation by NO_2 , O_2 and HC oxidation. Heat loss to ambient by convection and radiation are given by \dot{Q}_{amb} .

The \dot{Q}_{amb} term is only used for the outermost radial nodes of the SCR-F model. In the remaining radial nodes this term is neglected. This term accounts for heat loss to ambient by all three forms of heat transfer (conduction, convection and radiation) through the insulation and metal can layers. The conduction term accounts for influence of both the PM cake and substrate material by computing the thermal

conductivity value based on weighted average of the substrate material and PM cake thermal conductivities using their volumes. Detailed explanation of all the terms in these equation is given in Appendix B.

The temperatures calculated using these equations are compared against the thermocouple data from 20 thermocouples placed in the inlet and outlet channels of the SCR-F®. The first 10 thermocouples S1 - S10 are placed in the inlet channel and remaining thermocouples S11 - S20 are placed in the outlet channel as shown in Figure 3.6. By simulating the thermocouple data these equations were able to capture the temperature distribution in the SCR-F® in radial and axial direction. A detailed description of the calibration procedure for this sub model is given in the Chapter 4 of the dissertation.

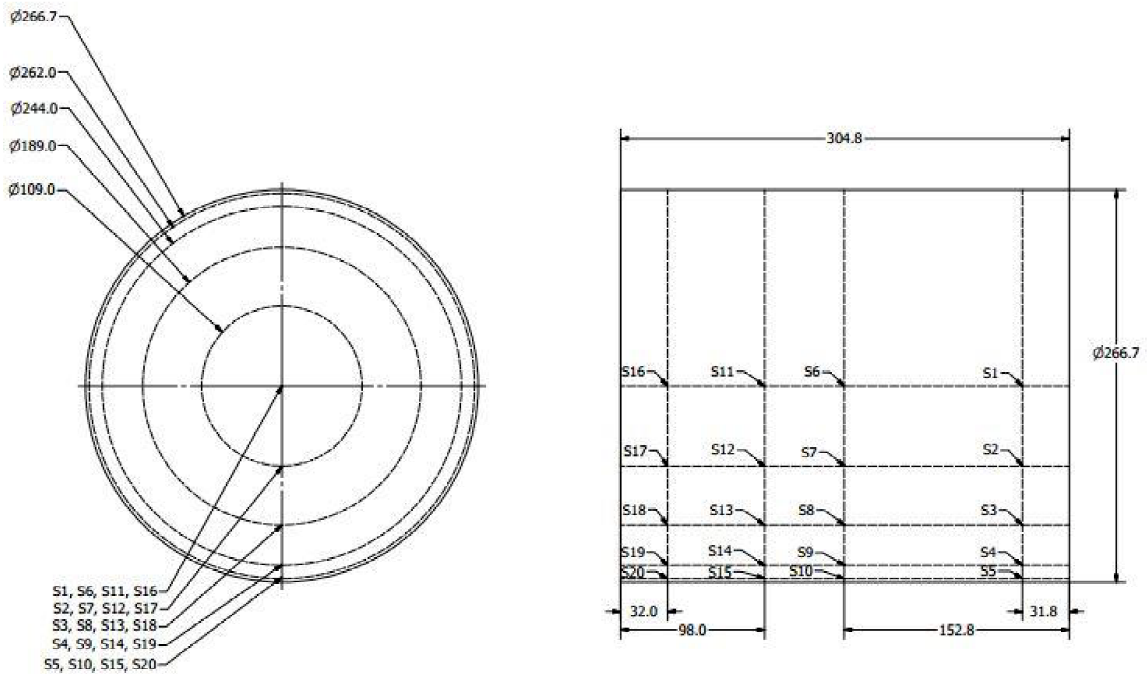


Figure 3.6: Schematic of SCR-F® thermocouple arrangement [4]

3.3.5 Species Model

The exhaust gas flowing through the SCR-F is modeled as consisting of NO, NO₂, NH₃, HC, O₂, N₂, H₂O, CO and CO₂ chemical species. The change in concentration of these chemical species as the exhaust gas flows in the inlet, outlet channels, PM

cake and substrate wall layers is computed using the chemical species model. The reactions in the PM cake and substrate wall layers include oxidation of CO, NO, NH₃ and HC, PM oxidation by NO₂ and O₂ and SCR reactions including fast, slow and standard reactions.

The coupled system of equations 3.19 to 3.21 are based on reaction - diffusion transport phenomena scheme are used to determine the concentrations in the inlet channel, the outlet channel and the filter (PM cake + substrate wall) in each zone.

$$\frac{dC_{1,l}}{dt} = -v_1 \frac{dC_{1,l}}{dx} + \left(\frac{4}{a}\right) k_1 (C_{1s,l} - C_{1,l}) + \left(\frac{4}{a}\right) v_f C_{1,l} \quad (3.19)$$

$$\frac{dC_{w,l}}{dt} = -v_w \frac{dC_{w,l}}{dy} + \frac{d}{dy} \left(D_l \frac{dC_{w,l}}{dy} \right) - \sum_k \xi_{l,m} R_m \quad (3.20)$$

$$\frac{dC_{2,l}}{dt} = -v_2 \frac{dC_{2,l}}{dx} + \left(\frac{4}{a}\right) k_2 (C_{2,l} - C_{2s,l}) + \left(\frac{4}{a}\right) v_f C_{2s,l} \quad (3.21)$$

l and m represent the indices of the chemical species and reactions. The inlet and outlet channel are represented by indices 1 and 2. The PM cake and substrate wall domains are combined into a single control volume called the filter and is represented by the index f, but in the species model the PM cake and slabs in the wall are treated as separate domains such that each domain has its own concentration and NH₃ storage states while the physical properties used to compute the reaction rates such as temperature and exhaust velocity are the same for all the domains.

The concentration of chemical species *l* in the inlet, outlet channel and filter are given by $C_{1,l}$, $C_{2,l}$ and $C_{f,l}$. The species concentrations at the boundary of the inlet channel - filter and filter - outlet channel are given by $C_{1s,l}$ and $C_{2s,l}$. The exhaust velocity in the inlet, the outlet channel and the filter is given by v_1 , v_2 and v_f . The mass transfer coefficients based on the molecular diffusivity for species *l* in the inlet and the outlet channel are k_1 and k_2 . *a* is the width of the clean inlet and outlet channel.

The length of the discretizations of the filter in the given zone in the axial and the radial directions are given by Δx and Δy . The diffusivity of species *l* is given by D_l . $\xi_{l,m}$ is the stoichiometric coefficient of species *l* in reaction *m*. R_m is the reaction rate of the reaction *m*. The number of reactions that species *l* participates in is given by index *k* discretization.

The physical representation of a single representative cell in a radial location of SCR-F is shown in Figure 3.7. This cell consists of the inlet channel, the outlet channel, the PM cake and the substrate wall. The PM cake layer thickness w_p in each zone of this cell is calculated by dividing the PM mass m_c in a zone by the total number of cells in the given zone followed by 4 to account for PM in one side of the inlet cell. The PM in each of the substrate wall slabs is calculated with the same approach as the PM cake. The substrate wall thickness w_s is considered in the representative cell.

The mesh from Figure 3.7 is used for all the species concentration calculations using equations 3.19 to 3.21 in all the three control volumes. The concentrations of species are calculated for the PM cake and each of the wall slabs as shown in the Figure.

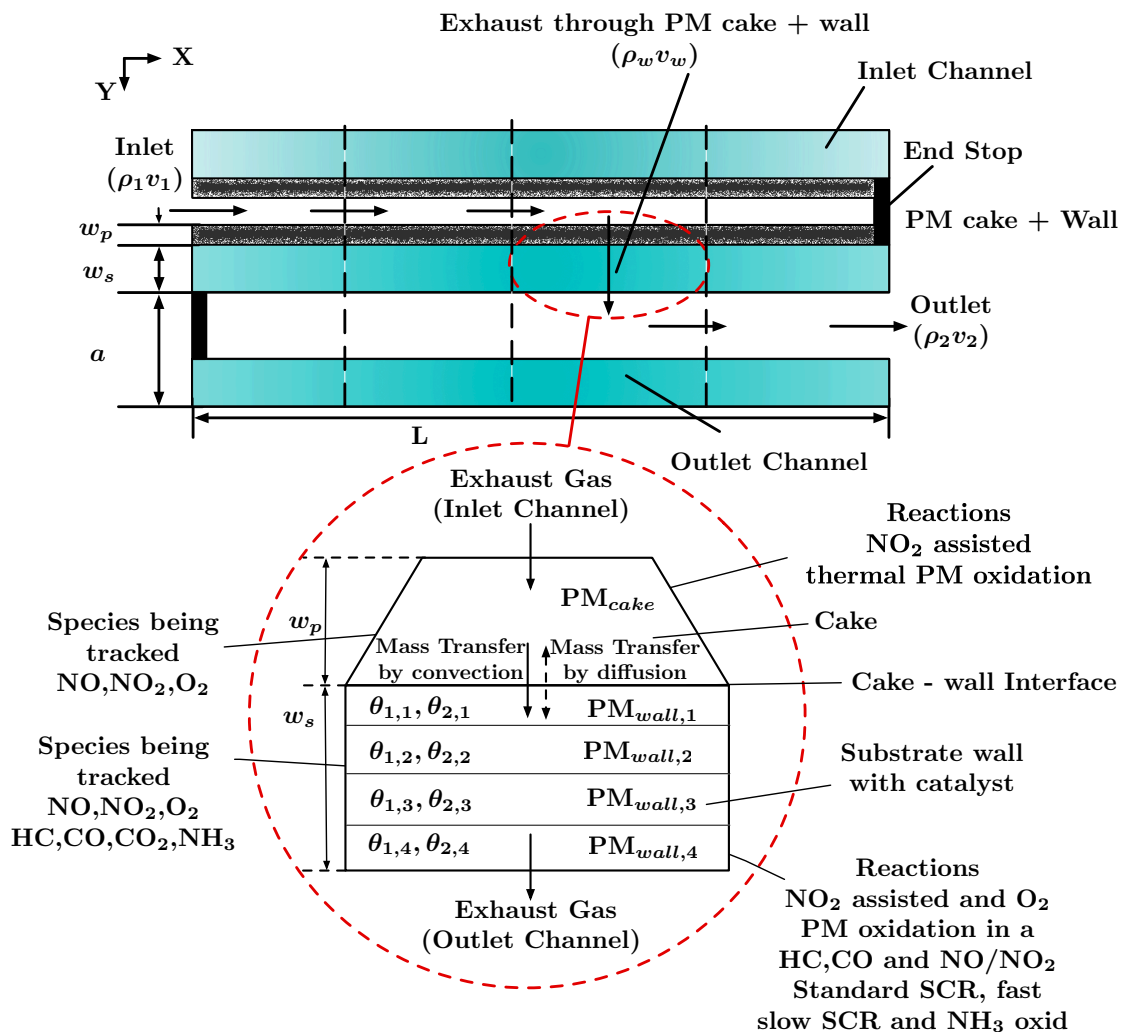


Figure 3.7: Schematic of cake and wall filtration and PM oxidation

The figure shows the schematic of the cake and the substrate wall. The exhaust gas passes through the inlet channel into the PM cake followed by the porous substrate wall which is divided into p number of slabs where the ammonia is stored in two storage sites in each of the slabs. After passing through the wall, the exhaust gas flows into the outlet channel and to the outlet of the SCR-F. The resultant outlet concentrations from each of the representative cells from each radial location are then volume averaged to obtain the SCR-F outlet concentrations of the chemical species.

The ammonia storage takes place in two storage sites. The first storage site is used for both storage and SCR reactions. The second storage site is used for storage only. Equations 3.22 and 3.23 are used to compute the ammonia storage rate in both the storage sites. An Arrhenius approach was used for calculating the rate constants of the reactions.

$$\frac{d\theta_1}{dt} = \frac{(R_{\text{ads}} - R_{\text{des}} - 4R_{\text{std}} - 4R_{\text{fst}} - 4R_{\text{slo}} - 4R_{\text{oxid}})}{\Omega_1} \quad (3.22)$$

$$\frac{d\theta_2}{dt} = \frac{(R_{\text{ads}} - R_{\text{des}})}{\Omega_2} \quad (3.23)$$

Figure 3.8 shows the approach used for the ammonia storage and the SCR reactions in the SCR-F model. The exhaust gas flows through the pores in the substrate wall. As the exhaust gas comes in contact with the catalyst surface coated on the substrate, the NH_3 molecules attach to the active sites which then react with NO and NO_2 to undergo the SCR reactions. In the case of the clean filter, the unit collector diameter computed in the Filtration sub model is δ_w which increases to δ_s in the filter with PM loading. This increase in the unit collector diameter leads to a reduction in the mass transfer from the gas stream to the catalyst surface leading to an inhibition of the SCR reactions which is simulated in the model using the effectiveness factor concept from reference [6]. Detailed explanation of all the reactions is in Appendix E. Table 3.1 shows all the reactions used in the species model.

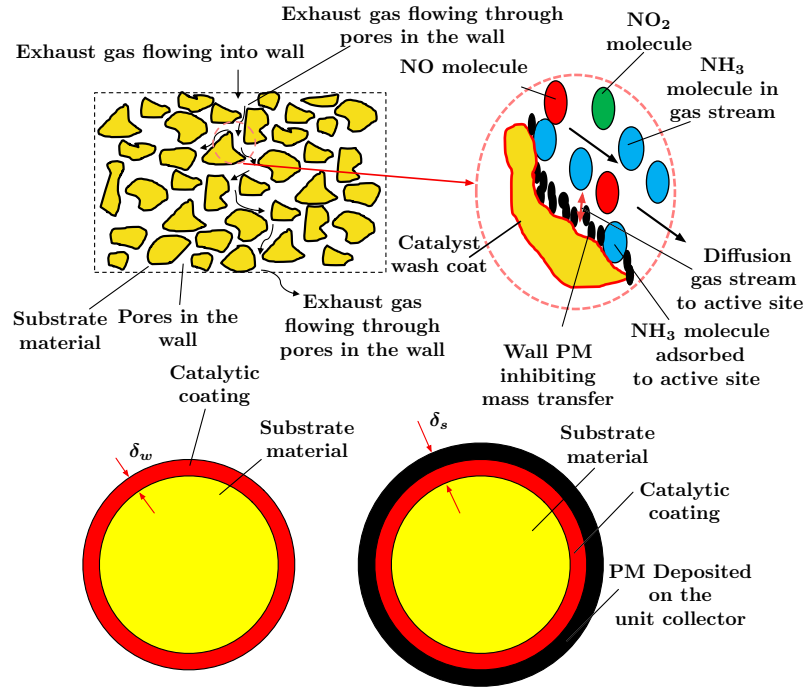


Figure 3.8: NH₃ storage inside substrate wall for the SCR-F model

Table 3.1
Reactions in the SCR-F model

Description	Reaction Rate equation	Units of k
O ₂ based PM oxidation	$R_{O_2,oxid} = K_{O_2} C_{O_2}$	$gmol/m^3.s$
NO ₂ based PM oxidation	$R_{NO_2,oxid} = K_{NO_2} C_{O_2}$	$gmol/m^3.s$
HC oxidation	$R_{HC} = k_{HC} C_{HC} \frac{1}{G_1}$	$gmol/m^3.s$
CO oxidation	$R_{CO} = k_{CO} C_{CO} \frac{1}{G_2}$	$gmol/m^3.s$
NO oxidation (Reversible)	$R_{NO} = k_{CO} \frac{1}{G_3} (c_{NO} - \frac{C_{NO_2}}{k_c})$	$gmol/m^3.s$
NH ₃ adsorption	$R_{ads} = K_{ads} C_{NH_3,s} (1 - \theta_1) \Omega_1$	$m^3/gmol.s$
NH ₃ desorption	$R_{des} = K_{des} (\theta_1) \Omega_1$	$1/s$
NH ₃ adsorption 2	$R_{ads,2} = K_{ads,2} C_{NH_3,s} (1 - \theta_2) \Omega_2$	$m^3/gmol.s$
NH ₃ desorption 2	$R_{des,2} = K_{des,2} (\theta_2) \Omega_2$	$1/s$
NH ₃ oxidation	$R_{oxid,1} = K_{oxid,1,NH_3} (\theta_1) \Omega_1 \eta_{o_2}$	$1/s$
Standard SCR	$R_{std,1} = K_{std,1} C_{NO,s} (\theta_1) \Omega_1$	$m^3/gmol.s$
Fast SCR	$R_{fst} = K_{fst} C_{NO,s} C_{NO_2,s} (\theta_1) \Omega_1$	$m^3/gmol.s$
Slow SCR	$R_{slo} = K_{slo} C_{NO_2,s} (\theta_1) \Omega_1$	$m^3/gmol.s$
N ₂ O formation	$R_{N_2O} = K_{N_2O} C_{NO_2,s} (\theta_1) \Omega_1$	$m^3/gmol.s$

The general form of the effectiveness factor is shown in Eq 3.24 and 3.25 as described in reference [7]. Detailed derivation of effectiveness factor equation is in Appendix C.

$$k_{actual} = k_{ideal}\eta_s \quad (3.24)$$

$$\eta_s = \frac{\sqrt{D_{eff}k_{ideal}\tanh(\Phi_w)}}{(\delta_s - \delta_w)\sqrt{D_{eff}k_{ideal}\tanh(\Phi_w)} + D_{eff}} \quad (3.25)$$

Where, k_{actual} is the actual rate constant after taking into account the inhibition caused by wall PM. k_{ideal} is the rate constant from Arrhenius equation and η_s is the effectiveness fraction. D_{eff} is the molecular diffusivity and Φ_w is the Thiele Modulus defined as the ratio of diffusion and reaction in the washcoat layer. The model has the ability to simulate SCR reaction rates based on the spatial distribution of the catalyst in the substrate wall in order to simulate the axial variation in SCR reaction rate and energy release. The capability is used to simulate the temperature distribution during NO_x reduction.

3.3.6 PM Mass Retained Model

The PM mass is deposited in the PM cake layer and slabs present in the substrate wall. The amount of PM deposited in each layer is calculated using the inlet PM concentration, exhaust flow rate and filtration efficiency of the layer computed by the filtration efficiency model. The deposited PM is oxidized by passive oxidation and thermal oxidation reactions. The resultant PM retained in the PM cake and substrate wall layers is tracked by the model as a function of time as PM cake and wall PM states.

PM mass balance

The mass balance used to track the PM mass in PM cake and substrate wall is given by equation 3.26

Each zone's cake oxidizes both thermally (O_2) and by NO_2 given by Eq. 3.28 . Figure 3.9 shows the schematic from the PM cake and substrate wall layers used for PM mass balance.

$$\dot{m}_{in} = \dot{m}_{ret} + \dot{m}_{ox} + \dot{m}_{out} \quad (3.26)$$

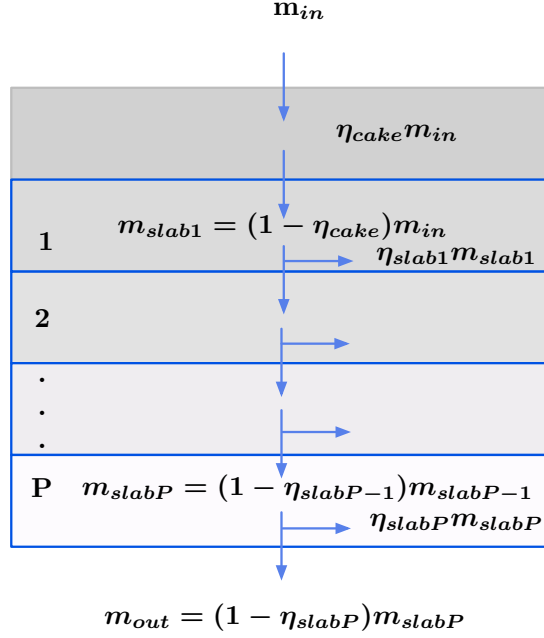


Figure 3.9: PM mass balance in SCR-F

The flow rate of the PM into the axial node of a representative cell in each zone of the SCR-F is given by Equation 3.27.

$$\dot{m}_{in,i,j} = \frac{C_{in} Q_{std,i,j}}{n_{cells}} \frac{v_w(x)}{\bar{v}_w} \quad (3.27)$$

Where C_{in} is the concentration of the PM in $\frac{kg}{std.m^3}$ flowing into the SCR-F. Q_{std} is the standard volumetric flow rate of the exhaust into the SCR-F. n_{cells} is the number of cells in each zone used to find the flow into each representative cell in each radial location. $v_w(x)$ and \bar{v}_w are the local exhaust gas velocity at axial location and average exhaust gas wall velocity used to determine the PM deposited in each axial location.

PM oxidation rate

The rate of PM oxidation in the PM cake is calculated using Equation 3.28

$$\frac{d(mc_{oxid,i,j})}{dt} = -\frac{s_p \rho_{i,j} Y_{O_2,i,j} k_{o_2,i,j} W_c}{\alpha_{O_2} W_{O_2} \rho_s} mc_{i,j} - \frac{s_p \rho_{i,j} Y_{NO_2,i,j} k_{NO_2,i,j} W_c}{\alpha_{NO_2} W_{NO_2} \rho_s} mc_{i,j} \quad (3.28)$$

Where, m_c is the cake mass and $\dot{m}_{c,oxid}$ is the PM cake oxidation rate. The molecular weight of carbon, the cake's specific surface area and the PM cake density are denoted by W_c , s_p and ρ_s respectively. The cake O_2 and NO_2 concentrations are denoted by C_{O_2} and C_{NO_2} . The thermal and NO_2 assisted PM oxidation rate constants are of the Arrhenius form of equation 3.29 and denoted by k_{o_2} and k_{NO_2} where A_i is its pre exponential constant and E_i is the activation energy, R is the universal gas constant, and T_f is the filter temperature. The reactions partial factors are denoted α_{O_2} and α_{NO_2}

$$k_i = A_i e^{\frac{-E_i}{RT_f}} \quad i = O_2, NO_2 \quad (3.29)$$

where k_m is the rate constant of reaction m. A_m and E_m pre exponential and activation energy of reaction m, R is the universal gas constant and T_f is the filter temperature. Similarly, the PM mass oxidation in each wall slab is given by Eq. 3.30.

$$\left[\frac{d(mw_{oxid,i,j})}{dt} \right]_n = \left[-\frac{s_p \rho_{i,j} Y_{O_2,i,j} k_{o_2,i,j} W_c}{\alpha_{O_2} W_{O_2} \rho_s} mw_{i,j} - \frac{s_p \rho_{i,j} Y_{NO_2,i,j} k_{NO_2,i,j} W_c}{\alpha_{NO_2} W_{NO_2} \rho_s} mw_{i,j} \right]_n \quad (3.30)$$

where k_m is the rate constant of reaction m. A_m and E_m pre exponential and activation energy of reaction m, R is the universal gas constant and T_f is the filter temperature. Similarly, the PM mass oxidation in each wall slab is given by Eq. 3.30

PM mass retained

The rate of PM mass retained in the PM cake and substrate wall slabs is computed using the PM deposited and PM oxidation rate by using Equations 3.31 and 3.32

$$\frac{d(mc_{ret,i,j})}{dt} = \frac{d(mc_{oxid,i,j})}{dt} + \dot{m}_{cake,in,i,j} \quad (3.31)$$

$$\left[\frac{d(mw_{ret,i,j})}{dt} \right]_n = \left[\frac{d(mw_{oxid,i,j})}{dt} \right]_n + \dot{m}_{wall,n,in,i,j} \quad (3.32)$$

Where $mc_{ret,i,j}$ is the PM mass retained in the PM cake and $mw_{ret,i,j}$ is the PM mass retained in each of the n substrate wall slabs. $\dot{m}_{cake,in,i,j}$ and $\dot{m}_{wall,n,in,i,j}$ is the rate

of PM deposited in the PM cake and substrate wall slab. In Equations 3.31 and 3.32 the rate of PM mass retained is computed as the summation of the PM oxidation rate and PM deposition rate. This rate is supplied to the ode solver that integrates over time to compute the PM mass retained at every time step.

3.3.7 Filtration Model

PM filtration takes place in the cake and the substrate wall. Where \dot{m}_{in} is the PM mass flow rate into the cake and \dot{m}_{out} is the PM mass flow rate out of the substrate wall shown in Figure 3.4c. The filtration efficiency is calculated based on the packed bed filtration theory [35] and implemented using the approach described in references [37] and [50]. The equations are summarized in Appendix D, with a brief review of the filtration efficiency provided here.

Each wall slab contains a representative spherical collector with diameter δ_w which grows to a diameter δ_s as PM accumulates until reaching a specified maximum. When the first slab's collector reaches its maximum diameter, cake growth begins along with continued accumulation in the remaining wall slabs.

The total filtration efficiency in a zone is given by Eq. 3.33

$$\eta_{total,i,j} = 1 - \left[(1 - \eta_{cake,i,j}) \prod_{n=1}^P (1 - \eta_{wall,i,j,n}) \right] \quad (3.33)$$

where, η_{cake} is the PM cake layer filtration efficiency and η_{wall_n} is the filtration efficiency of each wall slab calculated using Equations 3.34 and 3.35.

$$\eta_{cake,i,j} = A_\eta \left(1 - e^{-\frac{3\eta_{coll,cake}(1-\epsilon_p)w_p}{2\epsilon_p d_{c,cake}}} \right) \quad (3.34)$$

$$\eta_{wall,i,j,n} = 1 - e^{-\frac{3\eta_{coll,wall}(1-\epsilon_s)\Delta y}{2\epsilon_s d_{c,wall}}} \quad (3.35)$$

The detailed expressions for the terms used in Equations 3.33, 3.34 and 3.35 are included in Appendix D and references [50][37].

3.3.8 Pressure Drop Model

PM initially accumulates in the substrate wall followed by the formation of the PM cake. A zone's inlet-to-outlet pressure drop changes depending on the amount of PM in these domains. The total pressure drop in the zone is the sum of the pressure drops due to the substrate wall, PM cake layer and the frictional losses in the inlet and outlet channels. The pressure drop across each radial section of the SCR-F considering wall, cake and channel pressure is calculated using the streamlines approach explained in Appendix D. Using the streamlines approach, the pressure drop across each radial section of the SCR-F is given by Eq. 3.36

$$\Delta P_{SCR-F} = \Delta P_{\text{wall}} + \Delta P_{\text{cake}} + \Delta P_{\text{channel}} \quad (3.36)$$

Where, $P_1|_{x=0}$ and $P_2|_{x=L}$ are the absolute pressure values at the inlet and outlet of the representative cell in the inlet and the outlet channel respectively calculated using Equations 3.37 and 3.38 from reference [37].

$$\frac{dP_1}{dx} = -\frac{d}{dx}(\rho_1 v_1^2) - F \frac{\mu_1 v_1}{a^2} \quad (3.37)$$

$$\frac{dP_2}{dx} = -\frac{d}{dx}(\rho_2 v_2^2) - F \frac{\mu_2 v_2}{a^2} \left(\frac{a^*}{a}\right)^2 \quad (3.38)$$

Figure 3.10 shows the streamline approach used for the pressure drop model. Equations 3.37 and 3.38 are used in the channels with each of the n possible combinations of inlet and outlet channel divisions shown in the figure to determine the pressure drop across the SCR-F and the average of these stream lines is used as total pressure drop across the SCR-F.

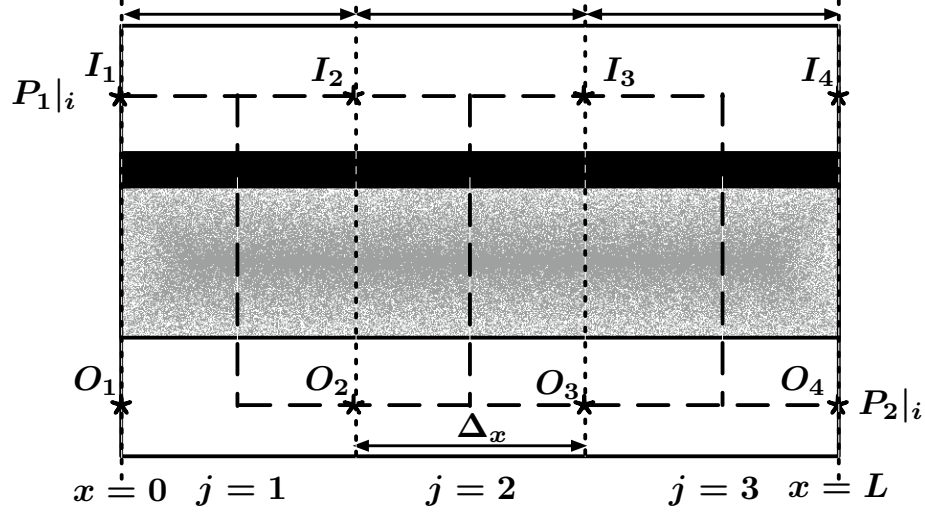


Figure 3.10: Schematic of the streamlines (shown as dashed lines) used for calculating the pressure drop across CPF/SCR-F for 3x1 zone model (4 axial and 1 radial discretization).

The wall pressure drop at each zone is given by Eq. 3.39

$$\Delta P_{\text{wall},i,j} = \mu_{i,j} v_{w,i,j} \frac{w_s}{k_{\text{wall},i,j}} \quad (3.39)$$

Where, Δp_{wall} is the wall pressure drop, v_w is the wall layer velocity, w_s is the substrate wall thickness and k_{wall} is the wall permeability. The cake pressure drop is given by Eq. 3.40

$$\Delta P_{\text{cake},i,j} = \mu_{i,j} v_{s,i,j} \frac{w_{p,i,j}}{k_{\text{cake},i,j}} \quad (3.40)$$

where, ΔP_{cake} is the PM cake pressure drop, v_s is the PM cake layer velocity, w_p is the PM cake layer thickness and k_{cake} is the PM cake layer permeability. The permeability of the wall and the PM cake layer are affected by the PM loading, oxidation and post loading of the SCR-F and are changing continuously. The equations used for the estimation of wall and PM cake permeability during loading, oxidation and post loading phases of the experiment are detailed in Appendix D.

$$\Delta P_{\text{SCR-F},i} = [P_1|_{x=0} - P_2|_{x=L}]_i \quad (3.41)$$

The total pressure drop across the SCR-F accounting for all radial zones is given by Eq. 3.42

$$\Delta P_{\text{SCR-F}} = \frac{\sum_{s=1}^{\text{smax}} \sum_{i=1}^{i=M} V F_i \Delta P_{\text{SCR-F},i}}{\text{smax}} \quad (3.42)$$

where, $\Delta P_{SCR-F,vol.avg.}$ is the volume averaged pressure drop across the SCR-F, M is the number of radial discretizations, $v_{f,i}$ is the volume fraction of exhaust gas flow at each radial section and s_{max} is the number of ways of obtaining the absolute pressure at the inlet of the inlet channel $P_{1|i,j+1}$ at each radial section of the filter. The detailed expressions of the terms in the pressure drop model from reference [50] are documented in reference Appendix D.

Chapter 4

Experimental Data and Model Calibration Procedure ¹

The experimental data used to calibrate the SCR-F model was collected on a Cummins 2013 ISB (280 hp) engine with after treatment system components consisting of the production DOC, CPF, SCR and a SCR-F[®] from Johnson Matthey and Corning. The specifications of the after treatment system components used in the experiments are shown in Table 4.1. The chemical species concentrations of NO and NO₂ were measured with mass spectrometer with an accuracy of +/- 20 ppm. The NH₃ outlet concentration was measured with NH₃ sensor with an accuracy of +/- 25 ppm. The PM mass retained was measured by weighing the SCR-F[®] at end of each stage with an accuracy of +/- 2 g [4].

The experimental data were collected on two aftertreatment configurations using the SCR-F[®]. The first configuration (Configuration 1) consisted of passive oxidation experiments with and without urea injection in which the system consisted of DOC+SCR-F[®]. In this dataset the SCR-F[®] was loaded with PM up to 2 g/l loading followed by PM passive oxidation (PO) of up to 70 % for 7 test experiments with the first set of 7 experiments consisting of no urea injection during PM oxidation and the second set of 7 experiments consisting of urea injection at a target inlet ANR = 1.0 during the PM oxidation. This set of fourteen experiments will be referred to as configuration 1 data with and without urea injection and are described in detail in reference [4]. Active regeneration experiments (AR) were also conducted without

¹Parts of this chapter are from reference [49]

Table 4.1
Aftertreatment system specification [4]

Description	DOC	SCR [®]	SCR	CPF
Substrate Material	Cordierite	Cordierite	Cordierite	Cordierite
Diameter (inch)	9	10.5	10.5	9
Length (inch)	4	12	12	10
Cell Geometry	Square	Square	Square	Square
Total Volume (L)	4.17	17.04	17.04	10.40
Open Volume (L)	3.5	10.2	14.4	7.3
Cell Density /in ²	400	200	400	200
Cell Width (mil)	46	55	46	59
Channel Wall Thickness (mil)	4	16	4	12
Porosity (%)	35	50	35	59
Number of in cells	25447	8659	34636	6362

urea injection to determine the O₂ based PM oxidation kinetics.

The second configuration (Configuration 2) consisted of 12 experiments performed at four test points with and without PM loading. In this dataset, four test points were used with a NO_x reduction cycle consisting of inlet ANR values of 0.8, 1, 1.2 followed by 0 and repeat of 1.2. The first 4 experiments in this dataset were performed on a system consisting of DOC+CPF+SCR[®] system where the CPF was used to remove all the PM upstream of SCR[®] in order to perform NO_x reduction experiments without any PM loading (0 g/l) in the SCR[®]. The remaining 8 experiments in the dataset were performed with a system consisting of DOC+SCR[®] where the CPF was replaced by a spacer and the NO_x reduction experiments were performed with 2 and 4 g/l PM loading in the SCR[®]. These 12 experiments will be referred to as configuration 2 data with and without PM loading. The configuration 2 data are described in detail in reference [5]. Both of these datasets were used to calibrate the 2D SCR-F model.

A third configuration (Configuration 3) consisting of a SCR[®] with a downstream SCR was used to determine the NO_x conversion efficiency of the SCR[®]+SCR system. This configuration consisted of seven test points consisting of six test points from configuration 1 and one test point from configuration 1. In all the experiments, a target inlet ANR of 1.1 was used. The NH₃ slip from the SCR[®] was used as the inlet NH₃ for the SCR and outlet NO_x acted as inlet NO_x for the downstream SCR. The 37 experiments from these 3 configurations will be described in detail in the following sections.

4.1 SCR[®] Configuration 1 Data PO With and Without Urea

The Configuration 1 data with the SCR[®] consists of seven passive oxidation and four active regeneration experiments with and without urea injection. The aim of the passive oxidation experiments without urea injection was to calibrate the pressure drop and filtration characteristics of the SCR[®] during loading and to determine the PM oxidation kinetics in the absence of the SCR reactions. Figure 4.1 shows the experimental setup used for configuration 1 experiments with and without urea injection.

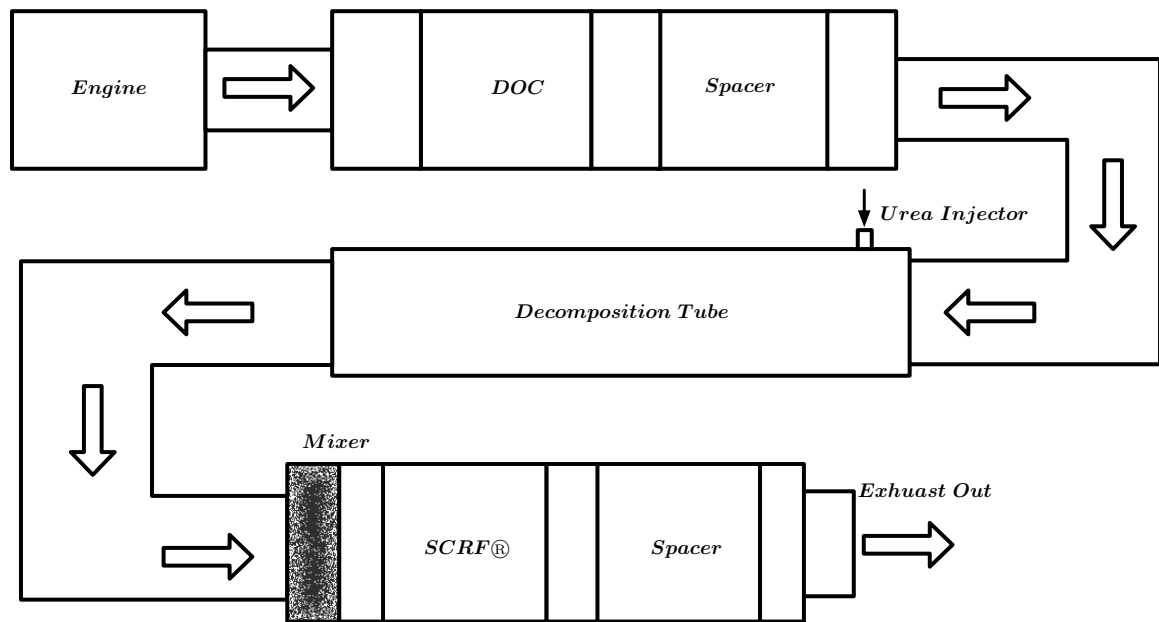
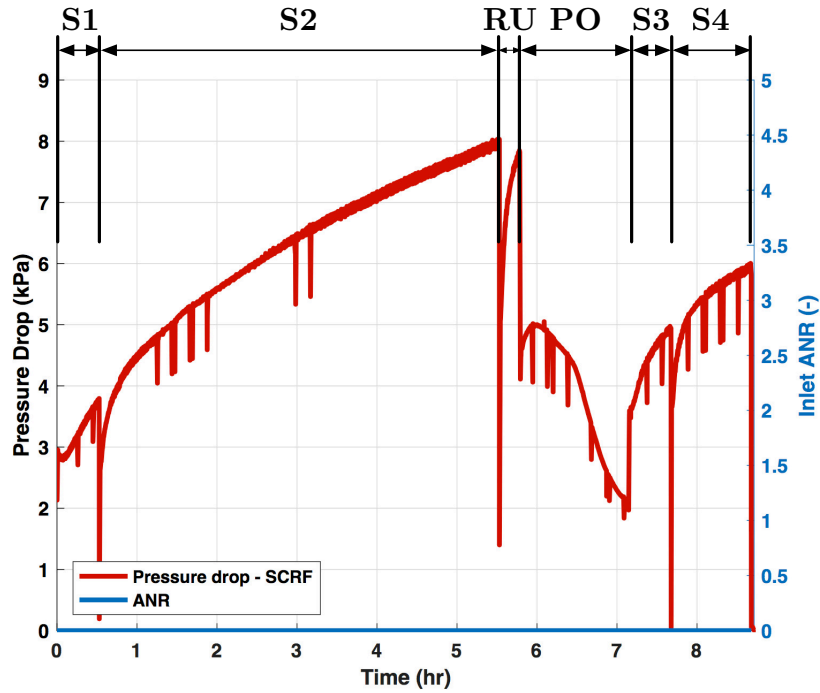
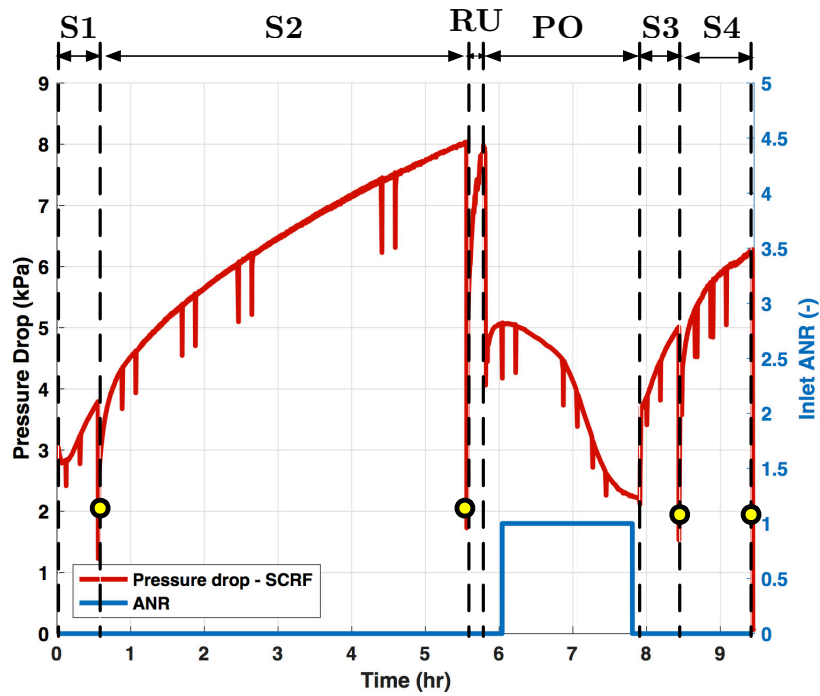


Figure 4.1: Configuration 1 with and without PM loading

For the experiments without urea injection the SCR[®] is loaded up to 2 g/l PM followed by the passive oxidation stage in which up to 70% of PM is oxidized followed by post loading stages. For experiments with urea injection during the passive oxidation stage, a target ANR of 1.0 is maintained by urea injection to enable NO_x reduction during passive oxidation. Figure 4.2 shows the pressure drop and the various stages of the passive oxidation experiments with and without urea injection. The active regeneration experiments were conducted in the same manner but fuel is injected after a ramp up after Stage 2, so that the PM is oxidized at temperatures from 550 - 600 °C



(a) Without urea Test C



(b) With urea Test C

Figure 4.2: Pressure drop for passive oxidation experiments configuration 1 without and with urea stages S1 - Stage 1, S2 - Stage 2, RU - Ramp up, PO - Passive oxidation, S3 - Stage 3, S4 - Stage 4

The SCRF [®] is loaded with PM in stages 1 and 2 to 2 g/l. These stages are used to calibrate the pressure drop, filtration and PM oxidation kinetics during loading. At the end of Stage 1 and 2 loading, the filter was weighed to determine the PM mass retained. After stage 2, the engine was run for 15 minutes at the loading condition till the system is stabilized in the ramp up stage followed by a change in engine condition to the passive oxidation (PO) phase of the experiment. During the passive oxidation condition, the PM oxidation kinetics and cake permeability parameters are calibrated. The PO stage is followed by stage 3 and stage 4 loading which were used to study the post oxidation characteristics of the SCRF [®]. Table 4.2 shows the engine conditions used for the passive oxidation experiments without urea injection.

The stage 1, 2 and ramp up as well as stages 3 and 4 for Configuration 1 with urea remain the same as the experiments without urea injection. During passive oxidation, urea is injected with a target ANR = 1. The addition of urea injection leads to a reduction of NO_x due to the SCR reactions which in turn leads to reduction in the amount of NO₂ available for passive oxidation of PM due to forward diffusion between the PM cake and the substrate wall. The resultant reduction in PM oxidation rate and diffusivity of NO_x is calibrated using these datasets. Table 4.3 shows the conditions used for the passive oxidation experiments with urea injection. The detailed description of these experiments is given in reference [4]

Table 4.2
Passive oxidation SCRF [®] inlet conditions for PO experiments without urea in configuration 1 [4]

Test Name	Temperature [C]	NO ₂ [ppm]	NO [ppm]	NO _x [ppm]
A	276	263	252	515
B	273	674	1053	1727
B Rpt.	281	792	823	1615
C	347	228	321	549
D	377	117	303	421
D Rpt.	374	147	236	383
E	347	523	803	1326

Table 4.3
Passive oxidation conditions for PO experiments with urea in configuration 1 [4]

Test Name	Temperature [°C]	NO ₂ [ppm]	NO [ppm]	NO _x [ppm]	ANR [-]	Space Velocity [k/hr]
A	274	304	286	590	1.03	15.5
B	284	821	789	1610	1.01	10.6
B Rpt.	284	758	822	1580	1.10	10.6
C	349	301	387	689	0.89	19.7
D	373	171	279	450	1.01	36.0
D Rpt.	371	191	306	497	0.99	36.0
E	360	653	798	1451	1.01	20.1

4.2 SCR[®] Configuration 1 AR Data

The four active regeneration experiments were used to find the thermal characteristics of the SCR[®] as well as PM kinetics of thermal PM oxidation and HC oxidation reactions. Figure 4.3 shows the pressure drop and the stages in the active regeneration experiment.

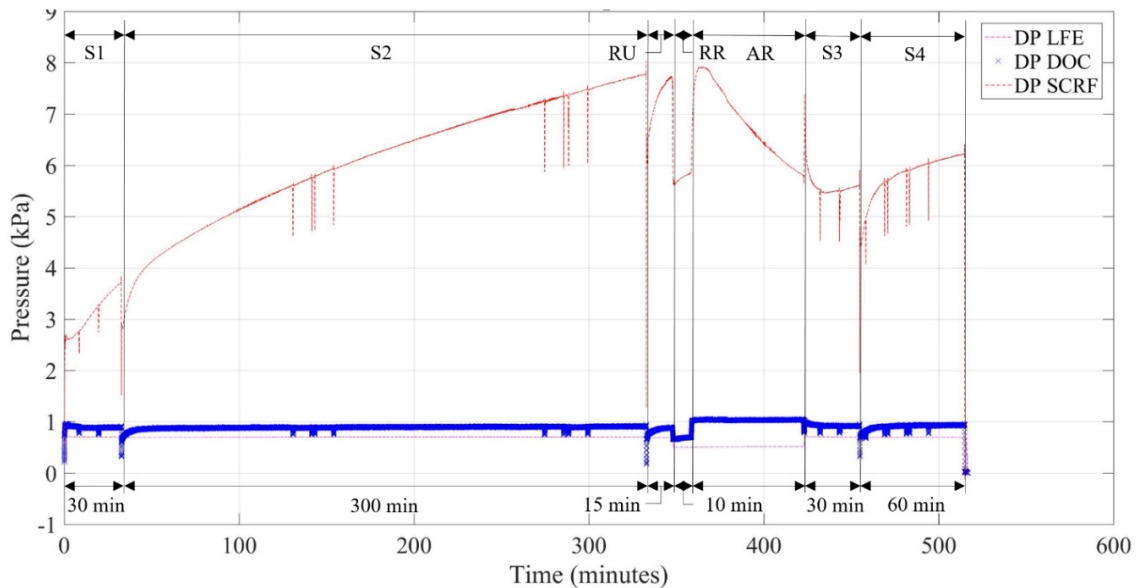


Figure 4.3: Active regeneration experiment without urea [4]

Stages 1, 2, ramp up, 3 and 4 used for loading the filter remain the same as the

passive oxidation experiment. At end of ramp up, the engine operating conditions are changed to active regeneration condition as shown in Table 4.4 and run for 2 minutes to stabilize the system followed by injection of diesel fuel to reach the desired exhaust gas temperature. The active regeneration stage is used to find the thermal PM oxidation and HC oxidation kinetics as well as to calibrate the temperature distribution inside the filter which is a function of heat loss to the ambient as well as energy release by the chemical reactions.

Table 4.4
Active regeneration conditions for AR experiments in configuration 1
without urea injection [4]

Test Condition	SCRF® Space Velocity	SCRF® Inlet Temperature	NO ₂ into SCRf®
[-]	[k/hr]	[C]	[ppm]
AR-1	38.6	504	5
AR-2	38.7	547	10
AR-3	38.8	590	20
AR-2 Repeat	38.7	496	10

4.3 SCRf® Configuration 2 Data With and Without PM Loading

The configuration 2 consists of 4 test points with 0, 2 and 4 g/l PM loading. The 4 experiments with 0 g/l PM loading were used to calibrate the SCR kinetics and NH₃ storage characteristics of the SCRf®. The 8 experiments with 2 and 4 g/l PM loading are used to simulate the inhibition effect of PM in the substrate wall on the SCR reaction rate. Figures 4.4 and 4.5 show the configuration 2 without and with PM loading. In the experimental setup without PM loading, the CPF upstream of the SCRf® is used to remove the PM from exhaust gas stream which is then passed through the clean SCRf® in order to evaluate the NO_x conversion performance and SCR kinetics of the clean SCRf®. In the experiments with PM loading the CPF is replaced with a spacer. The exhaust gas consisting of PM flows into the SCRf® where it gets deposited and oxidized along with NO_x reduction during urea injection.

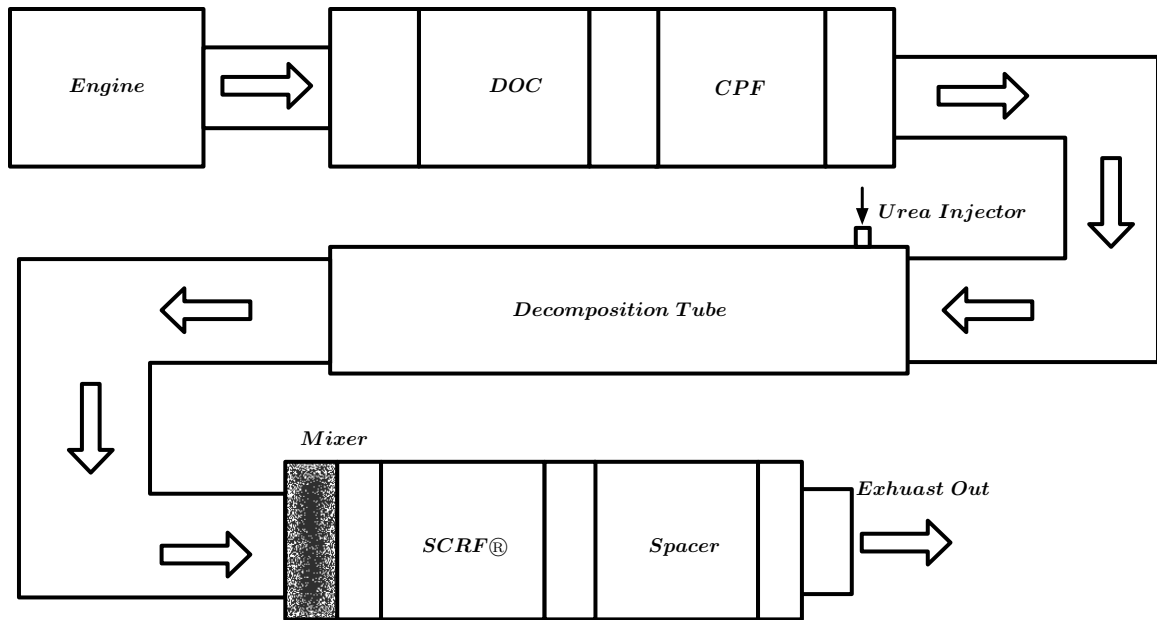


Figure 4.4: Configuration 2 without PM loading

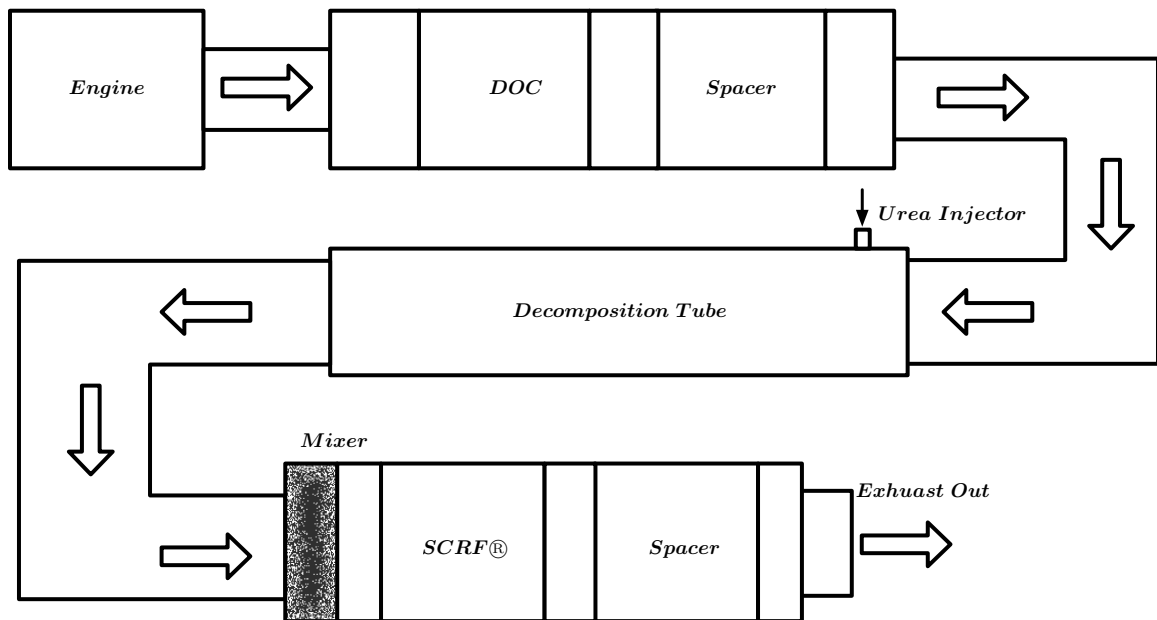


Figure 4.5: Configuration 2 with PM loading

Figure 4.6 shows pressure drop and the experimental stages used in the configuration 2 experiments with and without PM loading. A urea dosing cycle is used as shown in the Figure 4.6 with ANR values of 0.8, 1 and 1.2 followed by 0 and repeat of 1.2 for all the experiments. In the case with PM loading, the NO_x reduction stage is preceded by a PM loading stage as shown in Figure 4.6 where the SCRf ® is loaded

with PM from time $t = 0$ to 5.5 hrs. Table 4.5 shows the engine conditions used for the twelve experiments in the configuration 2. Four test points were used with PM loading values of 0, 2 and 4 g/l in the SCR_F®. A detailed description of these experiments is given in reference [5].

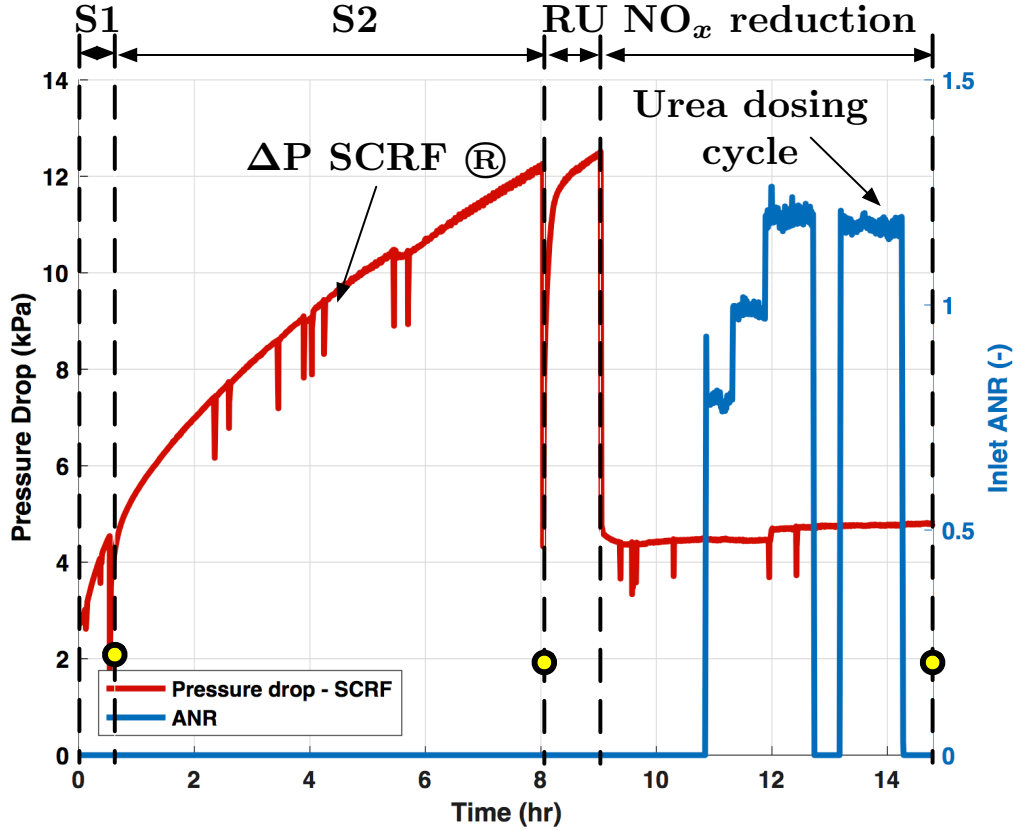


Figure 4.6: Configuration 2 experiment Test 1 with 2 g/l PM loading[5]

Table 4.5

Configuration 2 with and without PM engine and exhaust conditions [5]

Parameter	PM Loading (g/l)	Test Name			
		1	3	6	8
Speed [RPM]	0	1199	2200	1202	2401
	2	1200	2201	1200	2398
	4	1200	2203	1200	2401
Load [Nm]	0	201	330	580	826
	2	208	329	588	820
	4	203	331	587	818
Exhaust Flow [kg/min]	0	5.0	10.7	6.9	17.0
	2	5.0	9.9	6.8	17.6
	4	5.0	10.9	6.8	17.7
Upstream NO ₂ /NO _x	0	0.38	0.43	0.46	0.25
	2	0.34	0.45	0.47	0.23
	4	0.26	0.42	0.43	0.22
Engine Out PM [mg/scm]	0	N/A	N/A	N/A	N/A
	2	2.14	4.30	3.59	7.39
	4	1.97	4.93	2.85	4.97
SCRF® Inlet Temperature [°C]	0	218	304	345	443
	2	206	305	340	438
	4	207	302	343	446
SCRF® Std. Space Vel. [k/hr]	0	13.7	29.1	18.8	46.3
	2	13.7	27.0	18.6	48.0
	4	13.5	29.8	18.6	48.2
SCRF® Inlet NO [ppm]	0	345	158	795	411
	2	403	161	844	424
	4	452	198	793	415
SCRF® Inlet NO ₂ [ppm]	0	213	121	674	140
	2	203	131	744	125
	4	141	143	588	115

4.4 SCR F® Configuration 3 Data

Configuration 3 was used to determine the impact of a downstream SCR on NO_x conversion performance of a SCR F®+SCR system. The schematic of the setup used for collecting these data is shown in Figure 4.7 consisting of the DOC+SCR F®+SCR.

Figure 4.8 shows the pressure drop and stages of configuration 3 experiments. The

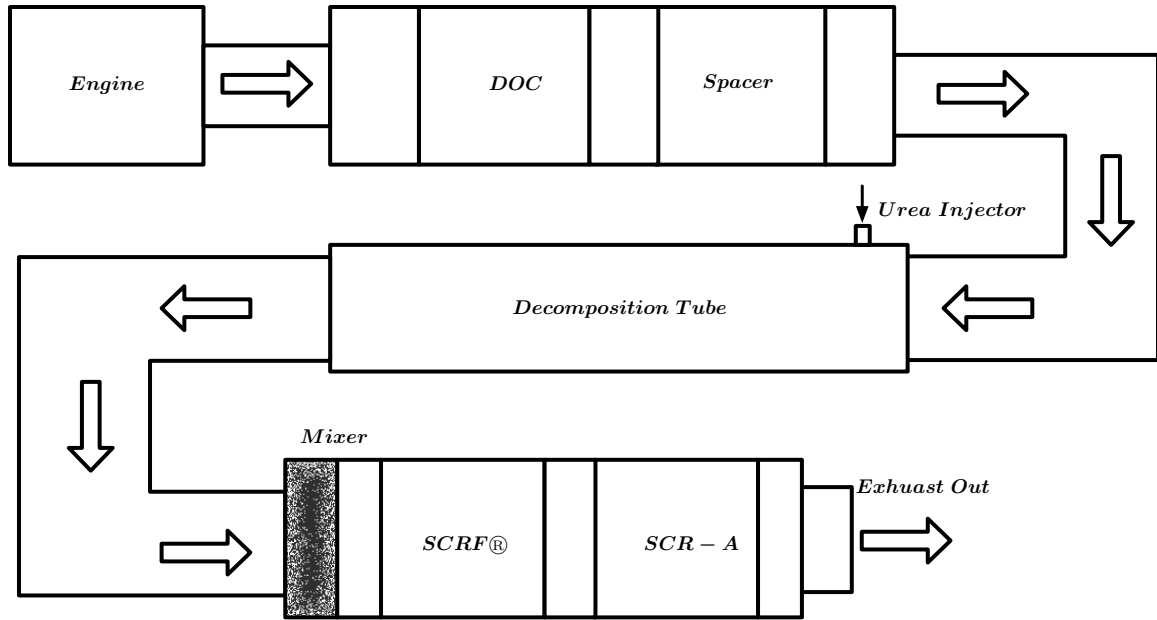


Figure 4.7: Configuration 3 test setup

test procedure consisted of SCRF® clean out, PM loading at engine condition 2400 rpm, 200 Nm designated as stage 1 and 2. This was followed by ramp up stage at the same engine condition as stage in order to bring the temperature of the substrate to the same value as stage 2 after weighing the filter. This was followed by passive oxidation condition that was carried out at one of the six test point engine conditions used for the dataset as shown in Table 4.6. Passive oxidation is followed by stage 3 and 4 with the same engine condition as stage 2. During the passive oxidation condition, the urea was dosed into the exhaust with a target ANR range of 1.02 -1.13 which was determined for each engine condition based on SCRF® inlet NO_x . The detailed procedure of the experiments is described in references [51]. The NO , NO_2 and NH_3 concentrations were measured at UDOC, DDOC, USCRF, DSCR, USCR and DSCR. Table 4.6 shows all the engine conditions used in the configuration 3 experiments.

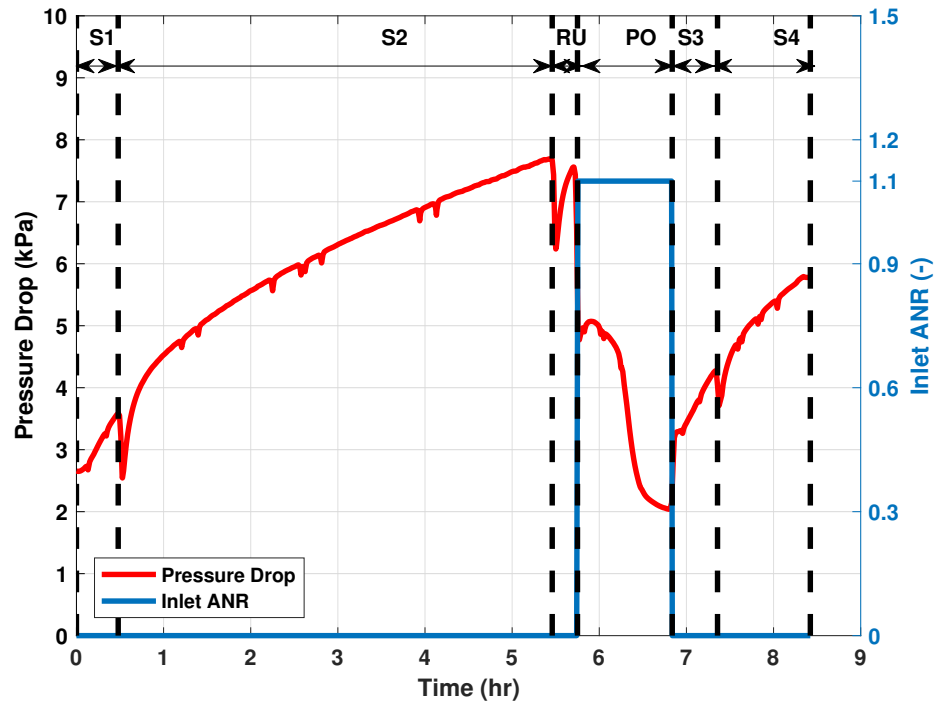


Figure 4.8: Pressure drop for Configuration 3 test cycle PO-C

Table 4.6

Configuration 3 engine and exhaust conditions [5]

Test	Exhaust Flow	Inlet Temperature	Inlet NO _x	Inlet NO ₂
[-]	[kg/min]	[C]	[ppm]	[ppm]
A	5.6	267	590	215
C	6.9	339	689	290
E	7.1	342	1450	584
B	3.7	256	1580	758
D	12.5	366	450	161
1	5.2	203	625	182

4.5 Experimental Data Uncertainties

4.5.1 Exhaust Mass Flow Rate

The exhaust mass flow rate is calculated as sum of the air and fuel flow rates which is then used as input for the SCR-F model. The air flow rate was measured using pressure drop in an Meriam Instruments Laminar Flow Element (LFE). The standard air flow rate measured with pressure transducer was converted to mass flow rate using density of air at standard conditions (20 °C and 1 atm pressure). The fuel flow rate was measured with a Micro Motion Coriolis Meter. The air flow rate based on specifications of the instruments in Table 4.7 had an accuracy of +/- 0.15 %.

Table 4.7
Coriolis meter specifications [5]

Manufacturer	Micro Motion		
Model	CMFS015M319N2BAECZZ		
Measurements	Flowrate	Density	Temperature
Units	[%]	[kg/m ³]	[°C]
Accuracy	+/- 0.10	+/- 0.5	+/- 1.0
Repeatability	+/- 0.05	+/- 0.2	+/- 0.2

4.5.2 Temperature

The exhaust gas temperature inside the SCR-F was measured in axial and radial direction using Omega K-type thermocouples. These thermocouples were placed in the inlet and outlet channels to obtain the required measurements. The specifications of the thermocouples is given in Table 4.8.

The sensor data was used as SCR-F model input to compare experimental and model data. Based on thermocouple specification the experimental thermocouple data was found to have an accuracy of +/- 5°C.

Table 4.8
Active regeneration Specifications of the thermocouples used in the
aftertreatment system [5]

Manufacturer	Type	Diameter	Length	Accuracy	Location
[-]	[-]	[in.]	[in.]	[%]	[-]
Omega	K	0.020	12	2.2 C	CPF
Omega	K	0.020	16	2.2 C	CPF
Omega	K	0.020	12	2.2 C	SCR [®] F
Omega	K	0.020	16	2.2 C	SCR [®] F
Omega	K	0.125	6	2.2 C	Exhaust, Air Intake, Coolant

4.5.3 Pressure Drop

The pressure drop across the SCR[®]F was measured continuously using differential pressure transducers. Absolute pressure transducer was used to measure barometric pressure in the test cell. Specification of these sensors is given in Table 4.9. Based on these specification the experimental data used to compare against experimental data was found to be accurate to within +/- 0.1%. FS indicates full scale reading.

Table 4.9
Active regeneration conditions for AR experiments in Specifications of
pressure transducers [5]

Parameters	Barometric Pressure	LFE	SCR [®] F
Sensor Make	Omega Engineering	Omega Engineering	Omega Engineering
Model Number	PX419-26B5V	PX429-10DWU-10V	PX429-5DWU-10V
Type	Absolute	Differential	Differential
Range	26.00-32.00	0-10	0-5
Units	in. Hg	in. H ₂ O	PSID
Accuracy, Linearity, Hysteresis	0.08% FS	0.08% FS	0.08% FS
Output Voltage	0-5 Vdc	0-10 Vdc	0-10 Vdc

4.5.4 Gaseous Emissions

An airsense ion molecule reaction mass spectrometer (IMR-MS) was used to measure NO, NO₂ and NH₃ concentration at SCR-F inlet and outlet. Specification of the MS are given in Table 4.10

Table 4.10
Specifications of IMR-MS and calibration gases [5]

Components	Detection level at 100ms	Monitoring Mass	Ionization Gas	Span Gas	Span gas conc.	Accuracy
[-]	[ppb]	[amu]	[-]	[-]	[ppm]	[%]
NO	100	30	Mercury	NO, N ₂	797	+/-1
NO ₂	50	46	Mercury	NO ₂ , Air	495	+/-2
NH ₃	120	17	Mercury	NH ₃ , N ₂	103.8	+/-2

The exhaust gas was sampled through stainless steel lines heated to 190 °C for emissions measurement into MS. The lines were heated to avoid condensation of water vapor and adsorption of NH₃ onto the sample lines.

Two UniNO_x sensors were used upstream of and downstream of SCR-F for NO_x measurements. These sensors were made by Continental. A prototype NH₃ sensor by Delphi was installed downstream of SCR-F/SCR to measure NH₃ slip. Specification of these sensor is given in Table 4.11. Based on specifications of MS and sensors the NO, NO₂ and NH₃ measurements were found to be accurate to within +/- 20 ppm.

Table 4.11
Specification NO_x and NH₃ sensor on production aftertreatment system [5]

Component	Range	Resolution	Accuracy	Voltage Range	Operating Temperature
[-]	[-]	[ms]	[%]	[V]	[°C]
NO _x Sensor	0-1500 ppm	0.1 ppm	+/- 10	12-32	100-800
NH ₃ Sensor	0-1500 ppm	0.1 ppm	+/- 10	13.5-32	200-500
λ Sensor, O ₂ (linear)	12-21%	0.10%	+/-0.3 - +/-1.4	24	100-800

4.5.5 Particulate Matter concentration and mass retained

The PM concentration was measured using hot sampling technique on glass fibre filter. Exhaust gas was passed on the glass fibre filter using manual sampling train. The pre and post sampling weights of the filter were used for measuring the PM concentration with an error of $\pm 0.5\%$ which resulted in model output uncertainty of $\pm 1\%$.

The PM mass retained was measured using a weight balance. The experiment was run in stages at the end of each stage the filter was removed from the system and weighed. The difference in weights corresponds to PM mass retained change during both PM loading and PM oxidation stages. The accuracy of the scale used is $\pm 1\text{g}$ however for the model additional uncertainty in terms of PM oxidation which is a function of NO_2 inlet concentration is present leading to effective model uncertainty of $\pm 2\text{gm}$. Table 4.12 gives the specifications of the weight scale used for measurement.

Table 4.12

Specifications of the weighing balance used to weigh the SCRF® [5]

Manufacturer	Ohaus
Model	Ranger
Capacity	35,000 g
Cartified Readability	$\pm 1.0\text{ g}$
Readability	$\pm 0.1\text{ g}$
Linearity	$\pm 0.3\text{ g}$

4.6 Procedure for the Model Calibration

The SCR-F model requires a set of time-varying inputs, the specifications of the SCRF® and a set of calibration parameters to simulate the engine conditions of the experiments.

The inputs used for the model include:

1. Mass flow rate of fuel and air

2. Inlet exhaust gas temperature
3. Concentration of chemical species at the inlet of the SCR-F
4. Relative humidity, temperature and barometric pressure in the test cell.

The calibration parameters used by the model are broadly classified as

- Thermal Parameters
- PM kinetics
- Gaseous species kinetics
- SCR reaction kinetics
- Pressure drop and filtration parameters
- Cake permeability parameters

4.6.1 SCR[®] Configuration 1 PO Tests Without Urea

The SCR[®] configuration 1 data without urea consisted of seven experiments with a temperature range of 273–377°C. These data were used to determine the thermal parameters, NO₂ assisted PM oxidation, cake permeability, and pressure drop parameters. A combination of manual and numerical optimization in MATLAB/Simulink using *fmincon* function was used to determine these parameters. Figure 4.9 shows the steps used for the calibration process. To use the numerical optimization scheme, cost functions of the form shown in Equation 4.1 were developed for each of the steps in the calibration process.

$$Cost = \sum_{t=Starttime}^{Endtime} (X_{model} - X_{exp})^2 \quad (4.1)$$

where cost is supplied to the *fmincon* function. Start time and end time are the time points between which the experimental and model data for a given quantity that is

being tracked for deviation. X_{exp} , X_{model} are the experimental and model quantities being compared. X can have different values such as PM mass retained, concentration of chemical species, temperature, the pressure drop across SCR-F (®) depending on the parameter being found.

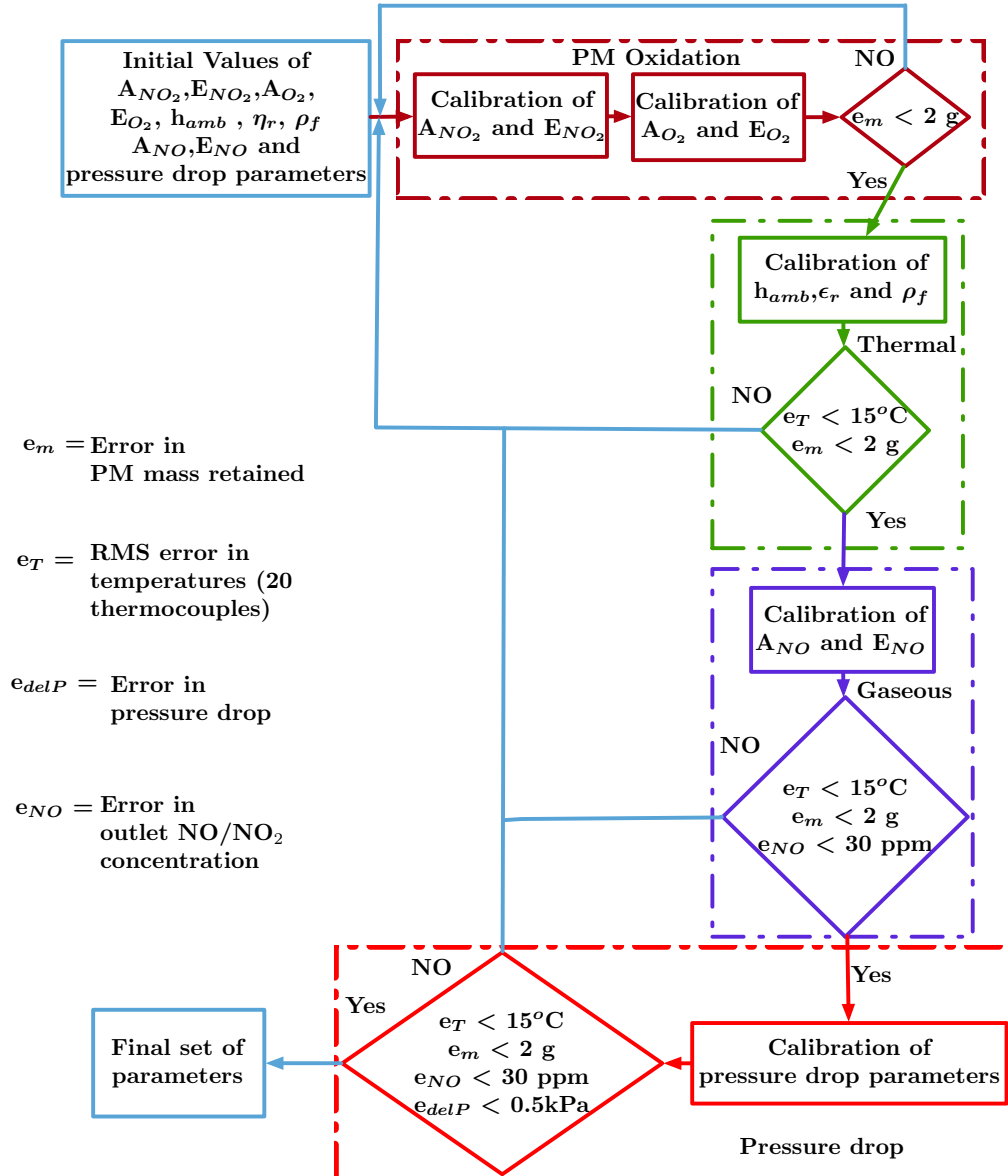


Figure 4.9: Schematic of SCR-F calibration with configuration 1 data without urea injection

The calibration procedure shown in Figure 4.9 consists of 4 major steps shown in different colored boxes. Each step is repeated such that the errors for the variables from each of the preceding steps are satisfied. If any one of the error criterion is not

met the preceding steps are repeated. This iterative procedure is followed till a final set of parameters that work for all the configuration 1 experiments are found. The order of the calibration procedure consists of 1) PM oxidation kinetics, 2) thermal parameter, 3) gaseous species kinetics and 4) pressure drop parameters. These steps are explained in detail in the following sections.

4.6.1.1 PM Oxidation Kinetics

The PM oxidation kinetics consist of pre-exponential and activation energies for NO₂ oxidation of PM and the thermal oxidation in both PM cake and the substrate wall. It was found that the SCR-F (®) had different NO₂ assisted PM oxidation rates during loading and the oxidation stages for all the seven experiments. So, different pre-exponential values were used for NO₂ assisted PM oxidation in the PM cake and substrate wall for the loading and oxidation stages. The deviation in the experimental and model PM mass retained values was used to determine the NO₂ assisted PM oxidation rate for each of the seven experiments. This deviation was reduced by finding pre-exponential values for each experiment followed by an Arrhenius plot to find common values of the pre-exponential and activation energy for the NO₂ assisted PM oxidation reaction for all the seven experiments. The PM mass retained data at the end of stage 1 and stage 2 of all the experiments were used to determine the kinetics for the loading stage. The difference between the PM mass retained at the end of stages 2 and 3 for all the seven experiments were used to determine the kinetics during the oxidation stage. The thermal oxidation pre exponential and the activation energy were found using the AR experimental data.

4.6.1.2 Temperature Distribution and Thermal Response

The temperature distribution in the SCR-F model is a function of heat loss to the ambient, physical properties of the filter for the thermal inertia and energy release by the chemical reactions taking place in the SCR-F (®). The heat loss to the ambient is affected by the convection heat transfer coefficient and radiation heat transfer coefficient parameters. The values of these two parameters were found using the experimental and model temperature values of all the 20 thermocouple locations in the SCR-F (®) for all seven experiments. By reducing the deviation in the temperature

distribution during passive oxidation, the energy loss to ambient and thus the value of these two parameters were found.

4.6.1.3 Filtration Efficiency and Pressure Drop

The filtration efficiency of the model is calibrated using the experimental data for each experiment using the outlet and inlet PM concentrations. The experimental pressure drop during loading stages and the experimental filtration efficiency values along with the pressure drop parameters for all the 7 experiments were used to calibrate the pressure drop and filtration efficiency during loading stages. The filtration and pressure drop parameters along with the calibration of the filtration model are described in reference [50]

The pressure drop during the PM oxidation stage is governed by the change in cake permeability of the PM cake and the PM mass retained. The cake permeability is a function of PM oxidation rate. All the required cake permeability parameters are found using pressure drop and PM oxidation rate data from the seven configuration 1 experiments without urea injection using numerical optimization with a tolerance of 0.2 kPa of experimental pressure drop values. Table 4.13 shows the list of parameters obtained.

The steps used to find these parameters are as follows:

1. The clean wall pressure drop is used to determine the initial wall permeability ($K_{o,wall}$)
2. Based on the slope of pressure drop curved during loading the value of transition permeability ($K_{o,trans}$) is determined such that it simulates the transition from deep bed filtration to cake using first 30 minutes of experimental data.
3. Based on the slope of pressure drop curve during loading stage after first 30 minutes the values of cake permeability correction factor C_5 , cake layer porosity ($(1-\alpha_{o,cake})$) and maximum cake efficiency parameter ($A_{eff,cake}$) are determined.
4. Wall packing density parameters $C_{1,wpm}$ and $C_{2,wpm}$ are determined using mass of PM in the wall.

5. In order to simulate the cake and wall pressure drop the permeability parameters C_4 and C_5 are found such that they reduce the pressure drop error during the change in pressure and temperature of the exhaust gas by simulating the change in the mean free length of the exhaust gas in the PM cake and wall. The pressure drop data during the loading stage is used for this step.
6. The wall PM oxidation pre exponential ($A_{wall,NO_2,loading}$) during is found such that wall pressure drop reaches a steady state value after transition to the cake filtration regime in order to simulate the slope of the pressure drop.
7. The wall PM oxidation pre exponential ($A_{wall,NO_2,oxidation}$) during passive oxidation stage is found at the end of the oxidation stage where due to cake permeability change the cake pressure drop is near zero so this parameter determines both the wall and total pressure drop.
8. The cake permeability parameters (C_8 and C_9) are found based on cake pressure drop data during PM oxidation.
9. Post loading pressure drop data is used to determine cake permeability parameters (C_{10} and C_{11})

Steps 8 and 9 are explained in detail in the next subsection.

Table 4.13
Pressure drop parameters during PM loading for the SCR-F model

Parameter	Description
$K_{o,wall}$	Initial permeability of substrate wall
$k_{o,trans}$	Transition permeability of substrate wall
$C_{1,wpm}$	First constant of wall packing density
$C_{2,wpm}$	Second constant of wall packing density
C_3	Ref. Pressure for wall permeability
C_4	Wall permeability correction factor
$A_{wall,NO_2,loading}$	Pre exponential of NO_2 based wall oxidation during loading
$\alpha_{o,cake}$	Initial solidosity of PM cake layer
$k_{o,cake}$	Initial / reference permeability of PM cake layer
C_5	Cake permeability correction factor
C_6	Ref. Pressure for lambda correction
C_7	Ref. Temperature for lambda correction

Table 4.14
Pressure drop parameters during PM loading SCR-F model

Parameter	Description
C_8	Slope of delta mass offset
C_9	Intercept of delta mass offset equation
α_k	Multiplicative constant for cake permeability correction
β_k	Power constant for cake permeability correction
C_{13}	Multiplicative constant for percentage PM oxidized
$A_{wall,NO_2,loading}$	Pre exponential of NO_2 based wall oxidation during loading

4.6.1.4 Cake Permeability

The permeability of PM cake is an important variable that determines the pressure drop across the SCR-F® during PM oxidation and in post oxidation stages of experiments in configuration 1 ,2 and 3. During oxidation of PM cake, the PM cake gets damaged due to oxidation of the PM cake. This damage leads to formation of pores and cracks in the PM cake layer. When these cracks join leading to a reduction in resistance of the PM cake to exhaust gas flow, the permeability of the cake increases significantly leading to a significant decrease in the cake pressure drop component since the exhaust gas follows the path of least resistance formed by the cracks.

The aim of the cake permeability model is to track the change in PM cake permeability during PM oxidation and during post oxidation stages where the cracks start getting filled up rapidly by new PM being loaded into the filter. The rate of damage is a function of PM oxidation rate, forward diffusion of chemical species and percent of PM cake. Equations 4.2 and 4.3 are used to compute the damage and equivalent cake permeability change using these factors. Table 4.14 shows the list of parameters from these equations that are determined for configuration 1 experiments without urea injection as part of the calibration process.

$$d = \frac{m_{cake,initial} - m_{cake,corrected}}{m_{cake,initial}} + C_{12} \left(\frac{m_{cake,initial} - m_{cake,retained}}{m_{cake,initial}} \right) \quad (4.2)$$

$$d_{i,j} = C_{13} \left(\frac{m_{cake,initial_{i,j}} - m_{retained_{i,j}}}{m_{cake,initial_{i,j}}} \right) - \frac{m_{offset_{i,j}}}{m_{cake,initial_{i,j}}} \quad (4.3)$$

The cost function from Equation 4.4 is used with PM oxidation pressure drop experimental and model data to determine the parameters in Table 4.14.

$$Cost = \sum_{T=PassiveOxidationStageStart}^{T=PassiveOxidationStageEnd} (delP_{model} - delP_{exp})^2 \quad (4.4)$$

Where *Cost* is the value of cost function that is a measure of deviation between experimental and model pressure drop during the passive oxidation stage of the experiment. *T* is the time, $delP_{model}$, $delP_{exp}$ are the model and experimental pressure drop values in kPa. This cost is computed for passive oxidation stages of all PO experiment and supplied to numerical optimizer to find the common set of cake permeability parameters.

The parameters in Table 4.15 are used to simulate cake permeability in post oxidation stages which are found using cost function Equation 4.5.

Table 4.15
Pressure drop parameters during PM loading SCR-F model

Parameter	Description
C ₁₀	Slope of post loading cake permeability
C ₁₁	Constant for post loading cake permeability

$$Cost = \sum_{T=Stage\ 3\ start}^{T=Stage\ 4\ End} (delP_{model} - delP_{exp})^2 \quad (4.5)$$

4.6.2 SCR[®] Configuration 1 PO Tests With Urea Injection

The SCR[®] configuration 1 PO data with urea was used to calibrate the diffusivity of the PM cake during PM oxidation in the SCR[®]. The data consisted of seven PO experiments covering a temperature range of (274–367°C) with urea injection during the passive oxidation stage.

The forward diffusion of NO/NO₂ during urea injection leads to a decrease in available

NO₂ in the PM oxidation leading to a decrease in the PM oxidation reaction rate. The diffusivity in the PM cake is a function of tortuosity (τ_{cake}) of the PM cake which is an unknown physical parameter for the PM cake and has a range of 0 to 10. A tortuosity value of 8 was found from the calibration process that was able to simulate the diffusion rate for all the thirty experiments. The value of this parameter is found using the change in PM mass retained at the end of stage 3 and 4 for the seven test points from the configuration 1 data with urea injection. Figure 4.10 shows the calibration process used in this step. In Figure 4.10 the value of the tortuosity is

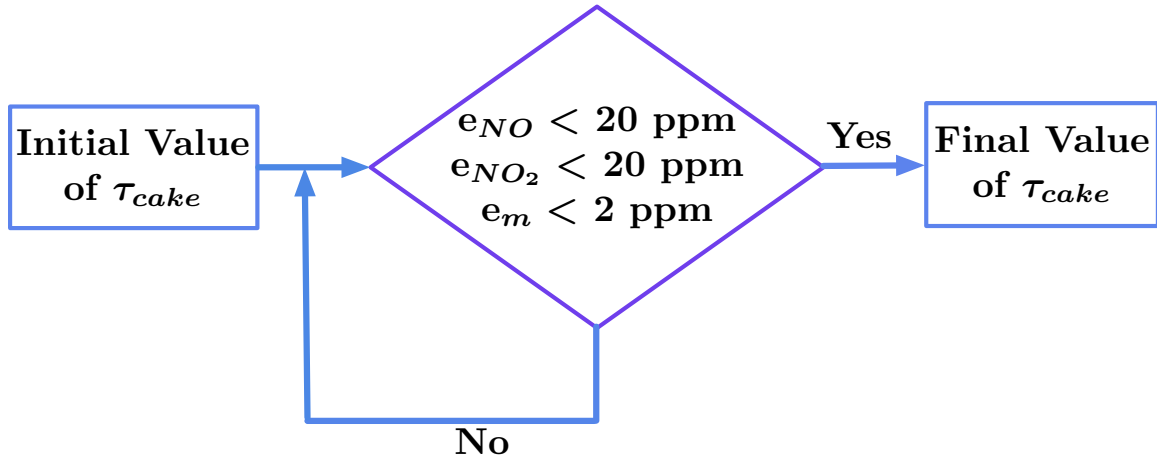


Figure 4.10: Schematic of SCR-F calibration with configuration 1 data with urea injection

changed such that the outlet NO and NO₂ concentration for the seven configuration 1 PO experiments with urea injection during PO stage are within 20 ppm and PM mass retained for all the 4 stages is within 2 gm of the experimental value. The process is repeated iteratively to obtain the final value of the turtuosity.

4.6.3 SCR-F[®] Configuration 1 AR Tests

The SCR-F configuration 1 AR data were used to calibrate the thermal PM oxidation kinetics, gaseous species kinetics for hydrocarbon oxidation in the SCR-F[®]. The data consisted of four AR experiments covering a temperature range of 500 – 600°C.

4.6.3.1 Active Regeneration PM Oxidation Kinetics

The active regeneration kinetics assume that passive oxidation kinetics found from passive oxidation experiments remain constant for the higher temperature experiments where the inlet NO₂ concentrations are low. The remaining oxidation occurs due to the thermal PM oxidation reaction. The pre exponential of this reaction was found for the individual experiments using the cost function shown in Equation 4.6 keeping the activation energy constant.

$$Cost = \sum_{k=3}^4 (PM_{retained,model,k} - PM_{retained,exp,k})^2 \quad (4.6)$$

The resultant pre exponential values are used in an Arrhenius plot to obtain common kinetics for the thermal PM oxidation reaction for all the four experiments.

4.6.3.2 HC Oxidation Kinetics

The HC oxidation reaction is responsible for the majority of the energy release (88%) in the SCRF (®) during active regeneration leading to a temperature rise of 10-15°C for the 4 AR experiments. Since the outlet hydrocarbon concentration values were not available, it was assumed that 92 % of inlet HC is oxidized across the SCRF (®) based on earlier work performed on the 2007 ISL data using the 2D SCR-F model [37]. The cost function shown in equation 4.7 is used to find the pre exponential of HC oxidation for all the 4 experiments.

$$Cost = \sum (C_{HC,model,k} - 0.08 * C_{HC,in})^2 \quad (4.7)$$

The pre exponentials are then used in an Arrhenius plot to obtain common kinetics for the HC oxidation reaction. The resultant reaction rates obtained for HC oxidation in all the four experiments were able to simulate the temperature distribution during the active regeneration to within 5°C.

4.6.4 SCR[®] Configuration 2 Tests With and Without PM

The configuration 2 data consisted of four test points with twelve experiments at 0, 2 and 4g/l PM loading. The experiments with 0 g/l loading were used in this step to determine the SCR kinetics and NH₃ storage parameters. The experiments with PM loading were used to validate the model. The calibration parameters of the 2D SCR-F model are found using the experimental data collected on 2013 Cummins ISB data. The primary aim of the calibration process is to determine one set of kinetics that can simulate the SCR[®] performance for all the engine conditions. The experimental data consisted of four experiments that were conducted over a wide range of space velocity, exhaust gas temperature and NO₂/NO_x ratio conditions to simulate the engine operating conditions. The kinetics and storage parameters from the Cummins ISB 2010 engine SCR from reference [2] were used as initial values for the calibration. The cost function used for the calibration is given by Equations 4.8 and 4.9.

$$Cost_i = \int_{t_0}^{t_{end}} e_i(t)^T e_i(t) dt \quad (4.8)$$

$$e_i(t) = (C_{i,model} - C_{i,exp}) \quad (4.9)$$

$Cost_i$ is the cost function with $i = \text{NO}, \text{NO}_2$ and NH_3 . t_0 and t_{end} are the start and end times for the simulation in seconds. e_i is the error between experimental and model concentrations. $C_{i,model}$ and $C_{i,exp}$ are the SCR[®] outlet concentrations of the chemical species i from the model and the experimental data.

The cost function consisting of integral of squared error is supplied to the numerical optimizer based on `fmincon` function in MATLAB/Simulink which changes the calibration parameters to minimize the value of the cost function by reducing deviation in the model and experimental outlet concentrations of NO, NO₂ and NH₃.

The SCR-F model consists of three SCR reactions, two adsorption, two desorption reactions, NH₃ oxidation and N₂O formation reaction. These nine reactions each consists of activation energy and pre-exponential parameters from the Arrhenius form used to model the NO_x reduction across the SCR[®]. These eighteen parameters are found by comparing experimental NO, NO₂ and NH₃ concentrations at the SCR[®] outlet to the 2D SCR-F model outlet concentration values.

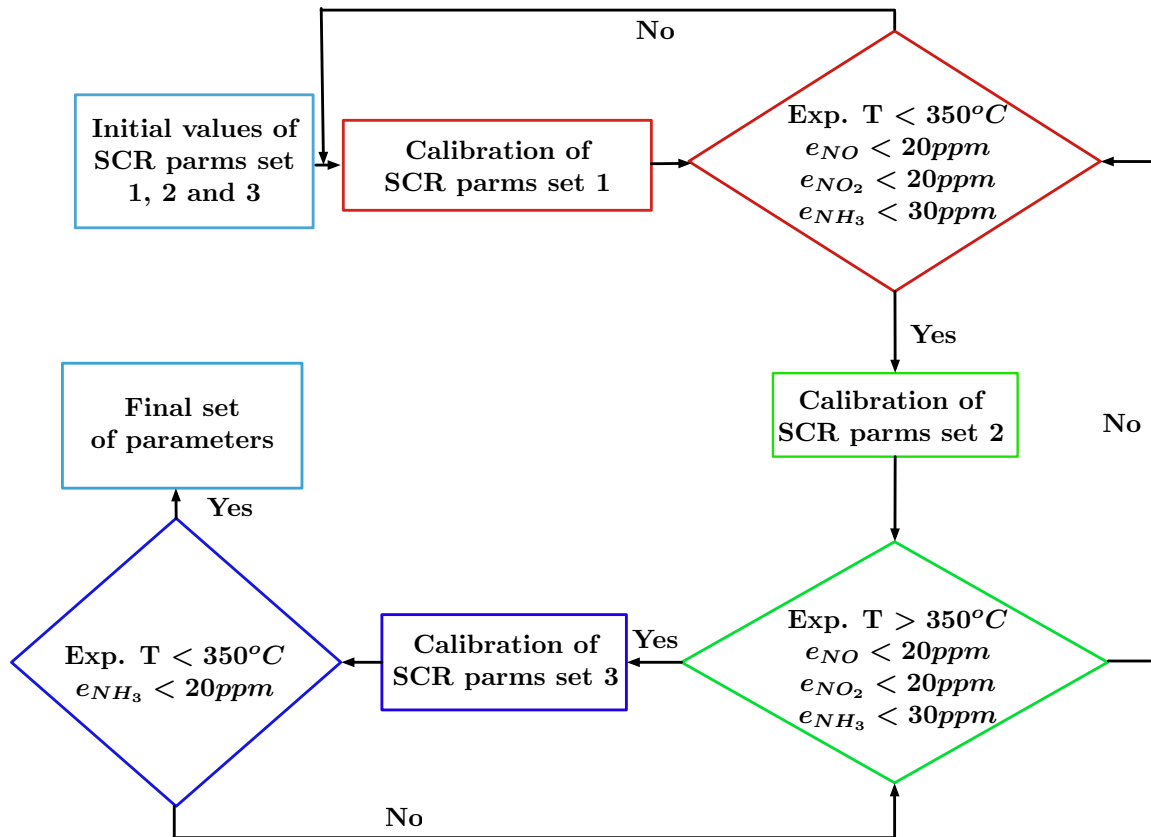


Figure 4.11: Schematic of SCR-F calibration with configuration 2 data SCR reaction kinetics

The activation energies of all the reactions are kept constant and pre-exponentials of the reactions are updated for individual experiments using the numerical optimization scheme. Based on the pre-exponentials obtained, the rate constant for each reaction are calculated. These rate constants are then used in Arrhenius plots to obtain a common set of kinetics for all the reactions. The updated activation energies are used in the next step with the numerical optimizer to further improve the calibration. This iterative procedure is continued until the set of kinetics is obtained which is able to simulate the outlet NO, NO₂ and NH₃ concentrations to within +/- 20 ppm of the experimental data for all the experiments.

The steps used in calibration of the SCR model are shown in Figure 4.11. Based on outlet NO and NO₂ SCR-F® outlet concentration data from experiments with inlet temperature less than 350°C, the set 1 (red) parameters are obtained. Set 1 consists of the kinetics of the three SCR reactions, adsorption and desorption reactions of the first site. Once these kinetics are found using the numerical optimization and Arrhenius

plots set 2 (green) is found in the next step. Set 2 consists of NH_3 oxidation reaction and three SCR reactions. These kinetics are found using NO , NO_2 and NH_3 outlet concentrations from experiments with inlet temperature greater than 350°C where significant NH_3 oxidation reaction is observed.

In the final step, set 3 (blue) kinetics consisting of the adsorption and desorption reactions of the second storage site and maximum storage of the two storage sites are found. NH_3 slip from experiments with inlet temperature less than 350°C is used for this step. The adsorption and desorption kinetics are found based on the steady state NH_3 slip value at ANR values 0.8 to 1.2. The transient change in NH_3 slip pattern during transition from ANR 1.0 to 1.2 used to find the final value of the maximum storage of the two storage sites.

The steps shown in Figure 4.11 are performed iteratively. Whenever a condition for a step is satisfied then the next step is followed. If the next step fails to converge then all the previous are repeated since the parameters are coupled. This iterative process is continued till a common set of kinetics that satisfy all the conditions is obtained.

The parameters obtained using the steps described in this chapter are described in detail in Appendix G. The resultant common set of parameters are used with the 2D SCR-F model to obtain the results described in Chapter 5.

Chapter 5

Results and Discussion ¹

This chapter presents the results obtained from the 2D SCR-F model using the common set of parameters obtained from the calibration process described in Chapter 4. The description of the parameters used for the model to obtain these results is given in Appendix G. The output data from the thirty-seven experiments consisting of passive oxidation, active regeneration and NO_x reduction experiments with and without urea loading is presented. A detailed analysis of the underlying internal variables primarily consisting of spatial distribution of temperature, PM mass retained and NH₃ coverage fraction of the two NH₃ storage sites is also presented. This chapter is divided into three sections: 1) Configuration 1 experiments with and without PM loading primarily focused on pressure drop, filtration characteristics and impact of urea injection on PM oxidation rate. 2) Configuration 2 experiments with and without PM loading focused on NO_x conversion performance and impact of PM loading on the SCR reaction rate. 3) Configuration 3 experiments with the SCR-F®+SCR system focused on determining the system NO_x conversion at different engine conditions.

¹Parts of this chapter are from reference [49]

5.1 SCRF® Configuration 1 Passive Oxidation With and Without Urea Data

The configuration 1 dataset consisted of five passive oxidation test points. These five test points were run with and without urea injection leading to a total of 14 passive oxidation experiments. These experiments had a temperature range of 273 to 377°C and a inlet NO₂ range of 117 to 792 ppm. A target oxidation of 70% at the end of PM oxidation stage was used to determine the time for the passive oxidation stage in each experiment.

Due to the temperature and inlet NO₂ conditions encountered in these tests, up to 93% of total PM oxidation during the PM oxidation stage was caused by NO₂ assisted PM oxidation reaction. During urea injection at ANR = 1.0 for the five test points, upto a 70% reduction in the PM oxidation rate was observed and compared to the experiments without urea injection. This change in PM oxidation rate was found to be a function of the forward diffusion of NO₂ from the PM cake to the substrate wall. The change in PM oxidation rate led to a change in the filtration, pressure drop and PM distribution characteristics of the SCRF®. An axial increase in exhaust gas temperature due to the SCR reactions was also observed for experiments with urea injection which impacted the PM distribution at the end of the passive oxidation stage. These phenomena will be discussed in the next section.

5.1.1 Impact of SCR Reactions on PM Oxidation Rate

The outlet NO₂ emissions in the SCRF® are impacted by the passive oxidation rate and the SCR reactions. The PM passive oxidation (PO) rate converts NO₂ to NO while the NO_x is conserved as can be observed in experiments without urea injection. In the experiments with urea injection, the NO₂ from the PM cake layer is further reduced to N₂ and H₂O, and the outlet NO_x is lower than the inlet NO_x in this case.

Figure 5.1 compares the outlet NO₂ from Test point C with and without urea injection showing the impact of NO₂ assisted PM oxidation and the SCR reactions on the outlet NO₂ concentrations. At time $t = 0$ to 5.5 hrs, the outlet NO₂ concentration

is impacted by the passive oxidation only, therefore the values from both the experiments are similar. The decrease in NO_2 with time is due to the increase in passive oxidation rate with increase in PM mass retained in the PM cake. At time $t = 5.9$ to 7 hrs for the experiment without urea injection shown with the black line, the NO_2 concentration decreases due to the PM passive oxidation reaction. The passive oxidation rate changes with time due to a decrease in PM retained as a result of the PM oxidation reaction which leads to the time varying outlet NO_2 concentration observed in this experiment. For the experiment with urea injection shown with the red line at time $t = 5.9$ to 8 hrs., the outlet NO_2 is a function of both passive oxidation and SCR reactions leading to a steady outlet NO_2 value of 5 ppm at ANR = 1.0 used in this case during the PO stage. The post loading stages have similar NO_2 concentrations for both cases as the loading stages. The experimental data for the case with urea injection (blue circles) and without urea injection (red circles) are within 20 ppm of model values.

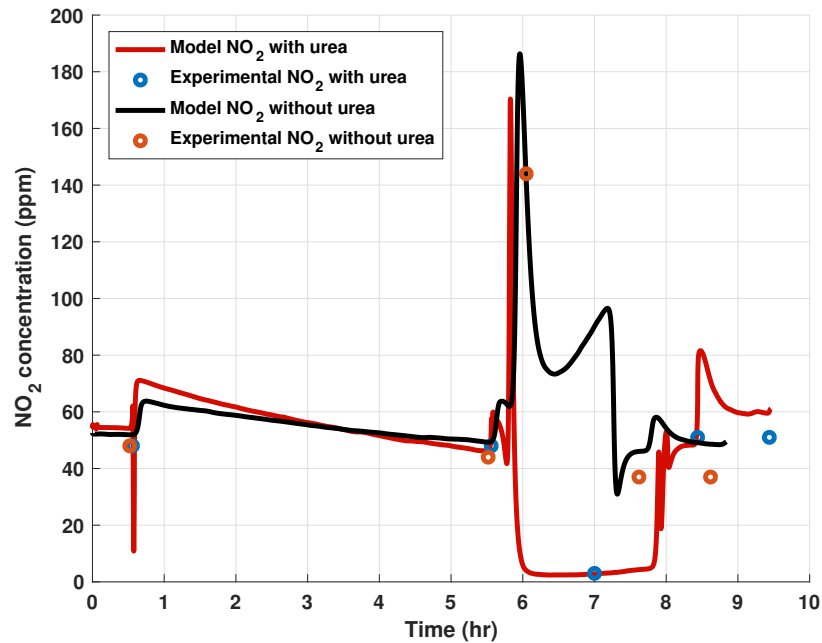


Figure 5.1: Outlet NO_2 emissions from PO-C experiment (with and without urea injection) inlet temperature = $349/347^\circ\text{C}$, $\text{NO}_2 = 301/228$ ppm, $\text{NO} = 387/321$ ppm

The change in the NO_2 in the SCR $\text{F}^{\text{®}}$ outlet during PO with urea injection is caused by the PM oxidation in the PM cake layer, SCR reactions in the substrate wall due to transport of NO_2 from the PM cake to the substrate wall layer by forward diffusion caused by the concentration gradient in the PM cake and substrate wall layers. This diffusion rate increases with an increase in the concentration and leads to a reduction

in the available NO_2 in the PM cake. The SCR-F model was able to capture this phenomena which has significant impact on the passive oxidation rate of the PM cake. Figure 5.2 compares the available NO_2 in the PM cake after taking forward diffusion into account for Test C without (blue dotted line) and with urea injection (black line). The available NO_2 in the cake decreases by 60 % from 100 ppm to 40 ppm for the case with urea injection. This led to a 60 % reduction in passive oxidation rate and a longer duration of the passive oxidation stage (80 minutes vs 120 minutes) for the same amount of PM oxidation.

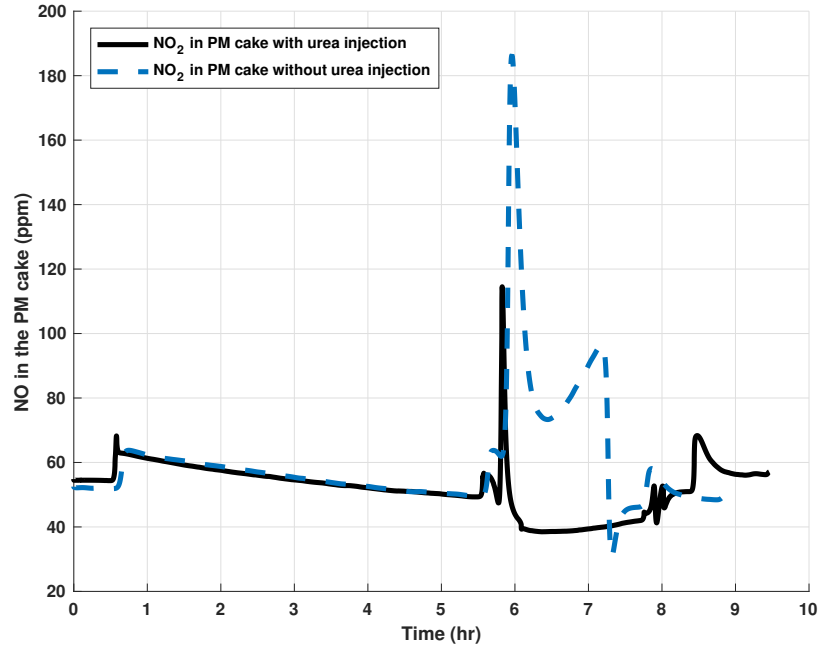


Figure 5.2: NO_2 in the PM cake for PO-C experiment (with and without urea injection) inlet temperature = 349/347°C, NO_2 = 301/228 ppm, NO = 387/321 ppm for Test C

Figure 5.3 shows the change in the NO_2 concentration across the inlet channel, PM cake, substrate wall and outlet channel due to reaction - diffusion scheme at the $x = 150$ mm along the length of the SCR-F®. For the experiment without urea injection, the NO_2 in the inlet channel decreases to 280 from 300 ppm due to diffusion at the inlet channel - PM cake boundary, and a further decrease from 280 to 130 ppm due to passive oxidation in the PM cake and forward diffusion to the substrate wall layer is experienced. In the substrate wall and outlet channel, the NO_2 concentration remains constant at 130 ppm. For the experiment with urea injection, the fast SCR reaction consumes most of the NO_2 in the substrate wall leading to a significant concentration gradient compared to the case with no urea injection. Due to the higher concentration gradient, a higher forward diffusion rate is observed leading to a decrease of NO_2 from

300 to 220 ppm in the inlet channel, 220 to 40 ppm in the cake and 40 to 5 ppm in the substrate wall. This higher diffusion rate leads to a lower effective NO_2 in the PM cake in the case with urea injection, 200 vs 40 ppm leading to a lower PM oxidation rate.

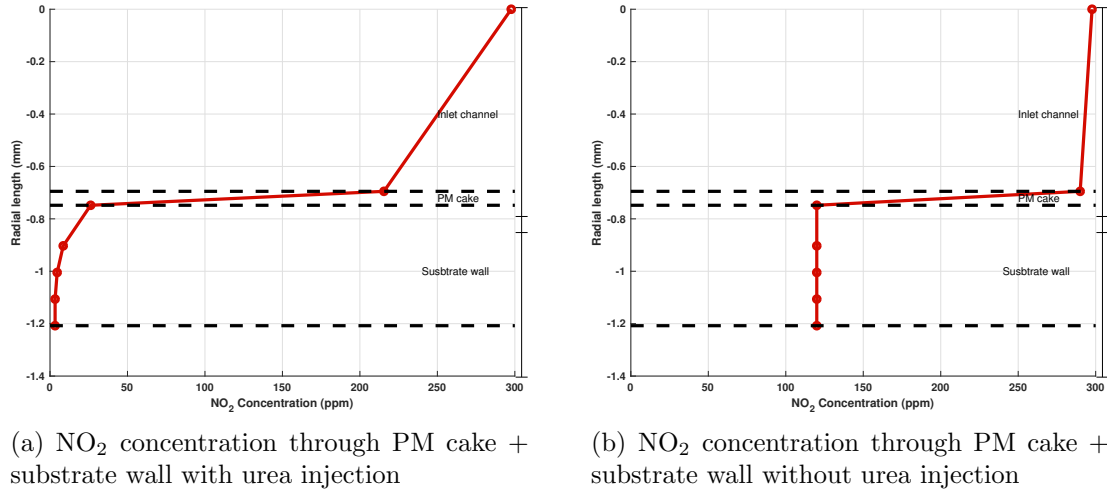


Figure 5.3: Change in NO_2 concentration through the PM cake and substrate wall for PO-C (with/without urea) inlet temperature = $349/347^\circ\text{C}$, $\text{NO}_2 = 301/228$ ppm, $\text{NO} = 387/321$ ppm with ($t = 6.7$ hrs, 47 minutes after start of PM oxidation) and without ($t = 6.7$ hrs, 52 minutes after start of PM oxidation) urea injection for Test C.

Figure 5.4 compares the 60-80% reduction in PM oxidation rate during urea injection for the 7 experiments in the configuration 1. The SCR-F model was able to simulate the experimental values to within 5% for all the cases using a common set of passive oxidation reaction kinetics.

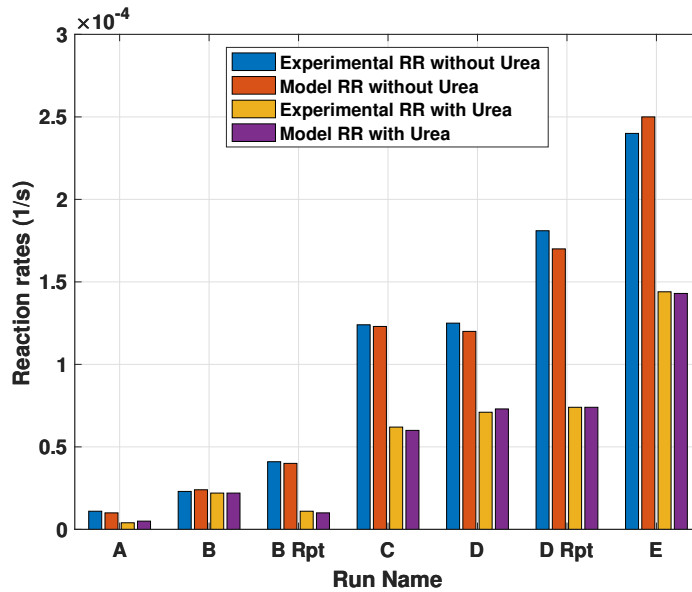
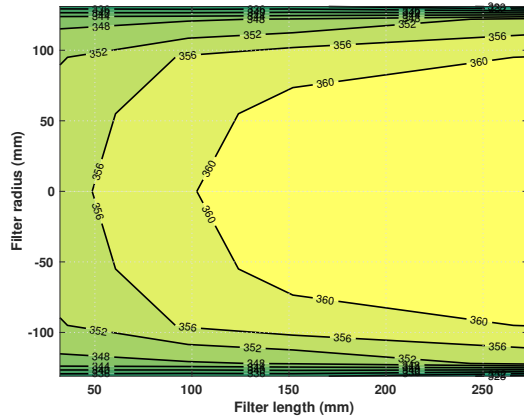


Figure 5.4: Experimental and model NO_2 assisted PM oxidation rates for all 7 SCRFR[®] configuration 1 experiments

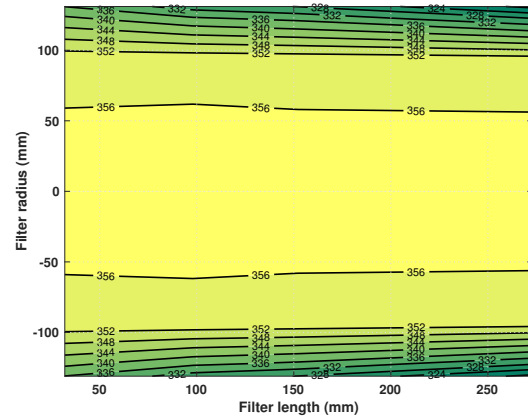
5.1.2 Change in Temperature, NO_2 concentration and PM Mass Distribution for Cases With and Without Urea Injection

The temperature distribution in the SCRFR[®] is governed by the heat loss to the ambient, conduction in the radial and axial direction and energy release by the chemical reactions. Figure 5.5 compares the 2D temperature distribution during passive oxidation with and without urea injection. For the case without urea injection, the axial temperature decreases from 357 to 355°C at the centre of the filter and at the outer edges, the temperature decreases from 336 to 324°C due to the addition of the heat loss to the ambient. For the case with urea injection, a temperature rise from 354 to 362°C is observed due to energy release by the SCR reactions. The temperature rise is observed to be higher at axial location $x = 50$ to 100 mm due to a postulated higher catalyst loading compared to the rest of SCRFR[®] and diffusion of chemical species from inlet channel to substrate wall. The model was able to simulate the temperature distribution to within 5°C of experimental value for all the 37 experiments.

The NO_2 concentration in the axial direction is a function of the diffusion from the inlet channel to the substrate wall. The diffusion rate is a function of the concentration



(a) 2D temperature distribution PO-C with urea injection



(b) 2D temperature distribution PO-C without urea injection

Figure 5.5: 2D temperature distribution for Test C (with/without urea) inlet temperature = 349/347°C, NO₂ = 301/228 ppm, NO = 387/321 ppm with (t = 6.7 hrs, 5 minutes after start of PM oxidation) and without (t = 6.7 hrs, 5 minutes after start of PM oxidation) urea injection.

gradient caused by the consumption of NO₂ by both passive oxidation reaction in the PM cake and SCR reactions in the substrate wall. Figure 5.6(a) shows the change in NO₂ concentration during urea injection in Test C. The axial and radial change in NO₂ observed in the Figure 5.6(a) is a function of the change in the local NO₂/NO_x ratio shown in Figure 5.6(b) which determines the change in the contribution of the SCR reactions in the substrate wall slabs.

The PM distribution is a function of the temperature distribution and chemical species (NO₂) distribution in the SCR® that were discussed earlier. Figure 5.7 compares the PM distribution at the end of the passive oxidation stage for test point C with and without urea injection. For the experiment without urea injection, the PM distribution is a function of the temperature distribution leading to uniform PM loading of 1 g/l at the center of the filter at radius of 0 to 90 mm. At the outer edges of the filter from radius 90 to 110 mm due to a radial decrease in the temperature, an increase in the PM loading from 1.1 to 1.8 g/l is observed due to reduced PM oxidation rate. Also an increase in the axial PM loading from 1.4 to 1.8 g/l at the outer edge of the SCR® is observed due to the axial temperature decrease caused by heat loss to ambient.

For the case with urea injection, the change in NO₂ concentration combined with the temperature increase due to the energy release by the SCR reactions play an

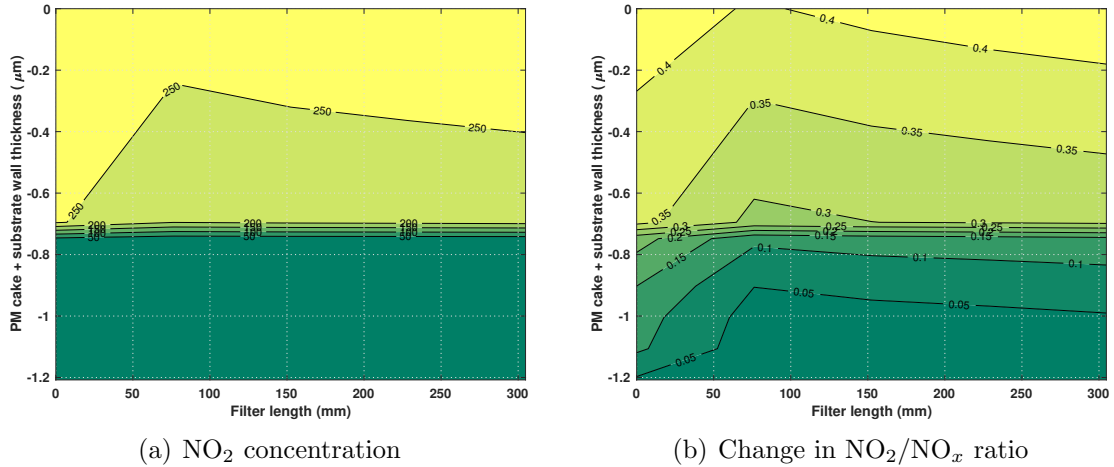
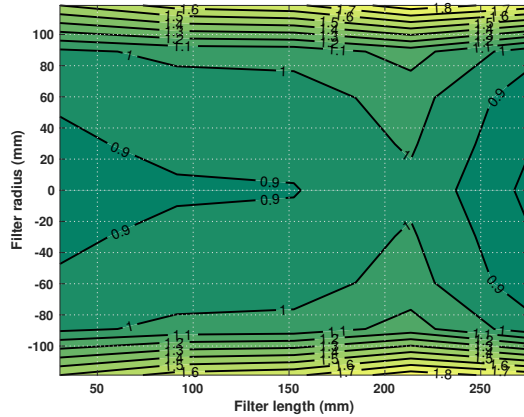


Figure 5.6: Change in NO_2 concentration and NO_2/NO_x ratio through the PM cake and substrate wall for PO-C inlet temperature = 347°C , $\text{NO}_2 = 301$ ppm, $\text{NO} = 387$ ppm with urea injection ($t = 6.7$ hrs, 47 minutes after start of PM oxidation) for Test C

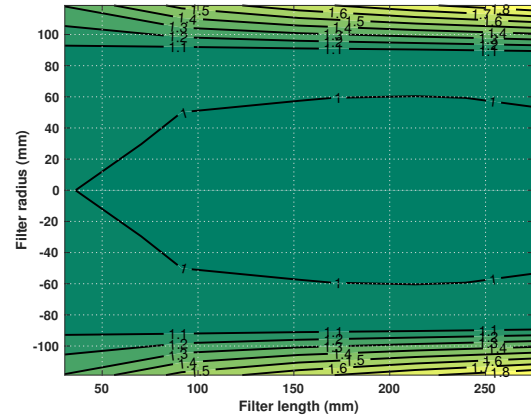
important role in the PM distribution of the SCR-F®. The center of the filter has lower PM loading 0.9 - 1 g/l due to the higher PM oxidation rate caused by the increased temperature. The axial variation in PM distribution is due to the NO_2 concentration profile inside the PM cake layer. At radius 90 to 110 mm, the loss of heat to the ambient leads to a higher PM loading of 1 to 1.8 g/l observed in Figure 5.7a.

5.1.3 Filtration Efficiency With and Without Urea injection

Filtration efficiency of the SCR-F® is modeled with two components, the cake and substrate wall. Figure 5.8 compares the filtration efficiency of Test point C with and without urea injection from the SCR-F model. For the experiment without urea injection at time $t = 0$ to 0.5 hrs the wall efficiency increases due to PM accumulation in the wall, at $t = 0.5$ hrs the filtration transitions from deep bed to cake filtration regime leading to a total filtration efficiency greater than 95 %. A maximum filtration efficiency of 98.5 % is observed during the loading stage at $t = 0.5$ to 5.5 hrs. At 5.5 hrs, due to PM oxidation, a significant drop in wall filtration efficiency and thus total filtration efficiency is observed. At $t > 7.1$ hrs the filtration efficiency of the wall starts increasing due to the wall being filled with PM. However, due to the presence of the PM cake layer, the rate at which PM fills up the substrate wall in this case is



(a) 2D PM mass distribution with urea injection



(b) 2D PM mass distribution without urea injection

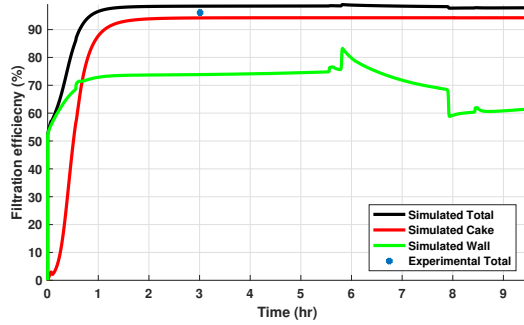
Figure 5.7: 2D PM mass distribution for Test C (with/without urea) inlet temperature = 349/347°C, NO₂ = 301/228 ppm, NO = 387/321 ppm with (t = 6.7 hrs, 47 minutes after start of PM oxidation) and without (t = 6.7 hrs, 52 minutes after start of PM oxidation) urea injection.

much lower.

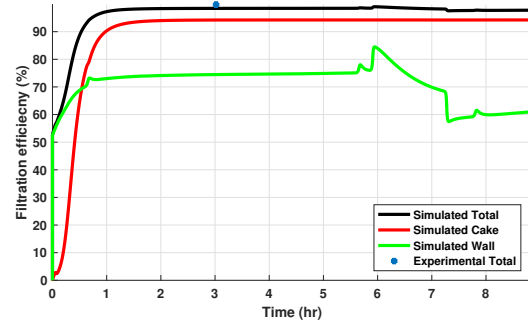
For the experiment with urea injection, the filtration characteristics during loading are similar to the case without urea injection with a maximum filtration efficiency of 98.5 %. After t = 5.5 hrs, the rate of decrease in wall filtration efficiency is much lower compared to the without urea case due to a 85 % reduction in the wall PM oxidation rate in this case. This decrease in PM oxidation rate of wall PM is due to competition for NO₂ between the passive oxidation rate and the SCR reactions. As a result of this lower oxidation rate in the post loading stages at time t > 7.9 hrs, the wall efficiency is higher compared to the without urea injection case (60 % vs 55%). This change in filtration characteristics has further impact on the pressure drop characteristics of the SCRF® during oxidation and post loading stages.

5.1.4 Impact of Urea Injection on PM Mass Retained

The PM mass retained is a function of the filtration efficiency, exhaust flow rate, inlet PM concentration and PM oxidation rate. Figure 5.9 shows the PM mass retained vs time plots for Test C with and without urea experiments. For both the cases, the model was able to simulate the experimental data to within 2 gm using the same set



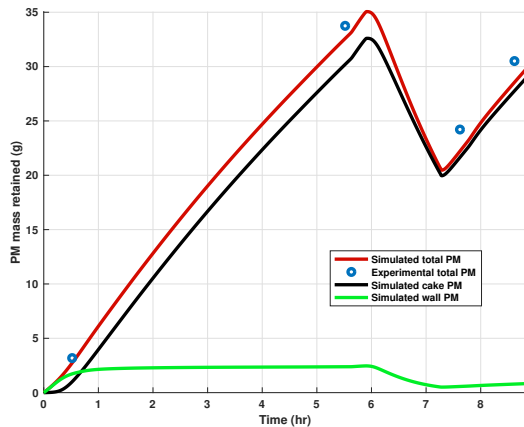
(a) Filtration efficiency with urea injection



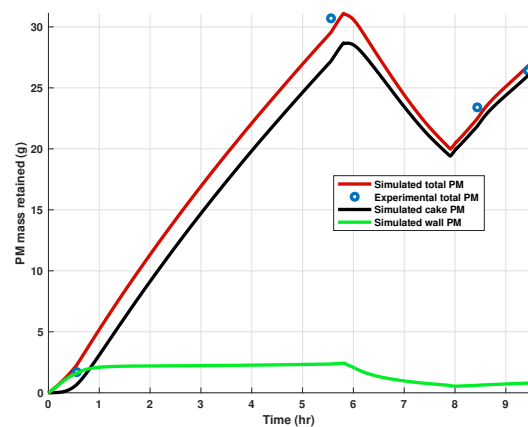
(b) Filtration efficiency without urea injection

Figure 5.8: Filtration efficiency PO-C with/without urea injection vs time.

of kinetics for passive oxidation and thermal oxidation reactions. In both the cases at the end of loading at time $t = 5.5$ hrs., 28 gm of PM was observed. During the passive oxidation stage, due to urea injection, a 70 % reduction in the PM oxidation rate is observed leading to a longer oxidation stage (120 minutes vs 80 minutes) for experiment with urea injection compared to case without urea injection for the same amount of PM oxidized. During post loading, for the case with urea injection, the slope of the PM mass retained is lower than the case without urea injection due to the change in the wall filtration characteristics.



(a) PM mass retained vs time for with urea injection



(b) PM mass retained vs time for without urea injection

Figure 5.9: PM mass retained vs time for Test C with and without urea injection

5.1.5 Impact of Urea Injection on Wall and Cake Pressure Drop Characteristics

The pressure drop characteristics of the SCRF® are impacted by three major components - pressure drop across the substrate wall, PM cake and inlet/outlet channel. Figures 5.10 and 5.11 show the pressure drop across the SCRF® vs time for Test C with and without urea injection. In both the cases, the pressure drop increases with an increase in the PM mass retained in both the PM cake and substrate wall. A linear increase in pressure drop slope can be observed for both the experiments from time $t = 0$ to 5.5 hrs. The major components of the pressure drop are also shown in the figures (cake pressure drop in green, wall pressure drop in blue and channel pressure drop in orange). The experimental and model total pressure drop are shown with dotted black and red lines.

After $t = 5.5$ hrs., due to PM oxidation, the pressure drop decreases in both cases. The slope of the pressure drop curve during passive oxidation is higher for the case without urea injection due to higher PM oxidation rate. For the case without urea injection, due to the reduction in the PM oxidation rate, the slope of the pressure drop curve is lower for the initial part of oxidation $t = 5.5$ to 6.5 hrs. Also, the slope of the wall pressure drop curve in this case is lower due to the 85% reduction in the wall PM oxidation rate caused by the competition for NO_2 between NO_2 assisted PM oxidation and the SCR reactions. At time $t = 6.5$ hrs. a slope change is observed due to the change in the permeability of the cake which represents the time point where the cracks are formed in the PM cake due to the damage by the PM oxidation leading to a rapid decrease in cake pressure drop as the exhaust gas follows the path of least resistance through these cracks. For the post loading condition, the cake permeability gradually reaches the initial value as the cracks in the PM cake fill up with PM. The slope of the pressure drop curves during post loading for the case without urea injection is higher due to a lower change in cake permeability change during oxidation and the wall pressure drop is lower in this case due to higher oxidation rate of wall PM. For the case with urea injection, the pressure drop curve in post loading increases significantly at $t = 8.5$ hrs., and this point represents the time at which the cracks in the cake fill up leading to a rapid increase in the pressure drop across the PM cake. Also, the wall pressure drop is higher due to the lower wall PM oxidation rate during the PO stage.

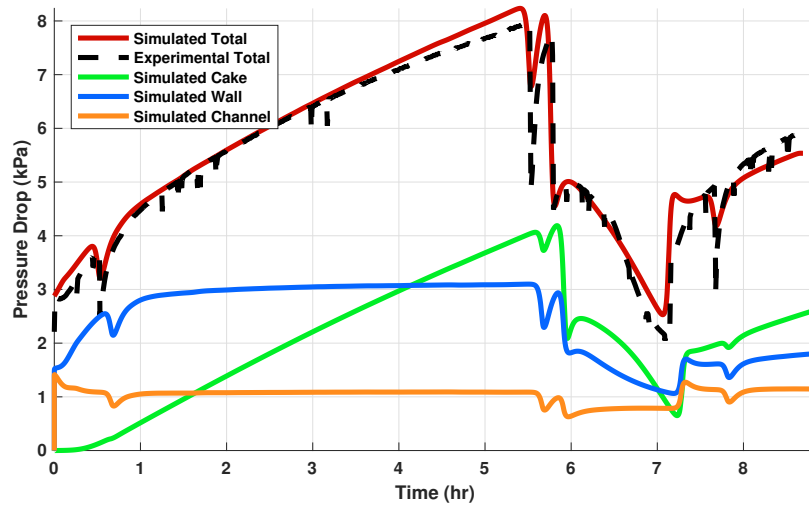


Figure 5.10: Pressure drop vs time for Test C with urea injection inlet temperature = 347 °C, NO₂ = 228 ppm, NO = 321 ppm

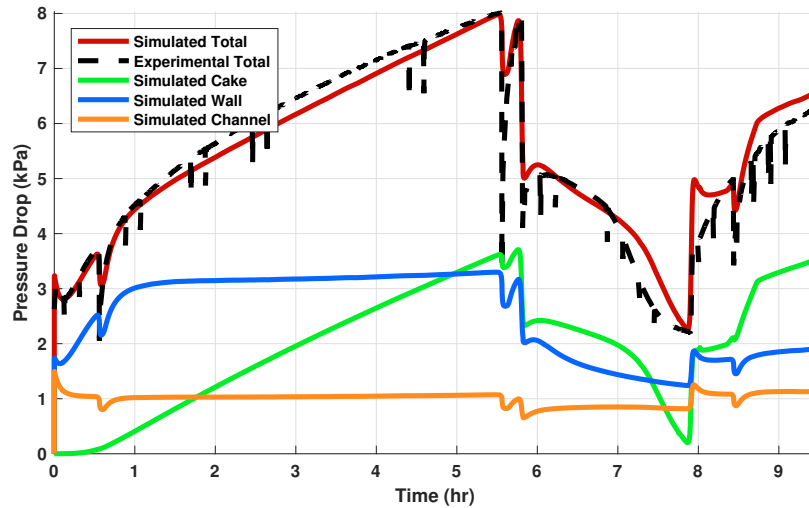


Figure 5.11: Pressure drop vs time for Test C with urea injection inlet temperature = 349 °C, NO₂ = 301 ppm, NO = 387 ppm

5.1.6 Change in Cake Permeability Due to Forward Diffusion

The cake permeability was modeled as a function of PM oxidation rate and percent PM oxidized during the oxidation stage. The equations used for the cake permeability were used to calculate the damage variable which represents the cracks formed in the cake that reduce the resistance of the PM cake layer to exhaust gas flow. During urea injection, it was observed that the cake permeability change was much higher than

predicted by the cake permeability model. This increase in permeability, which led to near zero cake pressure drop, can be attributed to higher damage caused by the forward diffusion of NO_2 from PM cake to substrate wall layer. Figure 5.12 shows a comparison of cake permeability for Test C with and without urea injection during the passive oxidation stage. Both the cases have the same percent oxidation, however the cake permeability for the case with urea injection case is 12 times higher. In order to account for impact of the forward diffusion, the model employed a higher maximum cake permeability correction compared to the case without urea injection.

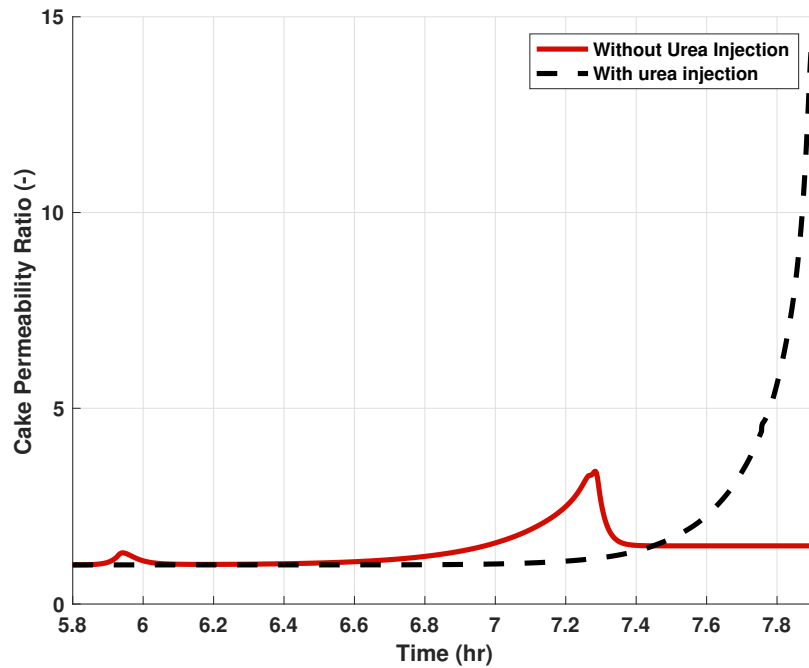


Figure 5.12: PM cake permeability vs time for Test C experiment (with and without urea injection) inlet temperature = 349/347 °C, NO_2 = 301/228 ppm, NO = 387/321 ppm

5.2 SCRF[®] Configuration 1 Active Regeneration Data

The configuration 1 data consisted of four active regeneration experiments that were used to determine the thermal and PM oxidation kinetics. These experiments showed

negligible change in PM cake permeability and low passive oxidation (<10%) rate compared to a CPF from reference [50]. A temperature rise of 15 to 20°C as a function of HC oxidation was observed in the experimental data and was simulated by the 2D SCR-F model to within +/- 5°C. This section covers the results from the active regeneration experiments.

5.2.1 Energy Release by HC Oxidation

The energy release from chemical reactions led to 10 - 20 °C rise in temperature of the exhaust gas of the SCR-F® during active regeneration stage. The reactions involved in the energy release are HC oxidation, passive oxidation and thermal PM oxidation reactions. Figure 5.13 compares the contribution of these reactions for the four active regeneration experiments in terms of total energy release during active regeneration. As can be observed from the Figure 5.13 the energy release by HC oxidation accounted for 94 - 96 % of the total energy release for all the four active regeneration experiments. The thermal PM oxidation led to further 3.5 - 5 % of energy release with passive oxidation accounting for 1 % of total energy release.

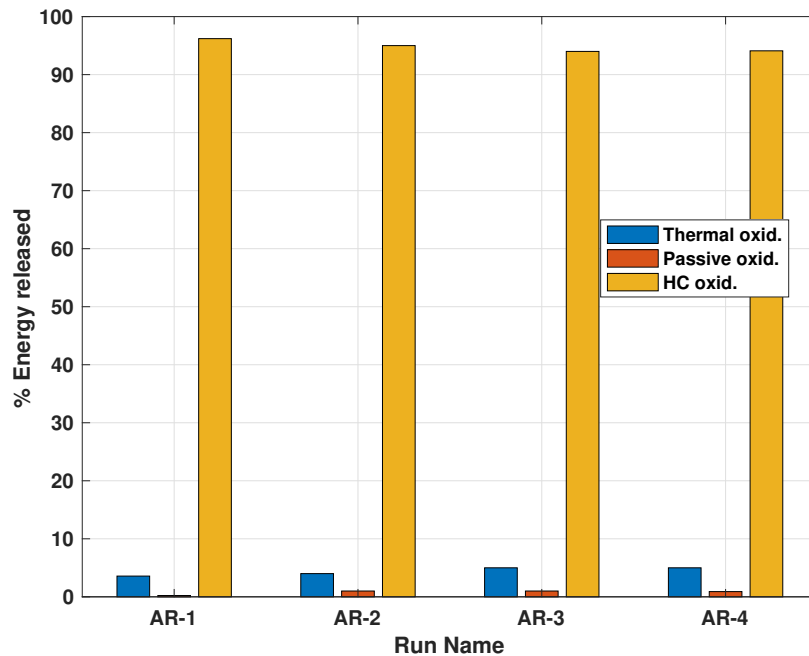


Figure 5.13: Contribution of HC, NO₂ assisted PM and thermal PM oxidation rate to the total energy release during AR stage

5.2.2 Contribution of Thermal and NO₂ Assisted PM Oxidation

For the active regeneration experiments, the PM oxidation is assumed to have two components - thermal and passive oxidation. For inlet exhaust gas temperatures greater than 500°C the thermal oxidation is the dominant form of PM oxidation. For these experiments due to the low NO₂ inlet concentration, the passive oxidation accounts for less than 10 % of the total PM oxidation rate. Figure 5.14 shows the percent PM oxidized by thermal and passive oxidation rate. For all cases, the thermal oxidation accounted for greater than 90 % of total PM oxidation rate. With an increase in temperature from 490 to 590°C the thermal PM oxidation rate increased from 92 to 96 % of the total PM oxidation rate and at the same time the passive oxidation reduced from 8 to 4%.

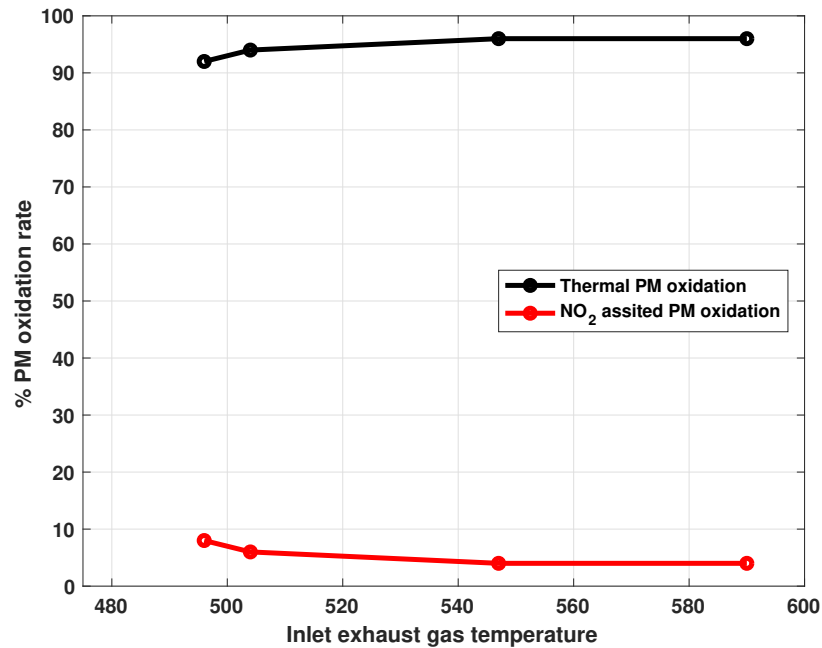


Figure 5.14: Percent of total PM oxidation rate for Thermal and NO₂ assisted vs exhaust gas temperature during active regeneration

Due to the presence of a different catalyst in the SCR® compared to a CPF [52] the passive oxidation rate contributed to 6% of the passive oxidation in the SCR® in the place of 20% observed for the CPF during active regeneration. In the CPF due to the presence of a oxidation catalyst, the NO₂ consumed in the PM cake was regenerated in the wall and through back diffusion supplied to the PM cake leading

to higher PM oxidation rate. In the case of SCR-F[®] due to the absence of a oxidation catalyst, the NO oxidation reaction was observed to be low resulting in a lower passive oxidation rate for the same engine condition.

5.3 Summary of Configuration 1 Results

The eighteen experiments in configuration 1 were simulated by the SCR-F model with the common set of parameters obtained as part of the model calibration. Important results from this dataset include:

1. The outlet exhaust gas temperature was simulated to within $\pm 5^{\circ}\text{C}$ for all the sixteen experiments for all stages.
2. The 2D temperature distribution during PO was simulated to within $\pm 5^{\circ}\text{C}$ RMS error of the experimental data using thermal parameters and energy release by the SCR reactions. The AR stage temperature distribution was simulated using the energy release from the HC oxidation, passive and thermal PM oxidation reactions to within $\pm 5^{\circ}\text{C}$ of experimental data.
3. The PM mass retained was simulated to within ± 2 gm of experimental data for all the fourteen PO and four AR experiments using a common set of kinetics for NO_2 assisted and thermal PM oxidation reactions.
4. The outlet NO , NO_2 and NH_3 concentrations were simulated to within ± 20 ppm of the experimental data for the fourteen PO experiments using the SCR reaction kinetics and storage parameters.
5. The outlet HC concentrations were simulated to within ± 10 ppmC of experimental data using HC oxidation reaction kinetics for the four AR experiments.
6. The 60-70 % decrease in PM oxidation rate for the seven PO experiments with urea injection was simulated to within 5% using a tortuosity value of 8.
7. The filtration efficiency during PM loading was simulated to within ± 1.5 % for all sixteen experiments.
8. The pressure drop across the SCR-F[®] was simulated to within ± 0.3 kPa for all the stages in all the 16 experiments using a common set of pressure drop

and cake permeability parameters. Due to lack of back diffusion of NO_2 and the high PM oxidation rate, the cake permeability change during AR was observed to be negligible.

Tables and figures comparing the 2D SCR-F model and experimental data from all the test points from this dataset are given Appendix F.

5.4 SCR^F® Configuration 2 With and Without PM Loading Data

The configuration 2 data consisted of twelve experiments with four test points which were run at 0, 2 and 4 g/l PM loading. Figures 5.15 and 5.16 compare the experimental and model NO , NO_2 and NH_3 outlet concentrations from Test 1 and 8 with 2 g/l PM loading. The general trends observed in both the cases consist of a decrease in the outlet NO and NO_2 with an increase in the ANR value from 0.8 to 1.2. The NO_2 values for $\text{ANR} > 0.8$ are near zero in both the cases. An increase in NH_3 slip for $\text{ANR} > 1.0$ is also observed.

In Figure 5.15, Test 1 was conducted at an inlet exhaust gas temperature of 218°C . The low temperature leads to a lower reaction rate and NO_x conversion performance compared to cases with temperature greater than 250°C . The low adsorption reaction rate for storage sites 1 and 2 lead to the slow response time of the model to changes in inlet ANR values. The NH_3 slip does not reach steady state in this case while the NO and NO_2 outlet concentration reach steady state for the different inlet ANR values implying the presence of the two NH_3 storage sites. The first storage site being responsible for storage of NH_3 and NO_x reduction by the SCR reactions and the second site is responsible for only storage of the NH_3 . The first storage site coverage fraction (θ_3) reaches steady state at $t = 8.5$ hrs. while the second site continues to increase in coverage fraction (θ_2) up to time $t = 9$ hrs. at $\text{ANR} = 1.2$. The presence of the second site enables simulation of the NH_3 slip for all the twelve experiments while simulating the steady state NO_x conversion resulting from the first site. The model NH_3 slip characteristics have a deviation compared to experimental data during the transient portion of the experiment due to wall PM and local NO_2/NO_x ratio while the NH_3 was simulated to within 20 ppm of the experimental value for the twelve configuration two experiments. The model NH_3 concentration in the figure has a smaller slope than

the experimental data. The change in slope is due to the calibration of the kinetic parameters over a wide range of experimental conditions in the calibration process and the inhibition of the desorption reaction of the second site which is a function of PM in the wall that changes with time as the PM gets oxidized at the given engine condition

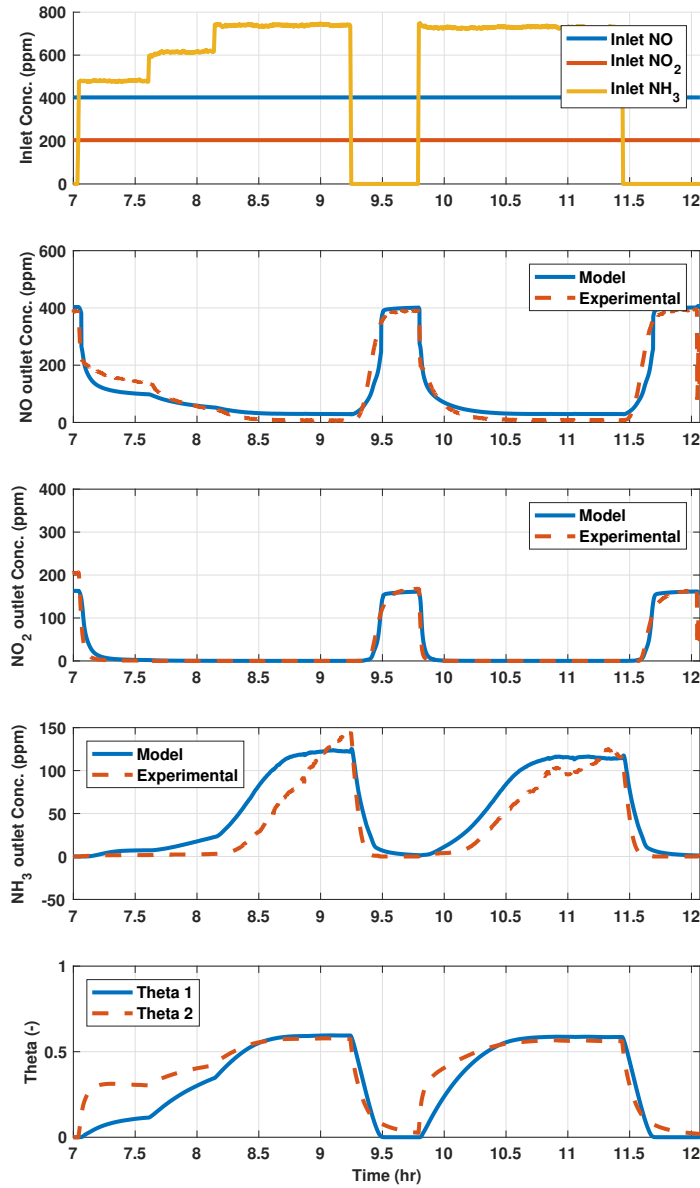


Figure 5.15: Inlet and outlet NO, NO₂, NH₃ concentrations Test 1 inlet temperature = 206°C, NO₂ = 203 ppm, NO = 403 ppm, 2 g/l PM loading configuration 2

In Figure 5.16, Test 1 was conducted at inlet temperature $T = 438^{\circ}\text{C}$. Due to the

higher exhaust gas temperature, the response time of the model to changes in the inlet ANR was faster and also the NH_3 oxidation reaction played an important role in the NH_3 slip characteristics in this experiment. For all the ANR values, the NH_3 and NO , NO_2 concentrations reach steady state values within 2 minutes of a ANR change due to the high adsorption reaction rate. The coverage fraction of the second storage site is negligible due to the high desorption reaction rate. The outlet NH_3 slip is lower than expected due to a 10 % higher NH_3 consumption caused by the NH_3 oxidation rate at this higher exhaust temperature.

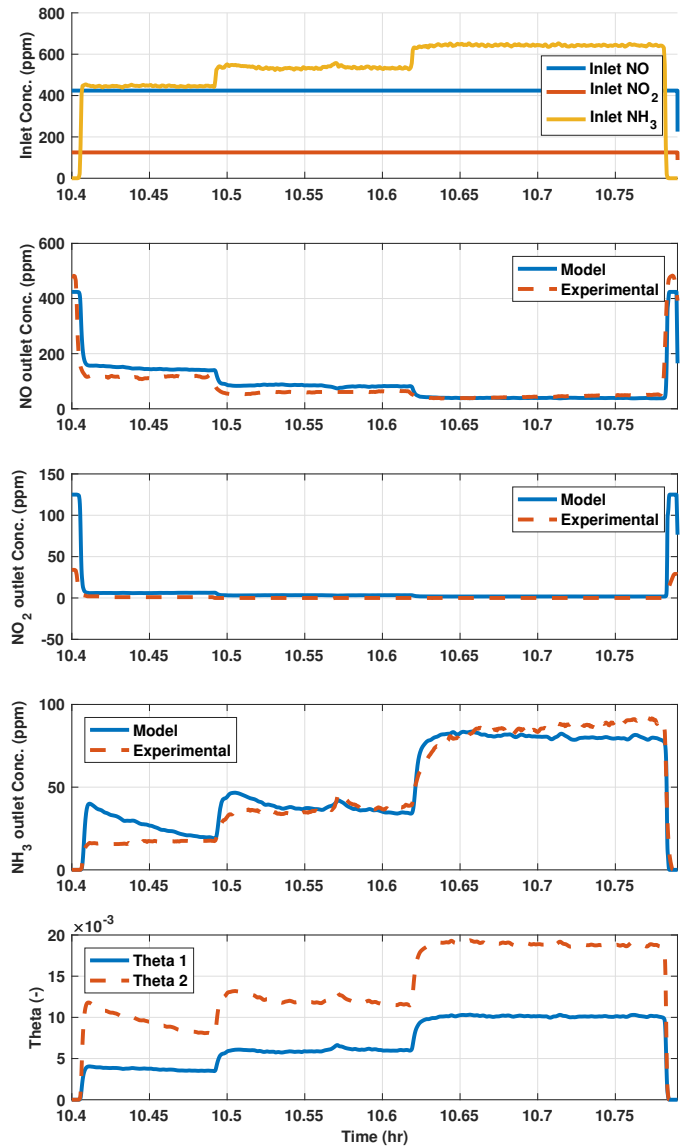


Figure 5.16: Inlet and outlet NO, NO₂, NH₃ concentrations Test 8 inlet temperature = 438°C, NO₂ = 125 ppm, NO = 424 ppm, 2 g/l PM loading configuration 2

5.4.1 Change in Local NO₂/NO_x Ratio Inside the Substrate Wall

The change in the local NO₂/NO_x ratio as the exhaust gas passes through different layers in the SCR® PM cake + substrate wall control volume plays an important role in determining the overall NO_x conversion performance of the SCR®. The

change in NO_2/NO_x ratio occurs due to NO_2 assisted PM oxidation and the SCR reactions. Figure 5.17 shows the change in the NO_2/NO_x ratio through the cake and substrate wall slabs in the SCRF® at the center of the filter. The inlet NO_2/NO_x ratio varies in the range of 0.28 - 0.6. In the PM cake at location at $y = 0$ to $-0.7 \mu\text{m}$ the ratio decreases by 16% due to the conversion of NO_2 to NO by passive oxidation of the PM in the cake. As the exhaust gas passes through the substrate wall layers there is a further reduction in the NO_2/NO_x ratio due to the fast and slow SCR reactions consuming NO_2 . The reduction in the NO_2/NO_x ratio leads to a shift in contribution of the fast and standard SCR reactions with the standard SCR reaction being the predominant reaction in the third and fourth wall slab at location $y = -1$ to $-1.2 \mu\text{m}$. The change in contribution of the SCR reaction also leads to a decrease in the effective NO_x reduction efficiency of the SCRF®. The consumption of NO_2 by the PM cake and the resultant decrease in NO_2/NO_x ratio is dynamic due to varying PM cake layer thickness and this phenomena plays an important role to be shown later in determining the SCRF®+SCR system NO_x conversion performance.

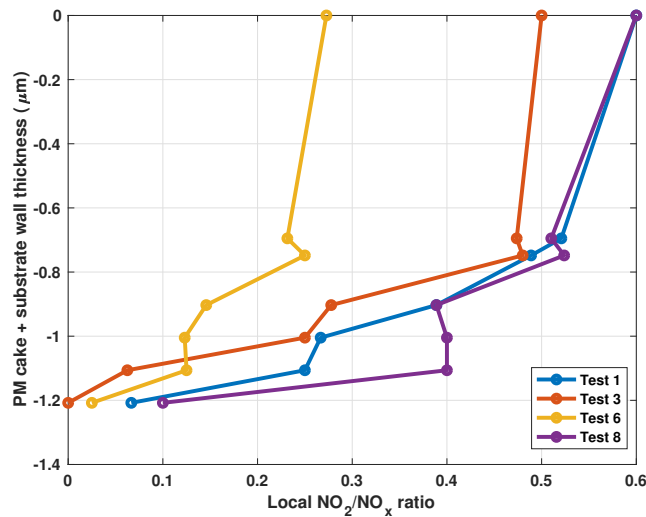


Figure 5.17: Change in local NO_2/NO_x ratio across PM cake and substrate wall slabs configuration 2 with PM loading experiments

5.4.2 Contribution of Each SCR Reaction on NO_x Reduction Performance

The NO_x reduction in the SCRF® is carried out by the - fast, standard and slow SCR reactions. The contribution of each of these reactions is a function of NO_2/NO_x

ratio with the fast SCR reaction being the preferred reaction pathway in the presence of equal concentration of NO and NO₂ leading to high rate constant. Figure 5.18 compares the SCR reactions rate for the three SCR reactions from Test 6 with 2 g/l at ANR = 1.0. At time t = 0 to 5.5 hrs and t= 8.1 to 9.5 hrs., the reaction rates are near zero due to no urea injection during PM loading of the SCR®. The slow SCR reaction (green line) is less than 10 % of total NO_x reduction, standard SCR reaction (red line) accounts for 30 % with the remaining 60% from fast SCR reaction (black line). Similar trends have been observed for all the experiments in the configuration 2 with and without PM loading.

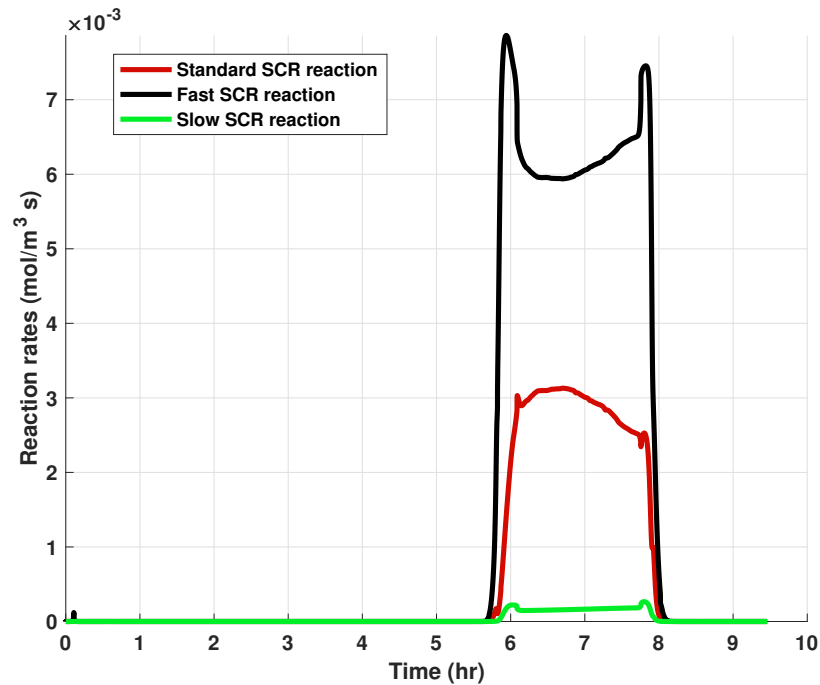


Figure 5.18: SCR reaction rates for configuration 2 vs time - Test 6 with 2 g/l

5.4.3 Inhibition of SCR Reactions Due to PM Loading

The SCR reactions are inhibited by the mass transfer limitation from the exhaust gas flow to the catalytic sites due to the PM accumulated in the substrate wall. This phenomena was modeled using the effectiveness factor concept using the filtration model to compute the unit collector diameter. Figure 5.19 shows the change in the

effectiveness factor versus change in PM mass retained in the substrate wall for the adsorption of the two sites and the three SCR reactions. For the clean wall, the effectiveness factor is equal to 1 due to no mass transfer limitation. With an increase in wall PM mass retained, the effectiveness factor decreases due to an increased mass transfer limitation. The rate of change in effectiveness factor for each of the reactions is different due to a change in kinetics for each reaction which were used to simulate the impact of wall PM on NO_x conversion efficiency for the configuration 2 experiments with PM loading. Also, the change in the effectiveness factor as a function of wall PM retained has a different path during oxidation compared to the loading stage due to nature of evolution of unit collector diameter from the filtration model which is an important parameter in calculation of the inhibition.

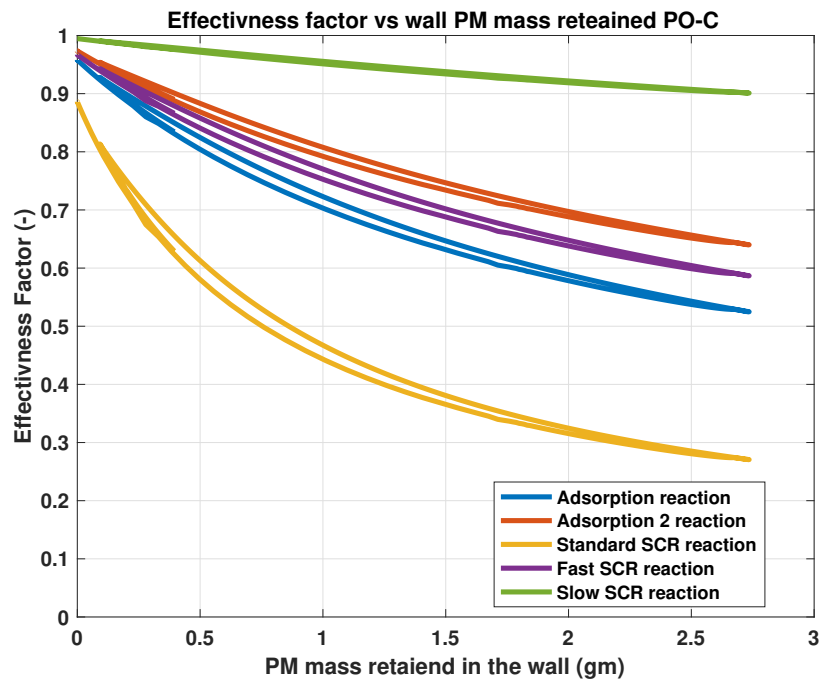


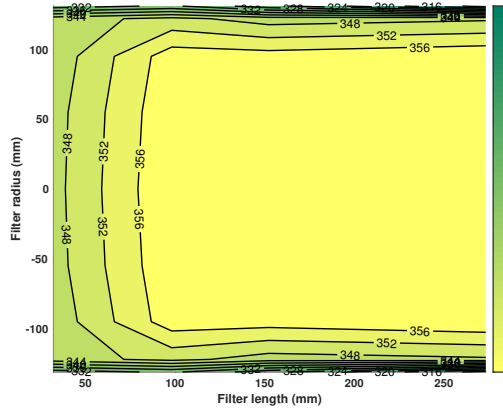
Figure 5.19: Change in Effectiveness factor for the three SCR reactions and adsorption reactions on site 1 and 2 vs PM mass retained in the wall

5.4.4 SCR-F Temperature as a Function of Inlet ANR

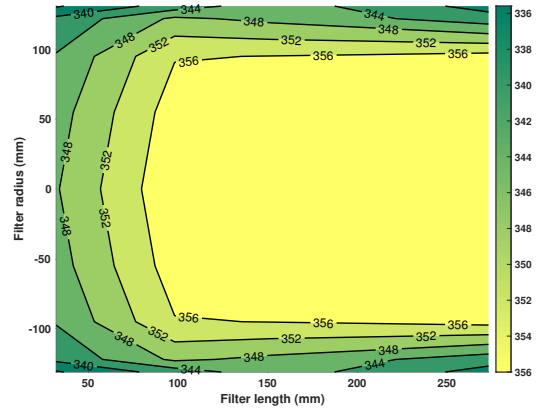
The energy release by each of the SCR reactions contributes to the axial increase in the temperature of the exhaust gas in the SCR-F®. Figure 5.20 compares experimental and model 2D temperature distributions at ANR values 0.8, 1 and 1.2 for Test 6 with 2 g/l PM loading.

The trends observed from the SCR-F model results in these figures are as follows :

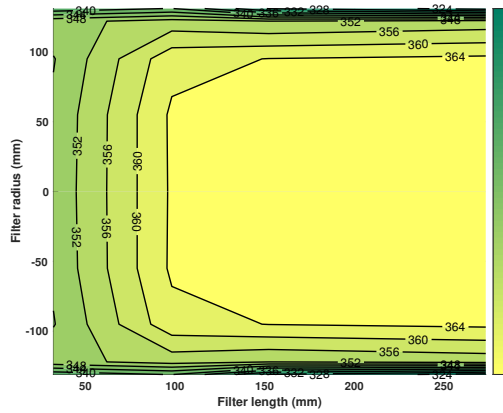
1. There is a decrease in inlet exhaust gas temperature with an increase in ANR value. For ANR 0.8 inlet $T = 346\text{ }^{\circ}\text{C}$, ANR 1.0 $T = 345\text{ }^{\circ}\text{C}$ and ANR 1.2 $T = 344\text{ }^{\circ}\text{C}$. This trend is attributed to decrease in exhaust gas temperature due to evaporation of urea solution in the decomposition tube.
2. The change in exhaust gas temperature across the SCR[®] increases with an increase in inlet ANR due to increase in the SCR reaction rate. For ANR = 0.8 a temperature rise of $13.1\text{ }^{\circ}\text{C}$ at the center of the filter is observed. Similarly for ANR = 1.0, a temperature rise of $16.2\text{ }^{\circ}\text{C}$ and for ANR 1.2 a temperature rise of $17.3\text{ }^{\circ}\text{C}$ is observed.
3. The change in temperature rise between ANR 1 to 1.2 is low ($1.1\text{ }^{\circ}\text{C}$) compared to 0.8 to 1 ($3.2\text{ }^{\circ}\text{C}$). This trend is due to the fact that the most of the NO_x is reduced at ANR 1.0 further confirming the fact that temperature rise is due to the SCR reactions.
4. At the outer edges of the SCR[®] the temperature rise is negligible in the axial direction since the gradient in the model is little affected.
5. The temperature rise is observed to be maximum at axial location 50 to 100 mm with negligible temperature change from 0 to 50 and 100 to end of filter. Since the temperature distribution was simulated by changing the axial catalyst loading distribution by dividing the filter into three zones.



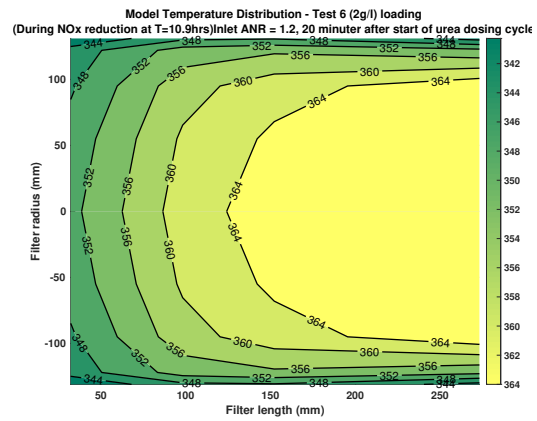
(a) 2D experimental temperature distribution at ANR = 0.8, 5 min. after PO start



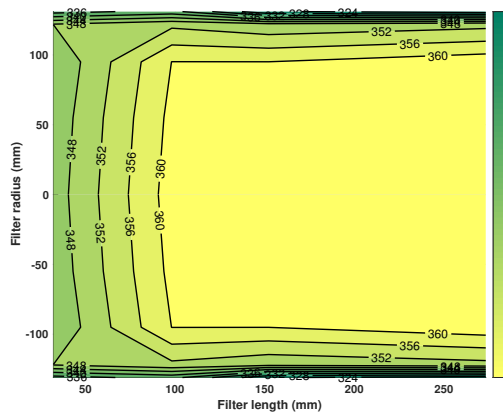
(b) 2D model temperature distribution at ANR = 0.8, 5 min. after PO start



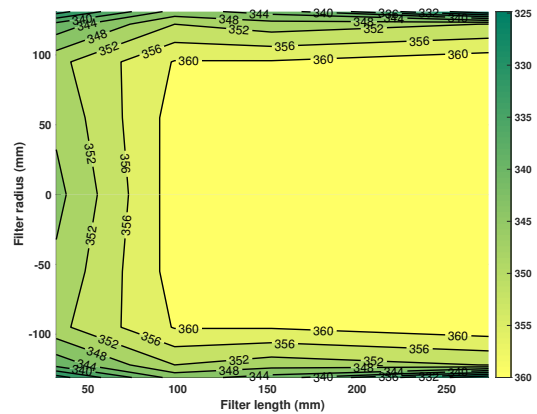
(c) 2D experimental temperature distribution at ANR = 1.0, 10 min. after PO start



(d) 2D model temperature distribution at ANR = 1.0, 10 min. after PO start



(e) 2D experimental temperature distribution at ANR = 1.2, 15 min. after PO start



(f) 2D model temperature distribution at ANR = 1.2, 15 min. after PO start

Figure 5.20: 2D Temperature distribution experimental and model for Test 6 with 2g/l PM loading, ANR = 0.8, 1 and 1.2

5.4.5 NO_x Reduction Efficiency

Figure 5.21 shows the experimental and model NO_x conversion efficiency for the twelve configuration 2 experiments at ANR 0.8, 1 and 1.2. A significant variation in the steady state NO_x conversion efficiency for the same ANR values and same test point was observed due to a change in the PM loading. This change in the NO_x conversion efficiency at different PM loading conditions is a function of local NO₂/NO_x ratio inside the substrate wall slabs which is dependent on both PM cake thickness and SCR reaction rates, inlet exhaust gas temperature and effectiveness factor for different SCR reactions based on the amount of PM in the substrate wall. The dependency of NO_x conversion efficiency on these three factors explains the variation in NO_x conversion trends with PM loading conditions for the different test points.

For Test 1, the NH₃ oxidation is negligible due to the low inlet exhaust gas temperature (<250⁰C) so a reduction in NO_x reduction with an increase in the PM loading is expected. However, due to the decrease in desorption reaction rate for the first NH₃ storage site with an increase in PM loading, the coverage fraction of the first site increases with an increase in PM loading from 0 to 2 g/l. This increase in coverage fraction of the first NH₃ storage site leads to an increase in NO_x conversion efficiency with an increase in PM loading for Test 1 as observed in Figure 5.21. From Test 1 at 2 g/l to 4 g/l, a decrease in NO_x reduction is observed due to the change in local NO₂/NO_x ratio at the substrate wall due to consumption of NO₂ by the higher NO₂ assisted PM oxidation rate at 4 g/l PM loading compared to 2g/l.

For Test 3, the NH₃ oxidation reaction has a significant impact on the NO_x reduction reactions leading to an increase in NO_x reduction with a decrease in the PM loading as observed in Figure 5.21. For this particular case, the NO_x reduction is dependent on both the inhibition of the PM oxidation reaction and desorption reaction leading to a change in the trends with a change in the ANR value. The decrease in NO_x reduction from 2 g/l to 4g/l is due to a change in local NO₂/NO_x ratio due to a higher PM cake passive oxidation reaction rate.

For Test 6, the case with 0 g/l loading, had higher NO_x reduction compared to cases with PM loading due to lower inhibition by PM in the wall. The 2 g/l case had lower NO_x reduction efficiency due to higher standard SCR reaction rate which competes with the fast SCR reaction leading to lower overall NO_x conversion compared to the 4

g/l loading where the higher fast SCR reaction leads to higher overall NO_x conversion.

For Test 8 with 4 g/l PM loading, the NH_3 plays an important role in determining the overall NO_x conversion efficiency due to the inlet exhaust gas temperature of 440°C . In this case, the inhibition effect on the NH_3 oxidation reaction is dominant at 4 g/l PM loading leading to higher NO_x conversion compared to 2 and 0 g/l PM loading cases where the NO_x conversion efficiencies are comparable.

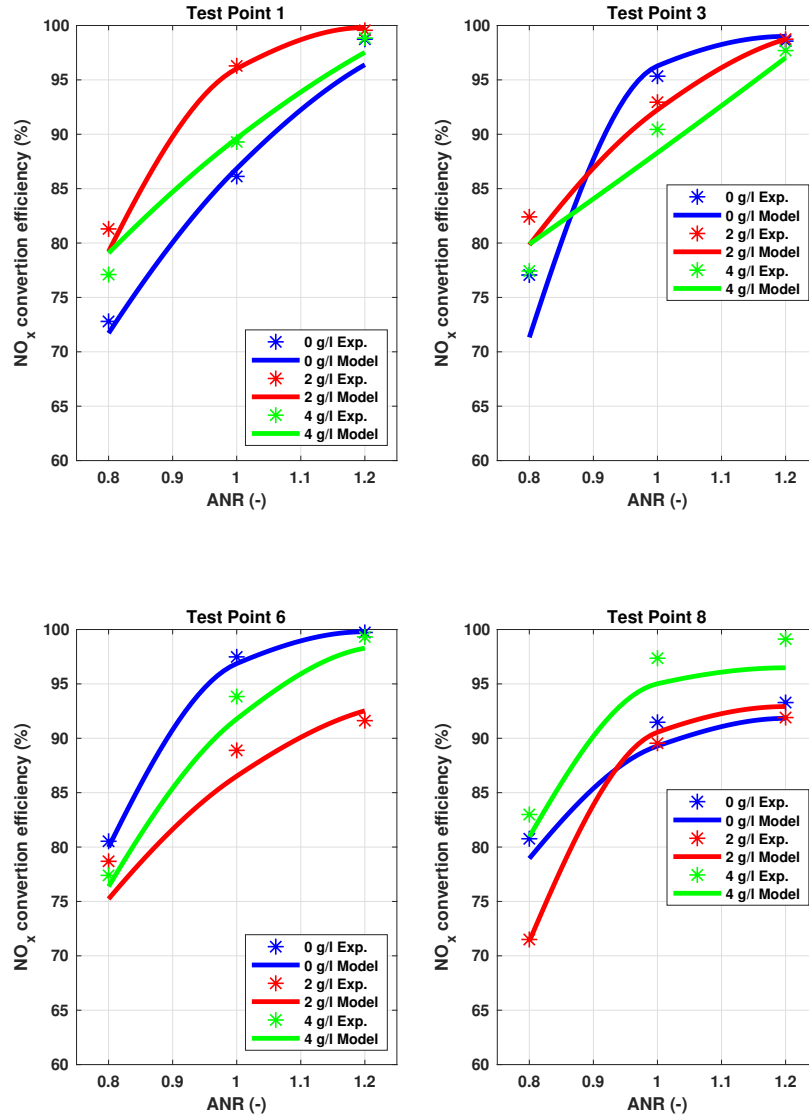


Figure 5.21: NO_x conversion efficiency experimental and model vs ANR for Configuration 2 data with and without urea injection

5.5 Summary of Configuration 2 Results

The twelve experiments in configuration 2 with 0, 2 and 4 g/l PM loading were simulated by the SCR-F model with the common set of SCR kinetics. Important results from this dataset include:

1. The SCR-F® outlet NO, NO₂ and NH₃ concentrations were simulated to within 20 ppm of the experimental value for different ANR, temperature, space velocity and PM loading conditions.
2. The inhibition caused by mass transport limitation in the substrate wall due to PM was simulated for the cases with 2 and 4 g/l PM loading using the effectiveness factor concept.
3. The 2D temperature distribution for different inlet ANR values was simulated to within 5°C for all the experiments using a assumed catalyst loading distribution and energy release by the SCR reactions in order to simulate the experimental temperature distribution.
4. The NO_x reduction for all the twelve experiments was simulated to within 5% of experimental values.

5.6 SCR-F® Configuration 3 Data

The 2D SCR-F model was combined with a 1D SCR model to simulate the experimental data collected as part of the configuration 3 studies. The calibration parameters identified as part of configuration the 1 and 2 for the 2D SCR-F model and the SCR kinetics found using the baseline SCR data for the 1D SCR model were used for this dataset. For all the cases, the combined 2D SCR-F + 1D SCR model shown in Figure 5.22 was able to simulate the outlet NO, NO₂ and NH₃ concentrations to within 20 ppm of the experimental values. The local NO₂/NO_x ratio at the inlet of the SCR-F® and the SCR were found to be important in determining the NO_x conversion performance of the system which was limited to a maximum value of 97.5% for the given system. The NO_x conversion of the system and its individual components along with NH₃ storage and slip characteristics are presented in this section.

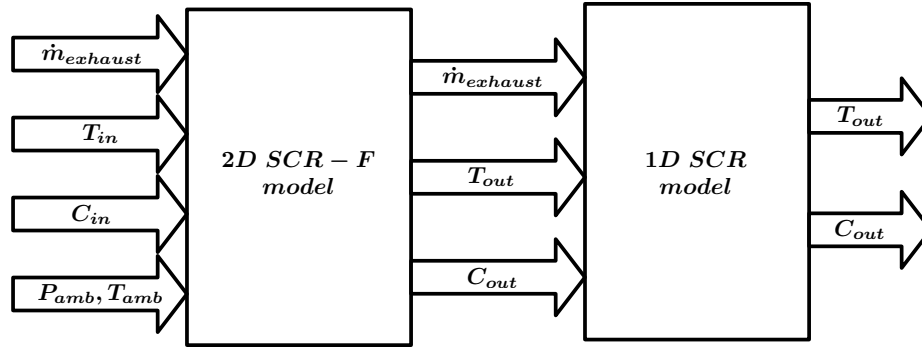


Figure 5.22: 2D SCR-F + 1D SCR model - Configuration 3

5.6.1 SCRF®+SCR system NO_x Reduction Efficiency

The NO_x conversion efficiency of the system was simulated for the six configuration 3 experiments with inlet temperature of 210 - 367°C. The NO_x conversion efficiency is affected by a change in local NO₂/NO_x ratio across the PM cake layer in the SCRF® due to NO₂ assisted PM oxidation reaction and change in NO₂ across the substrate wall due to consumption of NO₂ and NO_x by the SCR reactions. These reactions lead to a near zero NO₂/NO_x ratio at the SCR inlet, limiting the system NO_x conversion performance.

Figure 5.23 compares the model and experimental system NO_x reduction efficiency of the SCRF® and SCR for the six experiments. In all the cases, the model was able to simulate the experimental data to within 1.5%. Due to the near zero inlet NO₂/NO_x ratio at SCR inlet, the SCR NO_x conversion is limited to a maximum of 60% as the pre dominant SCR reaction in the SCR was the standard SCR reaction for the given conditions. In the case of SCRF®, a conversion efficiency of 97% was observed. The combined system efficiency is limited to 97.7% due to the limitation of the SCR reactions in the SCR .

The NO_x conversion efficiency in the SCRF® is a function of inlet NO₂/NO_x ratio and change in NO₂ across the PM cake due to passive oxidation reaction. Table 5.1 shows the change in NO₂/NO_x ratio across the SCRF®. On average, a 26 % decrease in the NO₂/NO_x across the PM cake in the SCRF® due to the passive oxidation rate is observed. The ratio further decreases to zero at the SCRF® outlet due to the fast SCR reaction in the substrate wall.

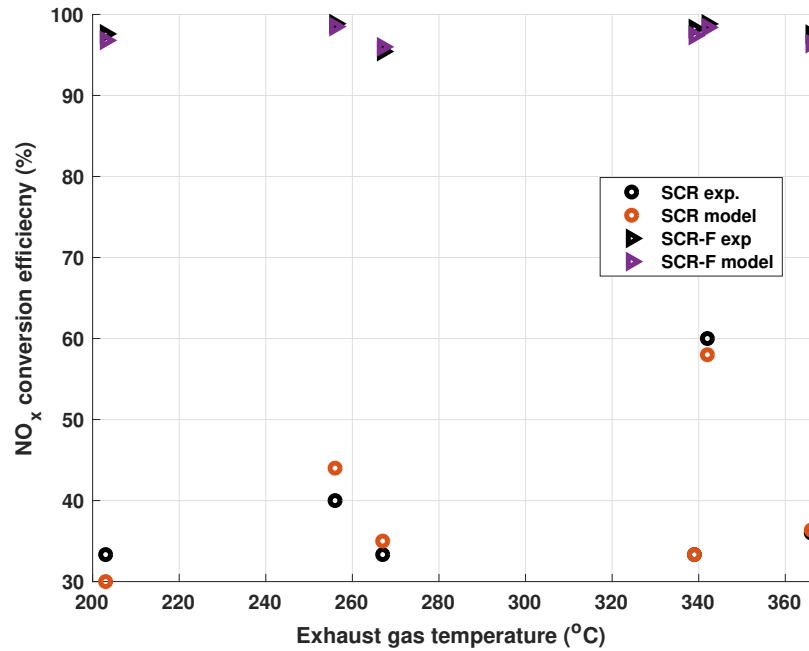


Figure 5.23: SCR-F[®] and SCR NO_x conversion efficiency vs exhaust gas temperature for the SCR-F[®]+SCR

Table 5.1

NO₂/NO_x at SCR-F[®] inlet, SCR-F[®] wall inlet and SCR inlet.

Test	SCR-F [®] inlet NO ₂ /NO _x ratio (-)	SCR-F [®] wall inlet NO ₂ /NO _x ratio (-)	SCR inlet NO ₂ /NO _x ratio (-)
A	0.44	0.31	0
C	0.44	0.29	0
E	0.37	0.25	0
B	0.48	0.39	0
D	0.38	0.22	0
1	0.29	0.28	0

The NO_x conversion across the SCR-F[®] was found to be a strong function of the inlet NO₂/NO_x ratio. Figure 5.24 shows the comparison between NO_x conversion efficiency and inlet NO₂/NO_x ratio for test point C from the configuration 3 dataset.

The NO_x conversion efficiency is shown in the left y-axis and the right y axis shows the inlet NO₂/NO_x ratio. At the test point C engine condition, the PM loading was kept constant at 2 g/l and the temperature at 339°C while the inlet NO₂/NO_x ratio

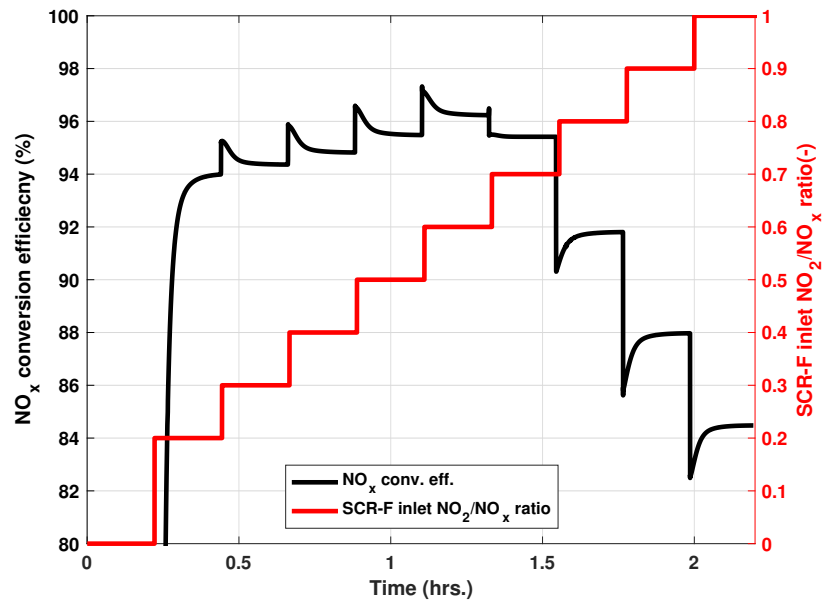


Figure 5.24: Simulated NO₂/NO_x ratio and NO_x conversion efficiency vs time for Test C inlet data for PM loading 2g/l and inlet temperature 339°C.

was changed in increments of 0.1 from 0.2 to 1.0. The NO_x conversion efficiency increase with an increase in inlet NO₂/NO_x ratio from 0 to 0.5 was 94 % to 97.5%. This increase is due to the increase in the contribution of the fast SCR reaction to the overall NO_x reduction due to higher availability of NO₂. For NO₂/NO_x ratios in the range of 0.6 to 1.0, the efficiency decreases from 97.5% to 84%. This decrease in conversion is due to the increased contribution of the slow SCR reaction due to excess NO₂. Since the slow SCR reaction has a lower rate constant than both the fast and standard SCR reactions, this regime is undesirable in SCR-F operation. The change in the NO_x conversion efficiency of the SCR-F® coupled with the SCR performance plays an important role in determining the system performance.

The outlet NO, NO₂ and NH₃ from the SCR-F® were observed to be a function of the inlet NO₂/NO_x ratio and inlet temperature. Figure 5.25 shows the change in these concentrations as the inlet NO₂/NO_x ratio is changed for the test point C in increments of 0.1 from 0.2 to 1.0 using the 2D SCR-F model.

The NH₃ slip decreases with an increase in the NO₂/NO_x ratio from 0.2 to 0.5 and a similar trend is observed for the outlet NO and NO₂. From 0.5 to 1.0 the NH₃ slip and the outlet NO₂ increase while the NO concentration remains near zero. Maximum NO_x conversion is observed at NO₂/NO_x ratio = 0.5. The slow SCR consumes more

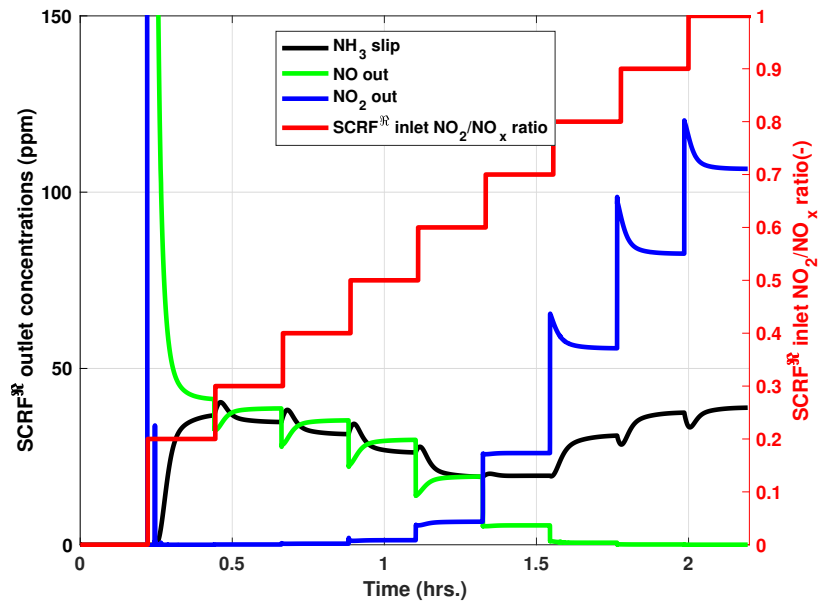


Figure 5.25: SCRFR® NO_2/NO_x ratio vs outlet NO, NO_2 and NH_3 concentrations for Test C at ANR = 1.0

NH_3 per mole of NO_x compared to the standard and fast SCR reactions leading to a lower NH_3 slip per mole of NO_x consumed for ratios >0.5 .

5.6.2 NH_3 Characteristics of SCRFR® and SCR

The NH_3 slip from the SCRFR® and SCR is a function of the storage capacity, inlet NH_3 , inlet NO_2/NO_x ratio, exhaust gas temperature and exhaust flow rate. For all the experiments in the configuration 3 dataset, the NH_3 slip was simulated to within 20 ppm of the experimental value after taking all these factors into account. The set of parameters used to simulate the data were obtained based on the low temperature ($<300^\circ\text{C}$) experiments from the configuration 2 dataset.

Figure 5.26 shows the change in NH_3 slip as a function of the inlet NO_2/NO_x ratio for the test point 5 from reference [5] at ANR = 1.2 where the ratio was changed in increments of 0.1 from 0 to 0.9. There is a decrease in the NH_3 slip with an increase in the ratio from 0 to 0.5 with 80 ppm slip at 0.5 due to maximum utilization of NH_3 for NO_x reduction. The red circle represents experimental data from test point C which was simulated by the model to within 2 ppm in this case. For higher values of

the NO_2/NO_x ratio > 0.5 , the NH_3 slip increases due to lower NO_x conversion.

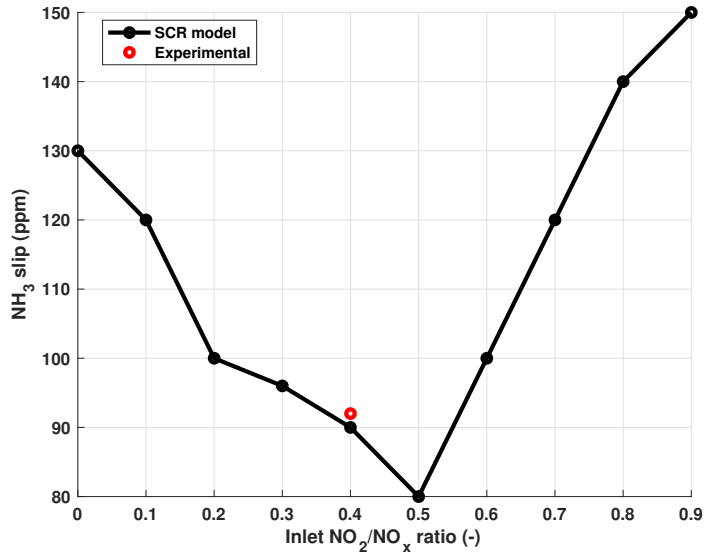


Figure 5.26: NH_3 slip SCR model vs inlet NO_2/NO_x ratio at ANR = 1.2 for test 5

The maximum storage capacity of the NH_3 storage sites is important in determining the NH_3 slip along with the adsorption and desorption reaction rates which are a function of the inlet exhaust gas temperature. Maximum storage capacity of 43 and 42 gmol/m^3 were found for the two storage sites in the SCR. Figure 5.27 shows the change in coverage fraction of these sites for all the seven baseline SCR experiments from reference [5] as a function of inlet exhaust gas temperature.

The coverage fraction of both sites increase with an increase in the inlet ANR with a significant change for ANR > 1.0 . The increase in the first storage site coverage fraction leads to an increase in the NO_x conversion efficiency while the second storage site controls the amount of NH_3 slip. Increased exhaust gas temperature leads to lower NH_3 coverage fraction of both the storage sites due to the higher desorption reaction rate. The increased temperature leads to a faster response time of the SCR to changes in the inlet ANR and this decreases the impact of the second storage site on NH_3 slip characteristics. Similar trends were observed for the SCR $\text{F}^{\text{®}}$.

Figures 5.28 and 5.29 compare the experimental and model NH_3 slip value of the SCR $\text{F}^{\text{®}}$ and SCR for all the seven experiments in configuration 3.

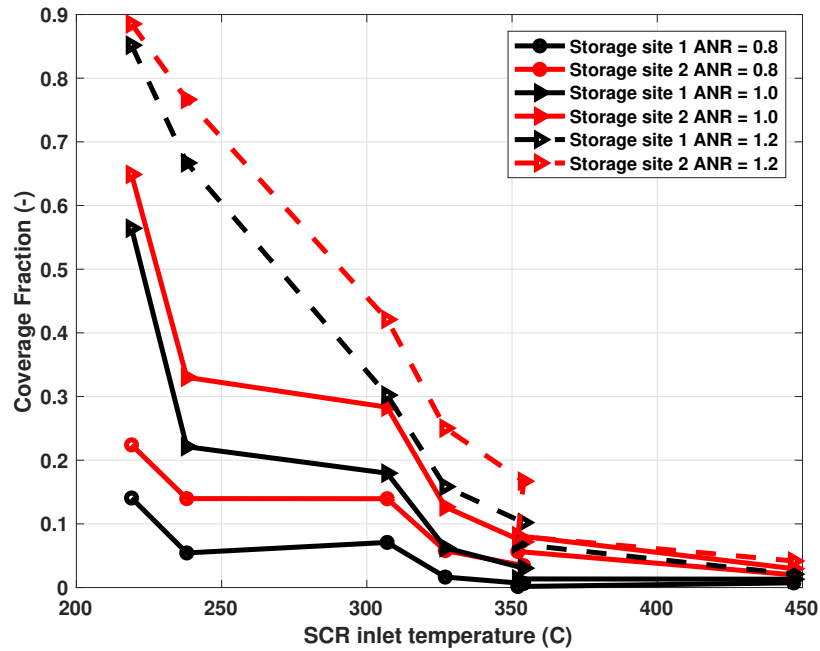


Figure 5.27: Coverage fraction of SCR NH_3 storage sites 1 and 2 vs SCR inlet temperature

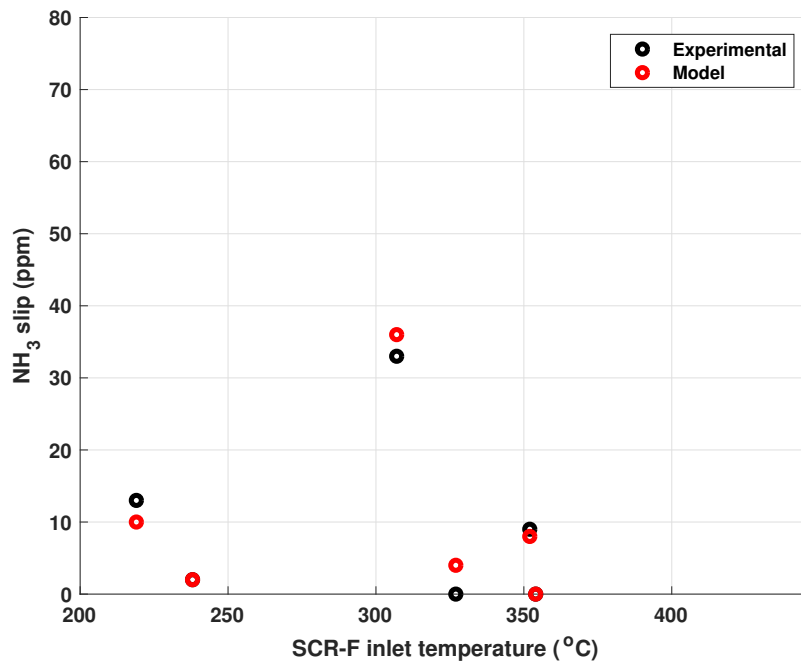


Figure 5.28: NH_3 slip for SCR-F model and experimental data at ANR = 1.0 vs SCR inlet temperature

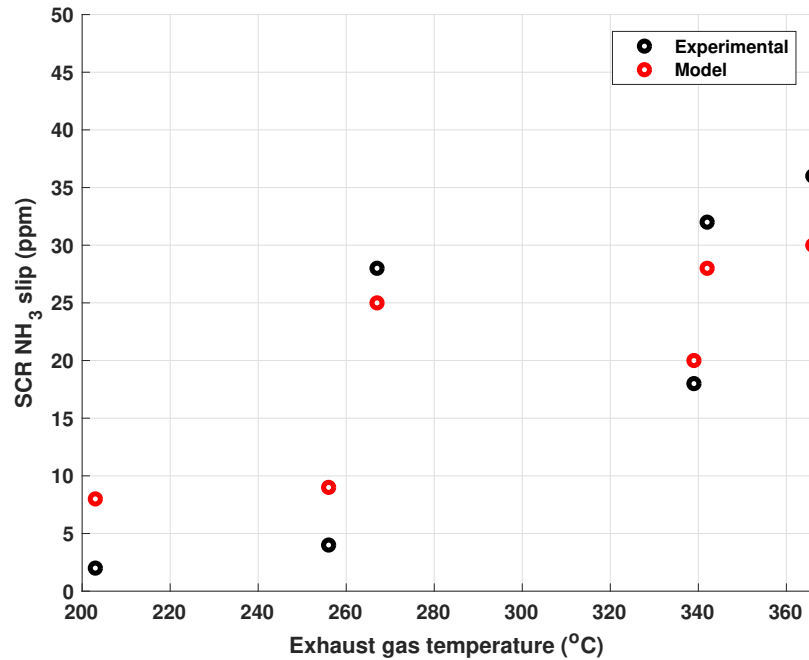


Figure 5.29: NH₃ slip for SCR model and experimental data at ANR = 1.0 vs SCR inlet temperature

Using the common set of SCR kinetics found for the 2D SCR-F and 1D SCR model, the 2D SCR-F + 1D SCR models were able to simulate the experimental data to within 20 ppm for both the components. The NH₃ slip at high temperature ($T > 350^{\circ}\text{C}$) was found to be impacted by the NH₃ oxidation reaction while the transient response during ANR changes is a function of exhaust gas temperature.

5.6.3 Contribution of Individual SCR Reactions in SCRF® and SCR

The percentage contribution of each of the three SCR reactions changes with the inlet NO₂/NO_x ratio due to the change in available NO₂. This change is shown for all the seven experiments from the baseline SCR data [5] in Figure 5.30.

For experiments with inlet NO₂/NO_x ratio < 0.35 (Test 8, 1 and 3), the standard SCR reaction led to 30 - 60% of the NO_x conversion. The fast SCR contributed 40 - 70% with the slow SCR being less than 10% of the total NO_x conversion. For experiments with inlet NO₂/NO_x greater than 0.35 (Test 2, 4, 5 and 6), the fast SCR reaction

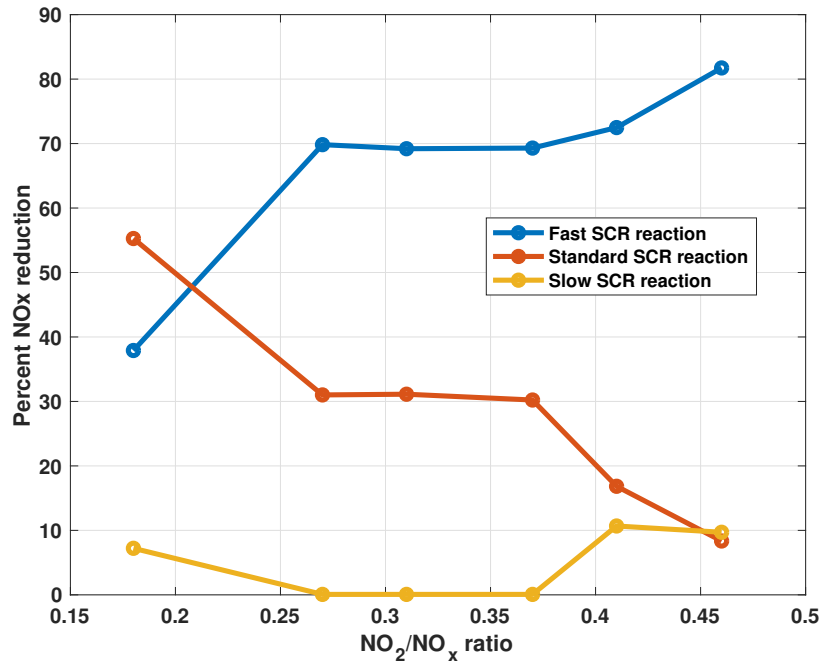


Figure 5.30: Contribution of the three SCR reactions in the NO_x reduction performance of the SCR from the model at ANR = 1.0

was predominant, accounting for 80 % of total NO_x reduction with the standard SCR accounting for 10 - 20% NO_x reduction and the slow SCR reaction around 10 % of total NO_x conversion.

The decrease in standard SCR reaction with inlet NO₂/NO_x ratio is due to higher NO_x consumption by fast SCR reaction when available NO₂ is higher. This shift in reaction pathways is due to the rate constants of the fast and standard SCR reactions which favor higher fast reaction when equal concentration of NO and NO₂ are available in the exhaust gas stream. The slow SCR reaction is <10% for NO₂/NO_x ratios less than 0.35 due to the lower rate constant. Above this value, a higher contribution is observed (>10%) due to excess NO₂ left after consumption by fast SCR reaction.

With a further increase in the NO₂/NO_x ratio, the trends indicate a higher fast SCR reaction till a ratio of 0.5 beyond which the slow SCR starts increasing due to excess NO₂ at the same time the standard SCR decreases to less than 10% total NO_x reduction for these conditions. Figure 5.31 shows these trends for the seven baseline test points. These runs were made on the 1D SCR model with NO₂/NO_x ratio increments of 0.1 from 0 to 0.9 keeping other conditions constant. The trends observed indicate a strong dependency of NO_x reduction performance of the SCR on

the SCR inlet NO_2/NO_x ratio. A NO_2/NO_x ratio of 0.5 was observed to be optimum for all the cases.

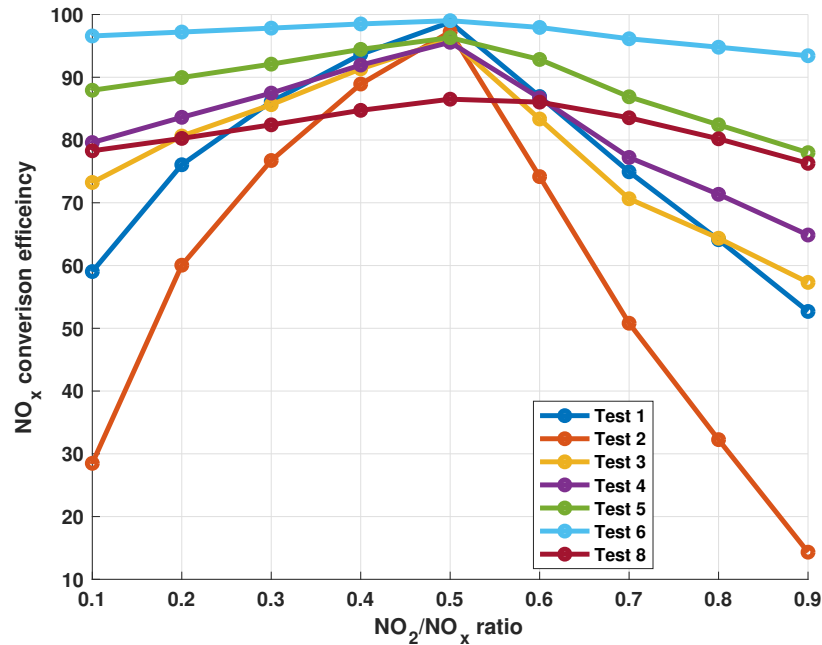


Figure 5.31: NO_x conversion efficiency vs SCR inlet NO_2/NO_x ratio from the model at ANR = 1.0

5.6.4 Impact of local NO_2/NO_x Ratio on System Performance

The change in NO_2/NO_x ratio has a significant impact on NO_x conversion performance of the system as observed in Figure 5.31. Table 5.1 shows the change in NO_2/NO_x ratio as the exhaust gas passes through PM cake, substrate wall in the SCR_F([®]) and the SCR. At the inlet of the SCR_F([®]), the NO_2/NO_x ratio is a function of the DOC NO conversion efficiency which in turn is a function of exhaust gas temperature, and space velocity. An inlet NO_2/NO_x ratio to the SCR_F([®]) of 0.29 to 0.48 was observed for the six engine conditions in the SCR_F([®])+SCR experiment. As the exhaust gas passes through the PM cake, a significant decrease in NO_2 concentration takes place due to the passive oxidation of PM. This leads to a decrease in the NO_2/NO_x ratio at the SCR_F([®]) wall inlet. The change in NO_2/NO_x ratio across the PM cake is variable and dynamic and it depends on the exhaust gas temperature, PM cake thickness and available NO_2 in the PM cake. As a result, the effective local

NO_2/NO_x ratio changes to a range of 0.22 to 0.39 for the six experiments. At the SCR $\text{F}^{\text{®}}$ exit, the NO_2 concentration for all cases was observed to be zero leading to a NO_2/NO_x ratio at the SCR inlet of zero for all cases.

Figure 5.32 shows the contribution of the three SCR reactions to the overall NO_x conversion in the SCR $\text{F}^{\text{®}}$ and SCR. For the SCR $\text{F}^{\text{®}}$, the fast SCR reaction starts at 70 % at a ratio of 0.29 and increases to 82 % for a inlet ratio of 0.48. The standard SCR reaction starts at 30 % but at values greater than 0.38, a significant decrease occurs to less than 20%. The slow SCR reaction is zero at 0 to 0.38 and beyond this value, the slow SCR reaction reaches a value of 10 %.

In the SCR where the NO_2/NO_x ratio is zero for all the cases, the fast and slow SCR reactions shown in black and blue dotted lines remain near zero due to a lack of available NO_2 . The standard SCR reaction contributes to nearly 100 % of all the NO_x conversion efficiency in the SCR for all experiments.

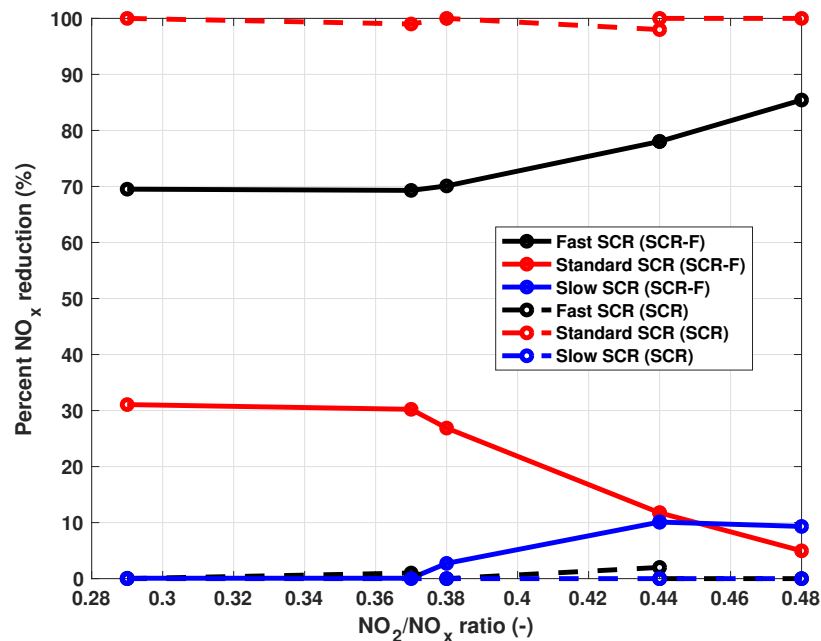


Figure 5.32: NO_2/NO_x ratio vs percent NO_x conversion SCR $\text{F}^{\text{®}}$ and SCR at ANR = 1.0 from the models

Local NO_2/NO_x ratio at the SCR inlet was found to be the important parameter that impacts the system performance in terms of NO_x reduction and NH_3 slip characteristics. The lack of NO_2 at the inlet to the SCR leads to a condition where the fast SCR reaction is near zero leading to low NO_x reduction (< 70 %) and low adsorption

of NH_3 leading to excess NH_3 slip compared to the case with optimal NO_2/NO_x ratio of 0.5 at the SCR inlet. This impact is higher at low temperatures ($<300^\circ\text{C}$) where the standard SCR reaction rate is low. Figure 5.33 and 5.34 show the change in NO_x conversion efficiency of the downstream SCR for all the experiments for NO_2/NO_x ratio = 0 and 0.5 at the SCR inlet using the SCR-F model.

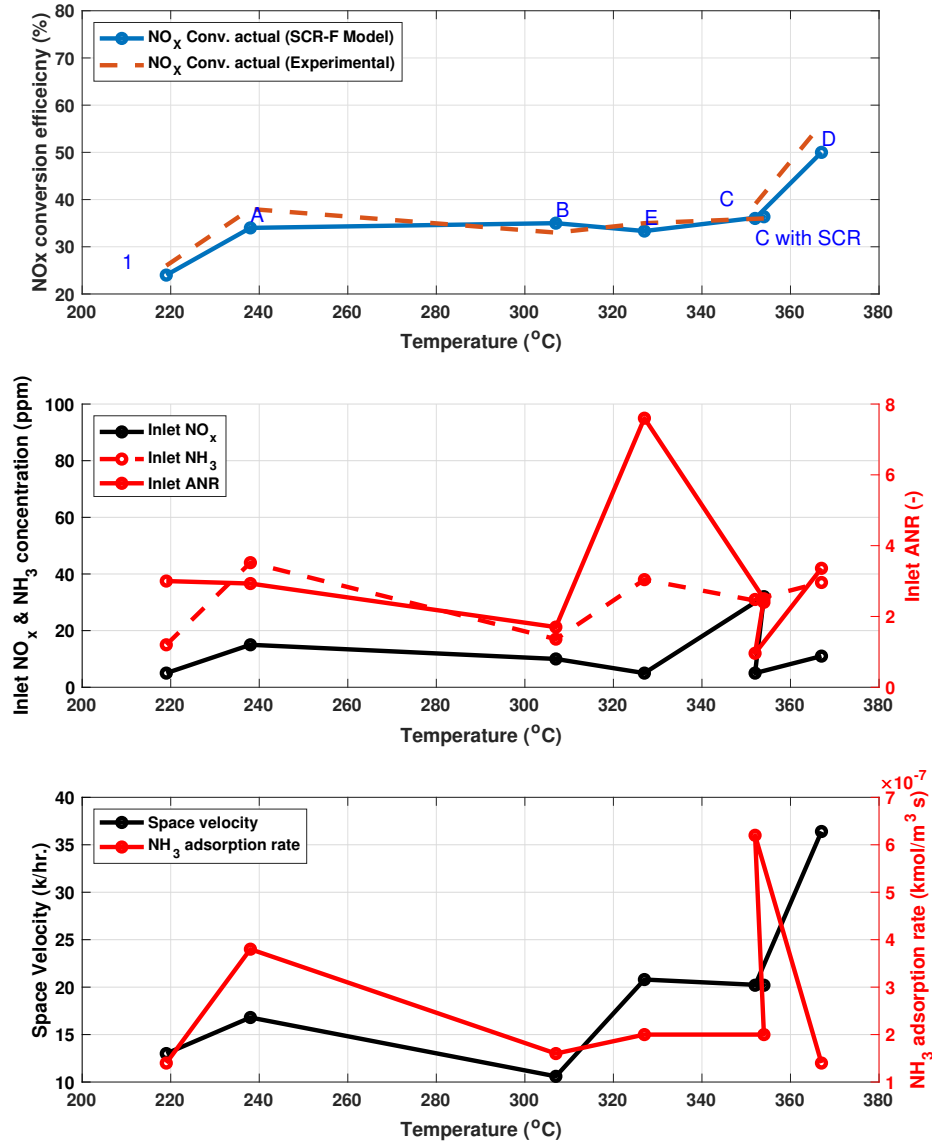


Figure 5.33: SCR NO_x conversion efficiency vs exhaust gas temperature for the SCR-F[®]+SCR system with NO_2/NO_x ratio = 0 (Experimental and 2D SCR-F Model data)

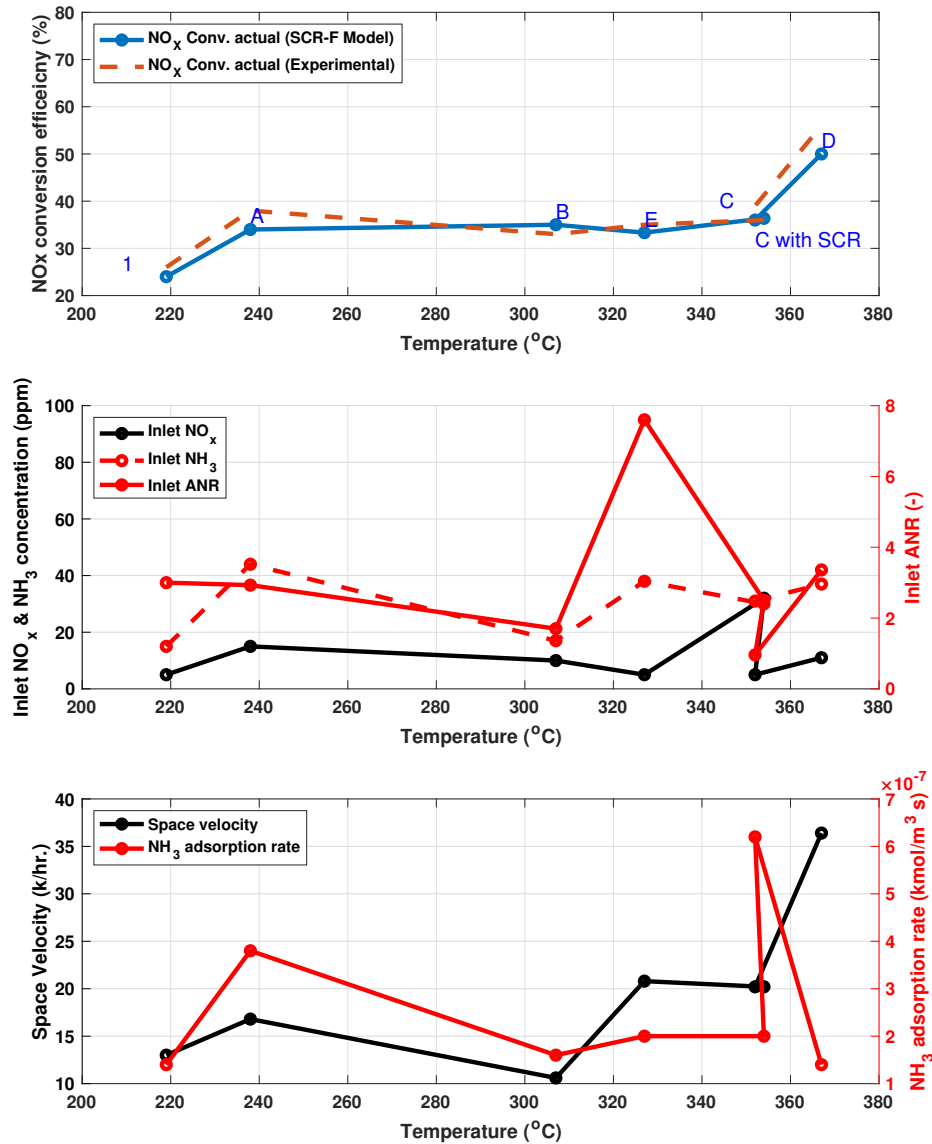


Figure 5.34: SCR NO_x conversion efficiency vs exhaust gas temperature for the SCR-F®+SCR system with NO₂/NO_x ratio = 0.5 (2D SCR-F Model data)

Figure 5.33 compares different variables at the inlet of the SCR and internal variables from the SCR model used to simulate the SCR performance for SCR-F + SCR experiments at NO₂/NO_x = 0. The top plot shows the experimental and model NO_x conversion efficiency which were simulated to within +/- 3 % of experimental data. The second plot shows the inlet NO_x and NH₃ concentration for each experiment on the left y axis in ppm. The right y axis shows the inlet ANR for each experiment which was found to be > 1 for all experiments. The third plot on the left y axis shows the space velocity in k/hr. which was observed to be less than 50 k/hr. for

all experiments. The left axis shows the adsorption rate of NH_3 onto the catalyst surface in $\text{kmol/m}^3\text{s}$. This value was found to be low for $\text{NO}_2/\text{NO}_x = 0$ cases leading to excess NH_3 slip and low NO_x conversion efficiency ($< 50\%$) for most cases.

Figure 5.34 based on the SCR-F model shows the SCR-F model NO_x conversion efficiency for $\text{NO}_2/\text{NO}_x = 0.5$ with SCR-F + SCR experimental inlet conditions in the top plot in Figure 5.33 . The second plot in Figure 5.34 shows inlet NO_x and NH_3 concentrations and inlet ANR similar to Figure 5.33 . The bottom plot has similar space velocity values as Figure 5.33 however the NH_3 adsorption rate for a given experiment was observed to 2-5 time higher compared to $\text{NO}_2/\text{NO}_x = 0$ case due to lower coverage fraction and higher NH_3 consumption by fast SCR reaction leading to $> 90\%$ NO_x conversion in all the cases except for $T > 360^\circ\text{C}$, where the NH_3 oxidation leads to a lower NO_x conversion rate of 87%.

The main reasons for the observed trends in Figures 5.33 and 5.34 are as follows:

1. Low inlet concentration of NH_3 in Figure 5.33 into the SCR led to low adsorption rate caused by mass limitation for the given flow rate conditions. This mass transfer limitation led to $< 50\%$ NO_x conversion for the SCR-F + SCR experiments which is consistent with the experimental data.
2. For $\text{NO}_2/\text{NO}_x = 0.5$, the mass transfer limitation was overcome due to the fast SCR reaction which increased the NH_3 adsorption to a value where the mass transfer limitation was not observed to be a limitation leading to NO_x conversion $> 90\%$ as shown in Figure 5.34.
3. At $T > 350^\circ\text{C}$, the NH_3 oxidation led to a decrease in NO_x conversion for the $\text{NO}_2/\text{NO}_x = 0.5$ case as shown in Figure 5.34.

It can be observed that for the low temperature experiments ($T < 300^\circ\text{C}$) up to a 70 % increase in NO_x conversion efficiency can be achieved with a optimum NO_2/NO_x ratio while for experiments with $T > 350^\circ\text{C}$, a 30 - 50 % increase is expected. This increase in downstream SCR performance leads to a increase in system NO_x conversion performance from 97.7% to 99.5% which is required for a potential system that can achieve the ultra-low NO_x standard. Increasing the NO_x conversion in the SCR by optimum NO_2/NO_x ratio could increase the low temperature performance of the system significantly since the fast SCR reaction rate is higher compared to the standard SCR reaction at temperatures less than 350°C .

5.7 Summary of Configuration 3 Results

The 2D SCR-F+1D SCR model was able to simulate the NO, NO₂ and NH₃ SCR outlet concentrations to within 15 ppm of the experimental data for all the eight experiments used. The major findings from modeling this dataset are:

1. A maximum NO_x conversion efficiency of 97.5 % at an inlet NO₂/NO_x ratio of 0.5 was found for the downstream SCR using the baseline data from reference [5].
2. Significant SCR NH₃ slip (> 30 ppm) for ANR > 1.0 was observed.
3. The change in NO₂/NO_x ratio by 26% across the PM cake played an important role in determining the system NO_x conversion efficiency.
4. The SCRF® outlet NO₂/NO_x ratio was observed to be zero for the given engine conditions which limits the SCR NO_x reduction performance to a maximum value of 60 % and at low temperatures (<300°C) further decrease to less than 50 % has been observed.
5. The combined efficiency of the SCRF®+SCR system was limited to 97.7 %.
6. The system performance can be improved by increasing the NO₂/NO_x ratio at the SCR inlet.
7. NH₃ slip in the SCRF®+SCR system is significant due to the low NO_x conversion rate in the downstream SCR.

The ultra low NO_x system SCRF®+SCR described and modeled in Chapter 7 is a system that can overcome the limitation of the SCRF®+SCR system by adding a second DOC between the SCRF® and SCR and a second urea injector before the SCR. This improved system has the potential to achieve >99.5% NO_x reduction for all engine conditions with a robust control system for the urea injectors.

Chapter 6

SCR-F State Estimator

This chapter describes the development of a discrete time SCR-F model and an Extended Kalman Filter (EKF) SCR-F state estimator. The SCR-F state estimator is combined with an EKF DOC estimator [42] to develop a system estimation strategy. The SCR-F estimator model is based on the 2D SCR-F model in terms of inputs, states and outputs. It was discretized using Euler integration for the energy and chemical species conservation equations. The states estimated in the SCR-F estimator are:

1. Temperature distribution of the substrate wall and the exhaust gas in both the inlet and outlet channels.
2. Spatial distribution of PM mass retained in the PM cake
3. Spatial distribution of the NH_3 stored in sites 1 and 2.

As the state estimator is expected to execute much faster than a typical controller update period hence the mesh size was reduced to 5x5 instead of the 10x10 mesh used in the analysis of the previous chapters. The governing equations of the species and energy conservation in both the inlet and outlet channels were simplified using a quasi steady state solution to further speedup the model. The model reduction strategy resulted in model with an execution time that is 16 times faster than real time.

6.1 SCR-F Estimator Model

The SCR-F estimator model was developed based on the 2D SCR-F model to reduce the computational cost when using the fixed time step solver. This SCR-F estimator model shown in Figure 6.1 uses a mesh consisting of 5 radial and 5 axial zones with 4 slabs in the substrate wall, instead of the 10x10 mesh with 4 slabs that was used in the 2D SCR-F model described in the previous chapters. The species model was modified based on the assumption that the species conservation equation solution was quasi steady state with an iterative solution at every time step. This converts the concentration states into output quantities. Both of these changes led to a model that is 16 times faster than real time with a fixed time step of 1 second and a maximum deviation of 3% from the 2D SCR-F model for all the engine conditions.

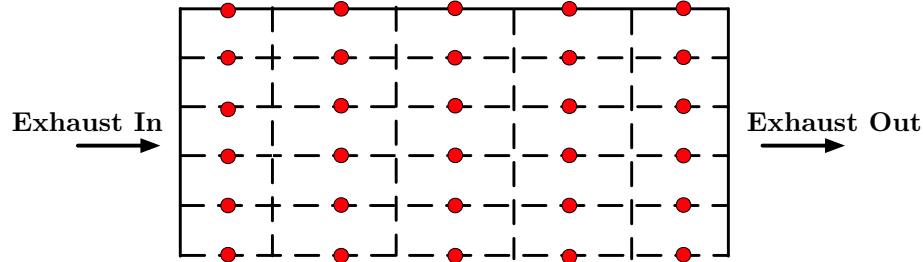


Figure 6.1: SCR-F estimator model 5X5 mesh

6.1.1 SCR-F Estimator Model Governing Equations

The steady state species conservation equation for the PM cake and substrate wall domains, given by Equation 6.1 [37], was used for the SCR-F estimator model.

$$av_w \frac{dC_i}{dx} - \frac{d}{dx} \left(D_i a \frac{dC_i}{dx} \right) = \sum_j \xi_{i,j} R_j \quad (6.1)$$

Equation 6.1 was solved iteratively for each zone for the PM cake and 4 slabs in the substrate wall to compute the change in chemical species concentrations. The change in the solution procedure to steady state enabled a reduction in the number of states in the model.

The exhaust gas temperature equations for the inlet and outlet channels were modified into a steady state form thus ignoring the transient terms which have a negligible impact (<3%) on the overall temperature distribution. The resultant system of energy conservation equations is shown in Equations 6.2 to 6.4

$$\rho_g c_p (a - \bar{t}_s l)^2 v_1 T_1|_{i,j} - \rho_g c_p (a - \bar{t}_s l)^2 v_1 T_1|_{i,j-1} = \dot{Q}_1|_{i,j} - \rho_g c_p 4a \Delta L v_w T_1|_{i,j} \quad (6.2)$$

$$(\rho_c C_c V_c + \rho_f C_f V_f) \frac{dT}{dt} = \rho_g C_p a \Delta L v_w (T_1 - T_f) + \dot{Q}_{cond,axial} + \dot{Q}_{cond,radial} + \dot{Q}_{cond,conv} + \dot{Q}_{amb} + \dot{Q}_{reac,SCR} + \dot{Q}_{reac,HC} + \dot{Q}_{reac,PM} \quad (6.3)$$

$$\rho_g c_p a^2 v_2 T_2|_{i,j} - \rho_g c_p a^2 v_2 T_2|_{i,j-1} = \dot{Q}_2|_{i,j} - \rho_g c_p 4a \Delta L v_w T_f|_{i,j} \quad (6.4)$$

This reduction in the number of states increased the model performance. The simplification of the channel energy conservation equations to steady state reduced the stiffness of the system enabling a fixed time step solver with a 1 second time step. The detailed description of the terms in these equations is given in Chapter 3 section 3.3.4.

6.1.2 SCR-F Estimator Model Results

The results from the SCR-F estimator model were compared against the output from the 2D SCR-F model to determine the effect on model accuracy caused by the simplification of the species conservation equation, energy conservation equations and the coarser mesh that was used for the temperature and species models. Figures 6.2 to 6.11 compare the SCR-F estimator model output from the configuration 1 with urea injection experimental data and output with the 2D SCR-F model. All the results shown are from the Test PO-C test condition at inlet temperature $T = 347^\circ\text{C}$ and inlet $\text{NO} = 387$ ppm, $\text{NO}_2 = 301$ ppm with an inlet ANR = 0.98 during passive oxidation.

The SCR-F estimator model development was validated against the 2D SCR-F model output for all the seven configuration 1 experiments with urea injection. In all the cases, the SCR-F estimator model output variables were within 3% of the 2D SCR-F model.

Figure 6.2 compares the total pressure drop of the 2D SCR-F model (dotted blue line), SCR-F estimator model (blue line) against the experimental pressure drop data (dashed red line) for Test C in configuration 1 data. The components of the total pressure drop - cake (yellow line), wall (violet line) and channel (green line) from the SCR-F estimator model are also shown in the plot.

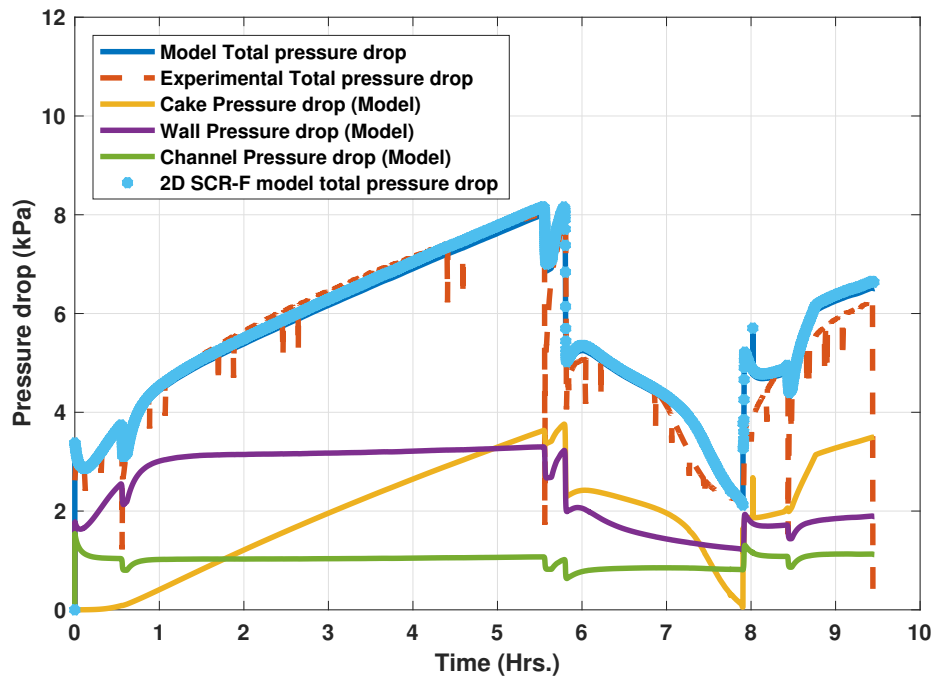


Figure 6.2: SCR-F estimator model pressure drop vs time PO - C with urea injection

For the entire duration of the experiment, the SCR-F estimator model simulated pressure drop within 0.01 kPa of the 2D SCR-F model and within 0.3 kPa of the experimental data. For time $t = 0$ to 5.5 hrs., the pressure drop increases due to an increase in the PM mass retained in the SCR-F®. At time $t = 5.5$ to 8 hrs., due to PM oxidation, the pressure drop decreases. Also, the change in the slope of the pressure drop curve at 7 hrs is due to the cake permeability change which is simulated by the SCR-F estimator model. In the post loading stages at time $t = 8$ to 9.4 hrs., the pressure drop increases due to the accumulation of PM in the cake and the wall. The change in pressure drop slope due to cake permeability and wall PM oxidation

are simulated by the SCR-F model for the post loading stages.

The filtration characteristics of the SCR-F® from the 2D SCR-F model and the SCR-F estimator model are shown in Figure 6.3.

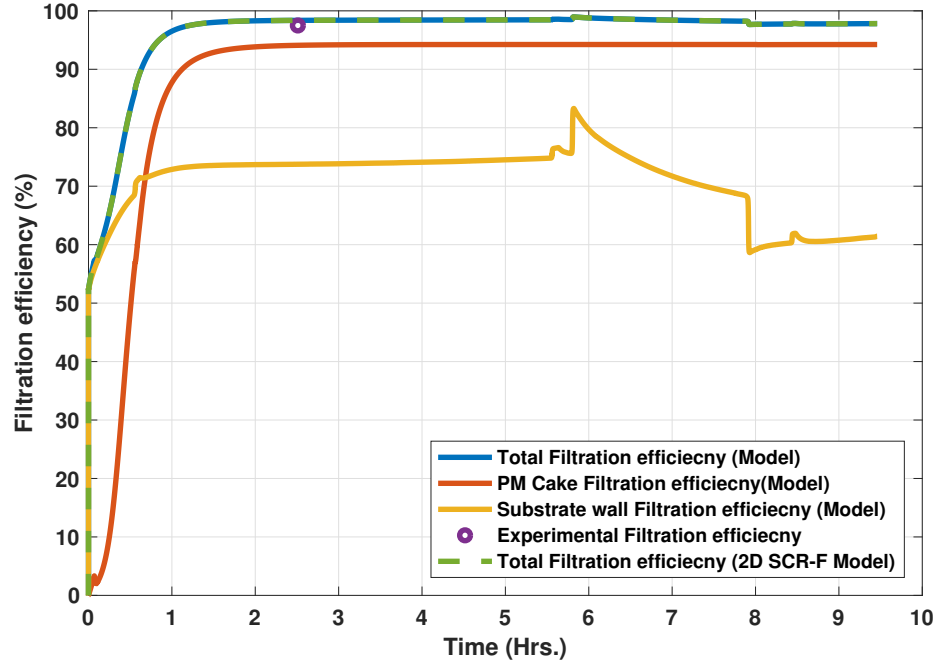


Figure 6.3: SCR-F estimator model filtration efficiency vs time PO - C with urea injection

The SCR-F estimator model was able to simulate the 2D SCR-F model filtration efficiency to within 0.01 % for the entire duration of the experiment. The experimental filtration efficiency value at stage 2 (violet circle) was simulated to within 0.1 %. The change in wall filtration efficiency due to PM oxidation and transition from deep bed to cake filtration were simulated by the SCR-F estimator model at time $t = 8$ hrs and $t = 0.5$ hrs respectively.

Figure 6.4 compares the experimental and SCR-F estimator model PM mass retained. The SCR-F estimator model (blue line) was able to simulate the PM mass retained to within ± 2 g of experimental data (red circle) and within 0.1 gm of 2D SCR-F model (dotted green line). Figure 6.5 compares the SCR-F estimator model outlet exhaust gas temperature (blue line) with the 2D SCR-F model (dotted yellow line) and experimental temperature (red line). For the entire run, the SCR-F estimator model was able to simulate exhaust temperature to within ± 2 °C of the experimental data including the PO stage where a 5 °C rise in exhaust gas temperature due to SCR

reactions was simulated.

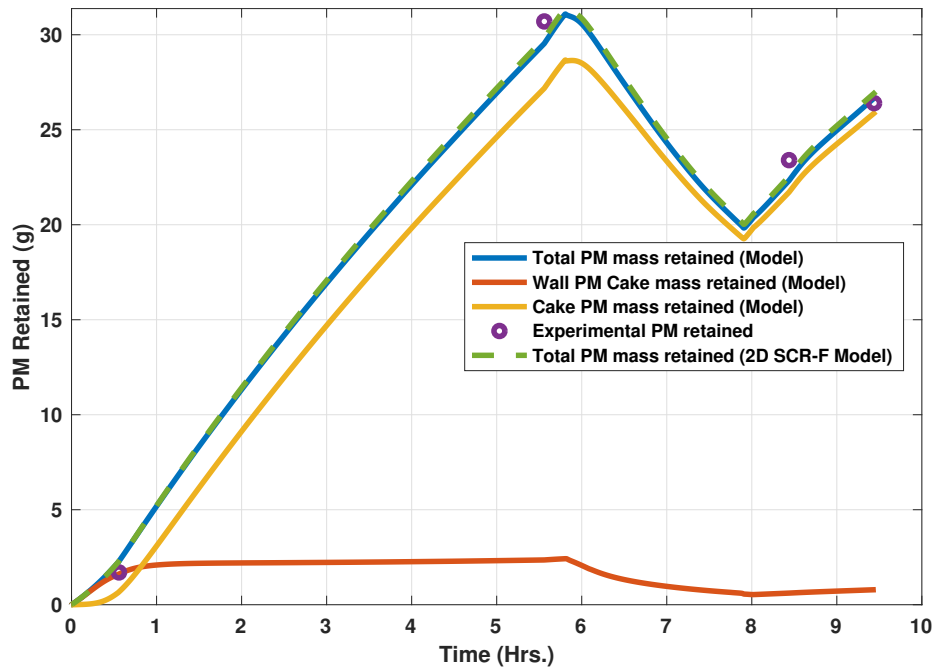


Figure 6.4: SCR-F estimator model PM mass retained vs time PO - C with urea injection

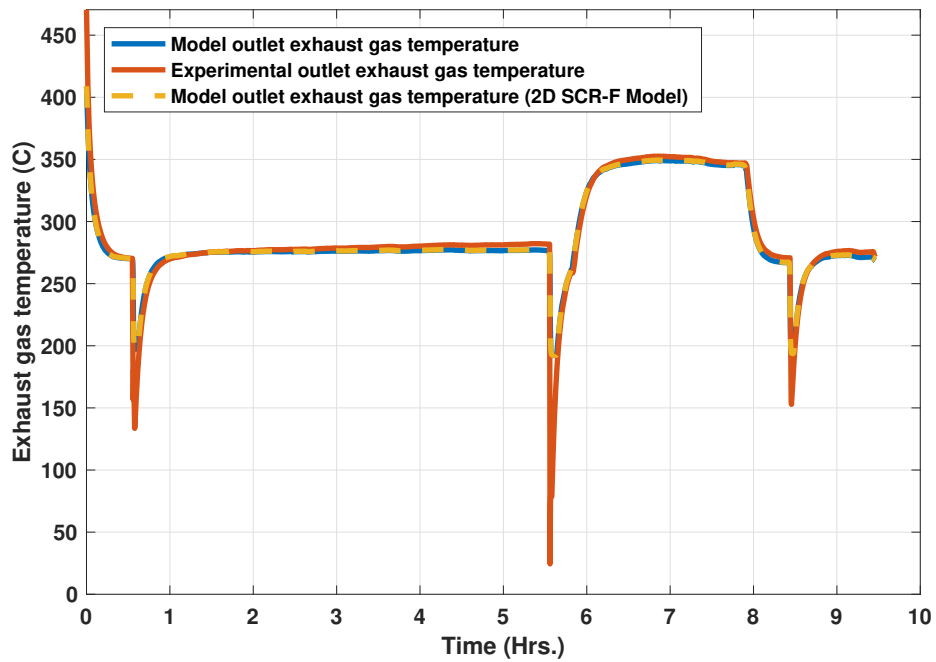


Figure 6.5: SCR-F estimator model outlet temperature vs time PO - C with urea injection

Figures 6.6, 6.7 and 6.8 compare the experimental (red circles) and SCR-F estimator model (blue Line), 2D SCR-F model (yellow dashed line) outlet NO, NO₂ and NH₃ concentrations. In all the cases the SCR-F estimator model was able to simulate the outlet concentrations to within 20 ppm of the experimental data and within 1 ppm of the 2D SCR-F model.

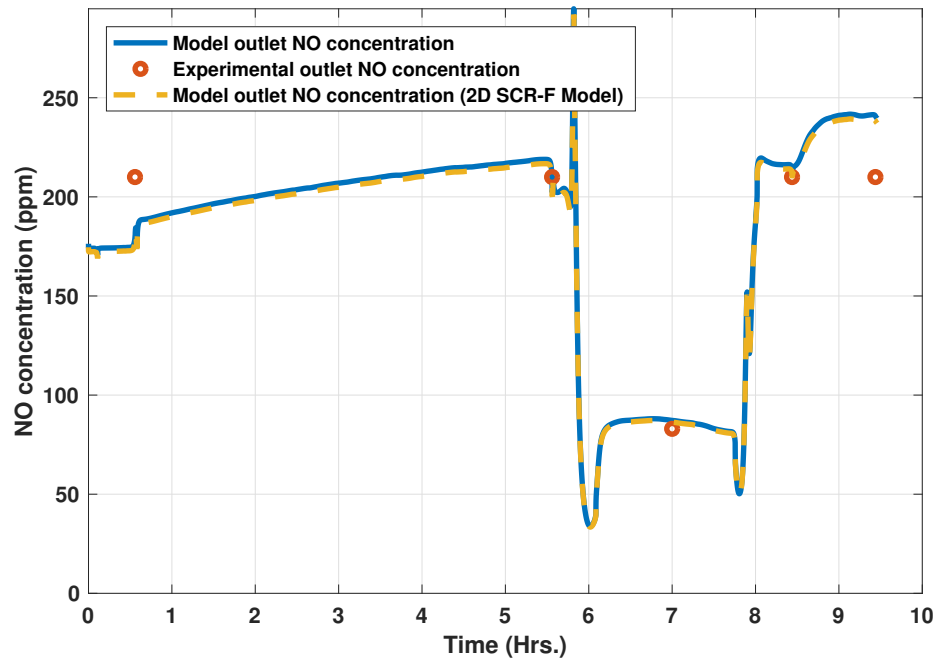


Figure 6.6: SCR-F estimator model outlet NO concentration vs time PO - C with urea injection

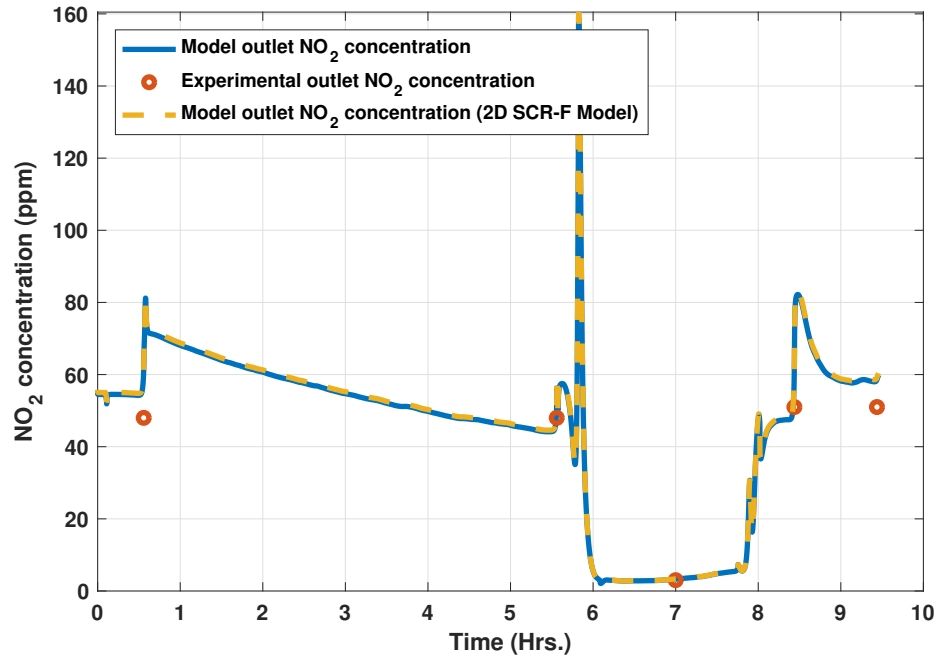


Figure 6.7: SCR-F estimator model outlet NO₂ concentration vs time PO - C with urea injection

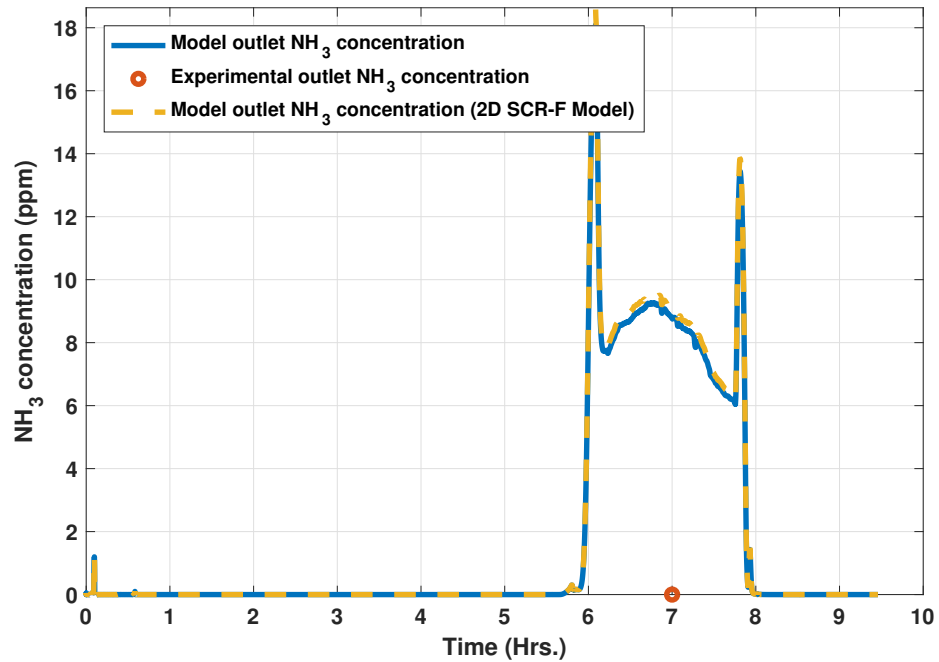


Figure 6.8: SCR-F estimator model outlet NH₃ concentration vs time PO - C with urea injection

The 2D temperature and PM mass distribution from the experimental data and SCR-F estimator model are shown in Figures 6.9, 6.10 and 6.11. The SCR-F estimator model was able to simulate the 2D temperature distribution to within 5°C of experimental data.

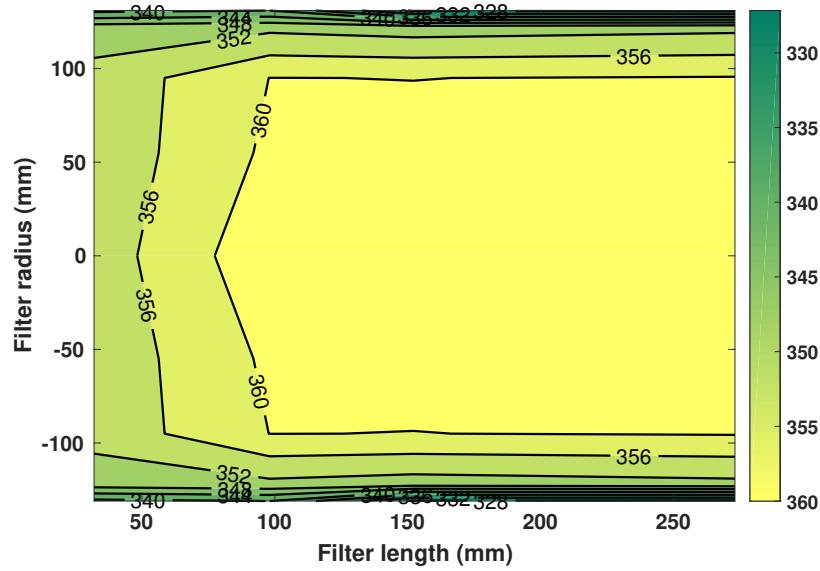


Figure 6.9: Experimental 2D temperature distribution - PO - C with urea injection

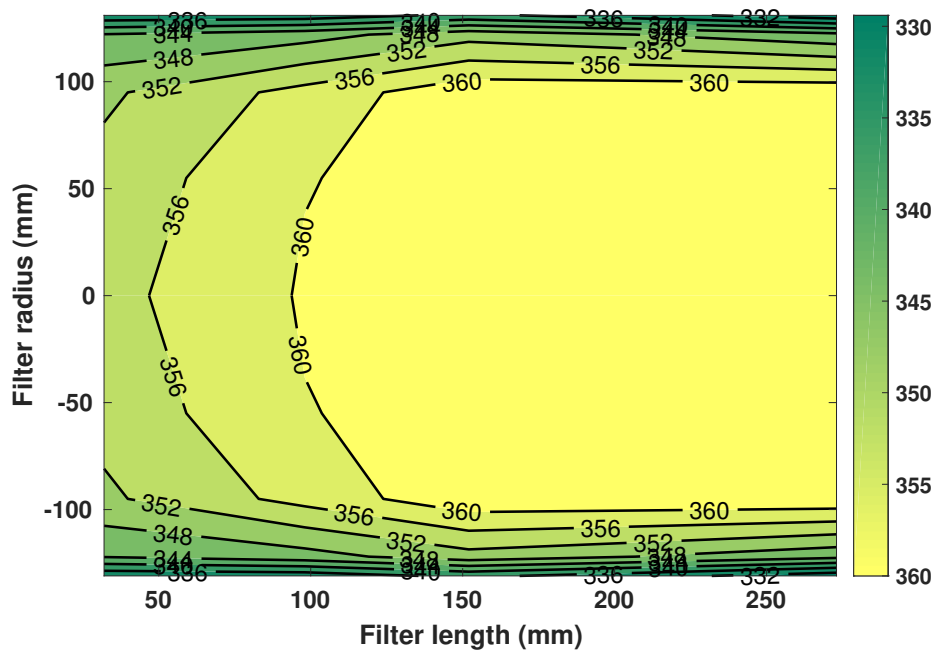


Figure 6.10: SCR-F estimator model 2D temperature distribution PO - C with urea injection

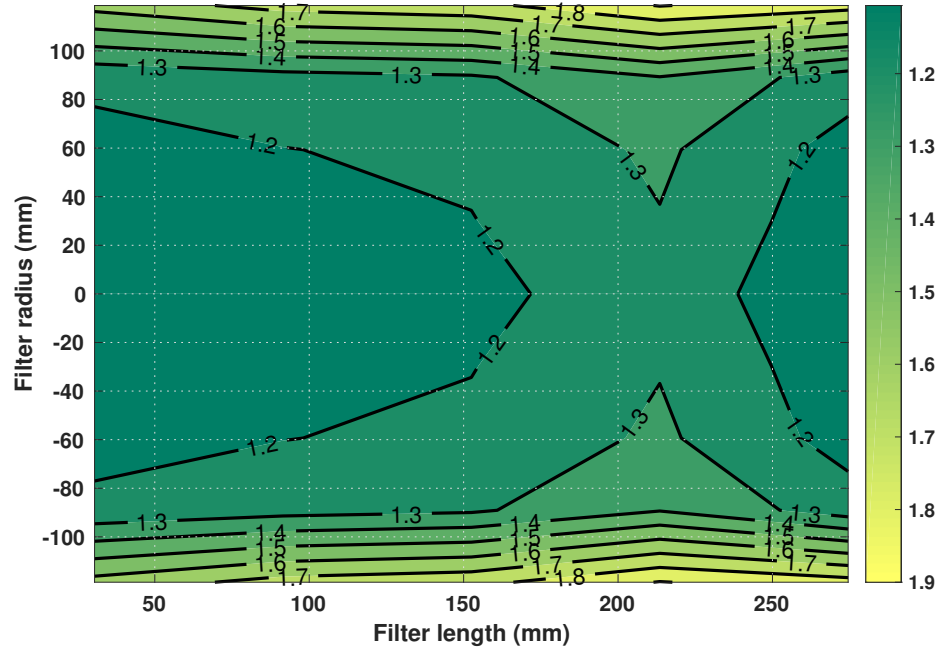


Figure 6.11: SCR-F estimator model 2D PM mass distribution PO - C with urea injection

6.2 SCR-F State Estimator

The SCR-F state estimator was developed using the SCR-F estimator model described above with the following execution steps:

1. Create the SCR-F estimator model where the species states are computed algebraically such that the model can be solved using a fixed time step integration scheme.
2. Develop the state estimator equations: Jacobian equations for temperature, NH_3 coverage fraction and PM mass retained states.
3. Validate the estimator using 2D SCR-F model data [49].

The discretized form of the temperature, chemical species and PM mass retained equations used in the SCR-F state estimator are given by equations 6.5 to 6.9 as described in references [53], [44], [54]

$$[T_{i,j}]_k = [T_{i,j}]_{k-1} + \frac{\dot{Q}_{cond,axial,i,j} + \dot{Q}_{cond,radial,i,j} + \dot{Q}_{conv,i,j}}{(\rho_s c_s V s_{i,j} + \rho_f c_f V f_{i,j})} \Delta t + \frac{\dot{Q}_{react,PM,i,j} + \dot{Q}_{react,HC,i,j} + \dot{Q}_{react,SCR,i,j}}{(\rho_s c_s V s_{i,j} + \rho_f c_f V f_{i,j})} \Delta t \quad (6.5)$$

$$C_{i,r} = C_{i,r-1} - \frac{\Delta x}{\epsilon u} RR_i \quad (6.6)$$

$$\theta_{j,k} = \theta_{j,k-1} + \sum_{k=1}^n \epsilon_{k,j} RR_{k,j} \Delta t \quad (6.7)$$

$$\Delta P_{est.cake} = \Delta P_{Total} - \Delta P_{channelSCR-Fmodel} - \Delta P_{wallSCR-Fmodel} \quad (6.8)$$

$$m_{cake,i,j} = \frac{\Delta P_{est,cake} k_s}{\mu_w \nu_w \Delta L a \rho_p} \quad (6.9)$$

Equation 6.9 is used to determine the PM mass retained in the PM cake for a given zone based on cake pressure drop component computed from the pressure drop sensor data in Equation 6.8, density of PM (ρ_p) and cake permeability (k_s). Detailed description of these terms is given in Chapter 3.

The list of estimated states are shown in the Equation 6.10. Where $T_{1,k}$ represents the temperature states in the substrate wall. $\theta_{1,1,k}$ and $\theta_{2,1,k}$ are the storage fractions

of site 1 and 2. $m_{1,k}$ is the PM mass retained state in the PM cake.

$$x_k = \begin{pmatrix} T_{1,k} \\ \cdot \\ \cdot \\ T_{25,k} \\ \theta_{1,1,k} \\ \cdot \\ \cdot \\ \theta_{1,25,k} \\ \theta_{2,1,k} \\ \cdot \\ \cdot \\ \theta_{2,25,k} \\ m_{1,k} \\ \cdot \\ \cdot \\ m_{25,k} \end{pmatrix} \quad (6.10)$$

The steps involved in implementing the Extended Kalman Filter (EKF) algorithm are described in Equations 6.11 to 6.12 based on reference [55] .

$$x_k = f_{k-1}(x_{k-1}, u_{k-1}, w_{k-1}) \quad (6.11)$$

$$y_k = h_k(x_k, v_k) \quad (6.12)$$

The function f_{k-1} is used to compute the various internal states such as temperature distribution of substrate wall, exhaust gas in the inlet and outlet channel, PM mass retained in the PM cake and substrate wall, NH_3 coverage fraction in both the storage sites for all the zones. w_k and v_k represent the process and observation noises in the system. The process noise was assumed to be zero and the measurement noise was assumed to be zero mean and Gaussian with covariance 0.1 based on reference [54].

Steps 1 to 5 with Equations 6.13 to 6.21 are followed for every time step to obtain

the optimal Kalman gain matrix and state estimates. Kalman update steps :
Step 1 - Compute the partials for F_k and L_k matrices :

$$F_k = \frac{\partial f_{k-1}}{\partial x} \Big|_{x_{k-1}, u_{k-1}} \quad (6.13)$$

$$L_k = \frac{\partial f_{k-1}}{\partial x} \partial w \Big|_{x_{k-1}, u_{k-1}} \quad (6.14)$$

Step 2 - Predict the state and error variance :

$$x_k^- = f_{k-1}(x_{k-1}^+, u_{k-1}, 0) \quad (6.15)$$

$$P_k^- = F_{k-1} P_{k-1}^+ F_{k-1}^T + L_{k-1} Q_{k-1} L_{k-1}^T \quad (6.16)$$

Step 3 - Compute the H_k and M_k matrices :

$$H_K = \frac{\partial h_k}{\partial x} \Big|_{x^-} \quad (6.17)$$

$$M_K = \frac{\partial h_k}{\partial v} \Big|_{x^-} \quad (6.18)$$

Step 4 - Optimal Kalman gain calculation :

$$K_k = P_k^- H_k^T (H_k P_k^- H_k^T + M_k R_k^- M_k^T)^{-1} \quad (6.19)$$

Step 5 - Compute state estimate and covariance :

$$x_k^- = x_k^- + K_k (Y_k - h_k(\bar{x}_k, 0)) \quad (6.20)$$

$$P_k^+ = (I - K_k H_k) P_k^- (I - K_k H_k)^T + K_k R_k K_k^T \quad (6.21)$$

The experimental data from the SCRF® pressure drop, SCRF® outlet temperature and NO_x sensors was added to the estimator along with the EKF that was described above. The states calculated using the above equations are then used to calculate the outlet quantities such as outlet exhaust gas temperature, NO, NO₂ and NH₃ concentrations, filtration efficiency, PM mass retained and pressure drop across the SCRF®. Equations 6.22 to 6.24 are used for these calculations.

6.2.1 Outlet value calculations

Outlet temperature

The exhaust gas outlet temperature is a function of inlet temperature T_{in} and the internal substrate wall temperatures $T_{i,j}$ which are computed based on energy conservation equations in the inlet, outlet channels and substrate wall. Equation 6.22 shows the function g used to compute the outlet temperature.

$$T_{out} = g_1(T_{i,j}, T_{in}) \quad (6.22)$$

NO_x and NH_3 outlet concentrations

The outlet $NO_{x,out}$ concentration is a function of the coverage fraction of the two NH_3 storage sites $\theta_{1,i,j}$ and $\theta_{2,i,j}$ states and substrate wall temperature states $T_{i,j}$. The inlet concentration of NO , NO_2 and NH_3 and inlet exhaust gas temperature are also used to compute the outlet concentrations using function g shown in Equation 6.23

$$NO_{x,out} = g_2([\theta_{1,i,j}, \theta_{2,i,j}, T_{i,j}], [C_{NO,in}, C_{NO_2,in}, C_{NH_3,in}, T_{in}]) \quad (6.23)$$

SCR-F pressure drop

The pressure drop across the SCR-F ΔP is a function of the PM mass retained states in the wall and PM cake and substrate temperature states $M_{i,j}, T_{i,j}$. The inlet quantities of NO , NO_2 and NH_3 concentrations and exhaust gas temperature are also used in function g of Equation 6.24 to compute the pressure drop.

$$\Delta P = g_3([M_{i,j}, T_{i,j}], [C_{NO,in}, C_{NO_2,in}, C_{NH_3,in}, T_{in}]) \quad (6.24)$$

6.2.2 Jacobian calculations

The Jacobians used for calculating the Kalman gain matrix for the temperature, NH₃ coverage fraction and PM mass retained states are listed below in equations 6.25 to 6.27.

Temperature - Equation 6.25 is used to compute the partial of the substrate temperature states with respect to substrate temperature T and coverage fraction of the two NH₃ storage sites θ_1 and θ_2 . These jacobians are used to compute the kalman gain for the substrate temperature state which is used with the SCR-F outlet thermocouple measurement to estimate the substrate temperature.

$$\frac{\partial T}{\partial T}, \frac{\partial T}{\partial \theta_1}, \frac{\partial T}{\partial \theta_2} \quad (6.25)$$

NH₃ coverage fraction - The NH₃ coverage fraction sites 1 and 2 θ_1 and θ_2 are computed based on NO_x sensor reading and Kalman gain computed using jacobians in Equation 6.26 where the relationship between temperature, and coverage fraction of the two NH₃ storage sites is used.

$$\frac{\partial \theta_1}{\partial \theta_1}, \frac{\partial \theta_1}{\partial \theta_2}, \frac{\partial \theta_1}{\partial T}, \frac{\partial \theta_2}{\partial \theta_1}, \frac{\partial \theta_2}{\partial \theta_2}, \frac{\partial \theta_2}{\partial T} \quad (6.26)$$

PM mass retained - The PM mass retained states in the PM cake M are computed based on pressure drop sensor measurements and kalman gain computed based on jacobians in Equations 6.27. The pressure drop is a function of temperature and PM mass retained leading to the two components in the equation.

$$\frac{\partial P}{\partial T}, \frac{\partial P}{\partial m} \quad (6.27)$$

6.2.3 State Estimator Results

Figures 6.12 to 6.21 show the results from the SCR-F state estimator. The results focus on three aspects of the estimator performance based on the three sensors used

to correct the internal states being predicted.

1. Temperature distribution states estimated using the SCR-F® outlet exhaust gas thermocouple
2. PM mass retained states estimated using pressure drop sensor
3. NH₃ coverage fraction states for storage sites 1 and 2 were estimated using outlet NO_x sensor

The comparison of each variable consists of output from four cases - 1) experimental data collected on the SCR-F® with the Cummins 2013 ISB engine, 2) output from the 2D SCR-F model, 3) Open loop SCR-F estimator case where the estimator model output is used with the Kalman gain = 0 thus removing feedback from the sensors, 4) Closed loop SCR-F estimator with feedback from sensors.

For each of the estimated variable such as exhaust gas temperature, PM mass retained in the cake and outlet NO, NH₃ concentrations, one of the underlying parameter has been changed in the state estimator to introduce errors in the plant model estimates. These errors can be observed from the open loop state estimator output due to the lack of outlet sensor feedback. In the closed loop estimator case due to feedback from the outlet sensor data the outputs are in agreement with experimental data due to accurate internal state prediction.

6.2.4 Temperatures States

Figure 6.12 compares the experimental SCR-F® outlet exhaust gas temperature for Test 6 with 2 g/l loading against the 2D SCR-F model and SCR-F state estimator output.

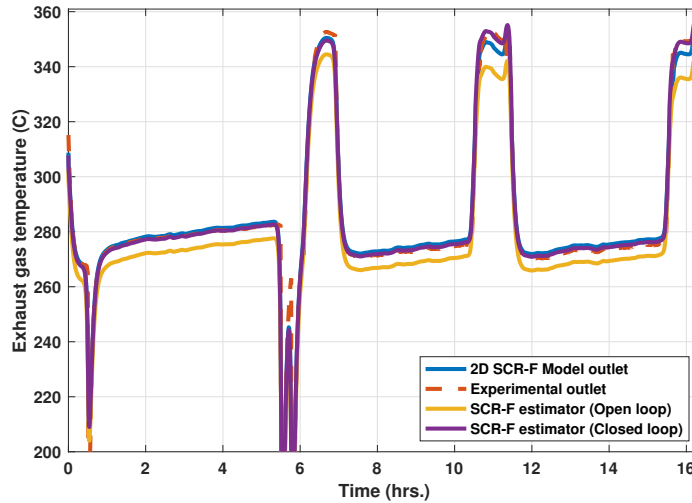


Figure 6.12: SCR-F State estimator outlet temperature vs time (estimator off and on case) Test 6 with 2g/l PM loading

The 2D SCR-F model (blue Line) output is within 3°C of the experimental data (red dotted line) for the entire duration. For the open loop SCR-F estimator (yellow Line) the ambient heat transfer coefficient was increased by 5 % to simulate an error in the system leading to a 15°C decrease in temperature. In the closed loop estimator (violet line) due to feedback from the SCR-F outlet thermocouple data the output was observed to be within 2°C of the experimental data for the entire duration of the experiment.

The feedback applied from the thermocouple is higher for the cases with urea injection where the temperature rise due to the chemical reactions further increases the uncertainty in temperature state estimation caused by the wrong value of ambient heat loss. Apart from compensating for the heat transfer coefficient increase by 5%, the estimator is also compensating for the zero mean Gaussian noise that was added to the outlet thermocouple data.

Figures 6.13 to 6.16 compare the 2D experimental temperature distribution with the temperature distributions from the 2D SCR-F model and the SCR-F state estimator open and closed loop cases described in the Figure 6.12. The role of ambient heat transfer and the sensor feedback from output thermocouple for the estimation of the unknown internal temperature states in the SCR-F[®] can be clearly observed in these plots. These temperature distributions play an important role in determining the final PM mass and NH_3 coverage fraction distributions.

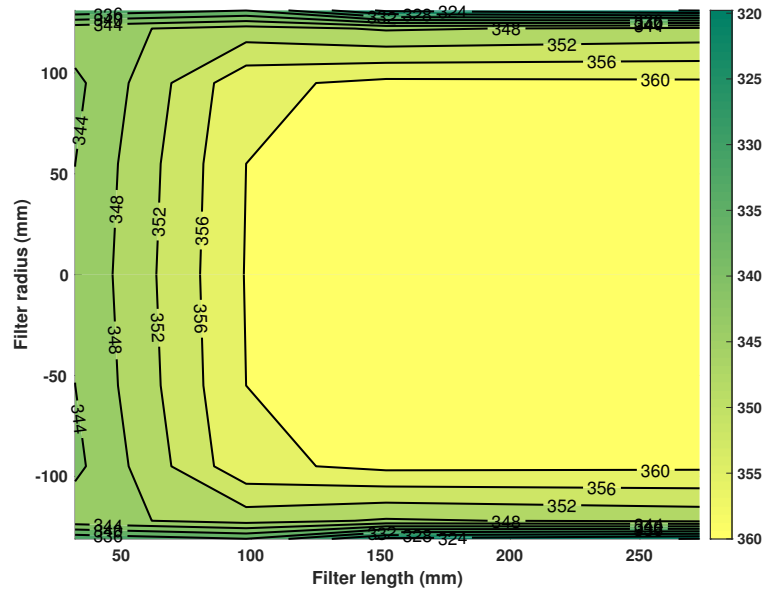


Figure 6.13: SCR-F® experimental temperature distribution 5 minutes after start of Passive oxidation in Test 6 with 2g/l PM loading

Figure 6.13 shows the experimental temperature distribution from Test 6 with 2g/l PM loading. A temperature rise of 16°C from 344 to 360 °C is observed. This temperature rise is primarily due to the energy release by the three SCR reactions. A decrease in the exhaust gas temperature is observed at radial location above 100 mm due to the heat loss to the ambient and radial conduction through the substrate material.

Figure 6.14 shows the 2D SCR-F model temperature distribution from Test 6 with 2g/l PM loading. The model was able to simulate the experimental temperature distribution to within 5° using energy release from the SCR reactions, heat loss to ambient and conductivity of the filter. The catalyst loading in the filter was changed to simulate the temperature rise at axial location between 50 to 100 mm.

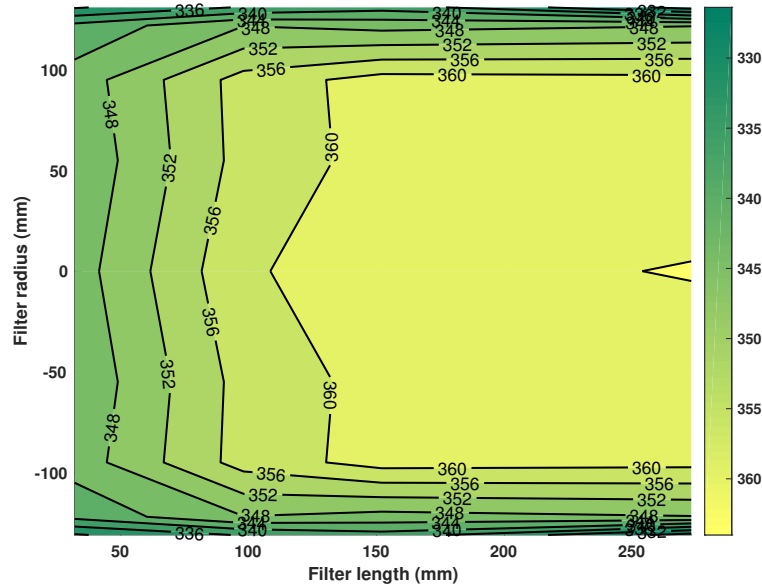


Figure 6.14: 2D SCR-F model temperature distribution 5 minutes after start of Passive oxidation in Test 6 with 2g/l PM loading

Figures 6.15 and 6.16 compare the SCR-F state estimator temperature distribution for the estimator open and closed loop cases. In both the cases, the axial rise in temperature of 16°C was simulated with energy release by SCR reactions. For the open loop estimator due to the 5 % higher ambient heat transfer coefficient, the radial temperature drop at radius greater than 100 is higher 30°C compared to 20°C in the closed loop estimator. This higher heat transfer coefficient leads to a change in the shape of the temperature distribution and deviation with respect to experimental data is 10°C . For the Figure 6.16 the thermocouple data feedback reduces the state estimation error to within 5°C of experimental data.

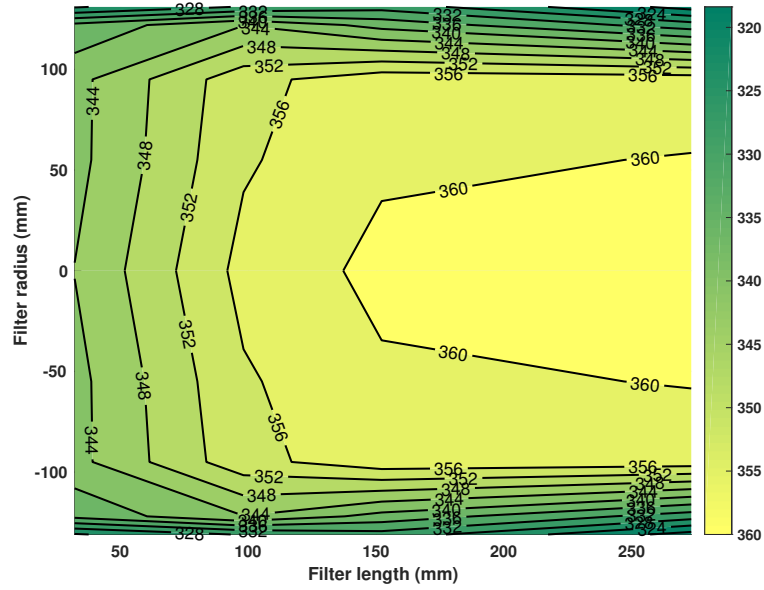


Figure 6.15: SCR-F state estimator temperature distribution 5 minutes after start of Passive oxidation in Test 6 with 2g/l PM loading with open loop estimator

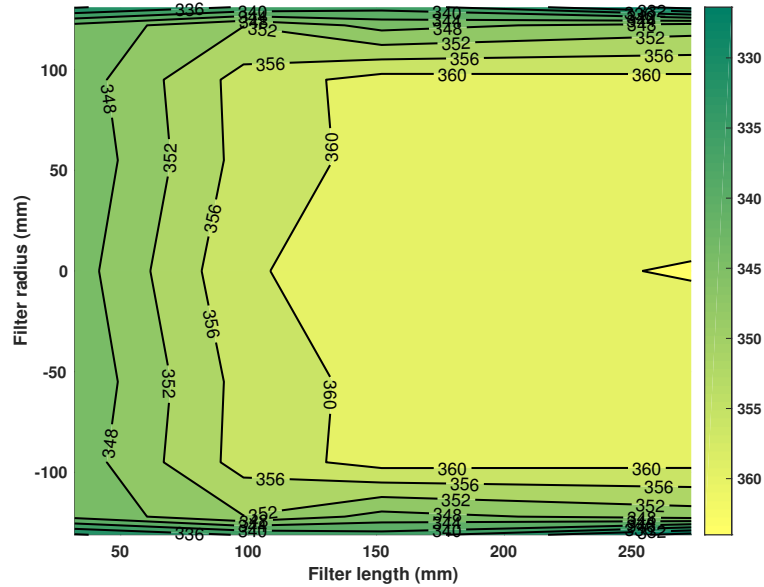


Figure 6.16: SCR-F state estimator temperature distribution 5 minutes after start of Passive oxidation in Test 6 with 2g/l PM loading with closed loop estimator

6.2.5 PM Mass Retained States and Pressure Drop

Figures 6.17 and 6.18 show the PM mass retained and pressure drop from the SCR-F state estimator. A comparison of the experimental data with 2D SCR-F model and state estimator was carried out. For the state estimator, the pre exponential of the PM cake passive oxidation reaction was reduced by 5% resulting in a reduced PM oxidation rate, higher PM mass retained and pressure drop for the open loop estimator. For the closed loop estimator due to feedback from the pressure drop sensor with Kalman gain an accurate estimation of PM mass retained states was achieved.

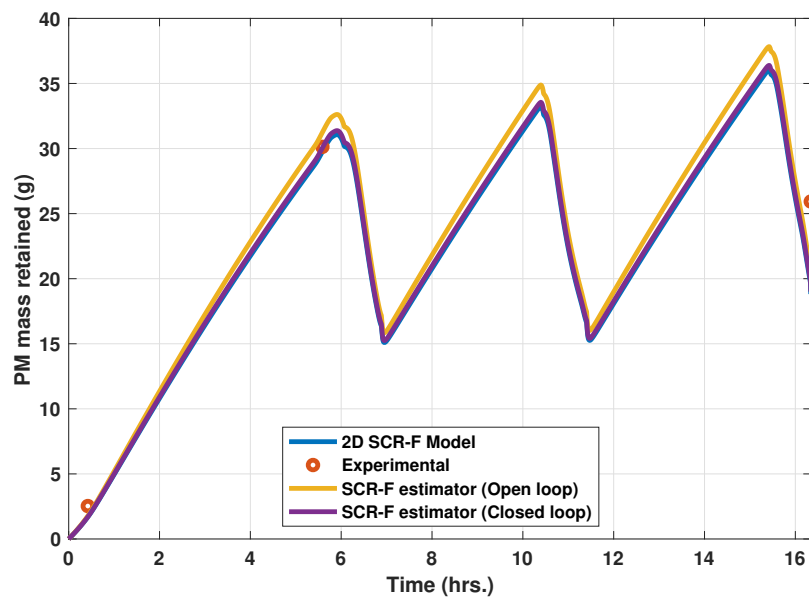


Figure 6.17: SCR-F PM mass retained vs time (Experimental, 2D SCR-F model, SCR-F state estimator) Test 6 with 2g/l PM loading

In Figure 6.17, the 2D SCR-F model (blue line) was able to simulate the PM mass retained to within 2g of the experimental value (red circle) for the entire duration of the experiment. The open loop estimator (yellow line) had a higher value compared to the model due to the lower PM oxidation rate leading to a deviation of +2.5 g compared to the experimental data. For the closed loop estimator with the feedback from the pressure drop sensor, the estimated PM mass retained (violet line) was within 1.5 gm of the experimental data. The pressure drop sensor feedback is applied to the PM mass retained states based on the cake pressure drop component computed from the experimental pressure drop sensor data and estimator model wall, channel

pressure drop components.

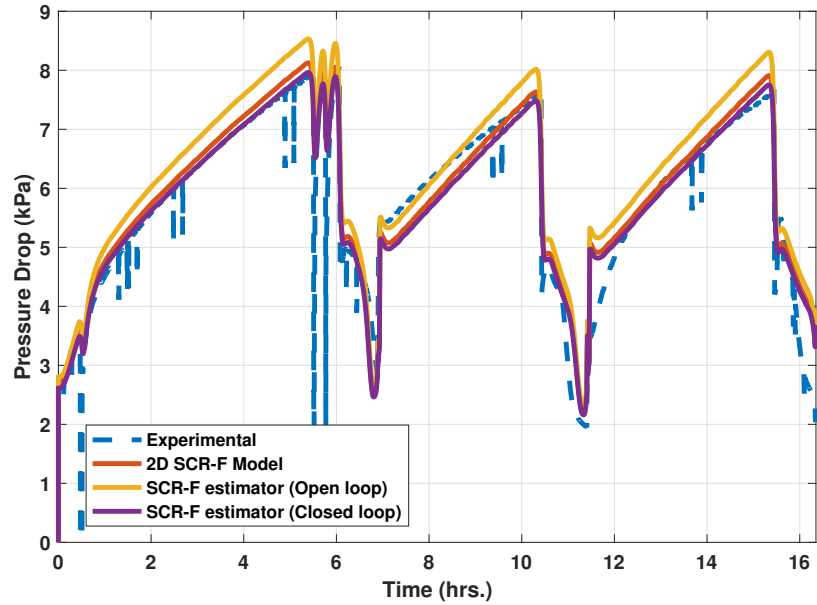


Figure 6.18: SCR-F pressure drop vs time (Experimental, 2D SCR-F model, SCR-F state estimator) Test 6 with 2g/1 PM loading

In Figure 6.18, the 2D SCR-F model pressure drop (red line) is within 0.3 kPa of experimental data (blue dotted). Due to error in PM mass retained in the PM cake, the estimator pressure drop for the open loop estimator (yellow line) is significantly higher (+ 0.5 kPa). In the closed loop estimator with feedback from the pressure drop sensor due to the reduced error in PM mass retained, the estimator pressure drop (violet line) is within 0.2 kPa of the experimental data.

Figure 6.19 shows the resultant state estimator PM mass distribution which is a function of the temperature distribution, NH_3 coverage fraction distribution and feedback from the pressure drop sensor.

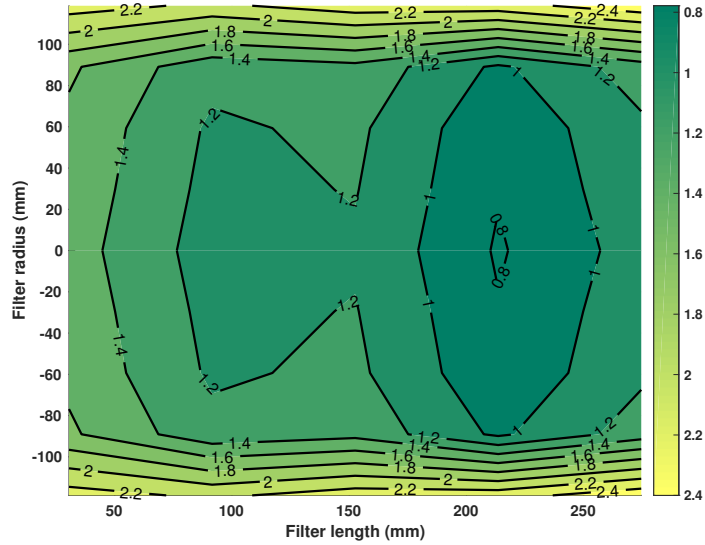


Figure 6.19: SCR-F state estimator 2D PM mass distribution Test 6 with 2g/l PM loading

6.2.6 NH₃ Coverage Fraction States (θ_1, θ_2) and Outlet NO, NO₂, NH₃ Concentrations

Figures 6.22 to 6.21 compare the experimental, 2D SCR-F model and state estimator outlet NO, NO₂, NH₃ and NH₃ coverage fraction of sites 1 and 2 for Test 6 with 2 g/l PM loading. The outlet concentrations are a function of the coverage fraction of the two storage sites with the first site being responsible for outlet NO_x concentration and second site determining the NH₃ slip from the SCR-F®. The 2D SCR-F model (red line) was able to simulate the outlet concentrations to within 20 ppm of the experimental data (dotted blue line) for all the cases. The pre exponents of the first and second storage site adsorption rates were reduced by 5 % leading to a decrease in both the coverage fraction and increase in NH₃ slip and NO, NO₂ concentrations in the open loop estimator (yellow line). For the closed loop estimator with outlet NO_x sensor feedback (violet line) for NH₃ coverage fraction of site 1 (θ_1) and site 2 (θ_2), the resultant outlet concentrations were within 5 ppm of experimental data. The Gaussian zero mean noise added to the sensor was also filtered.

Figures 6.20 and 6.21 show the internal states of the NH₃ coverage fraction for both the NH₃ storage sites. In both the cases, for the open loop estimator due to reduced adsorption rate, the coverage fraction (red line) reduced significantly compared to the 2D SCR-F model (blue line). For the closed loop estimator using the feedback

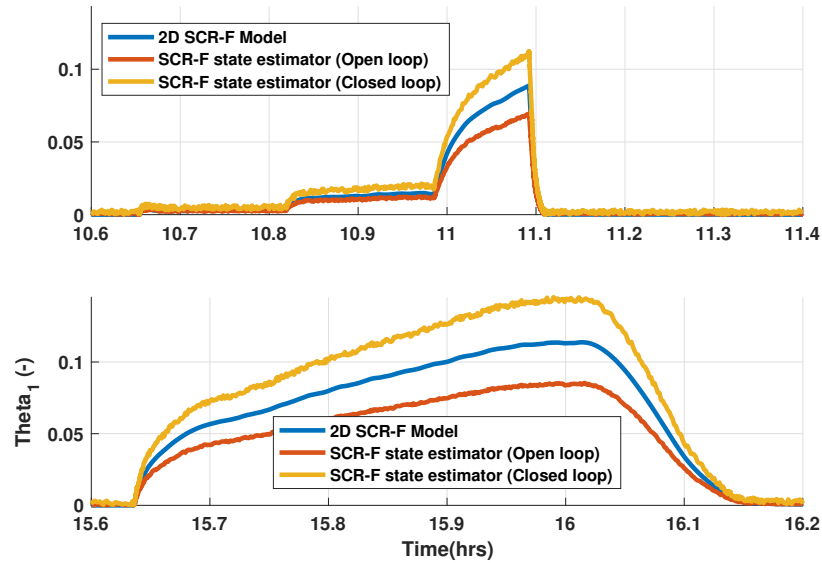


Figure 6.20: SCR-F NH₃ coverage fraction site 1 vs time (Experimental, 2D SCR-F model, SCR-F state estimator) Test 6 with 2g/1 PM loading

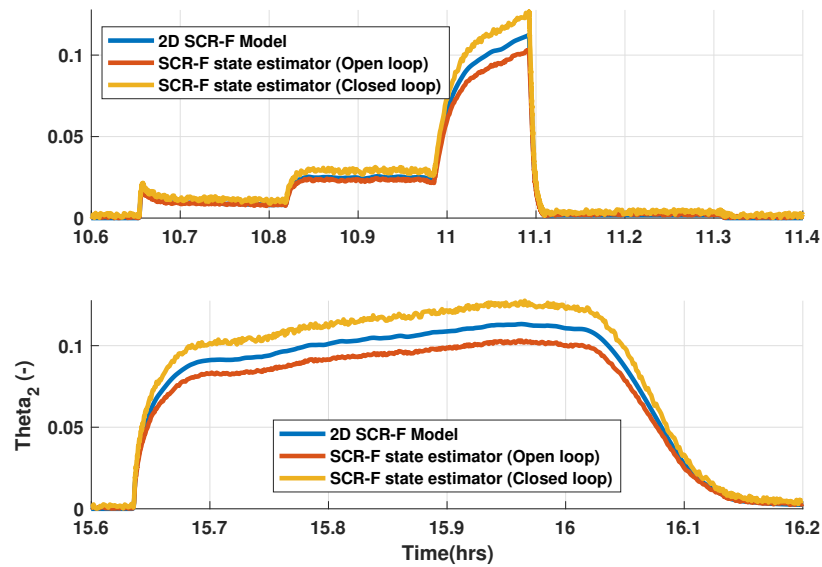


Figure 6.21: SCR-F NH₃ coverage fraction site 2 vs time (Experimental, 2D SCR-F model, SCR-F state estimator) Test 6 with 2g/1 PM loading

from the NO_x sensor (yellow line), the coverage fraction values increased. These new values represent a more accurate estimate of these internal states compared to the 2D SCR-F model based on the outlet NO_x sensor data. This accurate prediction of these internal states led to the improved prediction of outlet NO, NO₂ and NH₃ concentrations compared to the 2D SCR-F model (10 ppm vs 20 ppm) as observed in Figure 6.22, 6.23 and 6.24.

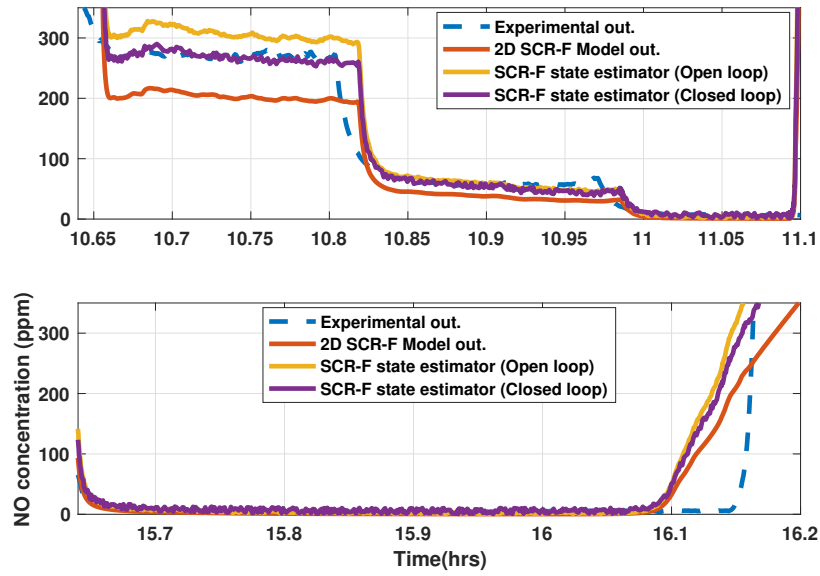


Figure 6.22: SCR-F outlet NO vs time (Experimental, 2D SCR-F model, SCR-F state estimator) Test 6 with 2g/l PM loading

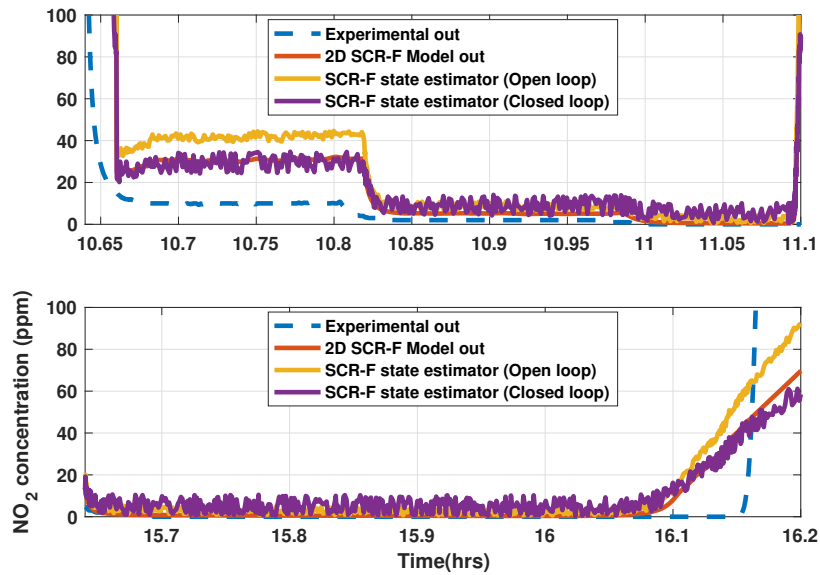


Figure 6.23: SCR-F outlet NO₂ vs time (Experimental, 2D SCR-F model, SCR-F state estimator) Test 6 with 2g/l PM loading

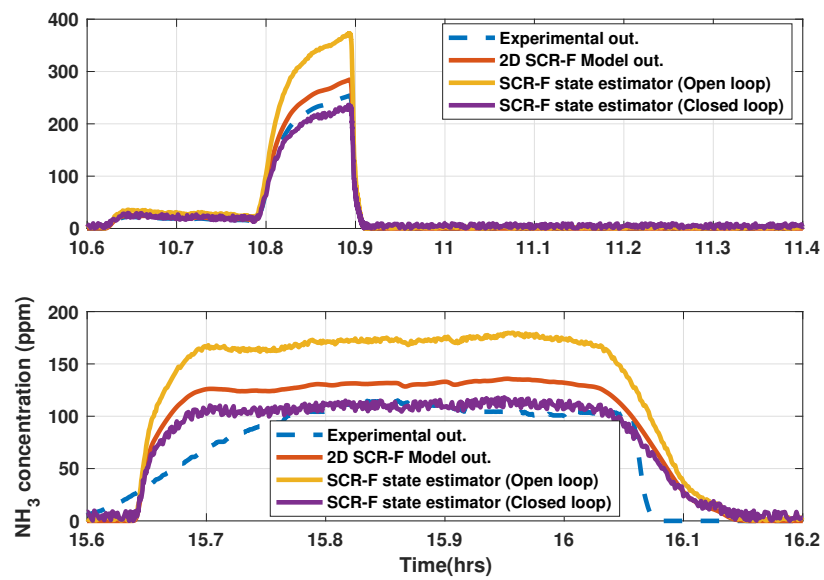


Figure 6.24: SCR-F outlet NH₃ vs time (Experimental, 2D SCR-F model, SCR-F state estimator) Test 6 with 2g/l PM loading

6.3 DOC+SCR-F State Estimator

The DOC + SCR-F state estimator was created by combining an existing 1D DOC state estimator from reference [54] with the 2D SCR-F state estimator. The outlet NO, NO₂, HC concentrations and exhaust gas temperature from the DOC model were used as inputs for the SCR-F model to simulate the SCR-F® performance and estimate the internal states. Figure 6.25 shows the schematic of a system with the DOC - SCR-F state estimator.

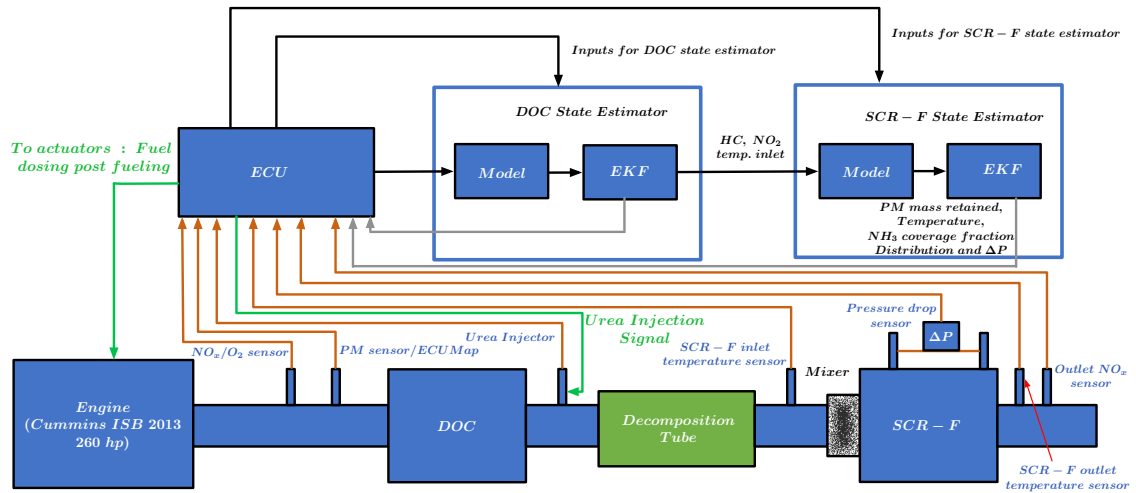


Figure 6.25: DOC+SCR-F® system

The ECU provides the necessary inputs to both the estimators using NO_x, delP sensor and the thermocouple data. Some of the input quantities that are not measured such as PM concentration are supplied from lookup tables by the ECU. The DOC estimator makes use of the input data from the ECU and the thermocouple data to estimate the DOC outlet NO, NO₂ and HC concentrations and exhaust gas temperature. These quantities are supplied along with other inputs from the ECU to the SCR-F state estimator.

The SCR-F state estimator uses the input data and outlet NO_x sensor, pressure drop sensor and thermocouple data to estimate the internal states of the 2D temperature, NH₃ coverage fraction and PM mass distributions. The outlet NO, NO₂ and NH₃ concentrations, pressure drop across SCR-F® and exhaust gas temperature are also estimated.

6.3.1 DOC+SCR-F State Estimator Results

Figures 6.26 to 6.29 compare the estimator and experimental outlet NO, NO₂, NH₃ concentrations and exhaust gas temperature for Test 6 without PM loading from configuration 2 dataset.

The NO and NO₂ outlet concentrations were simulated to within 20 ppm of the experimental values. In order to predict these values, the DOC estimator simulated the conversion of NO to NO₂ using the NO oxidation reaction. These DOC outlet quantities were given as input to the SCR-F state estimator with SCR-F® inlet NH₃ concentrations at ANR 0.8, 1 and 1.2. The SCR-F state estimator used the SCR-F® outlet thermocouple and NO_x concentrations to predict the NO and NO₂ quantities shown in Figures 6.26 and 6.27.

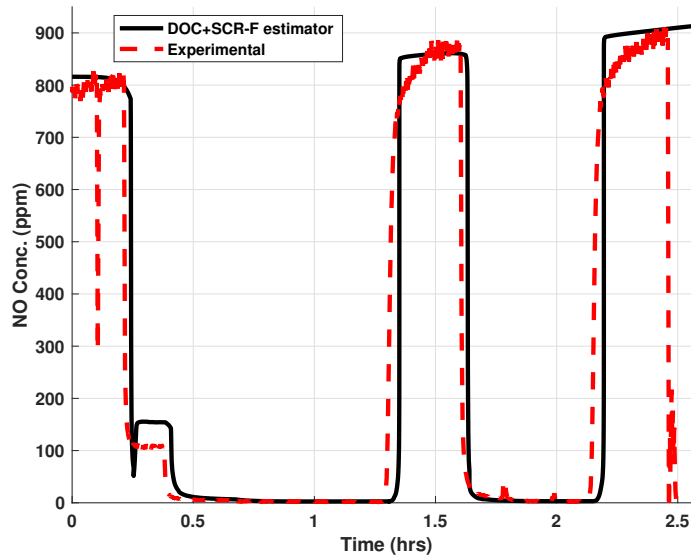


Figure 6.26: DOC-SCR-F® outlet NO concentration experimental and estimator vs time Test 6 0g/l PM loading

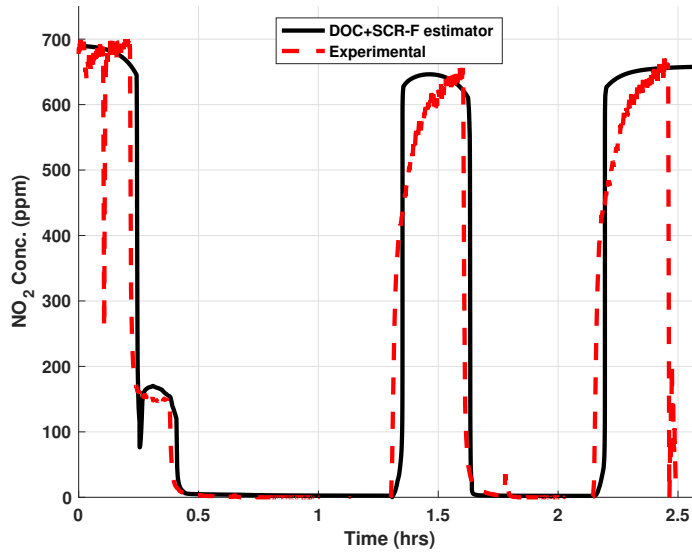


Figure 6.27: DOC-SCR-F® outlet NO₂ concentration experimental and estimator vs time Test 6 0g/l PM loading

The NH₃ slip shown in Figure 6.28 was predicted by the DOC-SCR-F estimator to within 20 ppm of experimental value based on correction from the outlet NO_x sensor using the two site NH₃ storage model.

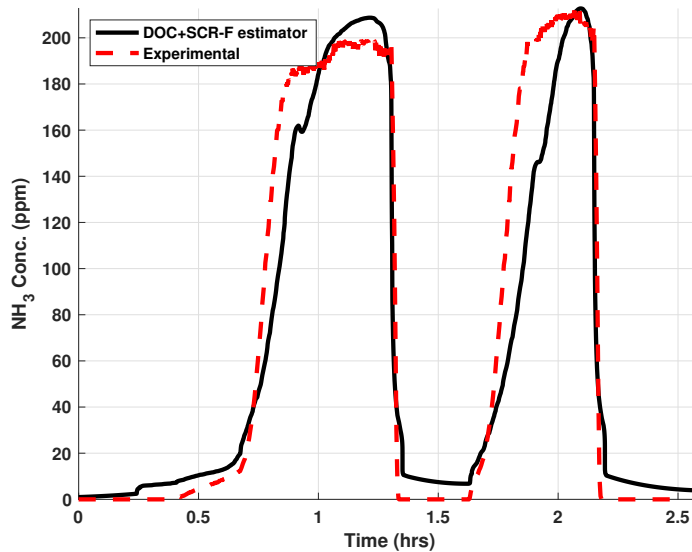


Figure 6.28: DOC-SCR-F® outlet NH₃ concentration experimental and estimator vs time Test 6 0g/l PM loading

The outlet temperature shown in Figure 6.29 was predicted based on DOC and SCR-F® outlet temperature data and energy release by the SCR reactions. The

estimator was able to simulate the DOC-SCR[®] outlet temperature to within 2 °C with temperature rise with a increase in ANR value.

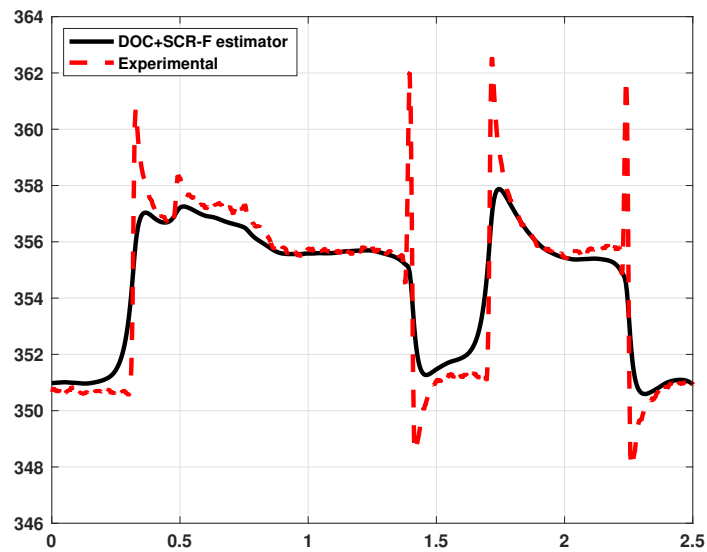


Figure 6.29: DOC-SCR[®] outlet exhaust gas temperature experimental and estimator vs time Test 6 0g/l PM loading

Chapter 7

Ultra Low NO_x Aftertreatment System

The SCR[®]+ SCR results discussed in Chapter 5 led to a conclusion that the SCR placed downstream of the SCR-F had low NO_x conversion performance due to the low NO₂/NO_x ratio. In order to overcome this limitation, a new aftertreatment system configuration is introduced here that can maintain optimum inlet NO₂/NO_x ratio of the SCR-F, SCR and achieve ultra low outlet NO_x objectives. The system uses a second DOC (DOC₂) downstream of SCR-F to boost the SCR inlet NO₂/NO_x ratio by using the NO oxidation reaction. This chapter describes such a system consisting of a DOC, SCR-F, DOC₂ and a SCR with two urea injectors and decomposition tubes. This system along with a cold start system has the potential to meet the NO_x reduction levels required to meet the proposed CARB standard of 0.02 g/bhp-hr. In addition, the urea dosing control strategy is robust to changes in engine operation. Southwest Research Institute (SwRI) has been carrying out research on similar systems that would meet the 0.02 g/bhp-hr. as described in references [45] [56] using a close couple SCR with a DOC, SCR-F and SCR.

7.1 Aftertreatment Systems

This section describes the production aftertreatment system and several aftertreatment systems using the SCR-F and other components. Different combinations of

DOC, SCRF[®], SCR and AMOX are used to reduce emissions from diesel engines with each system having their distinct advantages and disadvantages. Based on a modeling and analysis of these systems, an improved aftertreatment system has been proposed and modeled that can potentially meet ultra low NO_x standard.

7.1.1 Production System

Typical production heavy-duty diesel aftertreatment system for on-highway vehicles consists of a diesel oxidation catalyst (DOC), catalyzed particulate filter (CPF), a selective catalytic reduction (SCR) device and an ammonia oxidation (AMOX) catalyst as show in Figure 1.2. This system has been used in production since 2010 to remove CO, HC, NO_x and PM emissions from diesel engine exhaust.

The DOC is used to oxidize CO, HC and NO and to oxidize the dosed fuel from the fuel doser in order to enable periodic regeneration of the CPF to remove the excess PM retained in the CPF. The CPF is used to filter and oxidize the PM emissions. Urea is injected into the exhaust gas using the injector and is mixed with exhaust gas using the mixer in a decomposition tube where the urea decomposes to form NH₃, CO₂ and H₂O. The SCR reduces NO_x emissions into N₂ and H₂O by reduction reactions between NH₃, NO and NO₂. The AMOX oxidizes the NH₃ that slips out of the SCR. In both the CPF and SCR, an optimum ratio of NO₂/NO_x from 0.5-0.6 is required for passive PM oxidation and fast SCR reactions respectively to maximize the performance of these devices [57]. In order to achieve this ratio, the DOC is used to oxidize the NO to NO₂ and the oxidation catalyst in the CPF is used to oxidize NO to NO₂ leading to a higher PM oxidation rate by back diffusion of NO₂ in the CPF. In order to reduce the packaging volume and cost associated with the CPF and SCR, the selective catalytic reduction catalyst on a filter (SCR-F) has been in R&D over the past 17 years as reviewed by Song. et al. [3]. Figure 7.1 shows one system where the CPF and SCR are replaced with an SCR-F similar to the systems described by BASF patents for a SCR catalyst on a DPF [58][59][60][61][62][63][64][65][66][67]. In this system, the SCR-F is used to simultaneously remove and oxidize particulate matter and reduce NO_x emissions from the exhaust stream.

Figure 7.2 shows an alternative form of this system where a SCR is added downstream of the SCR-F (Configuration 3) to increase the NO_x reduction performance. In order to evaluate the performance of this system, the 2D SCR-F [49] (Chapter 3), 1D DOC

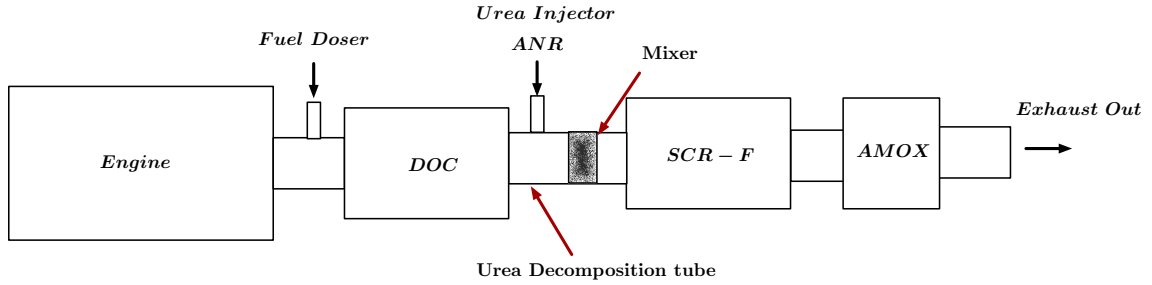


Figure 7.1: Aftertreatment system with SCR-F with 1 injector

[54] and 1D SCR [2] models were used to evaluate this system. These models were validated using engine experimental data as described in references [49][54][2][5]. The development of the 2D SCR-F model used in the simulations and the experimental research effort was started based on the literature review by Xiaobo Song et al. [3]. Based on this review, the important features of the SCR-F model including the forward diffusion of NO_2 , low temperature performance and catalyst placement and competition for NO_2 between PM oxidation and SCR reactions was included in the 2D SCR-F model. A set of experiments were conducted using the SCR-F + SCR system described in Figure 7.2 consisting of a 2013 6.7 L Cummins ISB engine described in reference [51] and were modeled using the SCR-F model [49] and the SCR model [2]. Similarly, a set of experiments were performed as described in reference [52] with the production aftertreatment system described in Figure 1.2.

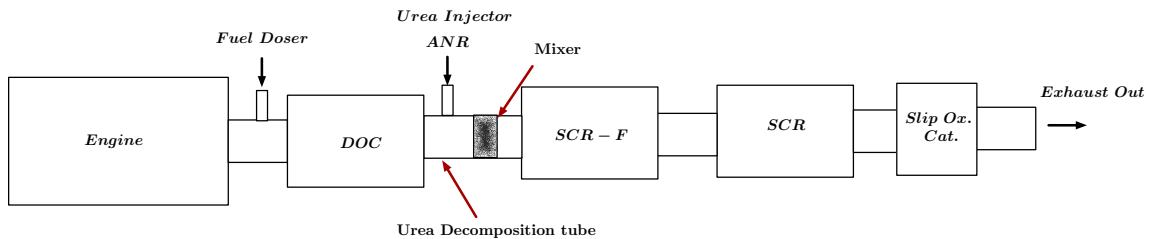


Figure 7.2: Aftertreatment system with SCR-F+SCR with 1 injector

7.1.2 Proposed - Ultra Low NO_x Aftertreatment System Configurations

Although the SCR-F reduces the aftertreatment system volume, the performance of this system is limited by two aspects. The first aspect being reduction in the passive

oxidation rate of the PM (up to 70%) compared to the SCR-F without urea injection due to the forward diffusion of NO_2 from the PM cake to the substrate wall leading to a higher pressure drop as described in reference [49]. Increased fuel consumption due to the need for active regeneration to reduce the PM retained in the filter would be needed. The second aspect being the consumption of the NO_2 in the PM cake and the substrate wall by the passive oxidation reaction of the wall and the cake PM and the SCR reactions leading to an unfavorable NO_2/NO_x ratio for the downstream SCR which limits the performance of that device and the overall NO_x conversion efficiency of the system. In order to overcome the deficiencies of the SCR-F only, the systems described in Figures 7.3, 7.4 and 7.5 will be modeled to show the progressive changes of the system when adding injection/decomposition tubes, DOC_2 and a DCSC^{TM} .

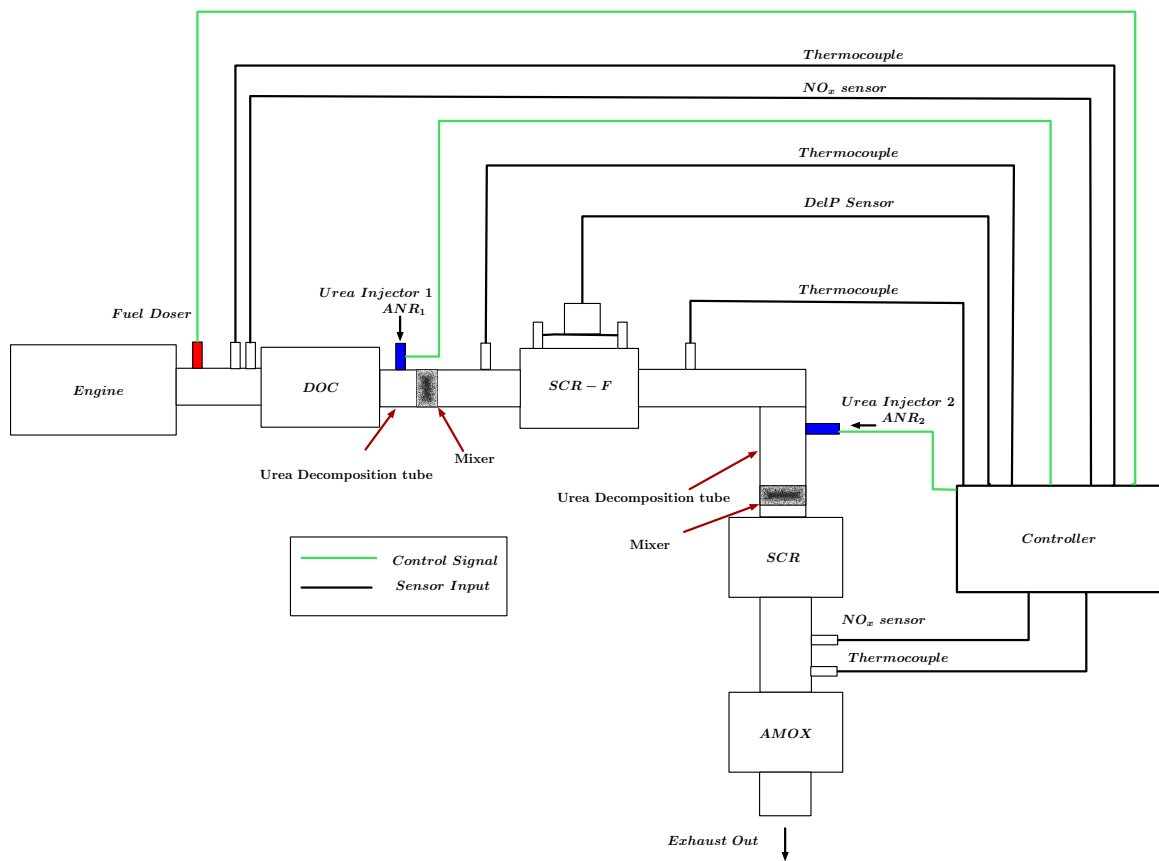


Figure 7.3: Aftertreatment system with SCR-F, SCR and two urea injectors

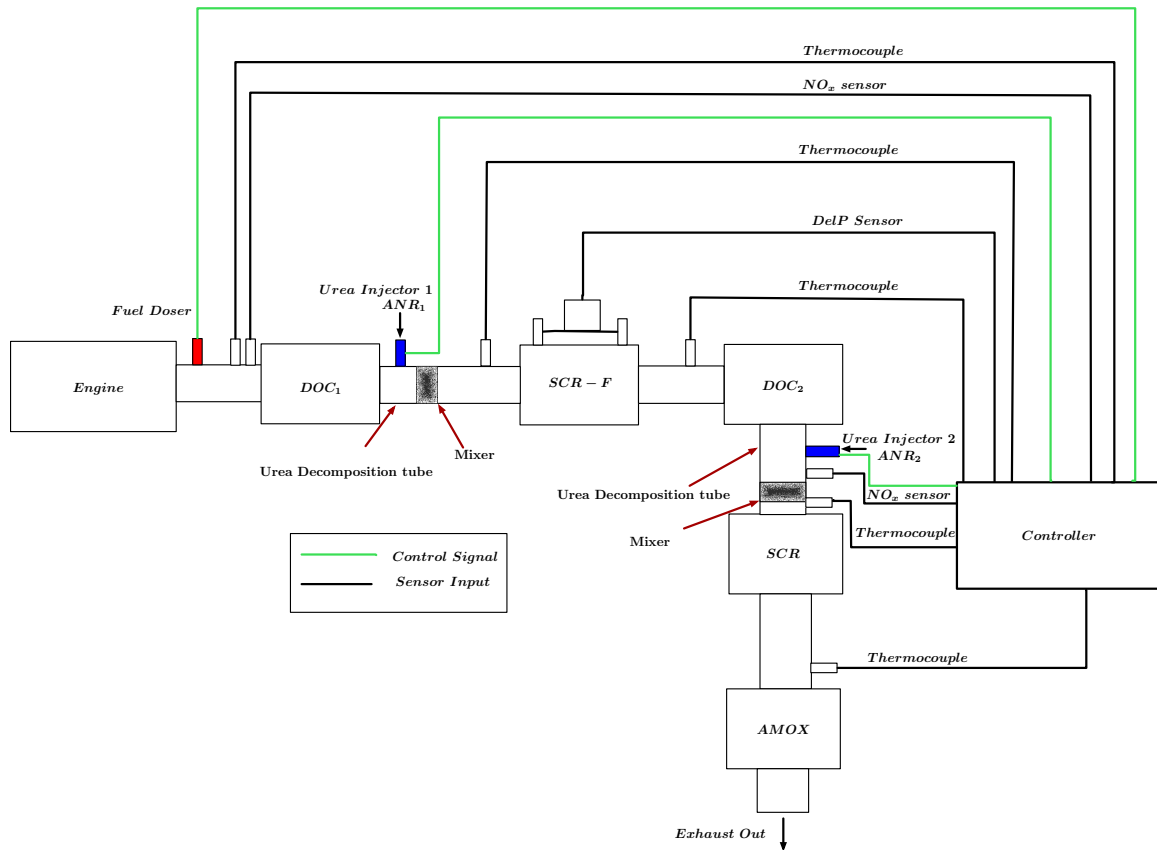


Figure 7.4: A new, ultra low outlet NO_x aftertreatment system with a SCR-F, a downstream DOC_2 and a SCR with two injectors

Figure 7.3 shows a form of the system where a second urea injector and decomposition tube were added to the system. For this system, due to addition of a second injector, the total urea flow rate is divided into components ANR_1 and ANR_2 which represents the ANR values at the two injectors. This modification to the system of Figure 7.2 increases the NO_x conversion and the PM oxidation rate over the SCR-F system alone (Figure 7.1). In order to achieve higher PM oxidation rate, urea injection rate in the first urea injector (based on ANR_1) is reduced for the SCR-F and to maintain the high system NO_x conversion, the urea injection rate from the second injector (based on ANR_2) to the SCR is increased to maintain higher NH_3 coverage fraction (as compared to SCR-F+SCR system with 1 injector) in the SCR.

The system in Figure 7.4 consists of a DOC_2 downstream of the SCR-F along with the two urea injectors and urea decomposition tubes to overcome all the deficiencies of the SCR-F and the SCR-F+SCR system performance described earlier. What is unique in this system is the addition of the DOC_2 downstream of the SCR-F to

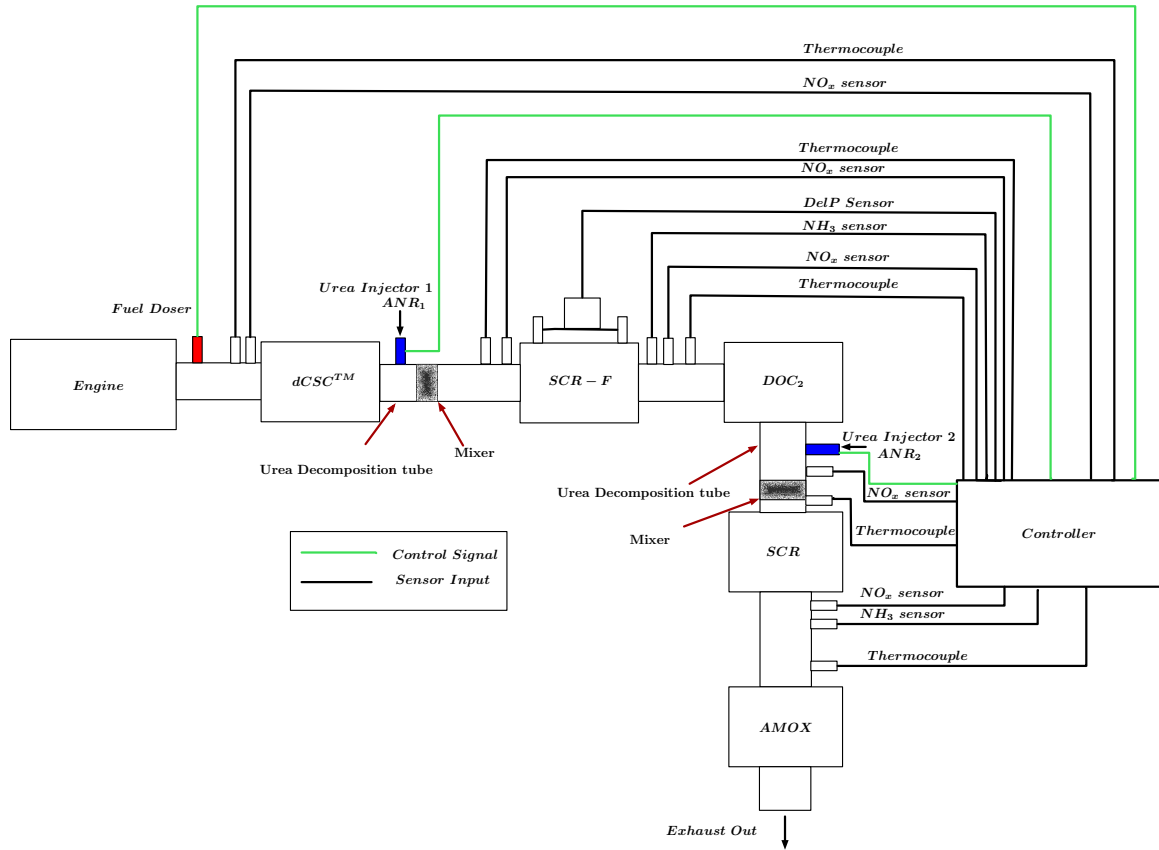


Figure 7.5: Aftertreatment system with dCSCTM, SCR-F, downstream DOC₂ and SCR with two injectors

oxidize the NO to NO₂ at the SCR-F outlet in order to increase the NO_x conversion efficiency of the SCR and the overall NO_x conversion efficiency of the system and to increase the SCR-F passive PM oxidation rate compared to the SCR-F only (Figure 7.1) and the SCR-F+SCR (Figure 7.2) systems. The test data in reference [51] for the SCR-F+SCR system (Figure 7.2) were used as the input to a simulation of the aftertreatment system of Figure 7.4 to evaluate the improvement in NO_x reduction, urea consumption, NH₃ slip and PM oxidation rate performance using the SCR-F model [49]. The results from the simulation of the systems in Figures 7.1, 7.2, 7.3 and 7.4 were compared later to determine the improvements obtained with the technology components being modeled.

In the SCR-F+DOC₂+SCR system (Figure 7.4), the addition of the DOC₂ downstream of SCR-F leads to near optimal NO₂/NO_x ratio by oxidizing NO to NO₂ with the DOC₂ for the SCR which in turn leads to higher NO_x conversion in the SCR which enables the system to attain maximum NO_x conversion efficiency. The addition of

the second urea injector allows control of both the SCR-F and SCR's NH_3 storage to purposely decrease NO_x conversion in the SCR-F while enhancing its passive PM oxidation functions while the SCR removes the remaining NO_x from the exhaust gas. This leads to a reduction in urea consumption, higher system NO_x conversion efficiency at all temperatures and flow rates, reduced NH_3 slip and reduced PM retained over the SCR-F only system (Figure 7.1).

The system in Figure 7.4 can also be coupled with a dCSC^{TM} [68] [69] upstream of the SCR-F instead of the DOC to enable NO_x storage during cold start resulting in lower NO_x emissions for the entire Federal Test Procedure (FTP). Such a setup would make it easier to meet the future California 0.02 g/bhp-hr NO_x standards. Figure 7.5 shows the setup with a dCSC^{TM} [68] [69].

7.2 Parametric Studies and Results

The 2D SCR-F, 1D DOC and 1D SCR models were used in different combinations to simulate the performance of the $\text{SCR-F}^{\text{®}}$, $\text{SCR-F}^{\text{®}}+\text{SCR}$ and $\text{SCR-F}^{\text{®}}+\text{DOC}_2+\text{SCR}$ systems in Figures 7.1, 7.2, 7.3 and 7.4. The system shown in Figure 7.4 was simulated in MATLAB/Simulink using a combination of the 2D SCR-F, 1D DOC and 1D SCR models. The urea injection in both injectors were set at a constant rate. The injected urea was assumed to be completely decomposed and any NH_3 slip from the $\text{SCR-F}^{\text{®}}$ is assumed to be completely oxidized in the DOC_2 . The engine conditions in the tests from reference [51] used for the simulations are shown in Table 7.1. The specifications of the three devices is given in Table 7.2 and they are described in detail in references [49][54][5]. Figures 7.6 to 7.13 compare the SCR-F and system NO_x conversion, NH_3 slip and urea consumed for all the four systems described above for one of the engine conditions (Test C) from the data described in reference [51]. The results from Test C are described here and the results from the remaining engine conditions are described in Appendix G. The models were run with different configurations as shown below :

1. $\text{SCR-F}^{\text{®}}$ (Figure 7.1)
2. $\text{SCR-F}^{\text{®}}+\text{SCR}$ with one urea injector (Figure 7.2)
3. $\text{SCR-F}^{\text{®}}+\text{SCR}$ with two urea injectors (Figure 7.3)
4. $\text{SCR-F}^{\text{®}}+\text{DOC}_2+\text{SCR}$ with two urea injectors (Figure 7.4)

Table 7.1
Engine conditions

Engine Condition	Exhaust Flow Rate	SCR-F® Inlet Temp.	SCR-F® NO ₂	SCR-F® Inlet NO	SCR-F® Inlet NO _x	SCR-F® Inlet NO ₂ /NO _x
[-]	[kg/min]	[°C]	[ppm]	[ppm]	[ppm]	[-]
1	5.2	203	182	443	625	0.29
A	5.6	267	215	375	590	0.44
C	6.9	339	290	399	689	0.44
E	7.1	342	584	866	1450	0.37
D	12.5	366	161	289	450	0.38

¹ - DOC from 2010 Cummins ISB engine described in [54]

^{2,3} - SCR from 2013 Cummins ISB engine and SCR-F® prototype from Johnson Matthey in 2014 described in [5]

The SCR-F® only system (Figure 7.1) was run with an inlet ammonia to NO_x ratio (ANR) value of 0 to 1.2 and a PM loading value of 2g/l to evaluate the performance of the SCR-F® over a wide range of ANR conditions. The results from modeling the SCR-F, applies to all the four systems and Figures 7.6 and 7.7 show the simulation results. Equation 7.1 is used to calculate the urea flow rate to the SCR-F® (ANR₁) and SCR (ANR₂) based on the ANR, NO_{x,in} and the exhaust flow rate.

$$\dot{m}_{DEF} = \frac{\dot{m}_{exh} * MW_{urea} * ANR * 1e - 6 * NO_{x,in}}{0.325 * 2 * MW_{exh} * \rho_{DEF}} \quad (7.1)$$

$$MW_{exh} = \sum_{i=1}^4 Y_i * MW_i \quad (7.2)$$

Where :

\dot{m}_{DEF} = Diesel exhaust fluid (DEF) mass flow rate (*ml/s*)

MW_{urea} = Molecular weight of urea (*kg/kmol*) = 60.06*kg/kmol*

ANR = Ammonia to NOx ratio (-) to SCR-F or SCR

$NO_{x,in}$ = NOx concentration at the inlet of the SCR-F/SCR (*ppm*)

0.325 = 32.5 % v/v concentration of the urea in the DEF solution (-)

MW_{exh} = Molecular weight of the exhaust gas (*kg/kmol*)

ρ_{DEF} = Density of DEF (*kg/m³*) = 1080 *kg/m³*

MW_i = Molecular weight of species *i* (*kg/kmol*)

Table 7.2
Aftertreatment components specifications

Component	DOC and DOC₂¹	SCR²	SCR^{®3}
Material	Cordierite	Cordierite	Cordierite
Material	Cordierite	Cordierite	Cordierite
Catalyst	Pt	Cu-zeolite	Cu-zeolite
Diameter (in)	9.5	10.5	10.5
Diameter of Substrate (mm)	241.3	266.7	266.7
Length (in)	4	12	12
Length (mm)	101.6	304.8	304.8
Cell Geometry	Square	Square	Square
Total Volume (L)	4.65	17.04	17.04
Open Volume (L)	3.5	14.04	10.2
Cell Density/in ²	400	400	200
Cell Width (mil)	46	46	55
Cell Width (mm)	1.16	1.16	1.39
Filtration Area (in ²)	N/A	N/A	11370
Open Frontal Area (in ²)	60	73.29	25.9
Channel Wall Thickness (mil)	4	4	16
Wall Density (g/cm ³)	1.2	0.91	-
Porosity (%)	35	35	50
Mean Pore Size (?m)	N/A	N/A	16
Number of Inlet Cells	28353	34636	8659
Actual Open Surface Area (m ²)	4.22	17.26	7.37
Surface Area of Cells (m ²)	12.08	49.33	14.74
Perimeter of Cell (mm)	4.67	4.67	5.58

Y_i = Mole fraction for species CO₂, O₂, H₂O and N₂ (*kmol of i/kmol of exhaust*)

Figure 7.6 shows the change in the outlet NO, NO₂ and NH₃ concentrations and the NO₂/NO_x ratio as a function of the SCR[®] inlet ANR for Test - C. The NO and NO₂ outlet concentrations decrease with an increase in the inlet ANR with NO₂ and NO₂/NO_x ratio reaching near zero value at ANR 1 and above. The outlet NH₃ concentration remains zero up to ANR = 0.8. At ANR values greater than 0.8, significant SCR[®] NH₃ outlet concentrations are observed with the NH₃ concentration being 144 ppm at a ANR 1.

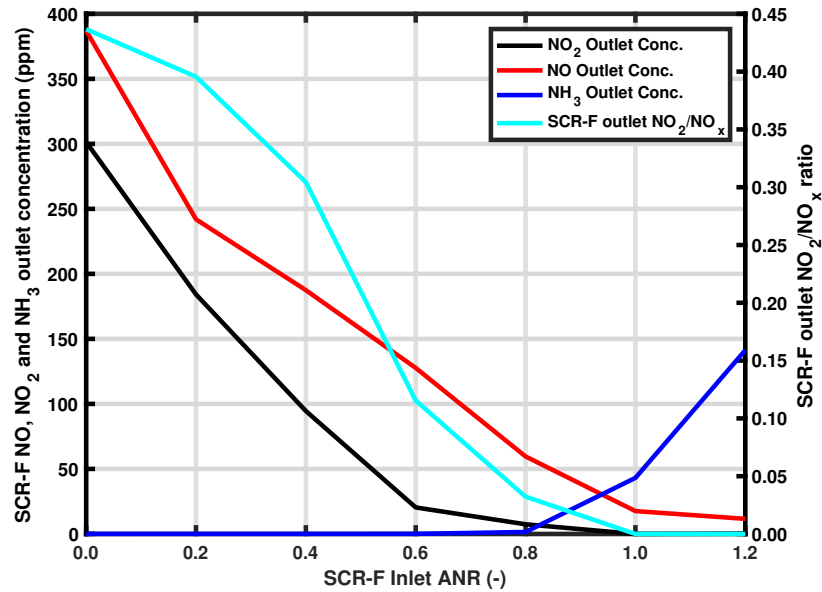


Figure 7.6: Outlet concentrations and SCR-F® outlet NO₂/NO_x ratio vs inlet ANR values at engine condition C (SCR-F® with 1 injector)

In Figure 7.7 the NO_x conversion increases with an increase in the inlet ANR value reaching a maximum value of 98.6% at ANR 1.2. The SCR-F® maximum NO_x conversion efficiency is limited by the exhaust flow rate, temperature and inlet NO₂/NO_x ratio conditions from Figure 7.6 for the given engine condition. The impact of the PM cake on the local NO₂/NO_x ratio in the substrate wall and inhibition of the SCR reactions due to the wall PM [49] have also been taken into account. The urea flow rate has a linear relationship with the inlet ANR increasing from inlet ANR = 0 to 1.2. The PM oxidation rate decreases with an increase in the inlet ANR due to an increase in the forward diffusion rate of the NO₂ from the PM cake to the substrate wall.

The SCR-F®+SCR system (Figure 7.1) with 1 urea injector was modeled with an inlet ammonia to NO_x ratio (ANR) value of 1 to 1.12 at the inlet of the SCR-F® (Figure 7.6), with the SCR-F® NH₃ outlet concentration being used as the inlet NH₃ for the SCR. Figure 7.8 shows the results from these simulations. The steep slope of the NH₃ outlet concentrations for ANR > 1.0 from Figure 7.6 shows that the control system must be precise in setting the SCR-F® inlet ANR so as to not have excess slip or lower NO_x conversion efficiency.

The NO_x conversion of the SCR-F®+SCR system increases with an increase in the SCR-F® inlet ANR reaching a maximum value of 99% at ANR = 1.12. The addition

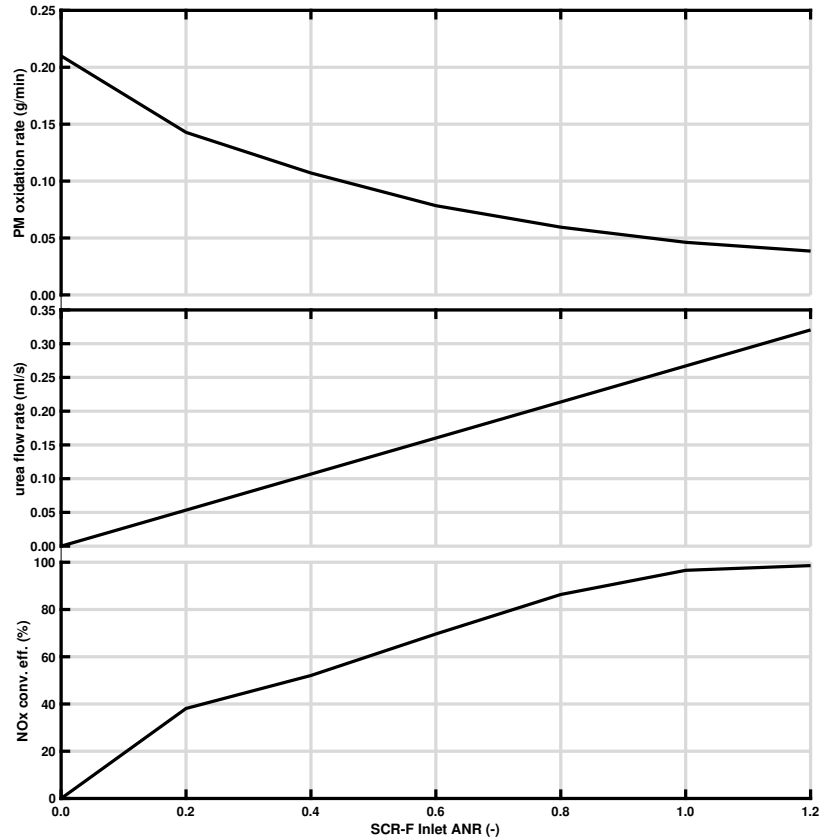


Figure 7.7: NO_x conversion efficiency, urea flow rate and PM oxidation rate vs SCR-F® Inlet ANR at engine condition C (SCR-F® with 1 injector)

of SCR leads to the 0.4% increase in the system NO_x conversion efficiency compared to the SCR-F® only system. The SCR efficiency is limited by the NO₂/NO_x ratio from Figure 7.6 at the inlet of the SCR due to the SCR-F® near zero NO₂ outlet concentration, leading to a lower SCR NO_x conversion efficiency due to only the standard SCR reaction. Since the SCR inlet NH₃ is a function of the SCR-F® NH₃ outlet concentration, the efficiency of the SCR is less than 50 % for values of ANR < 1.03 due to the low SCR-F® NH₃ outlet concentration. When the NH₃ concentration increases, the SCR and system NO_x conversion efficiencies increase resulting in the slope change observed in the NO_x conversion efficiency plots at ANR = 1.03. The urea flow rate increases linearly with an increase in the inlet SCR ANR value which reaches a maximum urea flow rate of 0.297 ml/sec at ANR = 1.12

The SCR outlet NO₂ is near zero for all values of ANR as the SCR-F® outlet NO₂ is zero. The SCR NO outlet concentration decreases to less than 10 ppm at ANR's greater than 1.09 as a result of the standard SCR reaction. The standard reaction

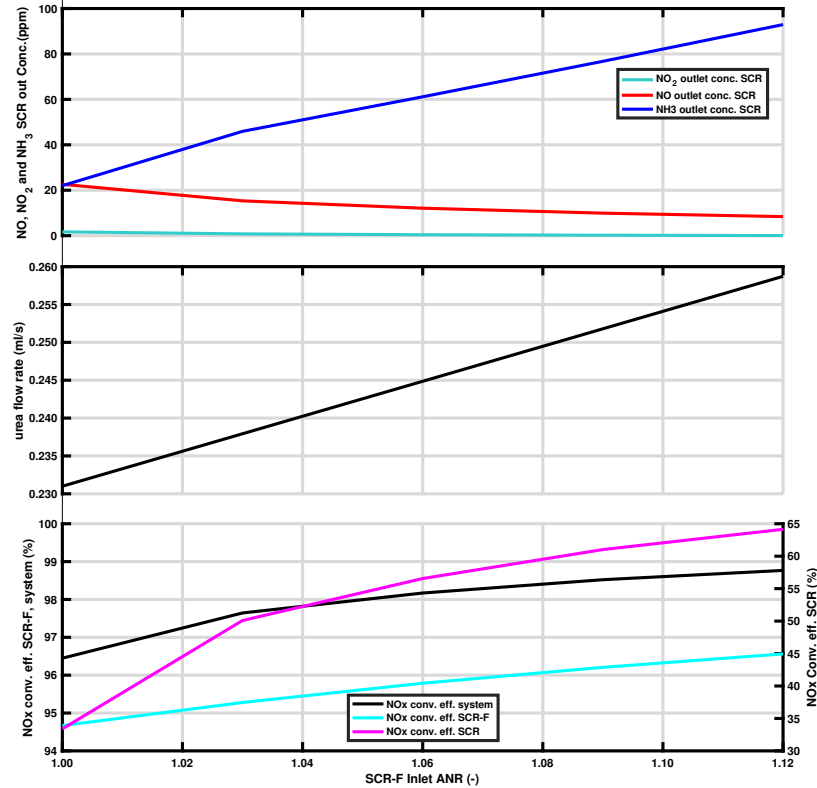


Figure 7.8: NO_x conversion efficiency, urea flow rate and outlet concentrations vs SCR-F® inlet ANR at engine condition C (SCR-F®+SCR with 1 urea injector)

starts reducing NO at ANR = 1.03 where the SCR-F® NH₃ outlet concentration (Figure 7.6) is over 70 ppm. The outlet NH₃ concentration of the system increases with ANR value to a maximum value of 92 ppm at ANR = 1.12 (Figure 7.8). The high NH₃ slip is due to the mass transfer limitations and 65% maximum efficiency of the SCR is a result of the unfavorable SCR inlet NO₂/NO_x ratio (Figure 7.6).

For the two systems modeled, the SCR-F®+SCR (Figure 7.3) and SCR-F®+DOC₂+SCR (Figure 7.4) systems, a second injector was added to enable better control of the NH₃ coverage fraction in both the SCR-F® and SCR. In order to control these systems, the ANR values for urea injection at the two injectors (ANR₁ and ANR₂) is determined from the control algorithm based on exhaust NO_x concentration, temperature and exhaust flow rate from the sensors and PM retained in the SCR-F estimator.

The SCR-F®+DOC₂+SCR system was run with ANR₁ in the range of 0 to 1.0

in Figure 7.9, in order to determine a good operating range of ANR_1 . ANR_2 was determined in such a way that total urea flow rate is constant (0.258 ml/sec) for all values of ANR_1 and $ANR_1 = 0.65$ and $ANR_2 = 1.07$ for this flow rate. The ANR_2 values shown in this figure were calculated based on maximizing the NO_x conversion efficiency while keeping the total urea flow rate constant for the given ANR_1 value. Figure 7.9 shows the change in the system NO_x conversion efficiency, ANR_2 , PM oxidation rate, SCR-F® outlet NO_2 and SCR outlet NH_3 concentrations as a function of ANR_1 .

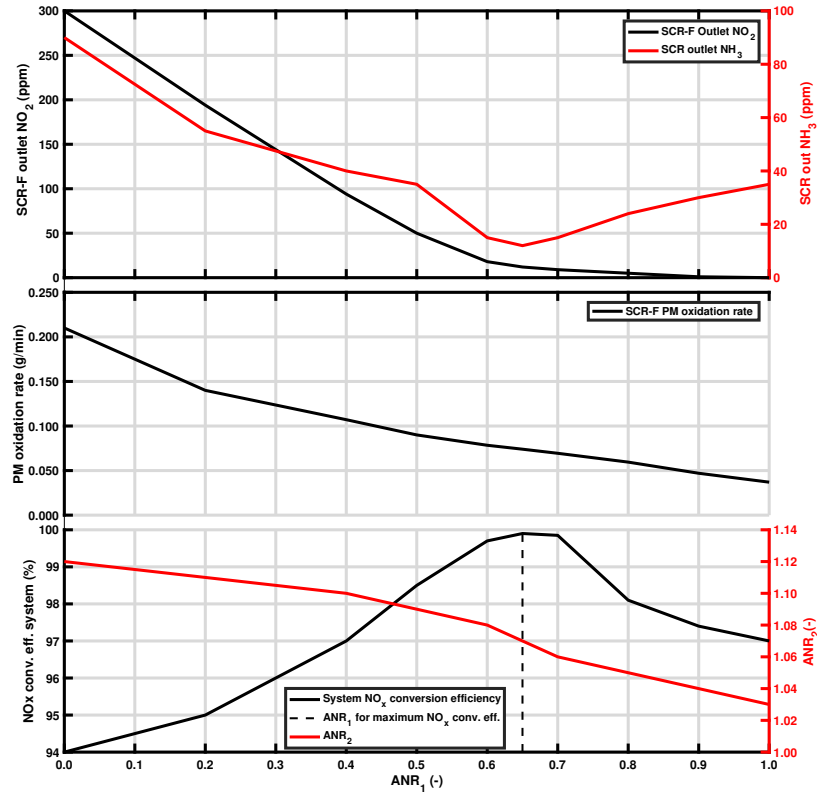


Figure 7.9: NO_x conversion efficiency, ANR_2 , PM oxidation rate, SCR-F® outlet NO_2 and SCR outlet NH_3 concentration vs ANR_1 at engine condition C (SCR-F®+DOC₂+SCR with 2 urea injectors)

The system NO_x conversion efficiency increases from $ANR_1 = 0.0$ to 0.65 reaching a maximum value of 99.9%. The ANR_2 also decreases with increase in ANR_1 reaching a minimum value of 1.03. The PM oxidation rate decreases with an increase in ANR_1 due to the forward diffusion of the NO_2 from the PM cake to the substrate wall in the SCR-F® with an increase in ANR_1 value.

The outlet SCR-F® NO_2 concentration decreases with an increase in ANR_1 and the

values beyond $ANR_1 = 0.65$ being less than 15 ppm. The SCR NH_3 outlet concentration follows the trend of the system NO_x conversion efficiency with a minimum NH_3 outlet concentration at $ANR_1 = 0.65$ where highest NO_x conversion was observed. Based on the trends in Figure 7.6, the PM oxidation rate can be increased further by using ANR_1 values less than 0.6 if a lower NO_x conversion efficiency is acceptable for a given engine load and speed condition. At $ANR_1 = 0.0$ the NO_x conversion efficiency of the system decreases to 94%. The region of ANR_1 greater than 0.7 is undesirable for operation for this engine condition since it offers neither an increase in PM oxidation rate nor improved NO_x conversion efficiency.

In order to determine the reason behind the trend in NO_x conversion efficiency in Figure 7.9, the NO_2/NO_x ratio at the outlet of the SCR $\text{\textcircled{R}}$ and the DOC_2 were plotted against ANR_1 as shown Figure 7.10. As can be observed in Figure 7.10, the

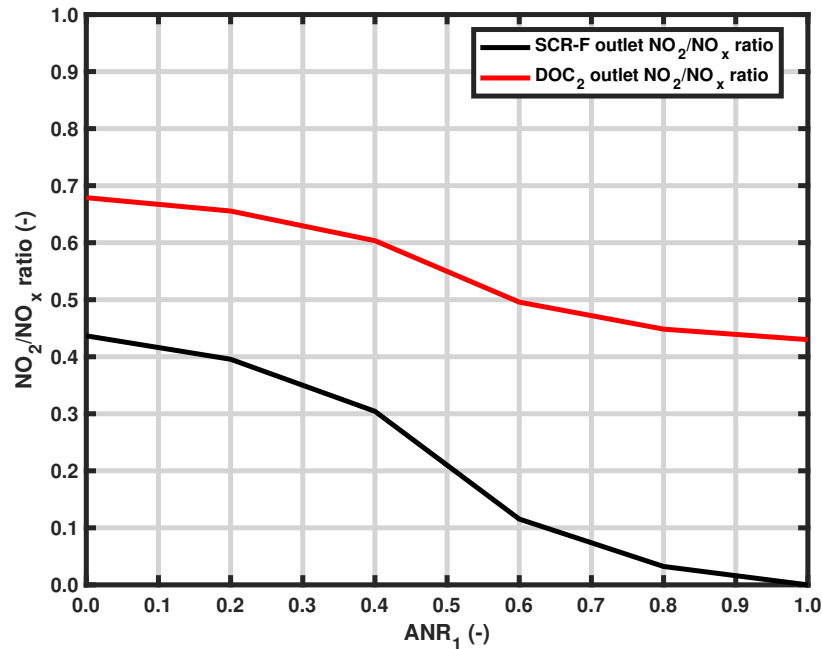


Figure 7.10: NO_2/NO_x ratio vs ANR_1 at engine condition C (SCR $\text{\textcircled{R}}$ + DOC_2 +SCR with 2 urea injectors)

addition of DOC_2 leads to the NO_2/NO_x ratio increase compared to the SCR $\text{\textcircled{R}}$ outlet value. This increased NO_2/NO_x ratio is the inlet NO_2/NO_x ratio for the SCR. The DOC_2 outlet NO_2/NO_x ratio starts at 0.69 and decreases to 0.5 for a ANR_1 of 0.6. There is a further decrease in DOC_2 outlet NO_2/NO_x ratio with an increase in ANR_1 value following the trend of the SCR $\text{\textcircled{R}}$ outlet NO_2/NO_x ratio but this is in the ANR_1 region where operation is not desirable.

For $ANR_1 = 0.65$, the SCR efficiency increases to 97 from the 71% in the system without DOC_2 (Figure 7.8, $ANR = 1.12$) due to the favorable NO_2/NO_x ratio of 0.5 [57]. This leads to a system NO_x conversion efficiency of 99.9% for $ANR_1 = 0.65$ and $ANR_2 = 1.06$.

Based on Figures 7.9 and 7.10, an ANR_1 of 0.6 and 0.7 with ANR_2 from 1 to 1.12 were chosen for simulating the SCR \textcircled{R} +SCR (with 2 injectors) and the SCR \textcircled{R} + DOC_2 +SCR (with 2 injectors) systems, as it represented ANR_1 values which provided the highest system NO_x conversion efficiency.

The SCR \textcircled{R} +SCR with 2 injectors system was run with the second urea injector at the inlet of the SCR with ANR_2 in a range of 1 to 1.12 to evaluate the system performance. The NH_3 outlet concentration from the SCR \textcircled{R} and the NH_3 decomposed from the urea injected from the second urea injector were used as the inlet NH_3 for the SCR. Figure 7.11 shows the results from the system simulation.

The NO_x conversion efficiency is comparable to the SCR \textcircled{R} +SCR system with 1 injector with an efficiency of 99.0% at $ANR_1 = 0.7$ and $ANR_2 = 1.12$. The SCR conversion efficiency is limited by the low NO_2 concentration at the inlet of the SCR (Figure 7.9) leading to a SCR NO_x conversion efficiency of 85 % at $ANR_2 = 1.12$. The urea flow rate at $ANR_2 = 1.12$ for the $ANR_1 = 0.7$ case is 0.284 ml/s. The addition of a second injector enables the operation of the SCR \textcircled{R} at ANR_1 at 0.7 which gives better control of the NH_3 coverage fraction in both the SCR \textcircled{R} and SCR. This leads to a higher PM oxidation rate in the SCR \textcircled{R} in this system as compared to the system with 1 injector.

The SCR \textcircled{R} + DOC_2 +SCR (Figure 7.4) system consists of two urea injectors similar to the SCR \textcircled{R} +SCR (Figure 7.3) system with 2 injectors however in this system a DOC_2 is added between the SCR \textcircled{R} and the SCR as shown in Figure 7.4 to oxidize NO to NO_2 enabling favorable NO_2/NO_x ratios (0.5 to 0.6) at the inlet of the SCR. The DOC_2 also oxidizes the outlet NH_3 concentrations from the SCR \textcircled{R} , and NH_3 from the SCR \textcircled{R} is negligible for ANR_1 values below 0.7 as seen in Figure 7.7. These simulations were run with ANR_1 of 0.6 and 0.7, and ANR_2 of 1 to 1.12 similar to SCR \textcircled{R} +SCR system. Results from these simulations are shown in Figure 7.12.

The NO_x conversion efficiency is higher for this system with a maximum efficiency of 99.9 % for $ANR_1 = 0.7$ at $ANR_2 = 1.12$. This system is not limited by the low NO_2 concentration from the SCR \textcircled{R} outlet since the DOC_2 for this engine condition

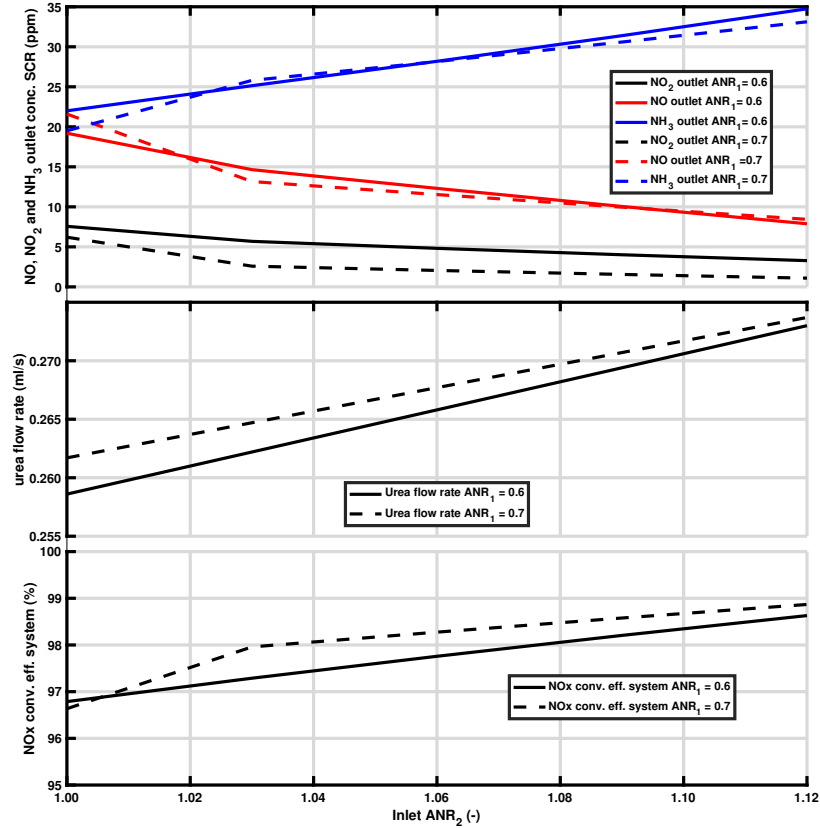


Figure 7.11: NO_x conversion efficiency, urea flow rate and outlet concentrations vs SCR® Inlet ANR₂ at engine condition C and for ANR₁ 0.6 and 0.7 (SCR®+SCR with 2 urea injectors)

converts 60% of the SCR® outlet NO to NO₂ (Figure H.17 Appendix G). The near 100% efficiency for ANR₁ = 0.7 is due to the favorable NO₂/NO_x ratio into the SCR. The outlet SCR NO₂ concentration for at ANR₁ = 0.7 is near zero with NO concentrations being less than 6 ppm. The NH₃ slip was also observed to be lower than the SCR®+SCR system with 2 injectors due to the higher utilization of the NH₃ for NO_x reduction with a maximum NH₃ slip of 20 ppm. The urea flow rate for this system ANR₁ = 0.7 and ANR₂ = 1.12 is 0.172 and 0.085 ml/sec for injections 1 and 2 respectively with total flow rate = 0.284 ml/s.

For the systems with two urea injectors a new performance characteristic called system ANR is computed. The system ANR represents the ratio of the total NH₃ produced from the urea injected at the two urea injectors divided by the SCR® inlet NO_x

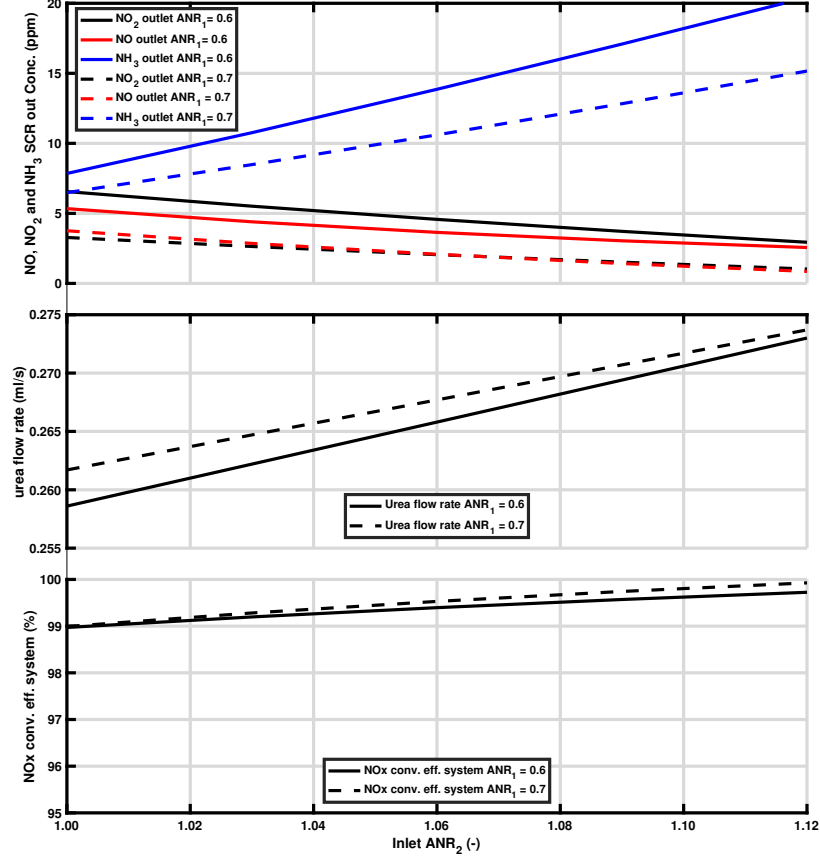


Figure 7.12: NO_x conversion efficiency, urea flow rate and outlet concentration vs SCR F^{R} inlet ANR at engine condition C (SCR F^{R} +DOC $_2$ +SCR with 2 urea injectors)

concentration and is defined by equation 7.3.

$$ANR_{system} = \frac{(ANR_1 * NO_{x,in,SCR-F} + ANR_2 * NO_{x,in,SCR})}{NO_{x,in,SCR-F}} \quad (7.3)$$

Where

ANR_1 = ANR at urea injector 1 $NO_{x,in,SCR-F}$ = NOx concentration at the inlet of SCR-F

ANR_2 = ANR at urea injector 2 $NO_{x,in,SCR}$ = NOx concentration at the inlet of SCR

The four systems were run with system ANR of 1.007 to 1.037. For systems with 1 injector ANR2 = 0 and ANR system = ANR1. The PM oxidation rate, urea flow rate and NOx conversion efficiency have been compared for these four systems in Figure 7.13 .

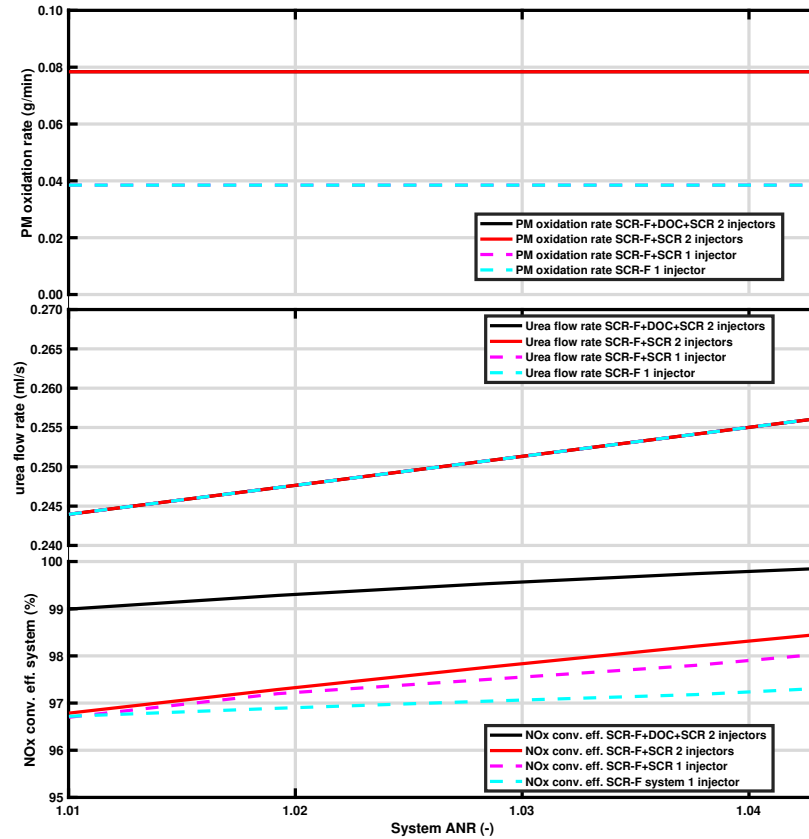


Figure 7.13: NO_x conversion efficiency, urea flow rate and PM oxidation rate vs system Inlet ANR at engine condition C

As observed from Figure 7.13, the NO_x conversion efficiency of the SCR-F® only was observed to be 97.5 % at system ANR 1.027, the SCR-F®+SCR with 1 injector has an efficiency of 97.5 % followed by SCR-F+SCR system with 2 injectors with 97.8%. The SCR-F®+DOC₂+SCR system had the higher NO_x conversion efficiency of 99.5%. The SCR-F®+DOC₂+SCR system due to the favorable NO_2/NO_x ratio in the SCR is consistently higher by 2 % compared to the SCR-F® system. The urea flow rate is the same for all the cases and is linearly proportional to the system ANR. For a given amount of urea flow rate, the SCR-F®+DOC₂+SCR system has higher NO_x conversion efficiency (99.9% efficiency at $\text{ANR}_1 = 0.65$ and $\text{ANR}_2 = 1.06$) than the remaining systems which can be used to reduce the urea consumption if a lower NO_x conversion efficiency is acceptable for a given engine condition and it is desirable to increase the PM oxidation rate.

The PM oxidation rate in Figure 7.13 shows a trend where the systems with 2 urea injectors at $\text{ANR}_1 = 0.7$ have oxidation rates of 0.079 g/min compared to 0.039 g/min

for systems with 1 urea injector. This 100% improvement in the PM oxidation rate is due to the lower forward diffusion rate at lower ANR_1 values leading to higher available NO_2 in the PM cake and higher PM oxidation rate. This trend is consistent with the PM oxidation rate vs Inlet ANR of SCR-F® only system from Figure 7.7.

Table 7.3 compares the performance of the four systems for a system of $ANR = 1.04$, $ANR_1 = 0.65$ and $ANR_2 = 1.06$ for the systems with 2 injectors at engine condition C. The values of ANR_1 and ANR_2 for the 2 injector systems were chosen based on the trends from Figure 7.9. As can be observed from Table 7.3, there is 2.1% increase in the NO_x conversion efficiency for the system with DOC_2 compared to SCR-F only system. The systems with 2 injectors have 80% higher PM oxidation rate. The NH_3 slip value for the system with a DOC_2 is 14 ppm compared to 75 ppm for the SCR-F only system due to better utilization of NH_3 in the SCR. The urea flow rate is 1.4% lower in the case of the system with the DOC_2 (0.275 vs 0.276 ml/sec) due to lower NH_3 slip and better NH_3 utilization.

Table 7.3
Performance of the four systems at system $ANR = 1.04$

System	NO_x conversion efficiency	PM oxidation rate	NH_3 slip	Urea flow rate
Units	(%)	(g/min)	(ppm)	(ml/s)
SCR-F® Only 1 injector ($ANR_1 = 1.04$, $ANR_2 = 0$) system $ANR = 1.04$	97.8	0.039	75	0.276
SCR-F® +SCR 1 injector ($ANR_1 = 1.04$, $ANR_2 = 0$) system $ANR = 1.04$	98.0	0.039	50	0.276
SCR-F®+SCR 2 injectors ($ANR_1 = 0.65$, $ANR_2 = 1.06$) system $ANR = 1.04$	98.5	0.070	22	0.275
SCR-F®+ DOC_2 +SCR 2 injectors ($ANR_1 = 0.65$, $ANR_2 = 1.06$) system $ANR = 1.04$	99.9	0.070	14	0.274

Tables 7.4 and 7.5 show the system performance at the engine conditions as given in Table 7.1 and based on the figures in the Appendix G for the maximum NO_x conversion and the maximum PM oxidation respectively.

Table 7.4
SCR_F(®)+DOC₂+SCR system performance for maximum NO_x conversion efficiency

Maximum NO _x Conversion Efficiency								
Engine Condition	ANR ₁	ANR ₂	Urea flow rate in injector 1	Urea flow rate in injector 2	Total urea flow rate	System NO _x conversion efficiency	SCR _F (®) PM oxidation rate	SCR NH ₃ slip
[-]	[-]	[-]	[ml/s]	[ml/s]	[ml/s]	[%]	[g/min]	[ppm]
1	0.72	1.04	0.109	0.047	0.156	99.3	0.010	39
A	0.80	1.03	0.391	0.102	0.156	99.3	0.010	39
C	0.65	1.06	0.172	0.085	0.156	99.3	0.010	39
D	0.80	1.04	0.209	0.058	0.156	99.3	0.010	39
E	0.80	1.04	0.408	0.106	0.156	99.3	0.010	39

Table 7.5
SCR_F(®)+DOC₂+SCR system performance for maximum PM oxidation rate at ANR₁ = 0

Maximum PM Oxidation Rate with PM Loading 2 g/l					
Engine Condition	ANR ₂	Urea flow rate in injector 2	System NO _x conversion efficiency	SCR _F (®) PM oxidation rate	SCR _F (®) NH ₃ slip
[-]	[-]	[ml/s]	[%]	[g/min]	[ppm]
1	1.12	0.169	93.5	0.041	80
A	1.12	0.548	91.5	0.057	70
C	1.12	0.297	94.0	0.210	83
D	1.12	0.293	91.0	0.130	60
E	1.12	0.571	94.9	0.500	90

As can be observed from Table 7.4, the NO_x conversion efficiency of the system is over 99.2 % for all the engine conditions. The value of ANR₁ is in the range of 0.65 to 0.8 (0.72 +/- 0.08) depending on PM oxidation rate in the SCR_F(®), exhaust temperature, NO and NO₂ concentrations at the SCR_F(®) inlet and exhaust flow rate conditions. The ANR₂ has a much narrower range of 1.03 to 1.07 (1.04 +/- 0.02) and

the system is less sensitive to a change in the ANR₂ value compared to ANR₁.

In Table 7.5, the ANR₂ value for all cases is 1.12 in order to maximize the NO_x conversion efficiency while the PM oxidation rate in the SCR-F is the maximum possible value for the given engine condition. A higher NH₃ slip is also observed compared to the Table 7.4 at the same engine condition. The PM oxidation rates are 3-4 times higher than the values from Table 7.4, so these ANR₁ = 0 conditions can be used where a higher PM oxidation rate is desired while having a reduced NO_x reduction performance. The only way the SCR-F® system can increase the PM oxidation rate is to reduce the ANR, through the SCR-F® with a significant loss of NO_x conversion efficiency (40 % at ANR = 0.2 vs 85% at ANR = 0.8 in Figure 7.7). Table 7.6 compares the performance of the SCR-F® system with the SCR-F®+DOC₂+SCR system for maximum NO_x conversion efficiency.

Table 7.6
SCR-F®+DOC₂+SCR System Performance for Maximum PM Oxidation
Rate at ANR₁ = 0

Engine Condition	SCR-F system					SCR-F+DOC ₂ +SCR system				
	ANR	Total Urea flow	System NO _x conv. effi.	SCR-F PM oxid. rate	SCR-F NH ₃ slip	ANR ₁ /ANR ₂	Total Urea flow	System NO _x conv. effi.	SCR-F PM oxid. rate	SCR-F NH ₃ slip
[-]	[-]	[ml/s]	[%]	[g/min]	[ppm]	[-]	[ml/s]	[%]	[g/min]	[ppm]
I	1.06	0.160	91.0	0.001	41	0.72/1.04	0.156	99.3	0.010	39
A	1.05	0.514	97.6	0.005	25	0.80/1.03	0.493	99.8	0.013	24
C	1.07	0.284	97.4	0.040	80	0.65/1.07	0.258	99.9	0.070	17
D	1.06	0.277	95.0	0.012	97	0.80/1.04	0.268	99.2	0.036	28
E	1.08	0.555	98.0	0.028	174	0.80/1.03	0.513	99.8	0.040	19

As observed in Table 7.6, the SCR-F®+DOC₂+SCR system has 1.8 - 8.3 % higher NO_x conversion efficiency compared to the SCR-F system. The NH₃ slip was observed to be 20-174 ppm in SCR-F® system compared to 17 - 39 ppm in SCR-F®+DOC₂+SCR system due to better utilization of the NH₃. The total urea flow rate was also observed to be 1-3 % higher in the SCR-F® system while the PM oxidation rate is 140-300 % higher in the SCR-F®+DOC₂+SCR system compared to SCR-F®.

The conclusions from this parametric study are as follows :

SCR-F®+SCR (1 injector) system as compared to the SCR-F® system, results in slightly improved NO_x conversion efficiency and lower NH₃ slip without an improvement in the PM oxidation rate for engine condition C (Table 7.3).

The SCR_F($\text{\textcircled{R}}$)+SCR (2 injectors) system as compared to the SCR_F($\text{\textcircled{R}}$)+SCR (1 injector) system results in a slightly improved NO_x conversion efficiency and lower NH₃ slip with a 80% improvement in the PM oxidation rate for engine condition C (Table 7.3), because it is possible to operate at ANR₁ = 0.65 with this 2 injector system.

The SCR_F($\text{\textcircled{R}}$)+DOC₂+SCR system (2 injectors) as compared to the SCR_F($\text{\textcircled{R}}$)+SCR (2 injectors) system results in a 1.4 % improvement in the NO_x conversion efficiency and lower NH₃ slip and the same PM oxidation rate for engine condition C (Table 7.3), because the DOC₂ improves the NO₂/NO_x ratio in the 0.5 - 0.6 range for optimum NO_x reduction.

For both of the 2 injector systems (SCR_F($\text{\textcircled{R}}$)+DOC₂+SCR and SCR_F($\text{\textcircled{R}}$)+SCR), the PM oxidation rate is 80% higher at ANR₁ = 0.65 while achieving 99.9% NO_x conversion for the SCR_F($\text{\textcircled{R}}$)+DOC₂+SCR system compared to the SCR_F($\text{\textcircled{R}}$) only system for engine condition C (Table 7.3). A further gain in PM oxidation rate can be obtained by decreasing the ANR₁ between 0.65 and 0, if an increased PM oxidation rate and decreased NO_x conversion rate is desired. Neither of the 1 injector systems (SCR_F($\text{\textcircled{R}}$), SCR_F($\text{\textcircled{R}}$)+SCR) can achieve this level of PM oxidation rate with over 90% NO_x conversion efficiency.

For all engine conditions ANR₁ was found to be 0.72+/-0.08 and ANR₂ was 1.04+/-0.02 for maximum NO_x conversion efficiency for the SCR_F($\text{\textcircled{R}}$)+DOC₂+SCR system (Table 7.4). It appears that the ECU controller should be able to easily control these two urea flow rates that are mainly a function of the NO_x concentrations and exhaust flow rates from the sensors (Equation 7.1 and Figure 7.4)

Table 7.5 shows the maximum PM oxidation rate that can be achieved by the SCR_F($\text{\textcircled{R}}$)+DOC₂+SCR system using ANR₁ = 0 for all engine conditions. The PM oxidation rate is 3 - 4 times higher than the oxidation rate for the SCR-F system at the same engine conditions. This change in ANR₁ can be used for engine and PM loading conditions where high PM oxidation rate and a NO_x conversion efficiency greater than 91 % is desirable.

The SCR_F($\text{\textcircled{R}}$)+DOC₂+SCR system has 1.8-8.3 % higher NO_x conversion efficiency and 140-300% higher PM oxidation rate with 1-3 % lower urea flow rate and 2-150 ppm lower NH₃ slip for all engine conditions at maximum NO_x conversion efficiency compared to the SCR_F($\text{\textcircled{R}}$) system (Table 7.6).

7.3 Control System Design

The SCR_F($\text{\textcircled{R}}$)+DOC₂+SCR system described in Figure 7.4 consists of a control system that will be implemented in the ECU (controller) to determine the amount of urea to be injected in both the urea injectors based on the given exhaust flow rate, exhaust gas temperature, NO and NO₂ concentration and SCR_F($\text{\textcircled{R}}$)PM loading.

The control system consists of DOC, SCR-F, DOC₂ and SCR state estimators that are coupled to estimate the states of PM mass retained, NH₃ coverage fraction and temperatures. The exhaust gas chemical species concentrations change as the exhaust flows through each of the devices. This variation in chemical species concentration of NO, NO₂ and NH₃ is also computed and tracked by the four estimators. These data are then used by the control algorithm to control the PM oxidation rate in the SCR_F($\text{\textcircled{R}}$) and system NO_x conversion efficiency.

Equations 7.4 to 7.17 show a possible set of governing equations for the energy and chemical species mass balances that can be used in the four state estimators. A detailed description of these estimators is given in references [49][42][44] . It should be noted that alternative state estimators could be used such as neural networks or other machine learning techniques.

DOC and DOC₂ state estimator equations [42]

$$T_{r,k} = T_{r,k-1} - \frac{\rho u c_p}{\rho_s c_s + \rho c_v} \frac{\Delta t}{\Delta x} (T_{r,k} - T_{r,k-1}) - \frac{A_g \Delta t}{(\rho_s c_s + \rho c_v)(1 - \epsilon)} \sum_{i=CO}^{C_3H_6} \frac{\Delta h_i R R_i}{MW_i} \quad (7.4)$$

$$C_{i,r} = C_{i,r-1} - \frac{\Delta x}{\epsilon u} R R_i \quad (7.5)$$

Where :

$T_{r,k}, T_{r,k-1}$ = Exhaust gas temperature at axial location r at time k and k-1 seconds.

$\Delta t, \Delta x$ = Time in seconds and axial distance in meters

ρ, ρ_s = Density of exhaust gas and substrate in kg/m^3

c_s, c_v = Specific heat of substrate and exhaust gas in $kJ/kg.K$
 A_g = Geometric surface area in m^3
 ϵ = Void fraction of the catalyst (-)
 i = Index for chemical species (-)
 RR = reaction rate in $kmol/s$
 Δh = Heat of formation of a given reaction in $kJ/kmol$
 MW_i = Molecular weight of species i
 $C_{i,r}, C_{i,r-1}$ = Concentration of chemical species i at location r and $r-1$ in $kmol/m^3$
 u = Velocity of exhaust gas in the channel in m/s

Equation 7.4 represents the energy conservation of the exhaust gas flowing through the DOC in order to calculate the temperature of the filter. In order to calculate the temperature of the substrate, the heat capacity of the filter and exhaust gas is taken into account in the first term. In the second term energy release by the HC oxidation reactions is added to the filter temperature states.

This filter temperature from Equation 7.4 is in turn used in the reaction rate calculations that form part of equation 7.5 that calculates the chemical species concentration of NO, NO₂, CO and HC as they flow through the DOC. These coupled system of equations are applicable for both the DOC and DOC₂.

SCR-F state estimator equations [49][44]

$$T_{r,k} = T_{r,k-1} - \frac{\dot{Q}_{cond,axial} + \dot{Q}_{cond,radial} + \dot{Q}_{conv}}{\rho_s c_s V s + \rho c_v V f} - \frac{\dot{Q}_{reac,PM} + \dot{Q}_{reac,HC} + \dot{Q}_{reac,SCR} + \dot{Q}_{amb}}{\rho_s c_s V s + \rho c_v V f} \quad (7.6)$$

$$C_{i,r} = C_{i,r-1} + \frac{D_i}{\Delta y} (C_{i,r-1} - C_{i-1,r-1}) - \frac{\Delta y}{v_w} RR_i \quad (7.7)$$

$$\theta_{1,k} = \theta_{1,k-1} + \frac{\sum_{k=ads,1}^{SCR\ oxid} \eta_k RR_k}{\Omega_1} \quad (7.8)$$

$$\theta_{2,k} = \theta_{2,k-1} + \frac{\sum_{k=ads,2}^{des,2} \eta_k RR_k}{\Omega_2} \quad (7.9)$$

$$(\Delta P_{Total})_k = (\Delta P_{channel} + \Delta P_{wall} + \Delta P_{cake})_k \quad (7.10)$$

$$\dot{m}_{c,retained} = \eta_{cake} \dot{m}_{in} - \dot{m}_{c,oxid} \quad (7.11)$$

$$\dot{m}_{w,retained,n} = \eta_{wall,n} \dot{m}_{slab,n-1} - \dot{m}_{w,oxid,n} \quad (7.12)$$

$$\dot{m}_{in,PM} = \left(\frac{\dot{m}_{exhaust}}{\rho_{exhaust}} \right) * \left(\frac{C_{PM}}{1e-6} \right) * \left(\frac{T_{ref}}{T_{exhaust}} \right) \quad (7.13)$$

Where :

Δy = Axial distance in y direction in meters

ρ_f, ρ_s = Density of PM cake and substrate in kg/m³

V_f, V_s = Volume of PM cake and substrate in m³

c_f, c_s = Specific heat of PM cake and substrate in kJ/kg.K

η = Stoichiometric coefficient (-)

$\dot{Q}_{cond,axial}, \dot{Q}_{cond,radial}, \dot{Q}_{conv}$ = Heat transfer by conduction in axial, radial direction and convection in kJ/s

$\dot{Q}_{reac,PM}, \dot{Q}_{reac,HC}, \dot{Q}_{reac,SCR}$ = Energy release by PM , HC oxidation and SCR reactions in kJ/s

D_i = Diffusivity of chemical species i in m²/s

v_w = Velocity of exhaust gas in the channel in m/s

k = Index for reactions (adsorption, desorption, Standard, fast and slow SCR, NH₃ oxidation reactions)

θ_1, θ_2 = Coverage fraction of first and seconds NH₃ storage sites (-)

Ω_1, Ω_2 = Maximum storage capacity of NH₃ first and seconds NH₃ storage sites in kmol/m³

ΔP_{Total} = Total pressure drop across the SCR-F in kPa

$\Delta P_{channel}, \Delta P_{wall}, \Delta P_{cake}$ = Pressure drop in the inlet/outlet channels, substrate wall and PM cake

$\dot{m}_{c,retained}, \dot{m}_{w,retained,n}$ = Rate of PM mass retained in the PM cake and wall slab n in the SCR-F in (kg/s)

$\eta_{cake}, \eta_{wall,n}$ = Filtration efficiency of PM cake and wall slab n (-)

$\dot{m}_{in}, \dot{m}_{slab,n-1}$ = PM mass flow rate into PM cake and given wall slab n in kg/s

$\dot{m}_{c,oxid}, \dot{m}_{w,oxid,n}$ = PM oxidation rate in the PM cake and wall slab n in kg/s

$\dot{m}_{exhaust}$ = Actual mass flow rate of exhaust in kg/s

$\dot{m}_{in,PM}$ = Rate of PM mass into the SCR-F kg/s

ρ_{exh} = Density of exhaust gas in kg/ actual m³

C_{PM} = Concentration of PM in mg/scm

$T_{exhaust}, T_{std}$ = Exhaust gas and ambient standard air temperature in K.

Equation 7.6 represents energy conservation of the SCR-F® substrate in both the

radial and axial directions. The conduction of heat in both the radial and axial direction is taken into account along with the convection heat transfer from the exhaust gas to the substrate wall. The energy release by HC oxidation, PM oxidation and SCR reactions are also modeled.

The filter temperature from equation 7.6 is used in equation 7.7 along with the concentrations of chemical species to calculate the change in concentration of NO, NO₂, NH₃, O₂ and HC across the SCR-F in equation 7.7. This species conservation equation consists of both convection and diffusion based mass transfer terms along with a third term that models chemical reaction effects.

The NO, NO₂ and NH₃ species concentrations from Equation 7.7 are used to calculate the reaction rates in Equation 7.6 and Equations 7.8 and 7.9. Equations 7.8 and 7.9 track the change in NH₃ coverage fraction of the two NH₃ storage sites.

The NO₂ concentration from equation 7.7 is also used in equation 7.11 to calculate the PM oxidation rate by NO₂ assisted PM oxidation reaction. This equation determines the PM mass retained in the PM cake and substrate wall due to filtration and PM oxidation. The PM mass retained from Equation 7.11 is the input to Equation 7.12 to calculate the cake and wall pressure drop components. Combined with a cake permeability model and channel pressure drop values Equation 7.10 determines the pressure drop across the SCR-F.

The system of coupled Equations 7.6 to 7.13 are solved in a 2D mesh in the SCR-F model to compute all the relevant states and. outputs consisting of temperature of filter, outlet concentrations, NH₃ coverage fraction of the two NH₃ storage sites, PM mass retained in the PM cake, substrate wall and pressure drop across the SCR-F.

SCR state estimator equations [42]

$$T_{r,k} = T_{r,k-1} - \frac{\rho u c_p}{(\rho_s c_s + \rho c_v)} \frac{\Delta t}{\Delta x} (T_{r,k} - T_{r,k-1}) - h_a \frac{4a_w \Delta t}{(\rho_s c_s + \rho c_v)(a_p^2 - a_w^2)} (T_{r,k-1} - T_a) \quad (7.14)$$

$$C_{i,r} = C_{i,r-1} - \frac{\Delta x}{\epsilon u} RR_i \quad (7.15)$$

$$\theta_{1,k} = \theta_{1,k-1} + \frac{\sum_{k=ads,1}^{SCR\ oxid} \eta_k RR_k}{\Omega_1} \quad (7.16)$$

$$\theta_{2,k} = \theta_{2,k-1} + \frac{\sum_{k=ads,2}^{des,2} \eta_k RR_k}{\Omega_2} \quad (7.17)$$

Where:

h_a = Convection heat transfer coefficient to the ambient in W/m^2K

a_w = Geometric surface area in m^2

T_a = Ambient temperature $^{\circ}C$

a_p, a_w = Width of monolith and open channel in m

Equation 7.14 represents energy conservation of the SCR substrate. The heat transfer to the ambient is modeled using the second term on the right hand side of the equations. The filter temperature from Equation 7.14 is used in Equation 7.15 along with species concentrations to calculate the change in concentration of NO, NO₂ and NH₃ across the SCR-F in Equation 7.15. This species conservation equation models a term for chemical reaction effects.

The NO, NO₂ and NH₃ species concentrations from Equation 7.15 are used in Equations 7.16 and 7.17 to model the change in NH₃ coverage fraction of the two NH₃ storage sites. The system of coupled equations 7.14 to 7.17 are solved to compute all filter temperatures, NH₃ coverage fraction for the two NH₃ storage sites and the outlet concentrations of NO, NO₂ and NH₃.

7.3.1 Summary of the Ultra Low NO_x Control System Design and Performance

In summary for the systems, equations 7.4 to 7.17 represent the system being described in Figure 7.4 (DOC+SCR_F([®])+DOC₂+SCR system). Equations 7.4 and 7.5 are used in the 1D DOC state estimator developed by Surehalli et al. [42] which are used for the state estimation of both the DOC and DOC₂ in Figure 7.4. Equations 7.6 to 7.13 are based on the 2D SCR-F model from reference [49] and 2D CPF state estimation work by Boopathi et al. from reference [44]. Equations 7.14 to 7.17 are based on the 1D SCR state estimator work by Surehalli et al. [42]. Figure 7.14 describes the complete system that can be used to determine the desired urea flow rate for the two urea injectors based on the control algorithm.

The control algorithm determines the ANR_1 and ANR_2 values based on the engine map to determine the PM oxidation rate in the SCR-F and the system NO_x conversion rate based on the desired reaction rates with respect to engine out temperature, NO , NO_2 and PM concentrations and PM mass retained in the SCR-F. This control algorithm can be configured to either maximize NO_x conversion efficiency, minimize urea consumption, maximize the PM oxidation rate in the SCR-F or any combination of these objectives based on engine out exhaust temperature and flow rate, pressure drop in the SCR-F®, PM loading, NO_x concentration for a given engine speed and load condition.

The advantages of the SCR-F®+DOC₂+SCR system (2 injectors) being modeled are :

- 1) The system has a 99.2 to 99.9 % NO_2 conversion efficiency as compared to 91.0 - 98.0 % for the SCR-F for all the engine conditions (Table 7.6)
- 2) The system has a 0.013 to 0.070 g/min PM oxidation rate as compared to 0.005 to 0.040 g/min for the SCR-F for all the engine conditions (Table 7.6)
- 3) The system has a 17 to 39 ppm NH_3 slip as compared with 20 to 174 ppm for the SCR-F® for all the engine conditions (Table 7.6)
- 4) The SCR-F®+DOC₂+SCR system enables 3-4 times higher PM oxidation as compared to the SCR-F® system (Table 7.5 and 7.6) when $ANR_1 = 0$ which is used in engine conditions where higher PM oxidation rate and 91 - 95% NO_x conversion efficiency is desirable (Table 7.5). The only way the SCR-F only system can increase the PM oxidation rate is to reduce the ANR through the SCR-F with a significant loss of NO_x conversion efficiency (40 % at $ANR = 0.2$ vs 85 % at $ANR = 0.8$ in Figure 7.8).
- 5) The tradeoff between PM oxidation rate and NO_x conversion efficiency can be determined by the control algorithm in the SCR-F®+DOC₂+SCR system based on the engine map for a given engine speed and load condition. The control system can also operate over a limited range of ANR_1 (0.72+/-0.08) and ANR_2 (1.04+/-0.02) conditions without a loss in NO_x conversion efficiency and PM oxidation rate, enabling a more robust control system.

The systems described in Figures 7.3 and 7.4 and the performance of these systems

is based on existing DOC, SCRF® and SCR components described in Table 7.2. The catalyst loading of each device can also be modified along with sizing of the components to better optimize for various engine applications and to improve the PM oxidation rate, NH₃ slip and the NO_x conversion efficiency including the volume and cost of the system. The estimator models used for the control system design and sensor layout can also be modified to make the system more suitable for a given application.

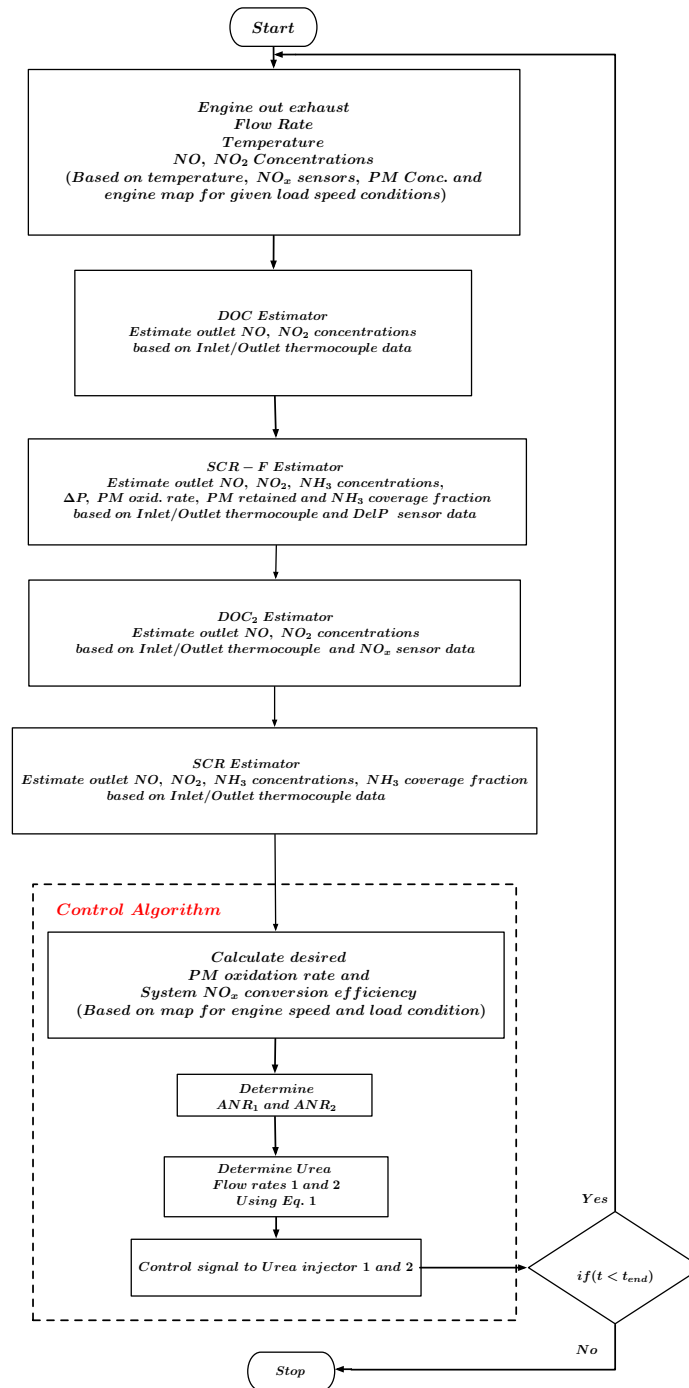


Figure 7.14: DOC+SCR(®)+DOC2+SCR control system flowchart

7.4 Further Improvements to the Ultra Low NO_x System

The DOC and DOC₂ are flow through devices that can be designed to consist of different types of catalysts such as platinum, palladium, rhodium, barium etc., which can be used to absorb, adsorb and oxidize hydrocarbons, carbon monoxide and NO present in the exhaust gas. The oxidation of NO to NO₂ is one of the main reactions that will be used in the DOC and DOC₂ in the proposed system to improve the system NO_x conversion efficiency.

The SCR-F is a wall flow type device which can contain different types of catalysts such as vanadium, copper zeolite, iron zeolite etc and different physical structure and cell design consisting of porous materials. The catalyst is responsible for adsorption of reductants such as NH₃ and reduction of NO_x to nitrogen and water vapor using the SCR reactions. The physical structure of the SCR-F can also be comprised of different materials such as silicon carbide, other ceramics, metallic meshes or any form of porous material. The SCR uses similar catalysts as the SCR-F in a flow through setup to reduce NOx emissions in the exhaust gas into nitrogen and water vapor by SCR reactions.

The AMOX downstream of the SCR is responsible for oxidation of outlet NH₃ from the SCR into nitrogen and water vapor using a flow-through substrate that can use various oxidation catalysts. The ammonia delivery systems can also be of various approaches that are in the literature. The concept of a DOC₂ downstream of the CPF before the urea injector in the production system shown in Figure 1.2 should also enhance the NO_x conversion efficiency of the system.

Recently degradation of the SCR-F and SCR NO_x reduction performance due to migration of platinum from upstream DOC was reported by Hurby et al. [70]. The negative impact of this degradation in SCR-F performance can be mitigated by switching the ratio of ANR₁ and ANR₂ such that the ANR₂ value is increased by the control algorithm to enable higher NO_x conversion in SCR enabling the system to meet the > 99.5% NO_x conversion target. Further studies on the migration of PGM catalyst from DOC to SCR-F need to be performed to design DOC's that are not susceptible to this issue. Reduction of number of active regeneration events which is one of the advantages of the proposed ultra low NO_x system can also reduce the degradation

rate. Further experimental work on ultra low NO_x system with these considerations need to be performed for the development of the ultra low NO_x aftertreatment system.

Chapter 8

Summary and Conclusions

This chapter presents the summary of the results obtained from the SCR-F model described in Chapter 3 using the calibration process described in Chapter 4 for using the experimental data collected on the 2013 Cummins ISB SCR-F® to determine the calibration parameters for the model. The chapter also describes the conclusions from the SCR-F® configuration 3 dataset which consisted of 2D SCR-F+1D SCR model, the 2D SCR-F state estimator and the ultra low NO_x aftertreatment system.

8.1 Summary of SCR-F Model Development

The 2D SCR-F model development was described in Chapter 3. The SCR-F model was developed using a set of governing equations consisting of conservation of energy, mass, momentum and concentration of chemical species. Pressure drop, filtration and cake permeability equations were used to simulate the pressure drop and filtration characteristics of the SCR-F. The model was used to simulate the performance of the SCR-F during active regeneration and passive oxidation with and without urea injection. The major phenomena that were simulated by the SCR-F model are as follows :

- 2D temperature distribution in the substrate wall and exhaust gas in the inlet/outlet channels

- 2D PM mass distribution and PM mass retained in the PM cake and wall
- 2D NH₃ coverage fraction of the two NH₃ storage sites
- Filtration efficiency of PM cake and substrate wall
- Change in chemical species concentrations of NO, NO₂, NH₃ and HC using reaction diffusion scheme with forward diffusion between PM cake and substrate wall.
- Inhibition of SCR reactions by PM in the substrate wall
- Impact of urea injection on PM oxidation rate
- Cake permeability during PM oxidation and pressure drop characteristics

A calibration procedure for this 2D SCR-F model was developed using the experimental data consisting of passive oxidation experiments with and without urea injection. The pressure drop, filtration, thermal, diffusion and cake permeability parameters along with NO₂ assisted PM oxidation kinetics were modeled. Active regeneration experiments were used to determine the HC oxidation and thermal PM oxidation kinetics. Experiments with the urea dosing cycle with and without PM loading were used to determine the SCR kinetics, NH₃ storage parameters and the inhibition of SCR reactions to mass transfer limitation by substrate wall PM.

8.2 Summary of the Results from SCRF[®] Configuration 1 and 2 Data

The configuration 1 and 2 data were used to calibrate the SCR-F model. The following inputs obtained from these experiments were used to run the SCR-F model :

- Exhaust gas and fuel mass flow rate at the SCRF [®] inlet
- Exhaust gas temperature at SCRF [®] inlet
- Concentration of chemical species (NO, NO₂, NH₃, CO, CO₂, HC, O₂ and PM concentration) at SCRF [®] inlet.

- Test cell conditions (temperature, pressure and relative humidity)

The model was calibrated using the experimental data along with the model values for the following variables

- Pressure drop across the SCR-F (R)
- Filtration efficiency
- Temperature distribution at the 20 thermocouple locations
- PM mass retained
- SCR-F (R) outlet chemical species concentration of NO, NO₂, NH₃ and HC.

The deviation in these values for all the thirty experiments in the configuration 1 and 2 datasets is quantified in Appendix G. Using the single set of filtration, pressure drop, cake permeability and thermal parameters in Tables G.1 to G.1 and SCR, PM oxidation kinetics from Table G.3 to G.4, the SCR-F model was able to simulate the experimental data :

- Pressure drop across the SCR-F (R) was simulated to within +/- 0.3 kPa
- Filtration efficiency was simulated to within +/- 1 %
- 2D Temperature distribution was simulated to within +/- 5°C
- PM mass retained was simulated to within +/- 2g
- SCR-F (R) outlet NO, NO₂ and NH₃ were simulated to within +/- 20 ppm

The following phenomena were determined during calibration of the SCR-F model with configuration 1 and 2 data.

- A 70% reduction in PM oxidation rate during passive oxidation due to forward diffusion during urea injection

- An increase in cake permeability due to forward diffusion during urea injection with passive oxidation
- A temperature rise of 5 - 15 °C of the exhaust gas due to SCR reactions during passive oxidation
- A temperature rise 10 - 20 ° C during active regeneration due to HC oxidation reaction
- 4 - 6 % reduction in NO_x conversion performance due to PM loading caused by mass transfer limitation in the substrate wall and change in the local NO₂/NO_x ratio across the PM cake due to the passive oxidation reaction

8.3 Summary of the Results from SCRF® Configuration 3 Data

The SCRF® configuration 3 data were collected with a SCRF® and a downstream SCR. These data were simulated with a model consisting of the 2D SCR-F model and 1D SCR model. This model used the calibration parameters identified for the individual component models. The interaction of SCRF® with the downstream SCR in terms of change local NO₂/NO_x ratio, NO_x reduction efficiency and NH₃ slip was studied using this dataset. The model was able to simulate the following variables

- Pressure drop across SCRF® to within +/- 0.3kPa
- Filtration efficiency of SCRF® to within +/- 1%
- Temperature distribution in SCRF® to within +/-5°C
- SCR outlet NO and NO₂ concentration to within +/- 15 ppm
- SCR outlet NH₃ concentration to within +/- 8 ppm

The major phenomena observed in this data consists of :

1. The NO₂/NO_x ratio at the SCR inlet is equal to 0 for all the experiments due to consumption of NO₂ in the SCRF® by SCR reactions and passive PM oxidation reactions.

2. The unfavorable NO_2/NO_x ratio at SCR inlet led to low conversion efficiency in the SCR (<70%) thus limiting system NO_x reduction performance to < 97.5%
3. Low NO_x and SCR inlet NH_3 concentrations led to significant NH_3 slip due to low adsorption rate of both the storage sites in the SCR.

8.4 Summary of the Results from SCRF[®] Ultra Low NO_x Aftertreatment System Modeling

Based on the limitation caused by NO_2/NO_x ratio at the SCR inlet in the SCR-F + SCR system from configuration 3, a new system was modeled that could reach a NO_x conversion efficiency > 99.5 % for inlet exhaust gas temperatures > 200°C. The major features of this aftertreatment system are as follows:

1. Addition of a second DOC downstream of SCR-F referred to as DOC_2 to boost the SCR inlet NO_2/NO_x ratio thus increasing the SCR and system NO_x conversion performance.
2. Addition of a second urea injector and decomposition tube for the SCR.
3. A control algorithm that optimizes the urea injection in the two urea injectors to enable > 99.5% NO_x reduction while maximizing PM oxidation rate in the SCR-F and minimize NH_3 slip at SCR outlet thus reducing the size of AMOX downstream of the SCR.

Based on these changes, a model that can simulate such a system was developed based on the 2D SCR-F, 1D SCR and 1D DOC models and existing kinetics for each of the models. A parametric study at different urea injection values for the two injectors was performed. The parametric study found operating points based on configuration 3 data where >99.5% NO_x conversion with upto 90 % increase in passive oxidation rate in the SCRF[®] can be achieved .

Based on these results, a possible control algorithm that can achieve the above stated performance targets has been developed. Further improvement in the system with the addition of an external electrical heater at the DOC inlet and improvement in the

low temperature performance of the SCR and DOC catalyst can lead to a system that has the potential to meet the 0.02 g/bhp-hr. NO_x standard using components for both cold start and hot conditions.

8.5 Summary of the Results from SCRF[®] State Estimator

The SCRF[®] state estimator was developed based on a simplified SCR-F model that was combined with the extended Kalman filter equations to estimate the following unknown internal states:

1. 2D temperature distribution of substrate and exhaust gas
2. 2D PM mass distribution
3. 2D NH₃ coverage fraction of the two NH₃ storage sites

In order to estimate these states, the following sensor data were used :

1. Thermocouple data at SCRF[®] outlet
2. Pressure drop sensor data
3. SCRF[®] outlet NO_x sensor data

The estimator was able to correct for errors in the calibration parameters and also filter out the zero mean Gaussian noise introduced into the sensor readings as described in Chapter 6. The resultant estimator can predict the PM mass retained to within +/- 1.5 g, temperature distribution to within +/- 5°C and outlet NO, NO₂ and NH₃ concentration to within +/- 15 ppm of actual values.

8.6 Summary of Major Findings from the Research

A 2D SCR-F model was developed in this work based on MPF model developed in [53][71][50] with an addition of a 2D species model based on the diffusion-reaction scheme and the addition of SCR reactions [37][2]. The model was calibrated with thirty experiments from the Cummins 2013 ISB SCRF® consisting of four active regeneration experiments, fourteen passive oxidation experiments with and without urea injection, twelve NO_x reduction experiments with PM loading of 0, 2 and 4 g/l loading. All the experimental data were calibrated to within 2 gm of the experimental PM mass retained, within 0.1 kPa of the experimental pressure drop and the outlet NO, NO₂, NH₃ concentrations were calibrated to within 20 ppm of the experimental data. The temperature distribution in 2D was calibrated to within 5°C of the experimental data for all the experiments during NO_x reduction, PM oxidation and active regeneration conditions. The major findings from this research are:

1. A two-site model was used for storage of the NH₃ inside the SCRF® with the first site participating in both the storage and SCR reactions and the second site was used for only storage.
2. The outlet NO, NO₂ and NH₃ concentrations during urea injection are a strong function of the PM loading in the substrate wall and the resultant inhibition effect on the SCR reactions. The concept of effectiveness factor was used to simulate the change in SCR reaction rate with a change in the PM loading inside the substrate wall.
3. The injection of urea during passive oxidation leads to a 60-70 % reduction in the NO₂ assisted PM oxidation rate due to a change in the effective NO₂ available in the PM cake caused by forward diffusion of the NO₂ from PM cake to the substrate wall. A Tortuosity value of 8 was found as part of the calibration to simulate this decrease in the oxidation rate during urea injection.
4. A significant decrease (85% decrease) in the PM oxidation rate in the PM present in the substrate wall was observed for the experiments with urea injection due to the competition for NO₂ inside the substrate wall between the NO₂ assisted PM oxidation and the SCR reactions.

5. The NO_x reduction by the SCR reactions release energy into the exhaust gas that affects the temperature distribution and the resultant PM distribution in the SCR-F®.
6. The pressure drop was significantly affected by urea injection in the SCR-F® during PM oxidation. The change in pressure drop characteristics was found to cause a change in the wall PM oxidation rate and cake permeability. The wall pressure drop was affected by the change in PM oxidation rate due to competition for NO_2 inside the substrate wall. The PM cake pressure drop change is due to a change in cake permeability characteristics of the SCR-F® due to forward diffusion of NO_2 between the PM cake and the substrate wall.
7. The contribution of NO_2 assisted PM oxidation during active regeneration was found to be 20 % for active regeneration experiments from the CPF experimental [52] compared to a contribution of 5 % in the case of active regeneration in the SCR-F®. This change in reaction rate is attributed to the lack of backward diffusion of NO_2 from substrate wall to the PM cake in the SCR-F® due to a change in the catalyst used, from an oxidation to reduction catalyst.
8. A SCR-F state estimator that can estimate the internal states of the SCR-F® including 2D temperature, PM mass and NH_3 coverage fraction distribution using pressure drop, outlet thermocouple and outlet NO_x sensor data was developed.
9. In the SCR-F®+SCR system, the downstream SCR NO_x conversion performance was limited by the SCR inlet NO_2/NO_x ratio to a maximum value of 60%.
10. A ultra low NO_x system based on a SCR-F® with downstream DOC and SCR with two urea injectors was modeled. This system can achieve > 99.5% NO_x conversion while providing the potential for up to 90% improvement in the PM oxidation performance of the system.

8.7 Major Conclusions from the Research

The main conclusions from this work are as follows :

1. A 2D SCR-F model capable of simulating the 2D spatial distribution on temperature, PM mass retained and coverage fraction of two NH_3 storage sites was developed. The model was able to simulate pressure drop, filtration efficiency, outlet NO , NO_2 and NH_3 concentrations and PM mass retained to within 5% of the experimental data collected on a Johnson Matthey SCR[®] with a Cummins 2013 ISB engine.
2. A 70% reduction in the PM oxidation rate during urea injection was observed and simulated for the passive oxidation cases using the forward diffusion of NO_2 from the PM cake to the substrate wall layer.
3. A 85% reduction in the substrate wall PM oxidation rate during urea injection due to the competition for NO_2 between the PM oxidation and SCR reactions was simulated.
4. A 10 - 15^oC increase in exhaust gas temperature due to HC oxidation reaction was observed in the SCR[®] during active regeneration. A similar temperature rise of 5 - 15 ^oC for the exhaust gas due to the SCR reactions was observed and simulated during urea injection.
5. Significant change in cake permeability due to forward diffusion of NO_2 during urea injection was observed compared to the cases with no urea injection (3 times higher change in cake permeability ratio)
6. Due to the absence of a oxidation catalyst in the substrate wall, the contribution of NO_2 assisted PM oxidation during active regeneration was observed to be less than 8% of the total PM oxidation rate compared to a CPF from reference [53] where a 20 % contribution was observed for the same engine conditions.
7. Inhibition of SCR reactions due to mass transfer limitation caused by PM in the substrate wall led to 2-4% reduction in NO_x reduction efficiency of the SCR[®].
8. Change in local NO_2/NO_x conversion efficiency due to PM oxidation led to 1-2% reduction in NO_x conversion efficiency of the SCR[®].

9. Local NO_2/NO_x ratio played an important role in the SCR-F®+SCR system (Configuration 3) NO_x conversion efficiency leading to a 30 - 60 % reduction in NO_x conversion efficiency of the downstream SCR due to unfavorable NO_2/NO_x ratio and a significant amount of NH_3 slip.
10. A SCR-F state estimator capable of estimating internal states of 2D spatial distribution of temperature, PM mass retained and NH_3 coverage fraction based on outlet thermocouple, NO_x and pressure drop sensors was developed.
11. The modeled ultra low NO_x system is capable of NO_x conversion efficiencies greater than 99.5% and the potential for a 90-100% increase in passive oxidation rate while minimizing the urea consumption and NH_3 slip for a temperature range of 200 - 450 °C encountered in typical engine operating condition.
12. Further work on the ultra low NO_x system in terms of improvements in low temperature Cu-Ze catalyst development, addition of diesel cold start catalyst (dCSCTM) and addition of a external heater could lead to a system capable of meeting the 0.02 g/bhp-hr. ultra low NO_x standard.

References

- [1] “DieselNet.” <https://www.dieseln.net/standards/us/hd.php>, 2017. Online; Accessed: 2017-09-30.
- [2] X. Song, *A SCR Model based on Reactor and Engine Experimental Studies for a Cu-zeolite Catalyst*. PhD thesis, Michigan Technological University, 2013.
- [3] X. Song, J. H. Johnson, and J. D. Naber, “A review of the literature of selective catalytic reduction catalysts integrated into diesel particulate filters,” *International Journal of Engine Research*, vol. 16, no. 6, pp. 738–749, 2015.
- [4] E. A. Gustafson, “An experimental investigation into no 2 assisted passive oxidation with and without urea dosing and active regeneration of particulate matter for a scr catalyst on a dpf,” Master’s thesis, Michigan Technological University, 2016.
- [5] V. Kadam, “An experimental investigation of the effect of temperature and space velocity on the performance of a cu-zeolite flow-through scr and a scr catalyst on a dpf with and without pm loading,” Master’s thesis, Michigan Technological University, 2016.
- [6] S. Park, C. Rutland, K. Narayanaswamy, S. Schmieg, Y. He, and D. Brown, “Development and validation of a model for wall-flow type selective catalytic reduction system,” *Proceedings of the Institution of Mechanical Engineers, Part D: Journal of Automobile Engineering*, vol. 225, no. 12, pp. 1641–1659, 2011.
- [7] S.-Y. Park, K. Narayanaswamy, S. J. Schmieg, and C. J. Rutland, “A model development for evaluating soot-no x interactions in a blended 2-way diesel particulate filter/selective catalytic reduction,” *Industrial & Engineering Chemistry Research*, vol. 51, no. 48, pp. 15582–15592, 2012.

- [8] M. Colombo, G. Koltsakis, and I. Koutoufaris, "A modeling study of soot and de-nox reaction phenomena in scr systems," Tech. Rep. 2012-01-1083, SAE Technical Paper, 2011.
- [9] J. Tan, C. Solbrig, and S. J. Schmiege, "The development of advanced 2-way scr/dpf systems to meet future heavy-duty diesel emissions," Tech. Rep. 2011-01-1140, SAE Technical Paper, 2011.
- [10] Y. Yang, G. Cho, and C. Rutland, "Model based study of denox characteristics for integrated dpf/scr system over cu-zeolite," tech. rep., SAE Technical Paper, 2015.
- [11] T. C. Watling, M. R. Ravenscroft, and G. Avery, "Development, validation and application of a model for an scr catalyst coated diesel particulate filter," *Catalysis Today*, vol. 188, no. 1, pp. 32–41, 2012.
- [12] A. Konstandopoulos, M. Kostoglou, S. Lorentzou, and N. Vlachos, "Aspects of multifunctional diesel particulate filters and their efficient simulation," *Catalysis today*, vol. 188, no. 1, pp. 2–13, 2012.
- [13] F. Schrade, M. Brammer, J. Schaeffner, K. Langeheinecke, and L. Kraemer, "Physico-chemical modeling of an integrated scr on dpf (scr/dpf) system," *SAE International Journal of Engines*, vol. 5, no. 2012-01-1083, pp. 958–974, 2012.
- [14] E. Tronconi, I. Nova, F. Marchitti, G. Koltsakis, D. Karamitros, B. Maletic, N. Markert, D. Chatterjee, and M. Hehle, "Interaction of nox reduction and soot oxidation in a dpf with cu-zeolite scr coating," *Emission Control Science and Technology*, vol. 1, no. 2, pp. 134–151, 2015.
- [15] S. Dosda, D. Berthout, G. Mauviot, and A. Nogue, "Modeling of a doc scr-f scr exhaust line for design optimization taking into account performance degradation due to hydrothermal aging," *SAE International Journal of Fuels and Lubricants*, vol. 9, no. 2016-01-2281, pp. 621–632, 2016.
- [16] Y. M. López-De Jesús, P. I. Chigada, T. C. Watling, K. Arulraj, A. Thorén, N. Greenham, and P. Markatou, "Nox and pm reduction from diesel exhaust using vanadia scrf®," *SAE International Journal of Engines*, vol. 9, no. 2016-01-0914, pp. 1247–1257, 2016.
- [17] V. Strots, A. Kishi, S. Adelberg, and L. Kramer, "Application of integrated scr/dpf systems in commercial vehicles," in *JSAE Annual Congress, 454*, vol. 20145174, 2014.

- [18] O. Mihai, S. Tamma, M. Stenfeldt, and L. Olsson, “Effect of soot on the scr reactions in an integrated scr coated dpf,” in *24th North American Catalysis Society Meeting. Nam*, 2015.
- [19] O. Mihai, S. Tamm, M. Stenfeldt, C. Wang-Hansen, and L. Olsson, “Evaluation of an integrated selective catalytic reduction-coated particulate filter,” *Industrial & Engineering Chemistry Research*, vol. 54, no. 47, pp. 11779–11791, 2015.
- [20] L. Cumararatunge, A. Chiffey, J. Stetina, K. McGonigle, G. Repley, A. Lee, and S. Chatterjee, “A study of the soot combustion efficiency of an scrf® catalyst vs a csf during active regeneration,” *Emission Control Science and Technology*, vol. 3, no. 1, pp. 93–104, 2017.
- [21] K. Johansen, A. Widd, F. Zuther, and H. Viecz, “Passive no 2 regeneration and nox conversion for dpf with an integrated vanadium scr catalyst,” Tech. Rep. 2016-01-0915, SAE Technical Paper, 2016.
- [22] J. H. Lee, M. J. Paratore, and D. B. Brown, “Evaluation of cu-based scr/dpf technology for diesel exhaust emission control,” *SAE International Journal of Fuels and Lubricants*, vol. 1, no. 2018-01-0072, pp. 96–101, 2009.
- [23] W. Tang, D. Youngren, M. SantaMaria, and S. Kumar, “On-engine investigation of scr on filters (scrof) for hdd passive applications,” *SAE International Journal of Engines*, vol. 6, no. 2013-01-1066, pp. 862–872, 2013.
- [24] M. Naseri, S. Chatterjee, M. Castagnola, H.-Y. Chen, J. Fedeyko, H. Hess, and J. Li, “Development of scr on diesel particulate filter system for heavy duty applications,” *SAE International Journal of Engines*, vol. 4, no. 2011-01-1312, pp. 1798–1809, 2011.
- [25] G. Cavataio, J. W. Girard, and C. K. Lambert, “Cu/zeolite scr on high porosity filters: laboratory and engine performance evaluations,” Tech. Rep. 2009-01-0897, SAE Technical Paper, 2009.
- [26] O. Mihai, S. Tamm, M. Stenfeldt, and L. Olsson, “The effect of soot on ammonium nitrate species and no2 selective catalytic reduction over cu–zeolite catalyst-coated particulate filter,” *Phil. Trans. R. Soc. A*, vol. 374, no. 2061, p. 20150086, 2016.
- [27] E. A. Kladopoulou, S. L. Yang, J. H. Johnson, G. G. Parker, and A. G. Konstantopoulos, “A study describing the performance of diesel particulate filters during loading and regeneration—a lumped parameter model for control applications,” Tech. Rep. 2003-01-0842, SAE Technical Paper, 2003.

- [28] K. Rose, H. Hamje, L. Jansen, C. Fittavolini, R. Clark, M. D. C. Almena, D. Katsaounis, C. Samaras, S. Geivanidis, and Z. Samaras, "Impact of fame content on the regeneration frequency of diesel particulate filters (dpfs)," *SAE International Journal of Fuels and Lubricants*, vol. 7, no. 2014-01-1605, pp. 563–570, 2014.
- [29] N. Nagar, X. He, V. Iyengar, N. Acharya, A. Kalinowski, A. Kotrba, T. Gardner, and A. Yetkin, "Real time implementation of doc-dpf models on a production-intent ecu for controls and diagnostics of a pm emission control system," *SAE International Journal of Commercial Vehicles*, vol. 2, no. 2009-01-2904, pp. 222–233, 2009.
- [30] V. Mulone, A. Cozzolini, P. Abeyratne, D. Littera, M. Thiagarajan, M. Besch, and M. Gautam, "Soot modeling for advanced control of diesel engine aftertreatment," *Journal of Engineering for Gas Turbines and Power*, vol. 133, no. 12, p. 122804, 2011.
- [31] C. Depcik, C. Langness, and J. Mattson, "Development of a simplified diesel particulate filter model intended for an engine control unit," Tech. Rep. 2014-01-1559, SAE Technical Paper, 2014.
- [32] C. Depcik, "Combining the classical and lumped diesel particulate filter models," *SAE International Journal of Engines*, vol. 8, no. 2015-01-1049, pp. 1261–1270, 2015.
- [33] Y. Miyairi, S. Miwa, F. Abe, Z. Xu, and Y. Nakasuji, "Numerical study on forced regeneration of wall-flow diesel particulate filters," Tech. Rep. 2001-01-0912, SAE Technical Paper, 2001.
- [34] Y. Yi, "Simulating the soot loading in wall-flow dpf using a three-dimensional macroscopic model," Tech. Rep. 2006-01-0264, SAE Technical Paper, 2006.
- [35] A. G. Konstandopoulos and J. H. Johnson, "Wall-flow diesel particulate filters—their pressure drop and collection efficiency," Tech. Rep. 890405, SAE Technical Paper, 1989.
- [36] O. Haralampous, I. Kandylas, G. Koltsakis, and Z. Samaras, "Diesel particulate filter pressure drop part 1: Modelling and experimental validation," *International Journal of Engine Research*, vol. 5, no. 2, pp. 149–162, 2004.
- [37] K. C. Premchand, *Development of a 1-D catalyzed diesel particulate filter model for simulation of the performance and the oxidation of particulate matter and nitrogen oxides using passive oxidation and active regeneration engine experimental data*. PhD thesis, Michigan Technological University, 2013.

- [38] D. Upadhyay and M. Van Nieuwstadt, "Model based analysis and control design of a urea-scr denox aftertreatment system," *Journal of dynamic systems, measurement, and control*, vol. 128, no. 3, pp. 737–741, 2006.
- [39] M. Devarakonda, G. Parker, J. H. Johnson, V. Strots, and S. Santhanam, "Model-based estimation and control system development in a urea-scr aftertreatment system," *SAE International Journal of Fuels and Lubricants*, vol. 1, no. 1, pp. 646–661, 2009.
- [40] M. F. Hsieh and J. Wang, "An extended kalman filter for no x sensor ammonia cross-sensitivity elimination in selective catalytic reduction applications," in *American Control Conference (ACC), 2010*, pp. 3033–3038, IEEE, 2010.
- [41] G. Zhou, J. B. Jørgensen, C. Duwig, and J. K. Huusom, "State estimation in the automotive scr denox process," *IFAC proceedings volumes*, vol. 45, no. 15, pp. 501–506, 2012.
- [42] H. S. Surehalli, G. Parker, and J. H. Johnson, "Extended kalman filter estimator for nh₃ storage, no, no₂ and nh₃ estimation in a scr," Tech. Rep. 2013-01-1581, SAE Technical Paper, 2013.
- [43] H. Zhang, J. Wang, and Y.-Y. Wang, "Sensor reduction in diesel engine two-cell selective catalytic reduction (scr) systems for automotive applications," *IEEE/ASME Transactions on Mechatronics*, vol. 20, no. 5, pp. 2222–2233, 2015.
- [44] B. Singalandapuram Mahadevan, J. H. Johnson, and M. Shahbakhti, "Development of a kalman filter estimator for simulation and control of particulate matter distribution of a diesel catalyzed particulate filter," *International Journal of Engine Research*, p. 1468087418785855, 2018.
- [45] C. Sharp, C. C. Webb, G. Neely, M. Carter, S. Yoon, and C. Henry, "Achieving ultra low no x emissions levels with a 2017 heavy-duty on-highway tc diesel engine and an advanced technology emissions system-thermal management strategies," *SAE International Journal of Engines*, vol. 10, no. 2017-01-0954, pp. 1697–1712, 2017.
- [46] C. Sharp, C. C. Webb, S. Yoon, M. Carter, and C. Henry, "Achieving ultra low no_x emissions levels with a 2017 heavy-duty on-highway tc diesel engine-no_x management strategies," *SAE International Journal of Engines*, vol. 10, no. 2017-01-0958, 2017.

- [47] C. Sharp, C. C. Webb, S. Yoon, M. Carter, and C. Henry, "Achieving ultra low nox emissions levels with a 2017 heavy-duty on-highway tc diesel engine - comparison of advanced technology approaches," *SAE International Journal of Engines*, no. 2017-01-0956, 2017.
- [48] E. Georgiadis, T. Kudo, O. Herrmann, K. Uchiyama, and J. Hagen, "Real driving emission efficiency potential of sdpf systems without an ammonia slip catalyst," Tech. Rep. 2017-01-0913, SAE Technical Paper, 2017.
- [49] V. R. Chundru, B. S. Mahadevan, J. H. Johnson, G. G. Parker, and M. Shahbakhti, "Development of a 2-d scr catalyst on a dpf model," *Emission Control Science and Technology*, pp. 1–39, 2019.
- [50] B. S. Mahadevan, J. H. Johnson, and M. Shahbakhti, "Predicting pressure drop, temperature, and particulate matter distribution of a catalyzed diesel particulate filter using a multi-zone model including cake permeability," *Emission Control Science and Technology*, vol. 3, no. 2, pp. 171–201, 2017.
- [51] S. Sharma, "The emission and particulate matter oxidation performance of a scr catalyst on a diesel particulate filter with a downstream scr," Master's thesis, Michigan Technological University, 2017.
- [52] K. G. Raghavan, "An experimental investigation into the effect of no2 and temperature on the passive oxidation and active regeneration of particulate matter in a diesel particulate filter," Master's thesis, Michigan Technological University, 2015.
- [53] B. S. Mahadevan, J. H. Johnson, and M. Shahbakhti, "Development of a catalyzed diesel particulate filter multi-zone model for simulation of axial and radial substrate temperature and particulate matter distribution," *Emission Control Science and Technology*, vol. 1, no. 2, pp. 183–202, 2015.
- [54] H. S. Surenahalli, *Dynamic model based state estimation in a heavy duty diesel aftertreatment system for onboard diagnostics and controls*. PhD thesis, Michigan Technological University, 2013.
- [55] D. Simon, *Optimal state estimation: Kalman, H infinity, and nonlinear approaches*. John Wiley & Sons, 2006.

- [56] C. Sharp, C. C. Webb, G. Neely, J. V. Sarlashkar, S. B. Rengarajan, S. Yoon, C. Henry, and B. Zavala, "Achieving ultra low no x emissions levels with a 2017 heavy-duty on-highway tc diesel engine and an advanced technology emissions system-no x management strategies," *SAE International Journal of Engines*, vol. 10, no. 2017-01-0958, pp. 1736–1748, 2017.
- [57] X. Song, J. Naber, and J. H. Johnson, "Nonuniformity and no 2/no x ratio effects on the scr performance under transient engine conditions," Tech. Rep. 2014-01-1556, SAE Technical Paper, 2014.
- [58] J. A. Patchett, J. C. Dettling, and E. A. Przybylski, "Catalyzed scr filter and emission treatment system," Dec. 2 2014. US Patent 8,899,023.
- [59] J. A. Patchett, J. C. Dettling, and E. A. Przybylski, "Catalyzed scr filter and emission treatment system," May 26 2015. US Patent 9,039,982.
- [60] J. A. Patchett, J. C. Dettling, and E. A. Przybylski, "Catalyzed scr filter and emission treatment system," May 26 2015. US Patent 9,039,983.
- [61] J. A. Patchett, J. C. Dettling, and E. A. Przybylski, "Catalyzed scr filter and emission treatment system," May 26 2015. US Patent 9,039,984.
- [62] J. A. Patchett, J. C. Dettling, and E. A. Przybylski, "Catalyzed scr filter and emission treatment method," May 26 2015. US Patent 9,040,006.
- [63] J. A. Patchett, J. C. Dettling, and E. A. Przybylski, "Catalyzed scr filter and emission treatment system," Sept. 1 2015. US Patent 9,121,327.
- [64] J. A. Patchett, J. C. Dettling, and E. A. Przybylski, "Catalyzed scr filter and emission treatment system," Sept. 29 2015. US Patent 9,144,795.
- [65] J. A. Patchett, J. C. Dettling, and E. A. Przybylski, "Catalyzed scr filter and emission treatment system," Dec. 13 2016. US Patent 9,517,455.
- [66] J. A. Patchett, J. C. Dettling, and E. A. Przybylski, "Catalyzed scr filter and emission treatment system," Dec. 13 2016. US Patent 9,517,456.
- [67] J. A. Patchett, J. C. Dettling, and E. A. Przybylski, "Method for disposing scr composition on a wall flow monolith," Sept. 12 2017. US Patent 9,757,717.
- [68] H.-Y. Chen, D. Liu, E. Weigert, L. Cumararatunge, K. Camm, P. Bannon, J. Cox, and L. Arnold, "Durability assessment of diesel cold start concept (dsc) technologies," *SAE International Journal of Engines*, vol. 10, no. 2017-01-0955, pp. 1713–1721, 2017.

- [69] H.-Y. Chen, S. Mulla, E. Weigert, K. Camm, T. Ballinger, J. Cox, and P. Blake-man, “Cold start concept (csc) a novel catalyst for cold start emission control,” *SAE International Journal of Fuels and Lubricants*, vol. 6, no. 2013-01-0535, pp. 372–381, 2013.
- [70] E. Hruby, S. Huang, R. Duddukuri, and D. Dou, “Nox performance degradation of aftertreatment architectures containing doc with scr on filter or uncatalyzed dpf downstream of def injection,” Tech. Rep. 2009-01-0897, SAE Technical Paper, 2019.
- [71] B. S. Mahadevan, J. H. Johnson, and M. Shahbakhti, “Experimental and simulation analysis of temperature and particulate matter distribution for a catalyzed diesel particulate filter,” *Emission Control Science and Technology*, vol. 1, no. 4, pp. 255–283, 2015.

Appendix A

Development of SCR-F Model Mesh Equations ¹

The equations that define the mesh of the 2D SCR-F model are defined in this chapter. Figure A.1 shows the mesh used for the 2D SCR-F model. The equations in this sections are based on the resistance node methodology defined by Depcik et al. [31] based on the assumption that inlet and outlet channels have a rectangular geometry with equal size.

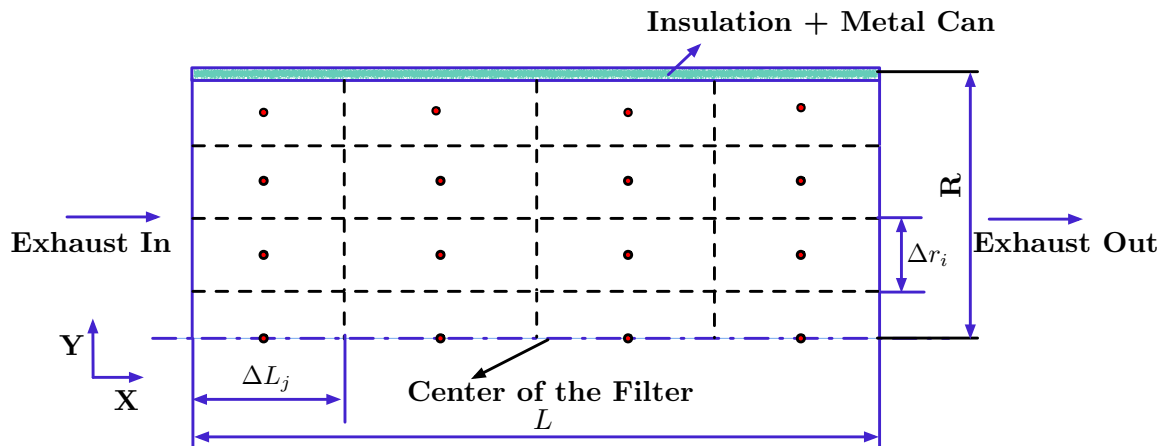


Figure A.1: 2D SCR-F model mesh

¹Parts of this chapter are from reference [31]

The SCR-F is divided into zones in radial and axial direction as shown in the figure. The total volume of each zone is equal to

$$V_{i,j} = \pi(r_i^2 - r_{i-1}^2)\Delta L_j \quad (\text{A.1})$$

Where r is the radius and L is the length in the axial direction. The subscript i indicates the radial direction and j indicates axial direction. ΔL represents the effective length of each zone which is computed as:

$$\Delta L_j = L_j - L_{j-1} \quad (\text{A.2})$$

The radial differences are computed from the centerline distances outwards:

$$\Delta r_i = r_i - r_{i-1} \quad (\text{A.3})$$

The number of cells per square meter (N) and corresponding frontal area is used to compute the number of cells in each zone (NC):

$$NC_i = \pi (r_i^2 - r_{i-1}^2) N \quad (\text{A.4})$$

The total empty volume (V_e) in each zone is determined using the side length of square channels (d):

$$V_{e,i,j} = NC_i d^2 \Delta L \quad (\text{A.5})$$

The volume of the filter (V_f) in each zone equals:

$$V_{f,i,j} = V_{i,j} - V_{e,i,j} \quad (\text{A.6})$$

The volume of soot in each zone is determined based on total PM mass retained in each zone (ms). A uniform initial loading of PM (ms_t) has been assumed in the model such that the PM mass retained in each zone is scaled up according to volume of each zone and total volume of the filter (V_t):

$$ms_{i,j} = \frac{ms_t \cdot V_{i,j}}{V_t} \quad (\text{A.7})$$

The average thickness of PM cake in each zone (t_s) is computed using the mass retained in each zone (ms), geometry of the inlet channel and density of the PM (ρ_s):

$$ts_{i,j} = \frac{1}{2} \left[d - \sqrt{d^2 - \frac{ms_{i,j}}{\left(\frac{NC_i}{2}\right) \Delta L_j \rho_s}} \right] \quad (\text{A.8})$$

The empty volume of the PM (V_{es}) is computed using:

$$V_{es_{i,j}} = \frac{N_{c_i}}{2} [(d - 2ts_{i,j})^2 + d^2] \Delta L \quad (\text{A.9})$$

The number of cells (N_c) is divided by 2 to account for the fact that PM deposits only in the inlet channels. The PM cake layer shrinks the effective channel open area. The PM cake volume (V_s) in each zone equals:

$$V_{s_{i,j}} = V_{i,j} - V_{f_{i,j}} - V_{es_{i,j}} \quad (\text{A.10})$$

The mesh setup by these equations is used to compute the PM mass retained in each zone along with pressure drop, temperature and chemical species calculations which are a function PM mass retained in each zone.

Appendix B

Development of Temperature Model and SCR Energy Release Terms

The SCR-F model computes the spatial distribution of the substrate and inlet/outlet channel exhaust gas temperatures using energy conservation equations. The energy balance in the SCR-F is affected by the heat transfer within and external to the filter. Figure B.1 shows the schematic of the temperature solver mesh used in the filter temperature model.

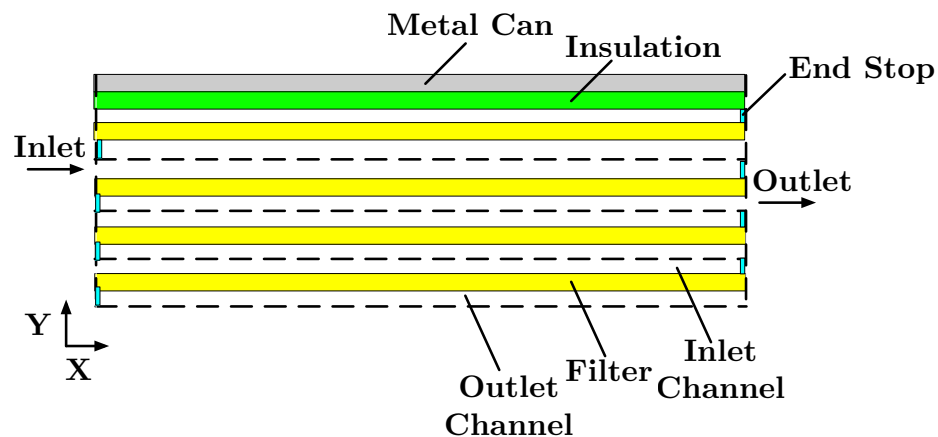


Figure B.1: Schematic of the 2D SCR-F model temperature solver mesh

The axial and radial temperature distribution of the substrate wall within the filter

at each zone is calculated using the gas energy balance Equations B.1 to B.3.

$$\rho_g c_v V_1 \frac{dT_1}{dt} |_{i,j} = \rho_g c_p (a - 2\bar{t}_{s,l})^2 v_1 T_1 |_{i,j-1} - \rho_g c_p (a - 2\bar{t}_{s,l})^2 v_1 T_1 |_{i,j} - \rho_g c_p 4a \Delta L v_w T_1 |_{i,j} + \dot{Q}_1 |_{i,j} \quad (\text{B.1})$$

$$(\rho_c c_c V_c + \rho_w c_w V_w) \frac{dT_f}{dt} |_{i,j} = \dot{Q}_{cond} + \dot{Q}_{conv} + \dot{Q}_{rad} + \dot{Q}_{reac} + \dot{Q}_{amb} + \rho_g c_p 4a \Delta L v_w (T_1 - T_f) |_{i,j} \quad (\text{B.2})$$

$$\rho_g c_v V_2 \frac{dT_2}{dt} |_{i,j} = \rho_g c_p a^2 v_2 T_2 |_{i,j-1} - \rho_g c_p a^2 v_2 T_2 |_{i,j} - \rho_g c_p 4a \Delta L v_w T_f |_{i,j} + \dot{Q}_2 |_{i,j} \quad (\text{B.3})$$

Where, T_f is the filter substrate temperature. The axial and radial conduction along the length of the filter is calculated using resistance node methodology [31][53]. The substrate energy balance equation B.2 accounts for the axial and radial conduction, convection, energy release due to PM and HC oxidation and heat transfer due to radiation within the channels.

Equation B.4 is used to compute the heat transfer due to conduction through the substrate material. The axial and radial conduction along the length of the filter are calculated using Equations B.5 and B.6.

$$\dot{Q}_{cond} = \dot{Q}_{cond,axial} + \dot{Q}_{cond,radial} \quad (\text{B.4})$$

$$\dot{Q}_{cond,axial} = \lambda k_{i,j} A_{f,i,j} \left[\frac{T_{f,i,j+1} - T_{f,i,j}}{\frac{1}{2}(\Delta L_{j+1} + \Delta L_j)} + \frac{T_{f,i,j-1} - T_{f,i,j}}{\frac{1}{2}(\Delta L_{j-1} + \Delta L_j)} \right] \quad (\text{B.5})$$

$$\dot{Q}_{cond,radial} = \lambda k_{i,j} A_{f,i,j} \left[\frac{T_{f,i+1,j} - T_{f,i,j}}{\ln \left(\frac{rc_{i+1}}{rc_i} \right)} + \frac{T_{f,i-1,j} - T_{f,i,j}}{\ln \left(\frac{rc_i}{rc_{i-1}} \right)} \right] \quad (\text{B.6})$$

Where

$$A_{f,i,j} = \frac{v_{c,i,j} + v_{w,i,j}}{\Delta L_i} \quad (\text{B.7})$$

$$A_{r,i,j} = 2\pi \Delta L_j \quad (\text{B.8})$$

$$\lambda K_{i,j} = \frac{\lambda k_c v_{c,i,j} + \lambda k_w v_{w,i,j}}{v_{c,i,j} + v_{w,i,j}} \quad (\text{B.9})$$

The convection heat transfer between the filter and channel gas is given as:

$$\dot{Q}_{conv} = v_{f,i,j} \rho_{i,j} c_p A_{w,i,j} (T_{f,i,j} - T_{1,i,j}) + h_g A_{c,i,j} (T_{2,i,j} - T_{1,i,j}) \Delta j \quad (\text{B.10})$$

Heat transfer from the filter to ambient by radiation is given by

$$\dot{Q}_{rad} = -A_{w,i,j} (F_{3-1}(j_3 - j_1)) + F_{3-2}(J_3 - J_2) \quad (\text{B.11})$$

The energy released during exothermic reactions is given by

$$\dot{Q}_{reac} = \dot{Q}_{reac,PM} + \dot{Q}_{reac,HC} + \dot{Q}_{reac,SCR} \quad (\text{B.12})$$

$$\dot{Q}_{reac,m} = RR_m \Delta H_m \quad (\text{B.13})$$

Where $\dot{Q}_{reac,m}$ is the energy released by reaction m, RR_m , and ΔH_m are the reaction rate and energy release by reaction m. At the inlet of the SCR-F model (for nodes $i = 1$ to i_{max} and $j = 1$), the temperature profile is calculated using the thermal boundary layer equations explained in the following section. The radial temperature distribution at the inlet of the SCR-F filter is affected by the thermal boundary layer development as explained in earlier references [53][71]. In order to account for the thermal boundary layer development, the empirical temperature factor profile is determined by analyzing experimental data. For a fully developed flow, the temperature factor shown below is constant across the length (temperature profile is constant):

$$\frac{\partial}{\partial x} \left[\frac{T_s x - T(r, x)}{T_s(x) - T_m(x)} \right] = 0 \quad (\text{B.14})$$

$$TemperatureFactor(x) = -2.493x^3 + 1.0585x^2 - 0.3285x + 1.7631 \quad (\text{B.15})$$

The SCR-F model uses the upstream inlet temperature measured by a single thermocouple (like ECU measuring the upstream exhaust gas temperature of SCR-F) and calculates the 2D temperature distribution of the exhaust gas entering the SCR-F using the equations B.14 and B.15.

At the center of the filter (for $i = 1$, $j = 1$ to j_{max}) due to the symmetry, the boundary condition equals to :

$$\left. \frac{dT_f}{dr} \right|_{r=0} = 0 \quad (\text{B.16})$$

At the outermost radial zones, the axial and radial temperature distribution is calculated using the gas energy balance Equation B.17 accounting for the ambient heat

loss through the can and insulation materials.

At the exterior of the SCR-F ($i = imax, j = 1$ to $jmax$)

$$(\rho_w c_w V_{w,i,j} + \rho_c c_c V_{c,i,j} + \rho_{can} c_{p,can} V_{can}) \frac{dT_f}{dt} = \dot{Q}_{cond,axial} + \dot{Q}_{cond,radial} + \dot{Q}_{conv} + \dot{Q}_{reac} + \dot{Q}_{rad} + \dot{Q}_{amb} + \rho_g c_p A a \Delta L v_w (T_1 - T_f)|_{i,j} \quad (B.17)$$

The heat transfer to the ambient is given as:

$$\dot{Q}_{amb} = h_{amb} k_{ins} k_{metal} A_{amb} \frac{T_{amb} - T_{f,i,j}}{k_{ins} k_{can} + \ln \left(\frac{r_{ins}}{r_f} \right)_{i,j} r_{c,i,j} k_{can} h_{amb} + \ln \left(\frac{r_c}{r_{ins}} \right)_{i,j} r_{c,i,j} k_{ins} h_{amb}} + \epsilon_r \sigma A_{amb} (T_{amb}^4 - T_{f,i,j}^4) \quad (B.18)$$

The conduction through the packing material and metal can is considered in the most outer radial zones. The surface area of the SCR-F is calculated as follows

$$A_{amb} = \pi D \Delta L_j \quad (B.19)$$

Appendix C

Development of Effectiveness Factor for the SCR Reactions

The inhibition caused by the presence of PM in the substrate wall on the SCR reactions was simulated using the effectiveness factor concept from reference [7]. Figure C.1 represents the geometry used to model the PM deposited in the substrate wall.

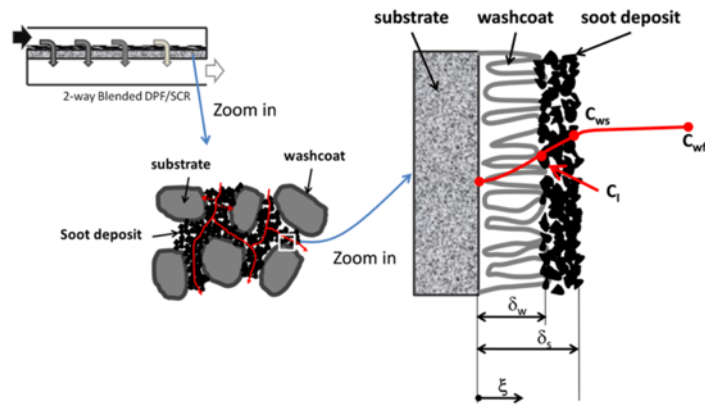


Figure C.1: Inhibition of NH_3 transport to active site due to PM in the substrate wall [7]

Based on Figure C.1 the reaction diffusion equations are given by

$$\frac{\partial^2 \bar{C}}{\partial \xi^2} - \Phi^2 \bar{C} = 0 \quad (\text{C.1})$$

$$\frac{\partial^2 \bar{C}}{\partial \bar{\xi}^2} = 0 \quad (\text{C.2})$$

where \bar{C}_s is concentration of chemical species at the catalyst surface and $\bar{\xi}$ is the non dimensional length scale defined by ratio $\frac{\xi}{\delta_w}$. The thickness of the PM cake is computed using the filtration model as $\delta_s - \delta_w$. Based on these quantities the value of Thiele modulus Φ_w is computed.

$$\Phi_w = \sqrt{\frac{k_{R,w} \delta_w^2}{D_{eff,w}}} \quad (\text{C.3})$$

Thiele modulus is the ratio of diffusion and reaction inside the wash-coat. A higher value of this variable indicates mass transport limitation in terms of reaction rate thus resulting in inhibition of the SCR reactions that take place on the catalyst surface. $k_{R,w}$ represents the rate constant of individual reaction. The boundary conditions for this equation are given by :

$$\text{at } \bar{\xi} = 0, \quad \frac{\partial \bar{C}}{\partial \bar{\xi}} = 0 \quad (\text{C.4})$$

$$\text{at } \bar{\xi} = 1, \quad \bar{C} = 1 \quad (\text{C.5})$$

$$\text{at } \bar{\xi} = \frac{\delta_w}{\delta_s}, \quad \bar{C} = \frac{C_{ws}}{C_I} \quad (\text{C.6})$$

$$\bar{C}(\bar{\xi}) = \frac{\sin(\Phi_w \bar{\xi})}{\sinh(\Phi_w)} \quad \text{for } 0 \leq \bar{\xi} \leq \delta_w \quad (\text{C.7})$$

$$\bar{C}(\bar{\xi}) = \frac{\delta_c(C_{ws} - C_I)}{C_I(\delta_s - \delta_w)} \bar{\xi} + \frac{C_I \delta_s - C_{ws} \delta_w}{C_I(\delta_s - \delta_w)} \quad \text{for } \delta_w \leq \bar{\xi} \leq \delta_s \quad (\text{C.8})$$

Where the chemical species concentration at the catalyst surface C_I is compute using

$$C_I = \frac{\frac{D_{eff,s}}{(\delta_s - \delta_w)}}{\sqrt{D_{eff,w} k_{R,w} \tanh(\Phi_w)} + \frac{D_{eff,s}}{(\delta_s - \delta_w)}} C_{ws} \quad (\text{C.9})$$

Based on the above equation an effectiveness factor is computed for each of the SCR reactions and adsorption, desorption reaction in the SCR-F model

$$\eta_s = \frac{RR_{act}}{RR_{ideal}} = \frac{D_{eff,s}}{k_{R,w}\delta_w} \left(\frac{1 - \frac{C_I}{C_{ws}}}{\delta_s - \delta_w} \right) \quad (C.10)$$

$$RR_{act} = \frac{1}{\delta_w} \left[-D_{eff,s} \frac{\partial C}{\partial \xi} \Big|_{\xi=\xi_w} \right] = \frac{-D_{eff,s}(C_{ws} - C_I)}{\delta_w(\delta_s - \delta_w)} \quad (C.11)$$

$$\eta_s = \frac{\sqrt{D_{eff}k_{ideal}} \tanh(\Phi_w)}{(\delta_s - \delta_w) \sqrt{D_{eff}k_{desl}} \tanh(\Phi_w) + D_{eff}} \quad (C.12)$$

$$k_{actual} = k_{ideal}\eta_s \quad (C.13)$$

$$\lim_{\delta_s \rightarrow \delta_w} \eta_s = \frac{\sqrt{D_{eff,w}k_{R,w}} \tanh(\Phi_w)}{k_{R,w}\delta_w} = \frac{\tanh(\Phi_w)}{\Phi_w} = \eta_c \quad (C.14)$$

The effectiveness factor is applied to the clean wall rate constant computed using the rate constant and chemical species concentrations of the reactants. The resultant is able to simulate the inhibition of wall PM on the SCR reactions and thus NO_x reduction performance of the SCR-F for different PM loading conditions.

$$RR_{act} = \eta_s RR_{clean} \quad (C.15)$$

Appendix D

Development of Cake Permeability, Pressure Drop and Filtration Models

The pressure drop across the SCR-F consists of three components 1) Cake 2) wall and 3) Channel pressure drop. The total pressure drop based on these 3 components is computed using Equation D.1.

$$\Delta P_{SCR-F} = \Delta P_{wall} + \Delta P_{cake} + \Delta P_{channel} \quad (D.1)$$

Where, $P_1|_{x=0}$ and $P_2|_{x=L}$ are the absolute pressure values at the inlet and outlet of the representative cell in the inlet and the outlet channel respectively. The equations used to obtain these values is described in reference [37]. The wall pressure drop at each zone is given by Eq. 3.39

$$\Delta P_{wall_{i,j}} = \mu_{i,j} v_{w_{i,j}} \frac{w_s}{k_{wall_{i,j}}} \quad (D.2)$$

Where, Δp_{wall} is the wall pressure drop, v_w is the wall layer velocity, w_s is the substrate wall thickness and k_{wall} is the wall permeability. The cake pressure drop at is given by Eq. 3.40

$$\Delta P_{cake_{i,j}} = \mu_{i,j} v_{s_{i,j}} \frac{w_{p_{i,j}}}{k_{cake_{i,j}}} \quad (D.3)$$

$$\Delta P_{SCR-F,i} = [P_1|_{x=0} - P_2|_{x=L}]_i \quad (D.4)$$

The total pressure drop across the SCR-F accounting for all radial zones is given by Eq. 3.42

$$\Delta P_{SCR-F} = \frac{\sum_{s1}^{smax} \sum_{i=1}^{i=M} VF_i \Delta P_{SCR-F,i}}{smax} \quad (D.5)$$

In pressure drop sub model, the pressure drop at each radial section is calculated by starting out with exit pressure $P_2|_{x=L} = P_{Baro}$ and then traversing through all possible streamlines as shown in Figure D.1.

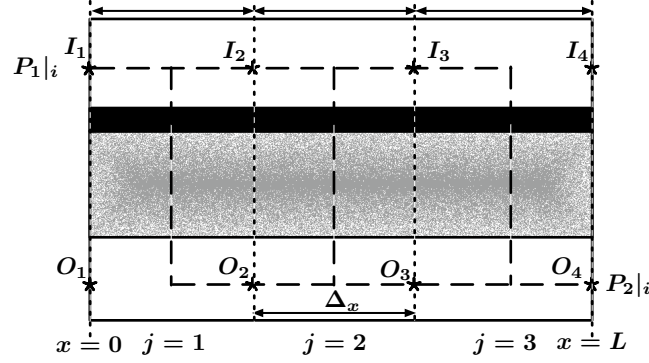


Figure D.1: Schematic of the streamlines (shown as dashed lines) used for calculating the pressure drop across CPF/SCR-F for 3x1 zone model (4 axial and 1 radial discretization).

The pressure drop across each radial section is calculated as

$$\Delta P_{i,s1} = [P_1|_{x=0} - P_2|_{x=L}]_{i,s1} \quad (D.6)$$

$$\Delta P_{i,s2} = [P_1|_{x=0} - P_2|_{x=L}]_{i,s2} \quad (D.7)$$

$$\Delta P_{i,s3} = [P_1|_{x=0} - P_2|_{x=L}]_{i,s3} \quad (D.8)$$

The pressure drop in the outlet channel stream lines (O_4 , O_3 , O_2 and O_1) are calculated using the following equation

$$P_2|_{i,j} = P_2|_{i,j+1} + \rho v_2^2|_{i,j+1} - \rho v_2^2|_{i,j} + F \Delta x \frac{\mu v_2}{a^2}|_{i,j} \quad (D.9)$$

The pressure drop in the inlet channel stream lines (I_4 , I_3 , I_2 and I_1) are calculated using the following equation

$$P_1|_{i,j} = P_1|_{i,j+1} + \rho v_1^2|_{i,j+1} - \rho v_1^2|_{i,j} + F \Delta x \frac{\mu v_1}{a^2} \left(\frac{a^*}{a} \right)^2 |_{i,j} \quad (D.10)$$

D.0.1 Wall and Cake Pressure drop

The wall pressure drop is calculated using the following equation

$$\Delta P_{wall} = \mu v_w \frac{w_s}{k_{wall}} \quad (D.11)$$

The cake pressure drop is calculated using the following equation

$$\Delta P_{cake} = \mu v_s \frac{w_p}{k_{cake}} \quad (D.12)$$

D.0.2 Total Pressure drop

The pressure across each radial zone section is calculated as

$$\Delta P_i = [P_1|_{x=0} - P_2|_{x=L}]_i \quad (D.13)$$

The overall pressure drop across SCR-F is given by

$$\Delta P_{SCR-F} = \frac{\dot{m}_{total}}{\sum_{i=1}^m \frac{\dot{m}_i}{\Delta P_{SCR-F,i}}} \dot{m}_i \quad (D.14)$$

Further, the mass flow rate into each radial zone is corrected by the following equation:

$$\dot{m}_{i,corr} = \frac{\Delta P_{SCR-F}}{\Delta P_{SCR-F,i}} \dot{m}_i \quad (D.15)$$

The mass flow correction in Equation D.15 continues until the pressure drop calculated in every radial zone becomes equal.

D.0.3 Filtration Efficiency

In filtration sub-model, the substrate wall is divided into p number of slabs. Each slab consists of several spherical wall collectors [37][27]. The diameter of unit collector increases as the PM accumulates in to the collector. The initial diameter of the unit

collector is given as:

$$dc_{0,w} = \frac{3}{2} \left(\frac{1 - \epsilon_{0,s}}{\epsilon_{0,s}} \right) d_{pore,wall} \quad (D.16)$$

The number of pores in the substrate wall is given as [27]

$$Np = \frac{V_{eo}}{\frac{4\pi}{3} \left(\frac{d_{pore,wall}}{2} \right)^2} \quad (D.17)$$

The empty volume of the substrate wall is given as

$$V_{eo} = \epsilon_{0,s} V_f \quad (D.18)$$

The number of pores in each slab at each zone is calculated as

$$[Np]_n = \frac{Np}{P} \quad (D.19)$$

where, $n = 1$ to P with increments of 1. Wall collector efficiency at each slab is calculated as

$$\eta_{wall,n} = [\eta_D + \eta_R - \eta_D \eta_R]_{wall,n} \quad (D.20)$$

The filtration efficiency of a unit collector in the PM cake layer is calculated as

$$\eta_{cake,n} = [\eta_D + \eta_R - \eta_D \eta_R]_{cake} \quad (D.21)$$

The overall efficiency of the filtration is equal to:

$$\eta_{total} = 1 - \left[(1 - \eta_{cake}) \prod_{n=1}^p (1 - \eta_{wall,n}) \right] \quad (D.22)$$

where, η_{cake} is the PM cake layer filtration efficiency and $\eta_{wall,n}$ is the filtration efficiency of each slab in the substrate wall. The transition from deep bed to cake filtration is computed using Partition coefficient:

$$\Phi = \frac{dc_{wall,1}^2 - dc_{0,wall,1}^2}{(\Psi_b)^2 - dc_{0,wall,1}^2} \quad (D.23)$$

Appendix E

SCR-F[®] Species Model Development

The SCR-F model consist of two sets of chemical reactions:

1. Oxidation reactions - NO, CO, HC and PM oxidation.
2. SCR Reactions - Standard, fast and slow SCR reactions, NH₃ oxidation, adsorption and desorption.

The species model uses the chemical species conservation equation to compute change in chemical species concentrations across the PM cake and substrate wall. The major assumptions made in the species model are:

1. Molecular density of exhaust gas mixture ($\rho_{exh,w}$) is constant in the PM cake + Substrate wall control volume.
2. Concentration of chemical species in the inlet channel is assumed to be constant and is equal to inlet concentrations.
3. Concentration of chemical species in the outlet channel is equal to concentration at wall outlet boundary. Mass transport is governed by convection and diffusion as shown in Equations E.1, E.2 and E.3

$$\frac{dC_{1,l}}{dt} = v_1 \frac{dC_{1,l}}{dx} + \left(\frac{4}{a}\right) k_1 (C_{1s,l} - C_{1,l}) + \left(\frac{4}{a}\right) v_f C_{1,l} \quad (\text{E.1})$$

$$\frac{dC_{f,l}}{dt} = v_f \frac{dC_{f,l}}{dy} + \frac{d}{dy} \left(D_l \frac{dC_{f,l}}{dy} \right) - \sum_k \xi_{l,m} R_m \quad (\text{E.2})$$

$$\frac{dC_{2,l}}{dt} = v_2 \frac{dC_{2,l}}{dx} + \left(\frac{4}{a}\right) k_2 (C_{2,l} - C_{2s,l}) + \left(\frac{4}{a}\right) v_f C_{2s,l} \quad (\text{E.3})$$

The first diffusivity D_l is governed by two mechanisms molecular diffusion and Knudsen diffusion. The overall diffusivity is calculated based on Equation

$$D_l = \frac{1}{\frac{\tau}{\epsilon} \left[\frac{1}{D_{mol,l}} + \frac{1}{D_{kn,l}} \right]} \quad (\text{E.4})$$

Where molecular diffusivity and Knudsen diffusivity are calculated by Equation E.5 and E.6 [37].

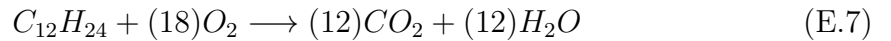
$$D_l = \frac{1 - Y_l}{\sum_{j \neq i} \frac{y_j}{D_{l,j}}} \quad (\text{E.5})$$

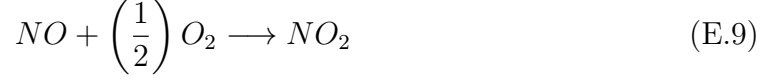
$$D_{kn,l} = \frac{d_p}{3} \sqrt{\frac{8RT}{\pi MW_l}} \quad (\text{E.6})$$

The diffusion phenomena plays an important role in oxidation of PM as it determines mass transport of NO and NO₂ between PM cake and substrate layer. In case of a CPF where oxidation catalyst is present in the substrate wall back diffusion of NO₂ takes place due to excessive concentration in the substrate wall. In the case of SCR-F forward diffusion of NO and NO₂ due to NO_x reduction in the substrate takes place. The chemical species are tracked as the exhaust gas passes through the PM cake and the substrate wall.

E.0.1 Oxidation Reactions

The oxidation reactions are assumed to take place inside the substrate wall where the catalyst is embedded. The oxidation reactions being considered are as follows





The corresponding reaction rate equations are as follows

$$R_{HC} = \frac{A_{HC}(T_w)^{x_{HC}} e^{-\frac{E_{a_{HC}}}{RT_w}} [C_{12}H_{24}][O_2]}{G_1} \quad (E.10)$$

$$R_{CO} = \frac{A_{CO}(T_w)^{x_{CO}} e^{-\frac{E_{a_{CO}}}{RT_w}} [CO][O_2]}{G_2} \quad (E.11)$$

$$R_{NO} = \frac{A_{NO}(T_w)^{x_{NO}} e^{-\frac{E_{a_{NO}}}{RT_w}} \left[[NO][O_2]^{\frac{1}{2}} - \frac{[NO_2]}{k_c} \right]}{G_2} \quad (E.12)$$

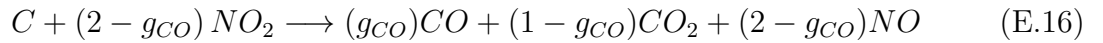
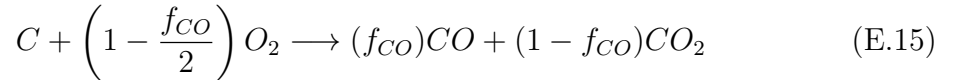
Where

$$K_c = K_p \sqrt{\frac{RT_w}{P}} \quad (E.13)$$

$$K_p = e^{\left(\frac{6950.09}{T_w} - 9.12\right)} \quad (E.14)$$

G_1 , G_2 and G_3 are inhibition factors caused by adsorption of HC, CO and NO in the substrate wall

The PM oxidation reactions are considered in both the PM cake and substrate wall. The rate equations for the thermal and NO_2 assisted PM oxidation are given by :



$$R_{O_2,oxid} = K_{O_2} C_{O_2} \quad (E.17)$$

$$R_{NO_2,oxid} = K_{NO_2} C_{O_2} \quad (E.18)$$

E.0.2 SCR Reactions

The SCR reactions considered in the SCR-F model include the standard, fast and slow SCR reactions. The adsorption and desorption of NH_3 has also been modeled as Arrhenius form for the two sites in which NH_3 adsorption takes place. Equations

E.19, E.20 and E.21 show the equations used for adsorption and desorption of NH_3 .

$$\frac{dC_l}{dt} = v_w \frac{dC_l}{dx} - \sum_j \xi_{l,m} R_m \quad (\text{E.19})$$

$$\Omega_1 \dot{\theta}_1 = R_{ads,1} - R_{des,1} - \sum_j \xi_{l,m} R_m \quad (\text{E.20})$$

$$\Omega_2 \dot{\theta}_2 = R_{ads,2} - R_{des,2} \quad (\text{E.21})$$

Where C_l is the concentration of species in the given domain, dt is time step size and dx is length of axial division, v_w is the velocity of exhaust gas through the PM cake + Substrate wall. $\xi_{l,m}$ is the stoichiometric coefficient of chemical species l in reaction m , R_m is the reaction rate of reaction m . Ω_1 maximum storage capacity of first NH_3 storage site in the SCR-F capable of both storage and consumption on NH_3 by SCR reactions, θ_1 is the storage fraction for the first site. Similarly, Ω_2 and θ_2 are the storage capacity and coverage fractions for second site responsible for only storage of NH_3 .

Appendix F

SCRF[®] Configuration 1, 2 and 3 Experimental Data Test Points

Tables F.1 to F.7 compare the experimental and model pressure drop, outlet temperature, outlet NO, NO₂, NH₃ concentrations and filtration efficiency values for the 18 Configuration 1 experiments. The Configuration 1 passive oxidation experiments without urea injections are referred to as PO - Test Name and experiments with urea injection are referred to as POU - Test Name. Test Name represents test conditions A - E used for the passive oxidation stage. The experimental data presented here comes from references [5], [4] and [51]

Table F.1Outlet NH₃ (experimental vs model) configuration 1 data

Outlet NH ₃ [ppm]				
Exp. Name	PO			
(-)	Expt. in	Expt.	Model	Diff.
POU-A	652	36	30	6
POU-B	1617	10	2	8
POU-B Repeat	1720	10	16	-6
POU-C	1124	0	8	-8
POU-D	477	21	31	-10
POU-D Repeat	510	25	30	-5
POU-E	1463	10	40	-30
RMS Difference	9			

Table F.2

Outlet temperature (experimental vs model) configuration 1 data

Outlet temperature [°C]			
Exp. Name	DNSCR-F		
(-)	Expt.	Model	Diff.
PO-A	274	277	-3
PO-B	274	275	-1
PO-B Repeat	275	278	-3
PO-C	352	354	-2
PO-D	374	366	8
PO-D Repeat	372	377	-5
PO-E	377	370	7
POU-A	274	269	5
POU-B	284	279	5
POU-B Repeat	284	280	4
POU-C	349	352	-3
POU-D	373	371	2
POU-D Repeat	371	367	4
POU-E	360	358	2
AR-1	507	506	1
AR-2	562	561	1
AR-3	602	599	3
AR-2 Repeat	556	555	1
RMS Difference	4		

Table F.3
Filtration efficiency (experimental vs model) configuration 1 data

Filtration efficiency [%]			
Exp. Name	Stage - 2		
(-)	Expt.	Model	Diff.
PO-A	97.5	98.5	-1.0
PO-B	99.2	98.6	0.6
PO-B Repeat	98.2	98.4	-0.2
PO-C	99.8	98.5	1.3
PO-D	98.6	98.8	-0.2
PO-D Repeat	97.2	98.5	-1.3
PO-E	98.3	98.6	-0.3
POU-A	96.3	98.4	-2.1
POU-B	96.7	98.2	-1.5
POU-B Repeat	97.6	98.2	-0.6
POU-C	96.1	98.4	-2.3
POU-D	96.8	98.3	-1.5
POU-D Repeat	96.8	98.2	-1.5
POU-E	98.1	98.1	0.0
AR-1	98.3	98.5	-0.2
AR-2	98.4	98.4	0.0
AR-3	98.8	98.4	0.4
AR-2 Repeat	98.5	98.5	0.0
RMS Difference	1.4		

Table F.4
Pressure drop (experimental vs model) configuration 1 data

Exp. Name	Pressure drop [kPa]											
	End of loading (Stage 1, 2)			End of PO/AR			End of post loading (Stage 3, 4)					
	Expt.	Model	Diff.	Expt.	Model	Diff.	Expt.	Model	Diff.	Expt.	Model	Diff.
(-)												
PO-A	8.18	8.53	-0.35	1.77	1.64	0.13	6.30	6.32	-0.02			
PO-B	7.10	8.54	-1.44	1.15	1.35	-0.20	5.88	5.25	0.63			
PO-B Repeat	8.73	8.14	0.59	0.97	1.39	-0.42	6.80	5.81	0.99			
PO-C	8.02	8.23	-0.21	2.13	2.01	-0.12	6.01	5.49	0.52			
PO-D	6.97	8.83	-1.86	3.30	4.16	-0.86	4.42	5.05	-0.63			
PO-D Repeat	8.44	8.34	0.10	3.52	4.00	-0.48	5.25	5.10	0.15			
PO-E	7.40	8.27	-0.87	2.23	3.10	-0.87	6.22	5.42	0.80			
POU-A	7.94	7.98	-0.04	2.66	3.30	-0.64	7.46	7.46	0.00			
POU-B	8.13	7.99	0.14	0.99	0.99	0.00	6.58	6.61	-0.03			
POU-B Repeat	8.51	8.21	0.30	1.35	1.35	0.00	7.31	7.50	-0.19			
POU-C	8.03	8.08	-0.05	2.16	2.16	0.00	6.28	6.30	-0.02			
POU-D	8.00	8.00	0.00	4.85	4.82	0.03	6.28	6.20	0.08			
POU-D Repeat	7.96	7.94	0.02	5.07	4.98	0.09	6.01	6.60	-0.59			
POU-E	8.29	8.30	-0.01	2.22	2.20	0.02	6.57	6.56	0.01			
AR-1	7.78	7.99	-0.21	5.74	5.71	0.03	6.27	6.56	-0.29			
AR-2	7.70	7.68	0.02	4.06	3.96	0.10	6.27	4.41	1.86			
AR-3	7.71	7.70	0.01	3.42	3.65	-0.23	5.16	4.58	0.58			
AR-2 Repeat	7.58	8.22	-0.64	4.87	4.51	0.36	5.83	5.64	0.19			
RMS Difference	0.13			0.25			0.23					

Table F.5
PM mass retained (experimental vs model) configuration 1 data

Exp. Name	PM mass retained [g]											
	Stage - 1			Stage - 2			Stage - 3			Stage - 4		
(-)	Expt.	Model	Diff.	Expt.	Model	Diff.	Expt.	Model	Diff.	Expt.	Model	Diff.
PO-A	4.3	4.8	-0.6	35.4	34.9	0.5	29.1	31.1	-2.0	35.3	36.8	-1.4
PO-B	2.5	3.8	-1.3	33.6	34.8	-1.2	28.9	27.5	1.4	35.4	31.5	3.8
PO-B Repeat	3.1	4.0	-0.9	31.7	32.9	-1.2	23.0	21.7	1.3	28.6	27.4	1.2
PO-C	2.8	3.6	-0.8	32.7	33.3	-0.6	23.2	23.4	-0.2	29.5	29.8	-0.3
PO-D	2.6	3.2	-0.6	32.5	34.5	-2.0	18.0	17.3	0.7	24.4	23.3	1.1
PO-D Repeat	3.2	3.7	-0.6	32.5	33.2	-0.7	15.5	13.6	1.9	21.1	20.0	1.1
PO-E	4.6	4.7	-0.2	33.5	32.6	0.9	22.9	20.4	2.5	25.9	26.2	-0.3
POU-A	1.6	1.6	-0.0	27.0	27.5	-0.5	33.8	35.3	-1.5	39.3	34.9	4.4
POU-B	1.8	1.5	0.3	28.0	28.4	-0.4	23.7	24.1	-0.4	27.4	28.2	-0.8
POU-B Repeat	1.5	1.5	-0.0	25.9	24.6	1.3	26.4	27.0	-0.6	30.9	30.1	0.8
POU-C	1.7	1.6	0.1	30.7	29.7	1.0	23.4	22.1	1.3	26.4	27.1	-0.7
POU-D	2.0	1.9	0.1	28.4	27.9	0.5	21.2	21.1	0.1	25.8	24.7	1.1
POU-D Repeat	1.8	1.9	-0.1	24.2	23.0	1.2	18.9	20.1	-1.2	23.7	25.2	-1.5
POU-E	2.1	2.2	-0.1	30.1	30.9	-0.8	23.5	22.9	-0.6	30.8	27.2	3.6
AR-1	1.5	2.3	-0.8	27.7	28.7	-1.0	18.1	19.7	-1.6	24.0	25.5	-1.5
AR-2	1.4	2.2	-0.8	27.7	27.9	-0.2	5.7	10.4	-4.7	11.2	15.7	-4.5
AR-3	1.6	2.3	-0.7	27.7	28.4	-0.7	6.8	7.7	-0.9	11.7	13.4	-1.7
AR-2 Repeat	1.8	2.3	-0.5	30.7	29.9	0.8	16.8	13.9	2.9	22.6	19.8	2.8
RMS Difference	0.1			0.8			0.8			1.0		

Table F.6
Outlet NO₂ (experimental vs model) configuration 1 data

Exp. Name	Outlet NO ₂ [ppm]															
	Loading						PO/AR						Post Loading			
	Expt. in	Expt.	Model	Diff.	Expt. in	Expt.	Model	Diff.	Expt. in	Expt.	Model	Diff.	Expt. in	Expt.	Model	Diff.
(-)																
PO-A	61	41	47	-6	263	221	235	-14	57	29	43	-14	57	29	43	-14
PO-B	39	23	23	0	674	611	602	9	50	22	38	-16	50	22	38	-16
PO-B Repeat	77	45	52	-7	792	732	720	12	72	41	60	-19	72	41	60	-19
PO-C	64	48	52	-4	228	144	128	16	59	37	46	-9	59	37	46	-9
PO-D	52	22	20	2	117	76	81	-5	52	36	47	-11	52	36	47	-11
PO-D Repeat	68	38	46	-8	147	84	89	-5	52	31	41	-10	52	31	41	-10
PO-E	66	58	56	2	523	339	330	9	62	36	52	-16	62	36	52	-16
POU-A	64	42	41	1	304	4	20	-16	82	46	50	-4	82	46	50	-4
POU-B	60	37	36	1	821	9	9	0	81	52	61	-9	81	52	61	-9
POU-B Repeat	66	43	41	2	758	0	0	0	69	42	50	-8	69	42	50	-8
POU-C	71	48	46	2	301	3	3	0	82	51	59	-8	82	51	59	-8
POU-D	80	50	47	3	171	0	4	-4	75	45	56	-11	75	45	56	-11
POU-D Repeat	71	51	54	-3	191	2	5	-3	72	51	57	-6	72	51	57	-6
POU-E	48	37	35	2	653	2	2	0	57	29	32	-3	57	29	32	-3
AR-1	53	31	44	-13	6	1	0	1	52	27	40	-13	52	27	40	-13
AR-2	61	38	58	-20	16	3	0	3	52	27	43	-16	52	27	43	-16
AR-3	57	40	57	-17	20	6	0	6	59	38	19	19	59	38	19	19
AR-2-Repeat	49	36	50	-14	2	7	0	7	46	21	34	-13	46	21	34	-13
RMS Difference	10						9						14			

Table F.7
Outlet NO (experimental vs model) configuration 1 data

Exp. Name	Loading						Outlet NO [ppm]						
	Expt. in	Expt.	Model	Diff.	Expt. in	Expt.	Model	Diff.	Expt. in	Expt.	Model	Diff.	
(-)	120	141	135	6	251	276	276	0	119	133	133	0	
PO-A	132	140	141	-1	1102	1160	1166	-6	131	145	146	-1	
PO-B Repeat	149	166	166	0	822	860	865	-5	137	155	157	-2	
PO-C	120	127	134	-7	320	398	390	8	187	190	198	-8	
PO-D	164	176	176	0	326	361	370	-9	164	176	170	6	
PO-D Repeat	125	144	146	-2	236	252	263	-11	102	114	112	2	
PO-E	100	106	113	-7	802	916	930	-14	95	106	105	1	
POU-A	118	131	135	-4	286	51	31	20	140	162	161	1	
POU-B	121	142	142	0	789	137	136	1	113	128	130	-2	
POU-B Repeat	141	162	159	3	822	10	8	0	120	133	140	-7	
POU-C	117	212	210	2	387	83	80	3	213	232	234	-2	
POU-D	150	172	172	0	279	16	30	-14	154	184	176	8	
POU-D Repeat	130	151	151	0	306	24	28	-4	135	165	149	16	
POU-E	164	180	181	-1	798	78	70	8	124	149	155	-6	
AR-1	142	158	151	7	320	324	326	-2	136	159	145	14	
AR-2	148	169	163	6	361	350	361	-11	137	159	141	18	
AR-3	140	159	151	8	294	318	318	0	135	155	146	9	
AR-2 Repeat	143	162	159	3	308	326	324	2	188	166	163	3	
RMS Difference	10						9						14

Tables F.8 to F.14 compare the experimental and model pressure drop, outlet temperature, outlet NO, NO₂, NH₃ concentrations and filtration efficiency values for the 12 Configuration 2 experiments.

Table F.8

Outlet temperature (experimental vs model) configuration 2 data

Outlet temperature [°C]			
Exp. Name	DNSCRF® ANR = 1.2		
(-)	Expt.	Model	Diff.
Test 1 - 0	214	215	-1
Test 1 - 2	217	215	2
Test 1 - 4	210	209	1
Test 2 - 0	311	310	1
Test 3 - 2	319	315	4
Test 3 - 4	315	315	0
Test 6 - 0	355	356	-1
Test 6 - 2	348	353	-5
Test 6 - 4	342	341	0
Test 8 - 0	453	452	1
Test 8 - 2	447	443	5
Test 8 - 4	453	451	2
RMS Difference	4		

Table F.9

Filtration efficiency (experimental vs model) configuration 2 data

Filtration efficiency [%]			
Exp. Name	Stage - 2		
Test # - g/l	Expt.	Model	Diff.
Test 1 - 2	96.9	98.4	-1.5
Test 1 - 4	99.9	98.3	0.7
Test 3 - 2	97.7	98.5	-0.8
Test 3 - 4	97.4	98.7	-1.3
Test 6 - 2	98.0	98.5	-0.5
Test 6 - 4	99.0	98.6	0.4
Test 8 - 2	97.8	98.4	-0.6
Test 8 - 4	99.0	98.4	0.6
RMS Difference	0.9		

Table F.10
Pressure drop (experimental vs model) configuration 2 data

Pressure drop [kPa]						
Exp. Name	End of loading (Stage 1, 2)			End of PO		
Test # - g/l	Expt.	Model	Diff.	Expt.	Model	Diff.
Test 1 - 2	8.31	8.05	0.26	3.28	3.38	-0.1
Test 1 - 4	12.49	12.15	0.34	4.81	4.92	-0.11
Test 3 - 2	8.00	7.61	0.39	7.11	6.93	0.18
Test 3 - 4	11.31	10.90	0.41	10.82	10.99	-0.17
Test 6 - 2	6.87	6.98	-0.10	2.00	2.22	-0.22
Test 6 - 4	13.46	13.15	0.32	2.09	2.30	-0.21
Test 8 - 2	8.12	8.37	-0.25	6.73	6.40	0.33
Test 8 - 4	13.41	13.75	-0.34	10.64	10.40	0.24
RMS Difference	0.33			0.44		

Table F.11
PM mass retained (experimental vs model) configuration 2 data

PM mass retained [g]									
Exp. Name	Stage - 1			Stage - 2			End of PO		
Test # - g/l	Expt.	Model	Diff.	Expt.	Model	Diff.	Expt.	Model	Diff.
Test 1 - 2	2.82	2.11	0.71	29.4	30.2	-0.89	32.3	33.3	-1.06
Test 1 - 4	3.98	4.56	-0.58	61.2	60.9	0.28	65.1	63.5	1.61
Test 3 - 2	2.58	2.34	0.24	29.9	30.1	-0.26	32.6	31.2	1.34
Test 3 - 4	2.53	3.51	-0.98	53.5	54.4	-0.89	51.8	50.6	1.16
Test 6 - 2	2.53	1.69	0.84	30.1	29.8	0.38	17.9	18.8	-0.89
Test 6 - 4	3.89	3.97	-0.08	59.1	58.9	0.18	58.7	60.7	-1.94
Test 8 - 2	2.83	2.03	0.80	32.5	32.8	-0.28	10.1	9.9	0.21
Test 8 - 4	4.35	4.64	-0.29	67.8	69.9	-2.14	52.8	53.4	-0.53
RMS Difference	0.64			0.90			1.2		

Table F.12
Outlet NO₂ (experimental vs model) configuration 2 data

Exp. Name	Outlet NO ₂ [ppm]															
	ANR = 0.8				ANR = 1.0				ANR = 1.2				ANR = 1.2 repeat			
Test # - g/l	Expt. in	Expt.	Model	Diff.	Expt. in	Expt.	Model	Diff.	Expt. in	Expt.	Model	Diff.	Expt. in	Expt.	Model	Diff.
Test 1 - 0	210	13	19	-6	210	0	0	0	210	0	0	0	210	0	0	0
Test 1 - 2	204	1	3	-2	204	0	0	0	204	0	0	0	204	0	0	0
Test 1 - 4	204	1	2	-1	204	0	0	0	204	0	0	0	204	1	0	1
Test 3 - 0	121	19	25	-6	121	1	0	1	121	0	0	0	121	0	0	0
Test 3 - 2	131	2	13	-11	131	0	4	-4	131	0	1	-1	131	0	1	-1
Test 3 - 4	143	1	9	-8	143	0	3	-3	143	0	2	-2	143	0	2	-2
Test 6 - 0	674	178	178	0	674	30	40	-10	674	0	0	0	674	0	1	-1
Test 6 - 2	744	30	59	-29	744	2	21	-19	744	0	2	-2	744	0	2	-2
Test 6 - 4	588	12	38	-26	588	2	12	-10	588	2	2	0	588	2	2	0
Test 8 - 0	140	7	6	1	140	3	4	-1	140	2	4	-2	140	1	4	-3
Test 8 - 2	125	1	6	-5	125	0	3	-3	125	0	2	-2	125	-1	2	-3
Test 8 - 4	141	22	10	12	141	2	4	-2	141	0	2	-2	0	0	0	0
RMS Difference	21				8				1				1			

Table F.13
Outlet NO (experimental vs model) configuration 2 data

Exp. Name	Outlet NO [ppm]															
	ANR = 0.8				ANR = 1.0				ANR = 1.2				ANR = 1.2 repeat			
Test # - g/l	Expt. in	Expt.	Model	Diff.	Expt. in	Expt.	Model	Diff.	Expt. in	Expt.	Model	Diff.	Expt. in	Expt.	Model	Diff.
Test 1 - 0	345	138	138	0	345	77	73	4	345	7	20	-13	345	8	20	-12
Test 1 - 2	403	138	124	14	403	65	63	2	403	7	15	-8	403	9	15	-6
Test 1 - 4	403	136	120	16	403	58	71	-13	403	14	18	-4	403	16	18	-2
Test 3 - 0	158	45	55	-10	158	12	2	10	158	4	0	4	158	4	0	4
Test 3 - 2	161	64	56	8	161	18	20	-2	161	2	4	-2	161	2	5	-3
Test 3 - 4	198	57	56	1	198	9	14	-5	198	3	10	-7	198	3	10	-7
Test 6 - 0	795	108	116	-8	795	7	6	1	795	4	3	1	795	4	3	1
Test 6 - 2	844	267	255	12	844	57	42	15	844	7	1	6	844	5	0	5
Test 6 - 4	844	240	241	-1	844	99	99	0	844	16	16	0	844	16	16	0
Test 8 - 0	411	99	115	-16	411	44	60	-16	411	35	41	-6	411	34	40	-6
Test 8 - 2	424	116	130	-14	424	61	71	-10	424	46	39	7	424	37	40	-3
Test 8 - 4	452	147	160	-13	452	60	52	8	452	48	40	8	0	0	0	0
RMS Difference	23				14				14				12			

Table F.14
Outlet NH₃ (experimental vs model) configuration 2 data

Exp. Name	Outlet NH ₃ [ppm]						ANR = 1.2 repeat									
	ANR = 0.8			ANR = 1.0			ANR = 1.2			ANR = 1.2						
Test # - g/l	Expt. in	Expt.	Model	Diff.	Expt. in	Expt.	Model	Diff.	Expt. in	Expt.	Model	Diff.	Expt. in	Expt.	Model	Diff.
Test 1 - 0	444	2	0	2	555	3	2	1	666	111	99	12	666	116	105	11
Test 1 - 2	483	2	7	-5	613	2	15	-13	613	111	121	-10	727	101	116	-15
Test 1 - 4	474	2	3	-1	594	4	20	-16	594	171	158	13	718	112	105	7
Test 3 - 0	223	4	2	2	279	10	11	-1	335	62	59	3	335	61	56	5
Test 3 - 2	233	1	0	1	292	1	4	-2	292	49	45	4	350	44	43	1
Test 3 - 4	283	0	2	-2	351	0	18	-18	351	63	64	-1	422	58	62	-5
Test 6 - 0	1175	4	5	-1	1496	8	10	-2	1762	208	210	-2	1762	209	217	-8
Test 6 - 2	1110	1	0	0	1330	31	11	20	1632	115	129	-14	1620	102	127	-25
Test 6 - 4	1090	2	6	-5	1342	9	27	-19	1640	110	132	-22	1640	124	151	-27
Test 8 - 0	441	11	12	-1	551	36	35	1	661	82	78	4	661	88	91	3
Test 8 - 2	450	17	27	-9	533	35	37	-2	533	87	80	7	655	74	87	-13
Test 8 - 4	453	11	13	-2	593	30	34	-3	593	77	64	13	0	0	0	0
RMS Difference	23			14			14			12			12			

Tables F.15 to F.21 compare the experimental and model pressure drop, outlet temperature, outlet NO, NO₂, NH₃ concentrations and filtration efficiency values for the 7 Configuration 3 experiments.

Table F.15

Outlet temperature (experimental vs model) configuration 3 data

Outlet temperature [°C]			
Exp. Name	DNSCR-F		
(-)	Expt.	Model	Diff.
Test 1	216	213	3
Test B	278	275	3
Test A	274	273	0
Test C	349	351	-2
Test C with SCR	355	352	3
Test C W/O SCR	362	360	2
Test D	376	378	-2
Test E	369	372	-3
RMS Difference	2		

Table F.16

Filtration efficiency (experimental vs model) configuration 3 data

Filtration efficiency [%]			
Exp. Name	Stage - 2		
(-)	Expt.	Model	Diff.
Test 1	98.4	98.4	0.1
Test B	97.6	98.3	-0.7
Test A	98.3	98.7	-0.4
Test C	98.4	98.4	0
Test C with SCR	98.2	98.2	0
Test C W/o SCR	98	98.3	-0.3
Test D	95.7	98.2	-2.5
Test E	98.4	98.3	0.1
RMS Difference	1.1		

Table F.17
Pressure drop (experimental vs model) configuration 3 data

Exp. Name	Pressure drop [kPa]											
	End of loading (Stage 1, 2)				End of PO/AR				End of post loading (Stage 3, 4)			
	Expt.	Model	Diff.		Expt.	Model	Diff.		Expt.	Model	Diff.	
(-)	7.2	7.2	0	2.9	3	-0.1		7.7	8	-0.3		
Test 1	8.51	7.7	0.8	1.4	1.6	-0.2		7.3	7.3	0.1		
Test B	7.7	7.7	0	2.7	3	-0.2		7.3	7.6	-0.4		
Test A	8	8.1	-0.1	2.1	2.2	-0.1		6.1	5.8	0.3		
Test C	7.9	7.9	0	2	2.1	-0.1		6	6.1	-0.1		
Test C with SCR	8.1	7.9	0.2	1.9	2.1	-0.2		5.9	5.8	0.1		
Test C W/o SCR	7.5	7.4	0.2	4.4	4.7	-0.3		5.5	5.2	0.3		
Test D	7.8	7.6	0.2	2	2.1	-0.1		5.8	5.9	-0.2		
Test E												
RMS Difference	0.1				0.3				0.2			

Table F.18
PM mass retained (experimental vs model) configuration 3 data

Exp. Name	PM mass retained [g]																			
	Stage - 1				Stage - 2				End of PO				Stage - 3				Stage - 4			
	Expt.	Model	Diff.		Expt.	Model	Diff.		Expt.	Model	Diff.		Expt.	Model	Diff.		Expt.	Model	Diff.	
(-)	2.4	2.2	0.2	25.8	25.2	0.5		27.9	28	-0.1		29.2	28	1.2		31	31	0		
Test 1	2.5	2	0.5	26.9	25.9	1		28.1	27.4	0.7		28.2	27.4	0.8		31.9	32.1	-0.1		
Test B	2.7	1.8	0.8	29.3	27.6	1.7		27.7	33.2	-5.5		31.1	33.2	-2.1		35.4	37.3	-1.9		
Test A	2.5	2.3	0.2	28	28.5	-0.5		17.2	20.5	-3.3		20.1	20.5	-0.4		24.8	24.8	0		
Test C	2.6	2.2	0.4	28.5	29	-0.5		18.1	19.6	-1.5		21	19.6	1.4		25	24.8	0.2		
Test C with SCR	2.4	2.3	0.1	27.8	28.1	-0.3		18	21	-3		20	21	-1		25.1	25	0.1		
Test C W/o SCR	2.4	2	0.3	25.8	24.7	1.1		17.3	19.9	-2.6		19.5	19.9	-0.4		24.6	24.4	0.2		
Test D	2.5	2.1	0.4	26.7	26.3	0.3		18.3	20.9	-2.6		22.2	20.9	1.3		25.9	26.3	-0.4		
Test E																				
RMS Difference	0.1				0.8				(-)				0.8				1.0			

Table F.19Outlet NO₂ (experimental vs model) configuration 3 data

Outlet NO ₂ [ppm]						
(-)	Outlet SCRF®			Outlet SCR		
Exp. Name	Expt.	Model	Diff.	Expt.	Model	Diff.
Test 1	0	0	0	0	0	0
Test B	0	0	0	0	0	0
Test A	1	0	1	0	0	0
Test C	0	0	0	0	0	0
Test C with SCR	3	0	3	2	0	2
Test C w/o SCR	1	0	1	1	0	1
Test D	0	0	0	0	0	0
Test E	1	0	1	0	0	0
RMS Difference	12			8		

Table F.20

Outlet NO (experimental vs model) configuration 3 data

Outlet NO [ppm]						
(-)	Outlet SCRF®			Outlet SCR		
Exp. Name	Expt.	Model	Diff.	Expt.	Model	Diff.
Test 1	7	12	-5	8	11	-3
Test B	5	10	-5	9	8	1
Test A	18	15	3	24	9	15
Test C	4	12	-8	17	8	9
Test C with SCR	25	32	-7	13	25	-8
Test C w/o SCR	15	24	-9	22	20	-2
Test D	3	11	-8	13	7	6
Test E	8	5	3	6	0	6
RMS Difference	14			12		

Table F.21Outlet NH₃ (experimental vs model) configuration 3 data

Outlet NH ₃ [ppm]						
(-)	Outlet SCRF®			Outlet SCR		
Exp. Name	Expt.	Model	Diff.	Expt.	Model	Diff.
Test 1	1	15	-14	2	8	-6
Test B	10	17	-7	4	9	-5
Test A	30	44	-14	28	25	3
Test C	17	30	-13	18	20	-2
Test C with SCR	19	5	14	12	0	12
Test C w/o SCR	32	25	7	27	15	12
Test D	41	37	4	36	30	6
Test E	29	38	-9	32	28	4
RMS Difference	10			14		

Figures F.1 to F.8 compare the experimental and model outlet emissions from the 8 configuration 2 experiments with 2 and 4 g/l PM loading and inlet ANR of 0.8, 1.0 and 1.2.

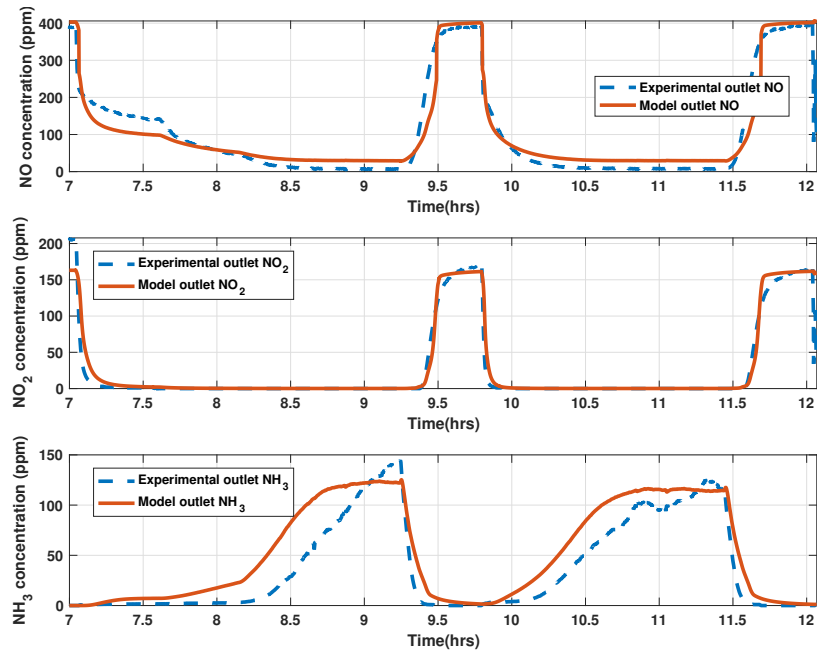


Figure F.1: Test 1 with 2g/l PM loading outlet emissions vs time

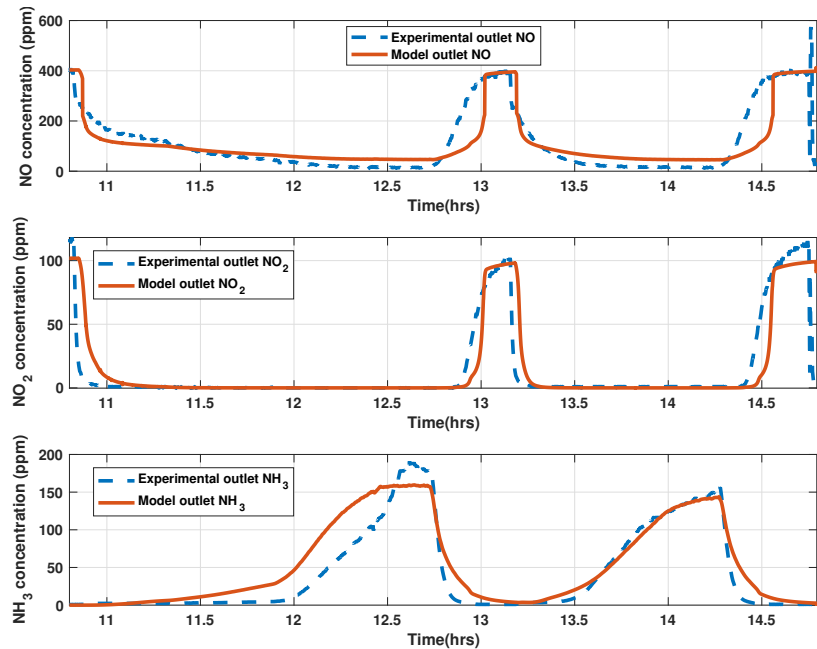


Figure F.2: Test 1 with 4 g/l PM loading outlet emissions vs time

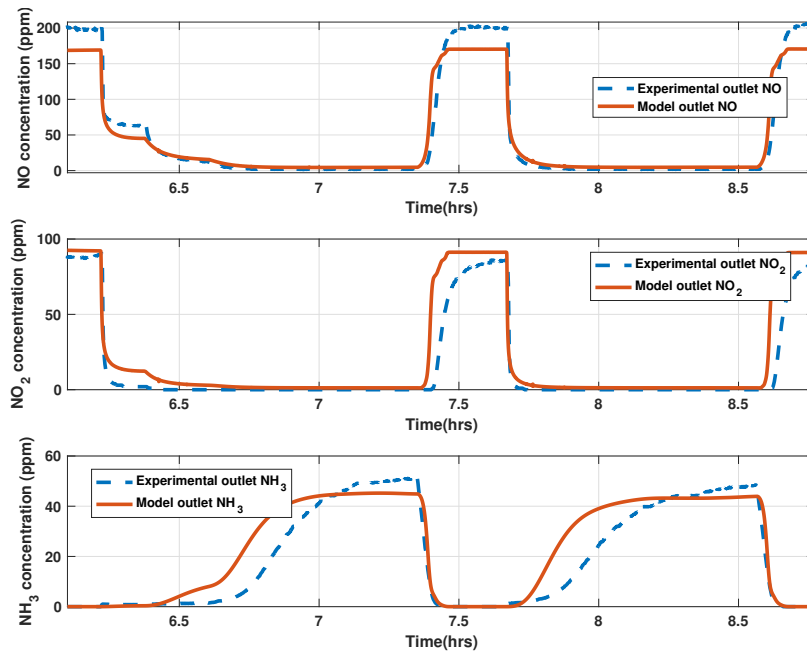


Figure F.3: Test 3 with 2 g/l PM loading outlet emissions vs time

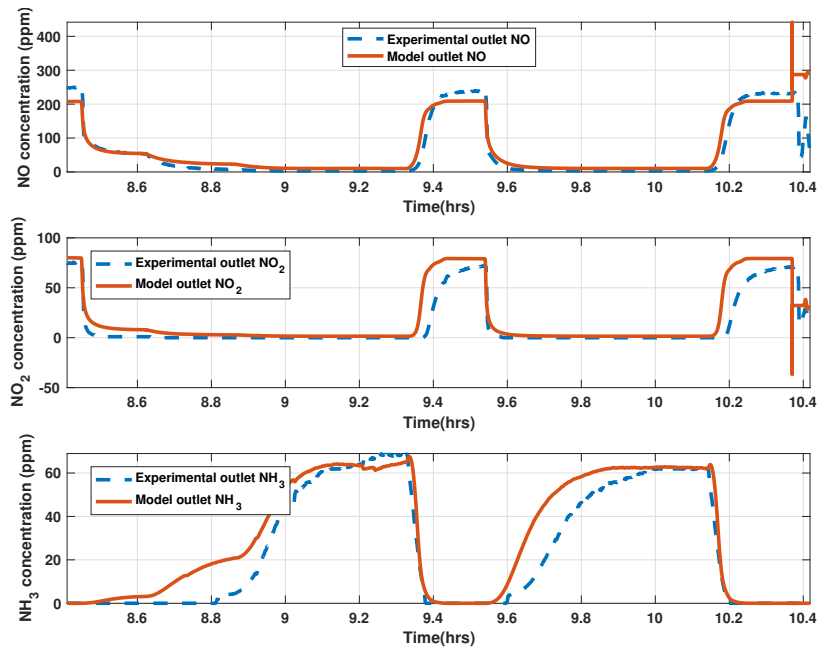


Figure F.4: Test 3 with 4 g/l PM loading outlet emissions vs time

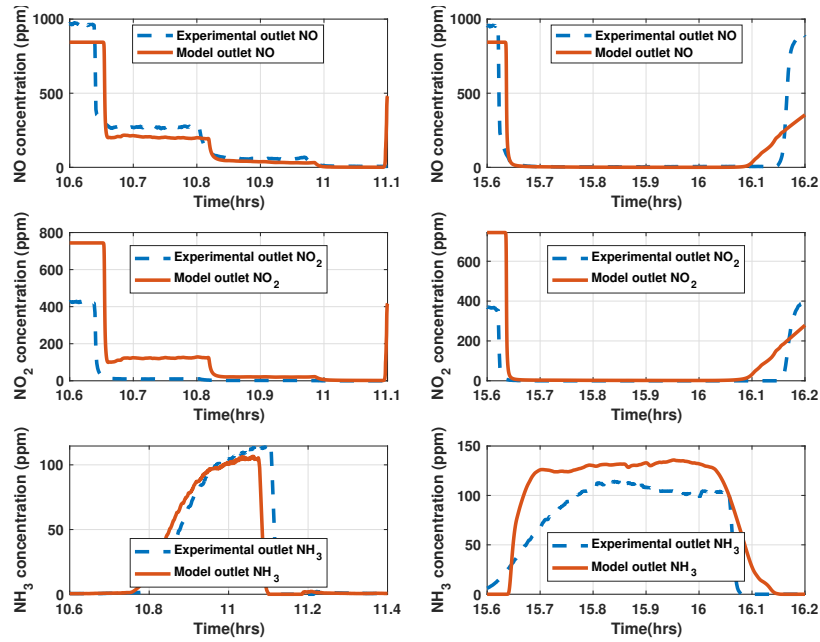


Figure F.5: Test 6 with 2 g/l PM loading outlet emissions vs time

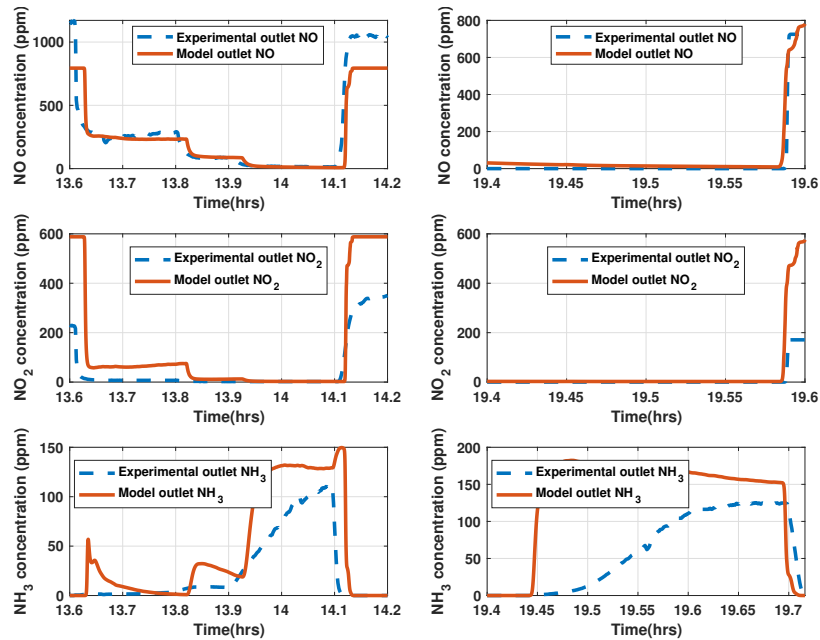


Figure F.6: Test 6 with 4 g/l PM loading outlet emissions vs time

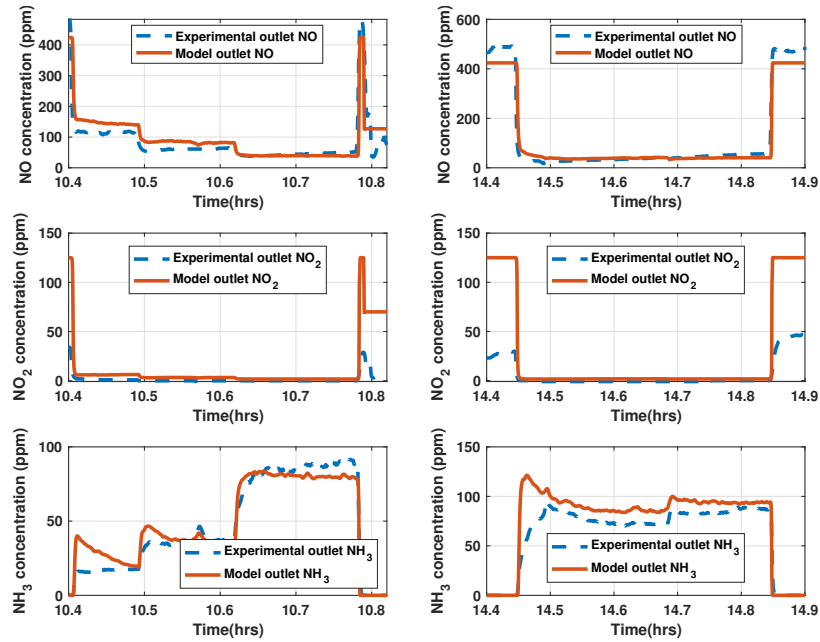


Figure F.7: Test 8 with 2 g/l PM loading outlet emissions vs time

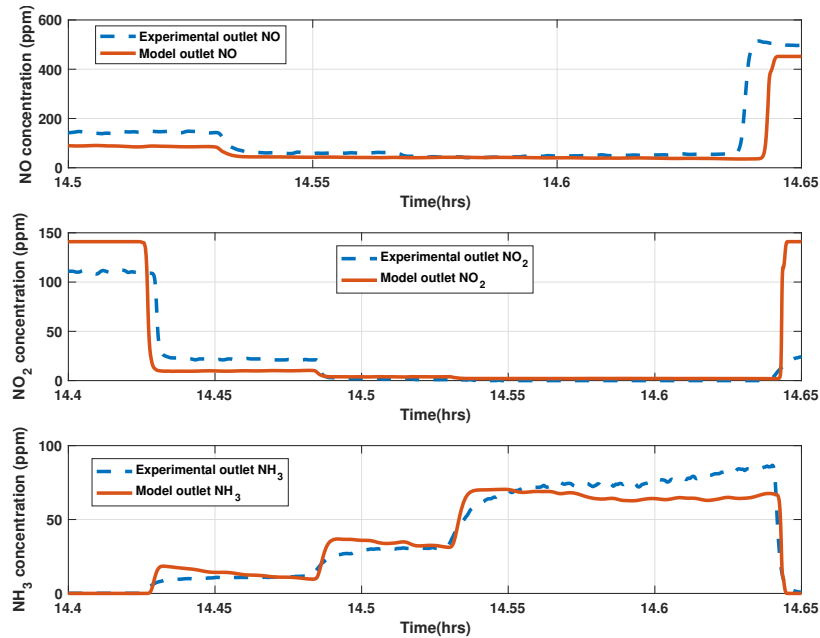


Figure F.8: Test 8 with 4 g/l PM loading outlet emissions vs time

Comparison of the experimental and model temperature distributions from the 8 configuration 2 experiments with 2 and 4 g/l PM loading at inlet ANR of 1.2 is show here.

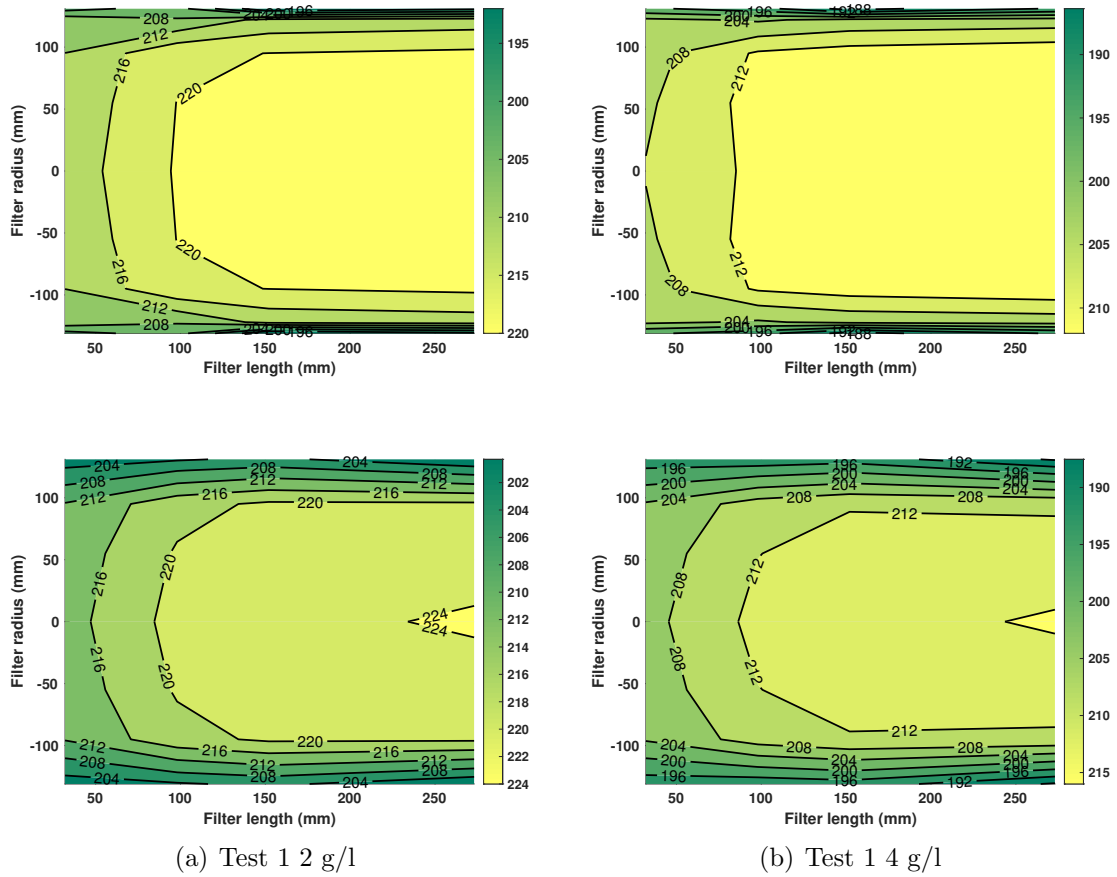


Figure F.9: Test 1 with 2 and 4 g/l PM loading experimental and model temperature distribution at ANR = 1.2

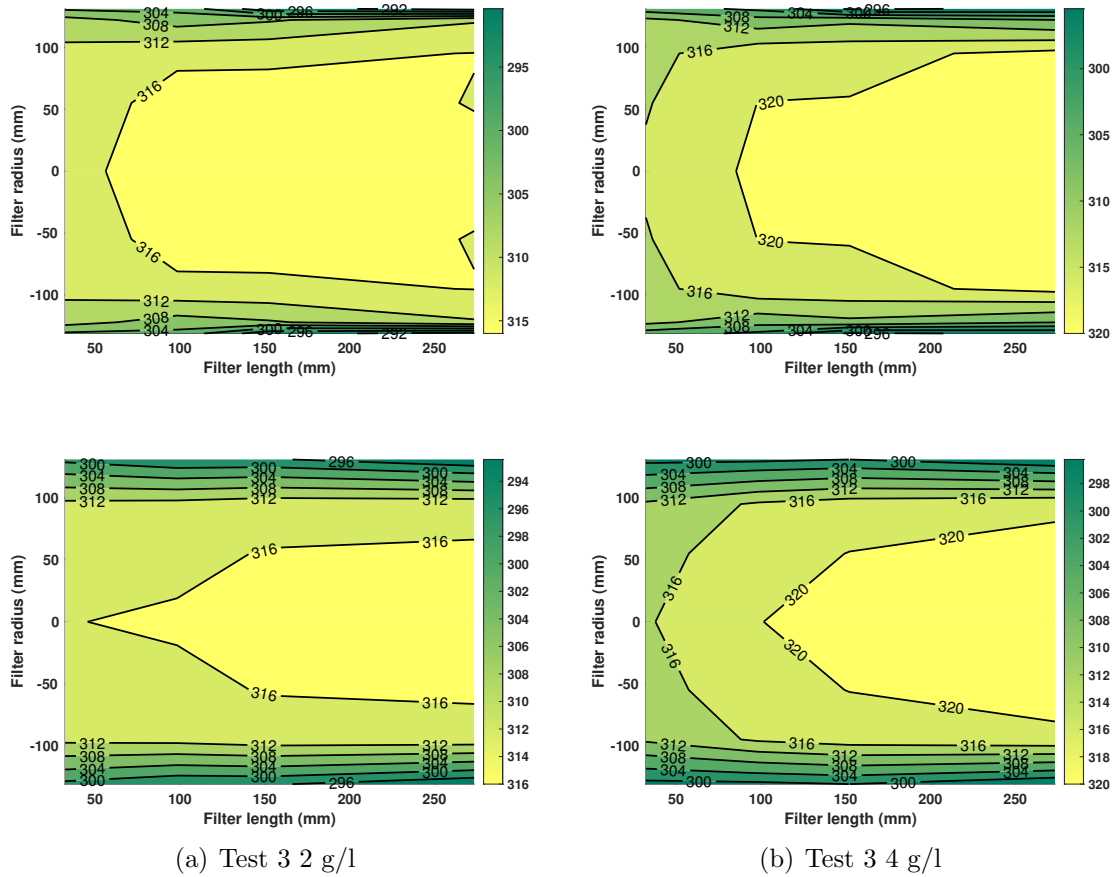


Figure F.10: Test 3 with 2 and 4 g/l PM loading experimental and model temperature distribution at ANR = 1.2

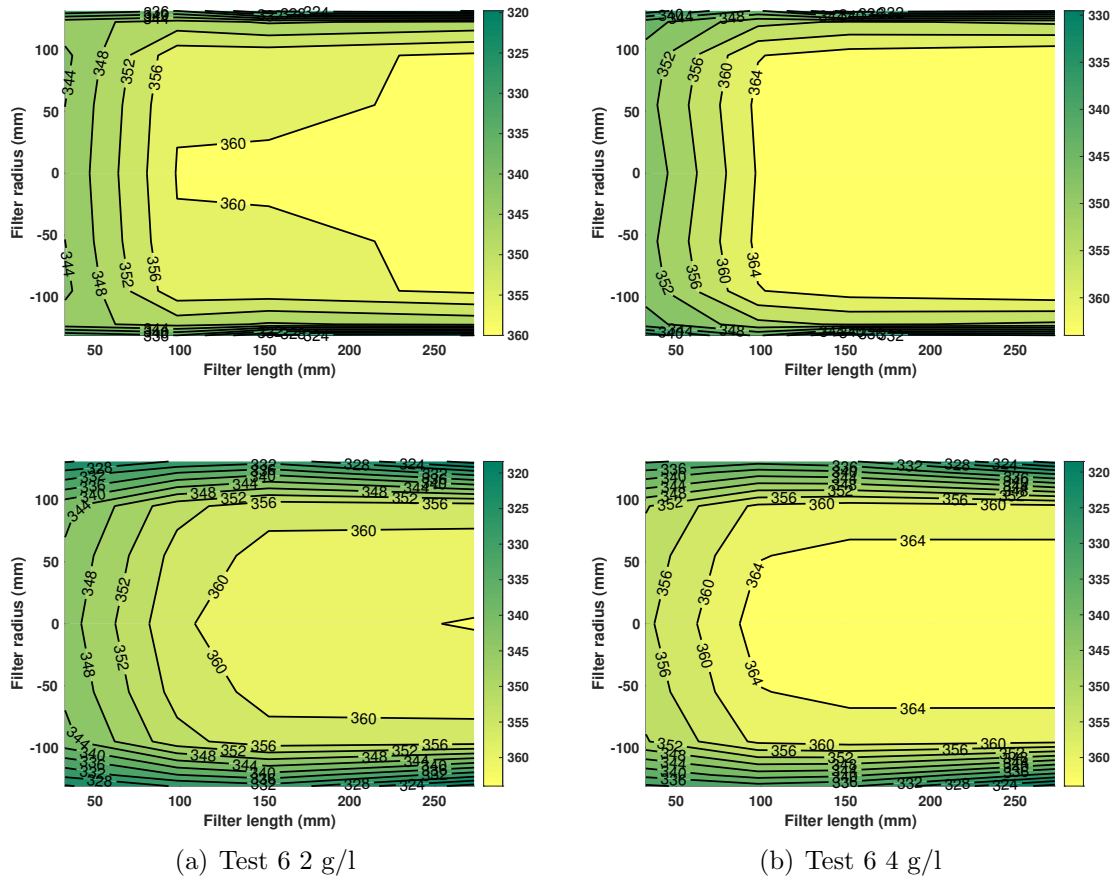


Figure F.11: Test 6 with 2 and 4 g/l PM loading experimental and model temperature distribution at ANR = 1.2

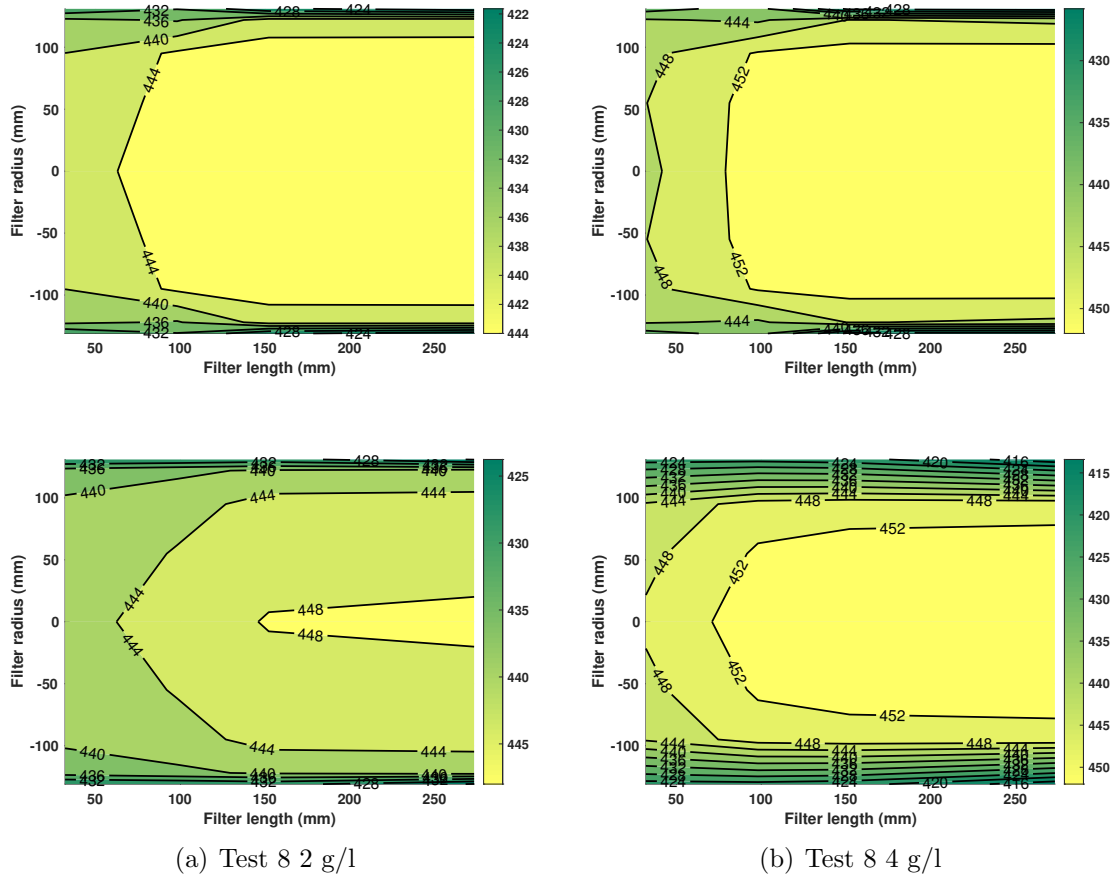


Figure F.12: Test 8 with 2 and 4 g/l PM loading experimental and model temperature distribution at ANR = 1.2

Appendix G

SCR-F[®] Calibration Parameters

G.1 Parameters from Model Calibration

The set of calibration parameters for the SCR-F Model were identified based on the calibration procedure described in Chapter 4. The following section describes the common set of parameters obtained and the Arrhenius plots used for the chemical reaction kinetics used. The list of calibration parameters are presented in the following sections

G.1.1 Filtration Parameters

There are several important parameters in the filtration efficiency model that were determined from the experimental data. The initial permeability of the wall $K_{o,w}$ determines the clean wall pressure drop of the SCR-F. For the 30 experiments used for the calibration process the values of initial permeability varied by $1.29 \pm 0.1 \text{ E-13}$ due to the variation in the pressure drop values with 1.29 E-13 being the value that was able to simulate the initial pressure drop to within $\pm 0.1 \text{ kPa}$ for all experiments. The transition permeability determines the time at which the filtration transitions from deep bed to cake filtration, based on the slope of the pressure drop curves. This value was determined to be in the range of $8 \pm 0.04 \text{ E-13}$ with 8E-13 being the final common value.

The first and second wall packing density $C_{1,wpm}$ and $C_{2,wpm}$ were determined based on the slope of the pressure drop curve in the first 30 minutes of the loading stage where the deep bed filtration is dominant. A value of 2.35 and 0.723 was found for each of these parameters comparable to the values from reference [37] for a CPF.

The parameters C_3 , C_4 , C_6 and C_7 were based on the pressure drop curve slope during the loading stages of all the experiments with values of 103.2, 110, 100 and 300 respectively being determined. The permeability of the cake ($K_{o,cake}$) and initial solidosity ($\alpha_{o,cake}$) were changed for different experiments however a common value of 7.01E-15 and 0.05 were found as the parameters for all the experiments. The post loading cake permeability parameters C_{11} and C_{13} with values of 1.485 and 0.664 were found based on the slope of stage 3 and 4 pressure drop curves for all the configuration 1 experiments.

Table G.1 shows the final pressure drop and filtration parameters found during the calibration of the SCR-F model with configuration 1 data with and without urea injection.

Table G.1
SCR-F model pressure drop parameters

Parameter	Description	Value	Units
Substrate Wall			
$K_{o,w}$	Initial permeability of substrate wall	1.29E-13	(m^2)
$K_{o,trans}$	Transition permeability of substrate wall	8.00E-13	(m^2)
Wall PM			
$C_{1,wpm}$	First constant for wall packing density	2.35	($1/m^3$)
$C_{2,wpm}$	Second constant for wall packing density	0.723	(kg/m^3)
C_3	Ref. pressure for wall permeability corr.	103.2	(kPa)
C_4	Wall permeability correction factor	110	(-)
PM cake layer			
$\alpha_{o,cake}$	Initial solidosity of PM cake layer	0.05	(-)
$K_{o,cake}$	Initial / ref. permeability of PM cake layer	7.01E-15	(m^2)
$A_{eff,cake}$	PM cake maximum filt. effi. parameter	0.95	(-)
C_5	Cake permeability correction factor	1.43E-13	($kg\ m^{-1}$)
C_6	Ref. pressure for lambda correction	100	(kPa)
C_7	Ref. temperature for lambda correction	300	(K)
C_{10}	Slope for post loading cake permeability	0	(-)
C_{11}	Constant for post loading cake permeability	1.485	(-)
C_{13}	Constant for oxidation cake permeability	0.664	(-)

G.1.2 Thermal Parameters

The thermal parameters are responsible for the 2D substrate temperature distribution and the SCR-F outlet exhaust gas temperature simulation. Initially the heat loss to the ambient in each configuration experiment was simulated by using different values of H_{amb} . A common value of $24.1 \text{ W/m}^2\text{K}$ was found for this parameter which was able to simulate the temperature distribution in the outer 20 % of the SCR-F diameter for all the experiments. The radiation heat transfer coefficient (η_{filter}) of 0.64 was found using the same procedure as H_{amb} . The density of the filter determines the transient response of the filter and changes as the filter is filled with PM. A value of 449 kg/m^3 was found for this parameter. Table G.2 shows the final thermal parameters found during the calibration of the SCR-F model with configuration 1 data with and without urea injection.

Table G.2
SCR-F model thermal parameters

Parameter	Description	Value	Units
Thermal Properties			
Hamb	Convection heat transfer coefficient	24.1	(W/m ² K)
η_{filter}	Radiation heat transfer coefficient	0.64	(-)
ρ_{filter}	Density of substrate	449	(kg/m ³)

G.1.3 Catalyst Parameters

The catalyst loading location in the SCR-F was an unknown quantity. Initially the catalyst loading was assumed to be uniformly coated in the axial and radial directions and the maximum storage capacity of the Cu-Ze catalyst was identified by the calibration of the SCR kinetics using NO, NO₂ and NH₃ outlet emissions in the configuration 2 data without PM loading. However, during the configuration 2 calibration, the temperature distribution in the SCR-F® was found to be a function of energy released by SCR reactions. Figure G.1 shows a case where the exhaust gas temperature in the SCR-F® is increasing in the axial direction during NO_x reduction by the SCR reactions.

As can be observed in the Figure G.1, the temperature rise occurs in the first 30 %

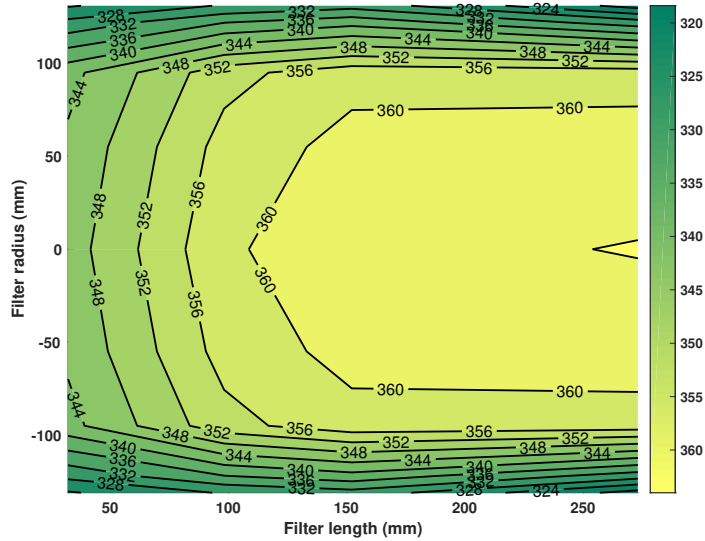


Figure G.1: Temperature distribution during NO_x reduction at ANR 1 - Test 6 with 2 g/l PM loading configuration 2

length of the filter from 0 to 100 mm. Based on the further analysis of the temperature distribution, it was concluded that the experimental temperature rise from 0 to 50 mm is negligible indicating a variation in axial distribution of the Cu-Ze catalyst loading with three distinct zones. Based on the temperature data, the SCR-F® was divided into three zones, the axial length 0 to 50mm was identified as first zone with 0.5 times the value of average catalyst loading, the zone 2 from 50 to 100 mm had 1.5 times the average catalyst loading with the third zone from 100 to 300 mm containing 0.8 times average catalyst coating loading. On applying this catalyst loading profile based on maximum storage capacity of NH_3 storage sites combined with the diffusion of chemical species in the axial direction in the inlet and the outlet channels, the SCR-F model was able to simulate the temperature distribution in the SCR-F® during NO_x reduction. Figure G.2 illustrate the zones used for catalyst loading distribution used in the model based on the calibration to the temperature distribution data.

G.1.4 Catalytic Reactions and PM Oxidation Kinetics

The PM oxidation in the SCR-F model takes place by two reactions - NO_2 assisted and thermal PM oxidation. The PM cake kinetics for both these reactions are shown in Table G.3. These kinetics were able to simulate the PM oxidation rate for all the 37 experiments. The activation energy of 116.5 kJ/gmol for NO_2 assisted PM oxidation

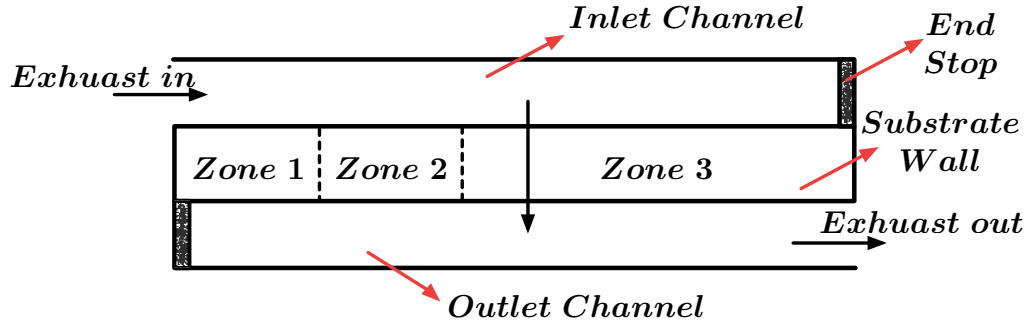


Figure G.2: Different catalyst loading zones in the SCR[®]

was found using the 7 PO experiments without urea injection in configuration 1 data. The thermal PM oxidation activation energy of 197.8 kJ/gmol was found using the four AR experiments from configuration 1. The pre exponential of the NO₂ assisted oxidation changed during the PO stage compared to the loading stage due to a change in the nature of the PM Oxidation from 688 to 164 m/K-s. The pre exponential of thermal oxidation remains constant at 374 m/K-s for all the engine conditions.

Table G.3
PM oxidation kinetics - PM cake

PM Oxid.	Symbol	Description	Loading/Oxidation	Units
Passive (NO ₂)	$A_{NO_2, cake}$	Pre Exponential	688/164	m/K-s
	$Ea_{NO_2, cake}$	Activation energy	116/116	kJ/gmol
Thermal (O ₂)	$A_{th, cake}$	Pre Exponential	374/374	m/K-s
	$Ea_{th, cake}$	Activation energy	197.8/197.8	kJ/gmol

Table G.4 shows the kinetics of the PM oxidation reactions in the substrate wall. A different pre exponential than the cake was used for the thermal and NO₂ assisted PM oxidation of the PM in the substrate wall. The activation energies remain the same as PM cake. The pre exponential of passive oxidation rate of wall PM was changed for the oxidation and loading stages.

Table G.4
PM oxidation kinetics - PM in the wall

PM Oxid.	Symbol	Description	Loading/Oxidation	Units
Passive (NO ₂)	$A_{NO_2,wall}$	Pre Exponential	1211/605	m/K-s
	$Ea_{NO_2,wall}$	Activation energy	116.5/116.5	kJ/gmol
Thermal (O ₂)	$A_{th,wall}$	Pre Exponential	486.9/486.9	m/K-s
	$Ea_{th,wall}$	Activation energy	197.8/ 197.8	kJ/gmol

Table G.5 shows the kinetics of the species oxidation reactions. These kinetics were found using the activation energies from reference [37]. The kinetics of CO and HC oxidation remained the same as the CPF while the NO oxidation kinetics decreased significantly due to the low NO oxidation reaction rate observed in the SCRF®. This reduction of NO oxidation can be attributed to a change in the catalyst from Pt group metals used in the CPF to Cu-Ze catalyst used in the SCRF®. Due to the low NO oxidation rate, the forward diffusion of NO₂ from the PM cake to the substrate wall in the place of back diffusion is observed. This change in diffusion rate has a impact on the PM oxidation rate and the pressure drop characteristics of the SCRF®.

Table G.5
Gaseous species kinetics

Reaction	Symbol	Description	SCRF® Values	Units
NO oxidation	A_{NO}	Pre Exponential of NO oxidation	1E+01	m/K-s
	Ea_{NO}	Activation energy of NO oxidation	1.87E+07	kJ/gmol
CO oxidation	A_{CO}	Pre Exponential of CO oxidation	6.00E+10	m/K-s
	Ea_{CO}	Activation energy of CO oxidation	4.35E+04	kJ/gmol
HC oxidation	A_{HC}	Pre Exponential of HC oxidation	5.00E+10	m/K-s
	Ea_{HC}	Activation energy of HC oxidation	4.35E+07	kJ/gmol

G.1.5 SCR Kinetics

Table G.6 shows the final SCR kinetic values found using the configuration 2 data without PM loading and using the procedure from Chapter 4. The SCR kinetics were found using the kinetic parameters from reference [2] as the starting value. Since the catalyst is similar to the one from reference [2] the activation energies of the SCR reactions remained close to the initial values. The storage parameters of $\Omega_1 = 0.18 \text{ kmol/m}^3$ and $\Omega_2 = 0.092 \text{ kmol/m}^3$ increased significantly 3 - 4 times compared to the flow through SCR. The adsorption and desorption kinetics also changed significantly with the adsorption reactions having a positive activation energy compared to negative values observed for the flow through SCR. The pre exponentials of the three SCR reactions and NH_3 oxidation were adjusted to simulate the SCRF® outlet NO , NO_2 and NH_3 concentrations to within 20 ppm of the experimental values for all the experiments. The inhibition of SCR reactions were computed using these kinetic parameters and the filtration model as explained in Chapter 3.

Table G.6
SCR kinetics

Parameter	SCRF® Kinetic parameters	Units
Ω_1	0.18	kmol/m^3
Ω_2	0.092	kmol/m^3
A_{ads}	9.00E+03	$\text{m}^3/\text{gmol.s}$
E_{ads}	6.00E+01	kJ/gmol
A_{des}	1.91E+09	1/s
E_{des}	1.83E+02	kJ/gmol
$A_{ads,2}$	1.14E+03	$\text{m}^3/\text{gmol.s}$
$E_{ads,2}$	1.24E+03	kJ/gmol
$A_{des,2}$	9.74E+06	1/s
$E_{des,2}$	8.54E+01	kJ/gmol
A_{std}	2.50E+08	$\text{m}^3/\text{gmol.s}$
E_{std}	6.76E+01	kJ/gmol
A_{fst}	2.15E+09	$\text{m}^6/\text{gmol}^2.\text{s}$
E_{fst}	4.58E+01	kJ/gmol
A_{slo}	2.69E+09	$\text{m}^3/\text{gmol.s}$
E_{slo}	1.08E+02	kJ/gmol
A_{oxid}	3.45E+13	1/s
E_{oxid}	2.00E+02	kJ/gmol

G.1.6 Diffusion Parameters

The forward diffusion between the PM cake and substrate wall layers played an important role in determining the PM cake oxidation rate by the NO₂ assisted PM oxidation reaction. The diffusion of the chemical species from the inlet channel to the PM cake and the substrate wall to outlet channel determined the chemical species concentration profiles in the axial direction. This diffusion phenomena became significant due to the non uniform catalyst loading in the axial direction of the SCRFR[®] which affected the 2D temperature distribution profile.

In order to calculate the forward diffusion rate between the PM cake and the substrate wall, both the Knudsen and molecular diffusion rate of the chemical species were considered. The unknown parameter in this case was the tortuosity of the PM cake which determines the contribution of the Knudsen and molecular diffusion components and thus the diffusion rate increases with an increase in the tortuosity value. A initial value of 1 was used for the tortuosity in experiments with no urea injection, using the configuration 1 data with urea injection. A final value of 8 for the tortuosity was determined for this parameter which enabled the forward diffusion rate required to simulate the 70% reduction in PM oxidation rate in experiments with urea injection without a change in the PO kinetics in the PM cake. Table G.7 and G.8 show the final parameters used for diffusion rate calculation in the PM cake, substrate wall and channels.

Table G.7
Diffusivity parameters

Parameter	Symbol	Value	Units
Tortuosity of PM cake	τ_{cake}	8	(-)

Table G.8
Chemical species diffusivity values

Parameter	Symbol	Values	Units
Molecular diffusivity of NO	$D_{eff,NO}$	1.98E-06	(m ² /s)
Molecular diffusivity of NO ₂	D_{eff,NO_2}	1.36E-06	(m ² /s)
Molecular diffusivity of NH ₃	D_{eff,NH_3}	1.90E-06	(m ² /s)

G.1.7 Cake Permeability Parameters

Cake permeability plays an important role in determining the pressure drop across the SCRF® during the PM oxidation stage. Table G.9 shows the list of parameters that were found using the calibration process explained in Chapter 4. For the active regeneration runs, due to lack of back diffusion of NO₂, combined with high oxidation rate by thermal PM oxidation, the cake permeability change was observed to be negligible hence the parameters C_{8th} and C_{9th} remained zero for the SCRF®. For passive oxidation runs without urea injection, due to the low PM oxidation rate, significant increase in cake permeability was observed leading to $C_{8,NO_2} = 2.77$ and $C_{9,NO_2} = 18$. These values further decreased for cases with urea injection due to forward diffusion of NO₂. Similarly, the value of $C_{13} = 0.6641$ and 1.2 were found to simulate the change in the cake pressure drop slope during the PM oxidation.

Table G.9
Cake permeability parameters

Symbol	Description	Values without urea	Values with urea	Units
C_{8th}	Slope of delta mass offset for the thermal PM (O ₂) oxidation	N/A	N/A	(s-g)
C_{9th}	Constant of the delta mass offset for the thermal (O ₂) PM oxidation	N/A	N/A	(-)
C_{8,NO_2}	Slope of delta mass offset for the NO ₂ - assisted PM oxidation	2.77	2.39	(s-g)
C_{9,NO_2}	Constant of the delta mass offset for the NO ₂ - assisted PM oxidation	18	19.9	(-)
C_{13}	Constant for damage equation	0.6641	1.2	(-)
α_{NO_2}	Variable in cake permeability equation	2.19	2.19	(-)
β_{NO_2}	Variable in cake permeability equation	9.46	9.46	(-)

Appendix H

Ultra Low NO_x Parametric Study Results

The Ultra Low NO_x system proposed in Chapter 7 was run with five different engine Test points to determine system performance at different temperature, flow rate and inlet NO_x, ANR conditions. Results from Text C from this dataset were described in detail in Chapter 7. Figures H.1 to H.16 show the performance of the system in the remaining four test conditions. These experiments cover a wide range of exhaust temperature and flow rate conditions along with inlet NO₂/NO_x ratio and NO_x concentrations at the inlet of the SCRF®.

H.1 Test1

Inlet T = 203°C, NO = 443 ppm, NO₂ = 182 ppm, NO_x = 625 ppm, Flow Rate = 5.2 kg/min

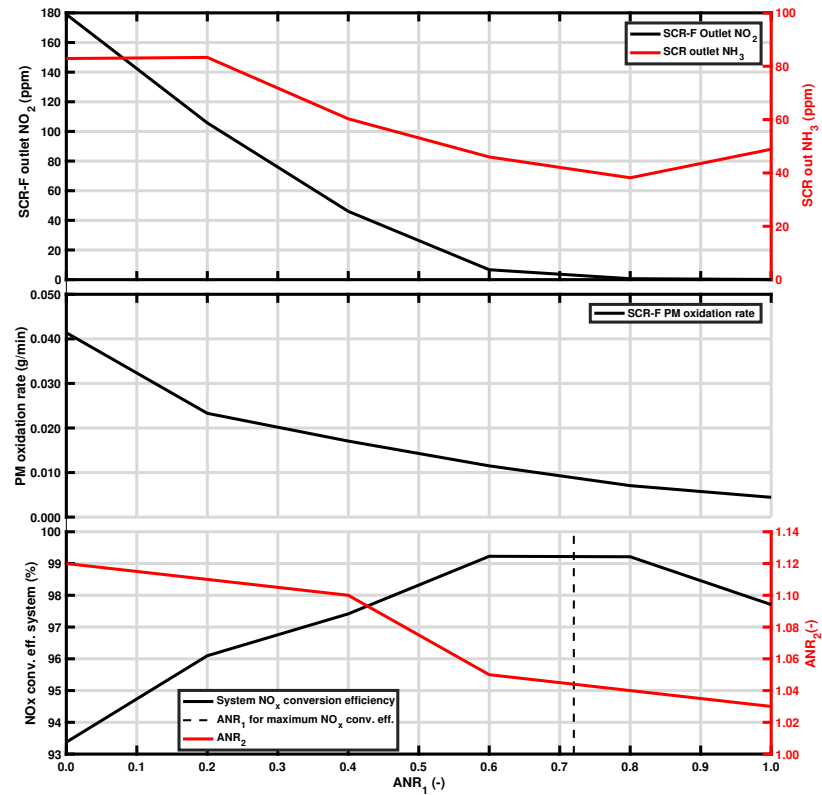


Figure H.1: NO_x conversion efficiency, ANR₂, PM oxidation rate, SCR-F® outlet NO₂ and SCR outlet NH₃ concentration vs ANR₁ at engine condition 1 (SCR-F®+DOC₂+SCR with 2 urea injectors)

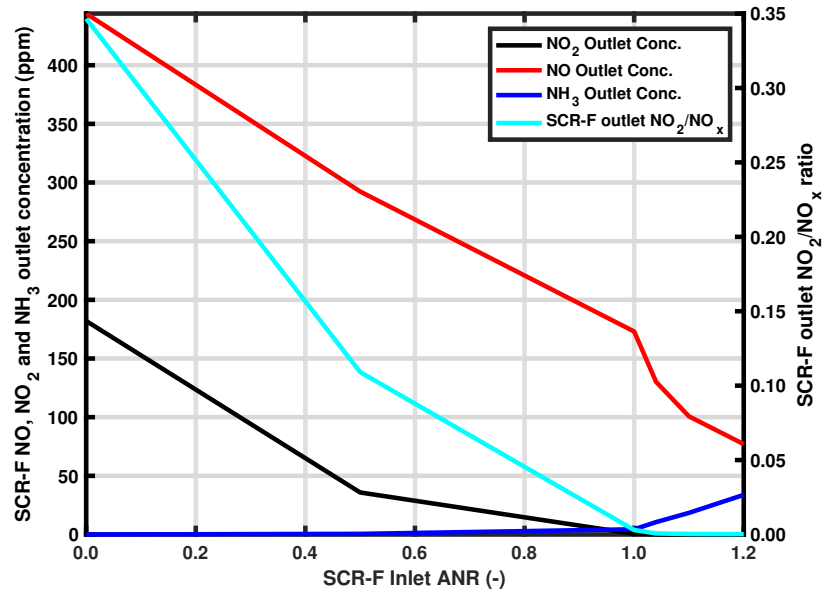


Figure H.2: Outlet concentrations and SCR-F® outlet NO₂/NO_x ratio vs inlet ANR values at engine condition 1 (SCR-F® with 1 injector)

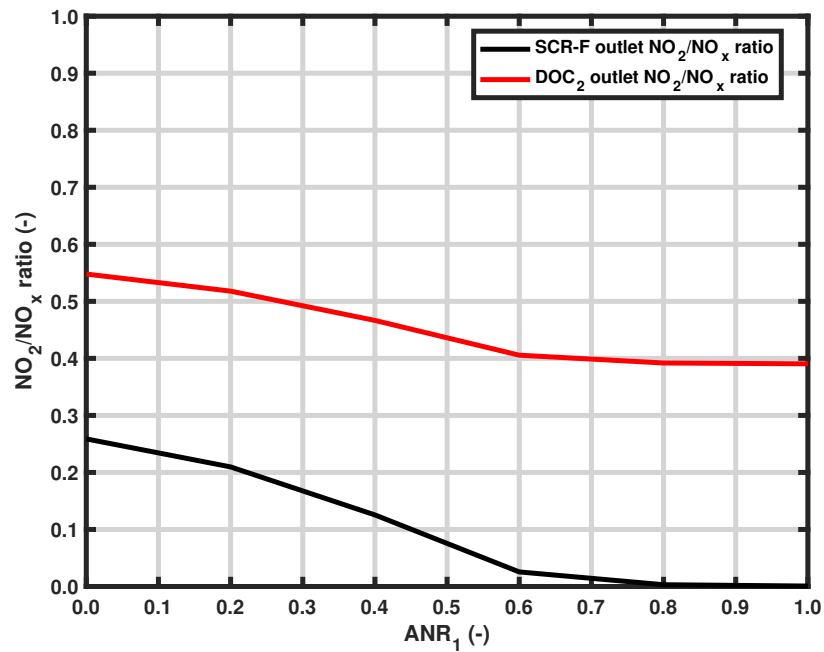


Figure H.3: NO₂/NO_x ratio vs ANR₁ at engine condition 1 (SCR-F®+DOC₂+SCR with 2 urea injectors)

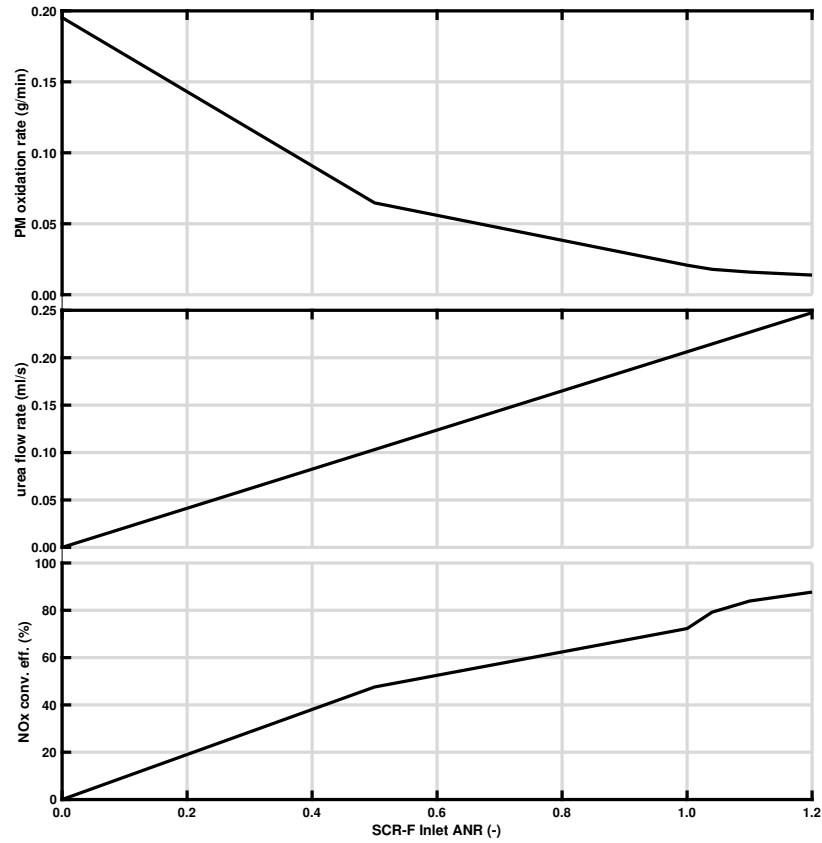


Figure H.4: NO_x conversion efficiency, urea flow rate and PM oxidation rate vs SCR-F® Inlet ANR at engine condition 1 (SCR-F® with 1 injector)

H.2 TestA

Inlet T = 267°C, NO = 375 ppm, NO₂ = 215 ppm, NO_x = 590 ppm, Flow Rate = 5.6 kg/min

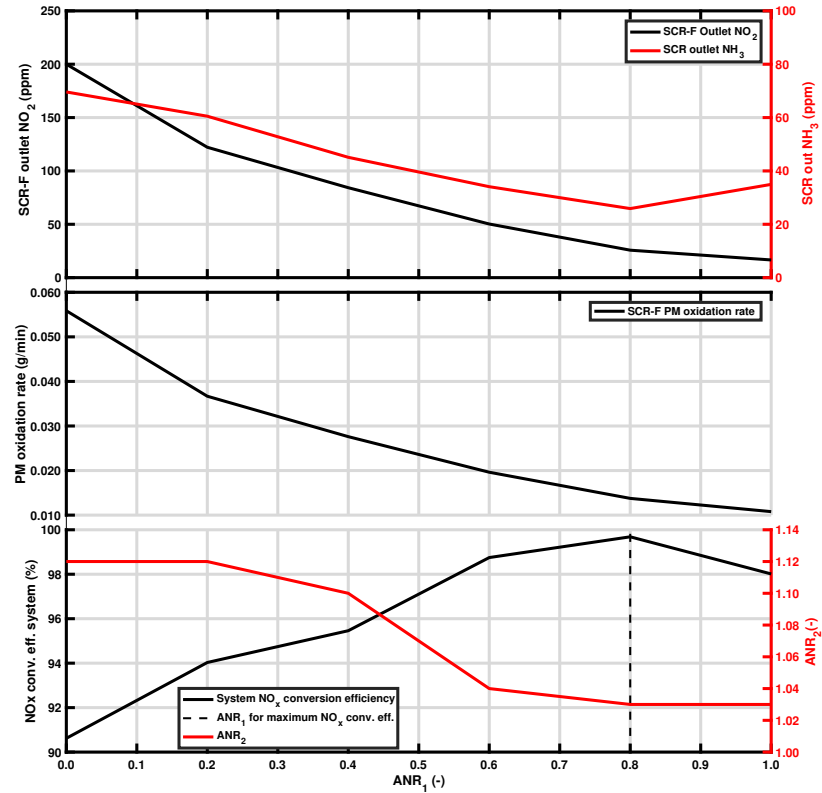


Figure H.5: NO_x conversion efficiency, ANR₂, PM oxidation rate, SCR-F® outlet NO₂ and SCR outlet NH₃ concentration vs ANR₁ at engine condition A (SCR-F®+DOC₂+SCR with 2 urea injectors)

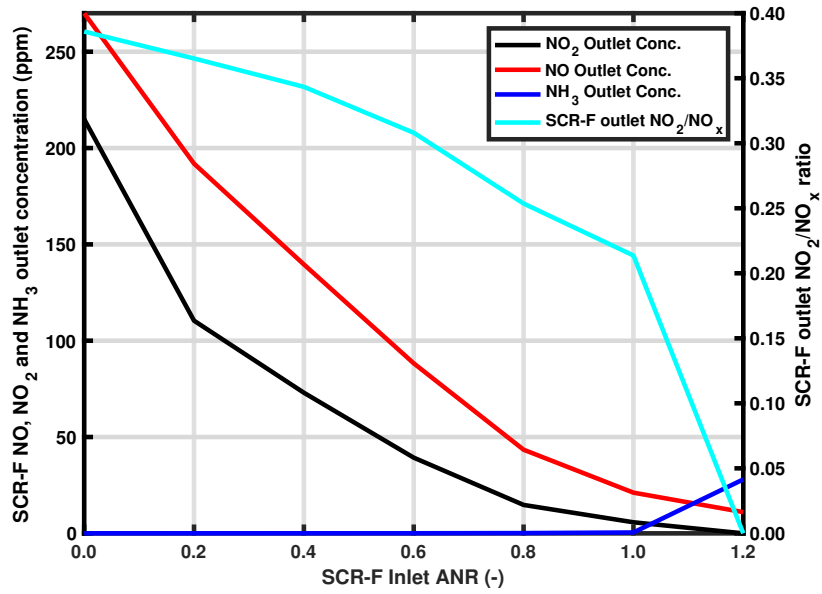


Figure H.6: Outlet concentrations and SCR-F® outlet NO₂/NO_x ratio vs inlet ANR values at engine condition A (SCR-F® with 1 injector)

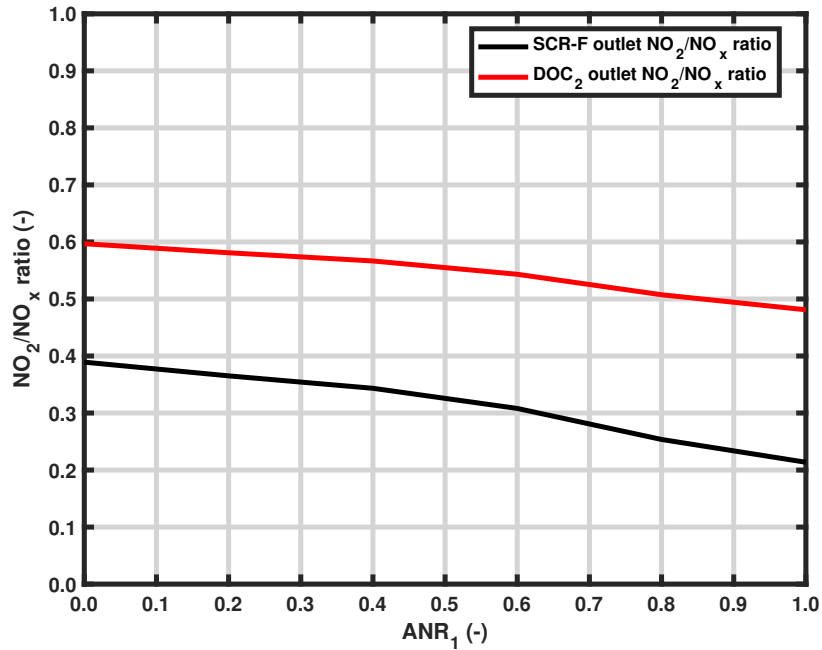


Figure H.7: NO₂/NO_x ratio vs ANR₁ at engine condition A (SCR-F®+DOC₂+SCR with 2 urea injectors)

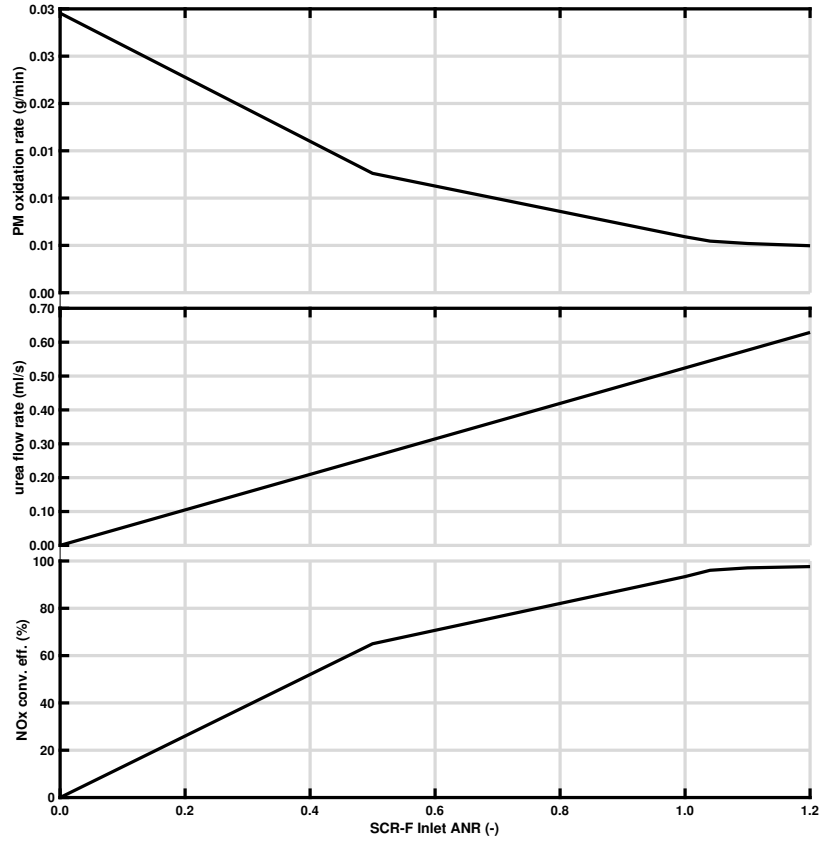


Figure H.8: NO_x conversion efficiency, urea flow rate and PM oxidation rate vs SCR-F® Inlet ANR at engine condition A (SCR-F® with 1 injector)

H.3 TestD

Inlet T = 366°C, NO = 289 ppm, NO₂ = 161 ppm, NO_x = 450 ppm, Flow Rate = 12.5 kg/min

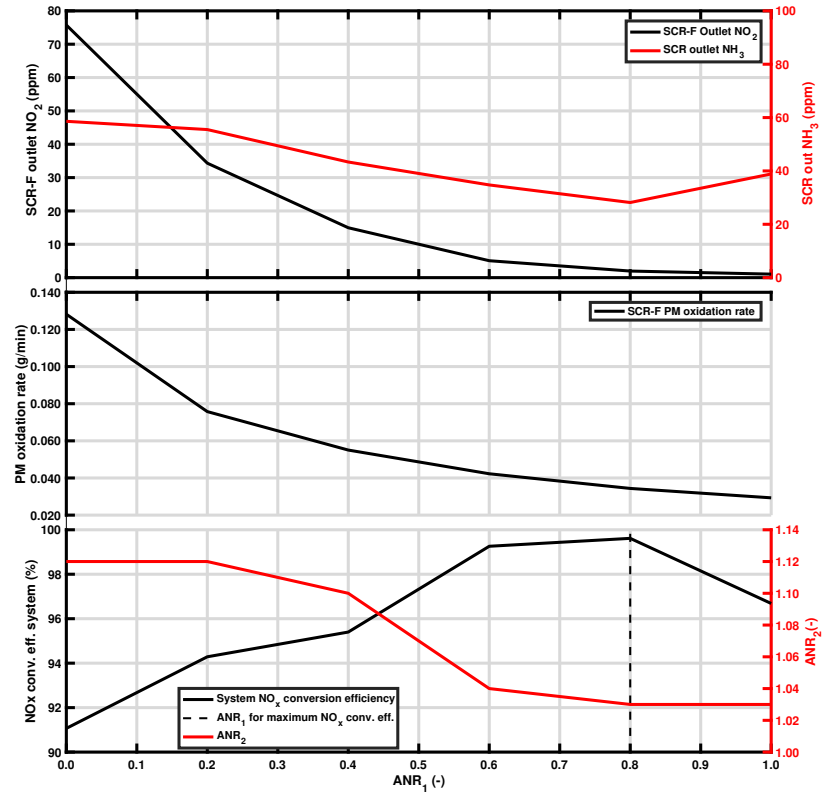


Figure H.9: NO_x conversion efficiency, ANR₂, PM oxidation rate, SCR-F® outlet NO₂ and SCR outlet NH₃ concentration vs ANR₁ at engine condition D (SCR-F®+DOC₂+SCR with 2 urea injectors)

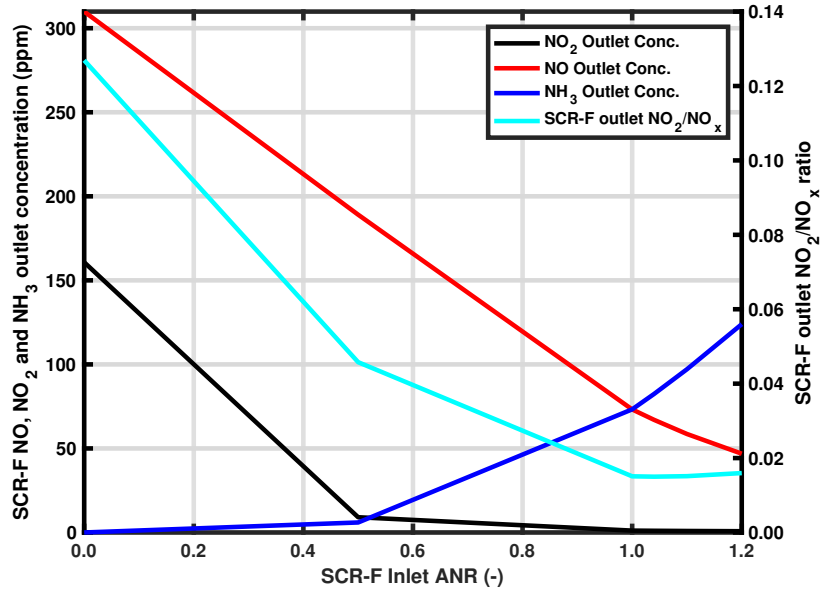


Figure H.10: Outlet concentrations and SCR-F® outlet NO₂/NO_x ratio vs inlet ANR values at engine condition D (SCR-F® with 1 injector)

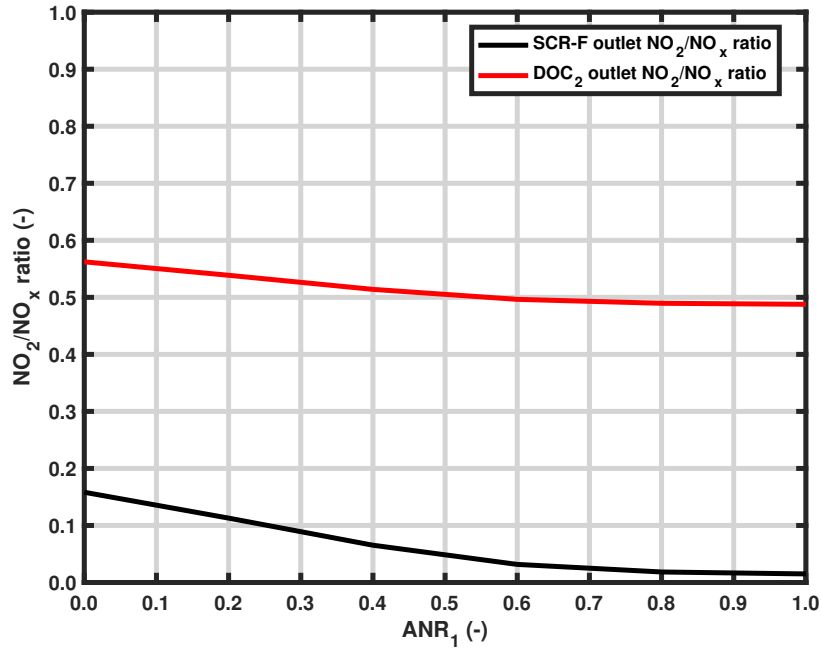


Figure H.11: NO₂/NO_x ratio vs ANR₁ at engine condition D (SCR-F®+DOC₂+SCR with 2 urea injectors)

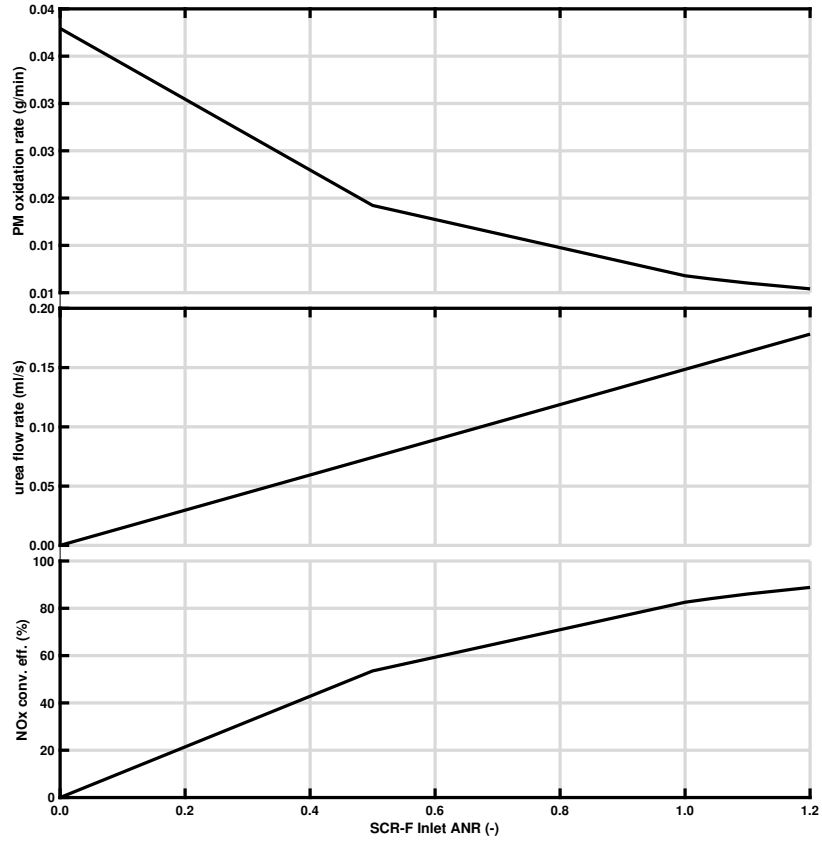


Figure H.12: NO_x conversion efficiency, urea flow rate and PM oxidation rate vs SCR-F® Inlet ANR at engine condition D (SCR-F® with 1 injector)

H.4 TestE

Inlet T = 342°C, NO = 866 ppm, NO₂ = 584 ppm, NO_x = 1450 ppm,
Flow Rate = 7.1 kg/min

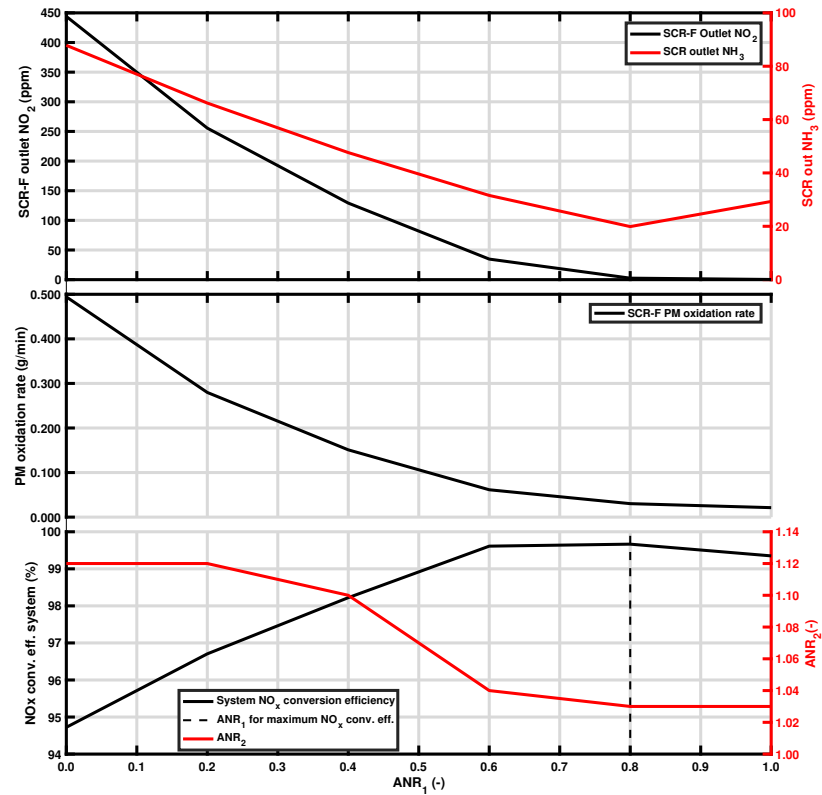


Figure H.13: NO_x conversion efficiency, ANR₂, PM oxidation rate, SCR-F® outlet NO₂ and SCR outlet NH₃ concentration vs ANR₁ at engine condition E (SCR-F®+DOC₂+SCR with 2 urea injectors)

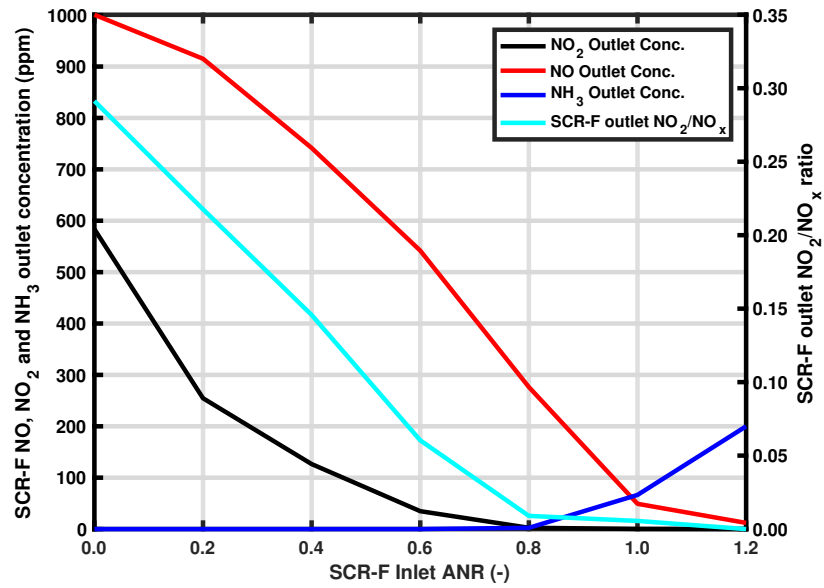


Figure H.14: Outlet concentrations and SCR-F® outlet NO₂/NO_x ratio vs inlet ANR values at engine condition E (SCR-F® with 1 injector)

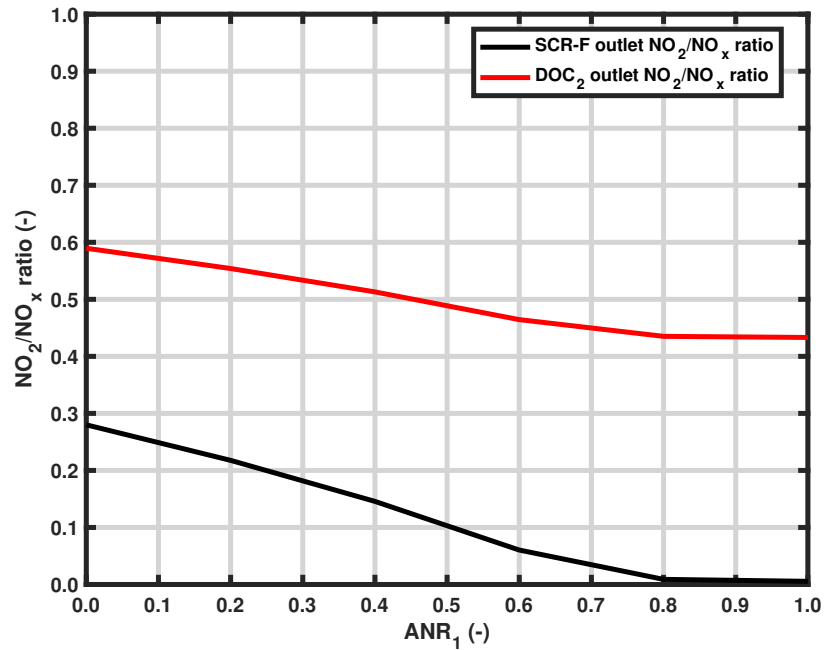


Figure H.15: NO₂/NO_x ratio vs ANR₁ at engine condition E (SCR-F®+DOC₂+SCR with 2 urea injectors)

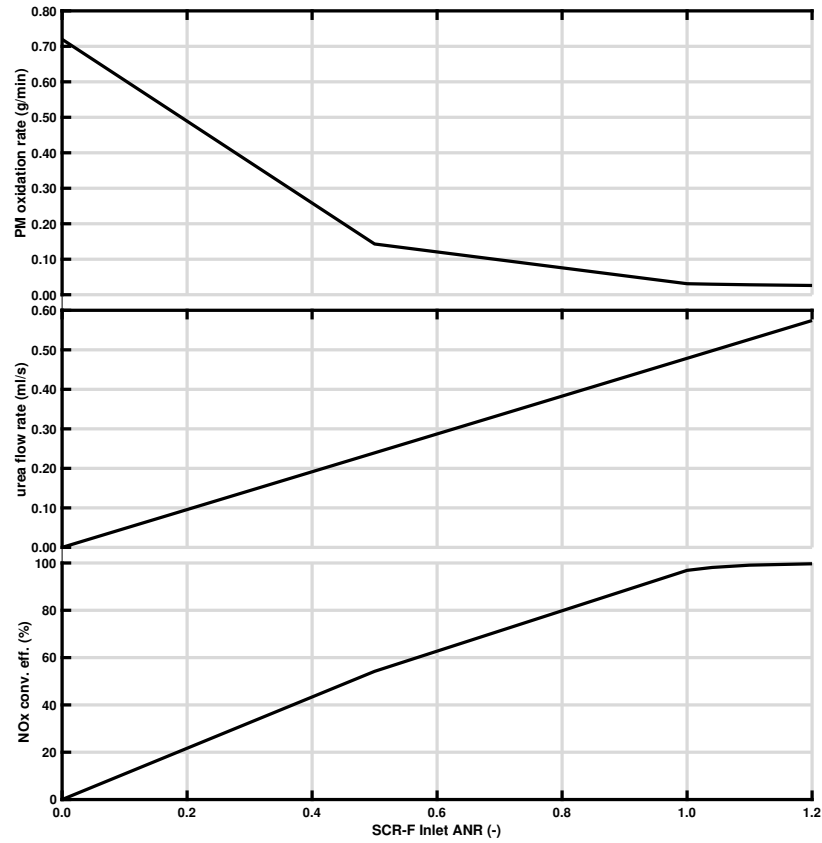


Figure H.16: NO_x conversion efficiency, urea flow rate and PM oxidation rate vs SCR-F® inlet ANR at engine condition E (SCR-F® with 1 injector)

Figure H.17 shows the change in NO conversion efficiency as a function of DOC temperature for the engine conditions used in the simulations.

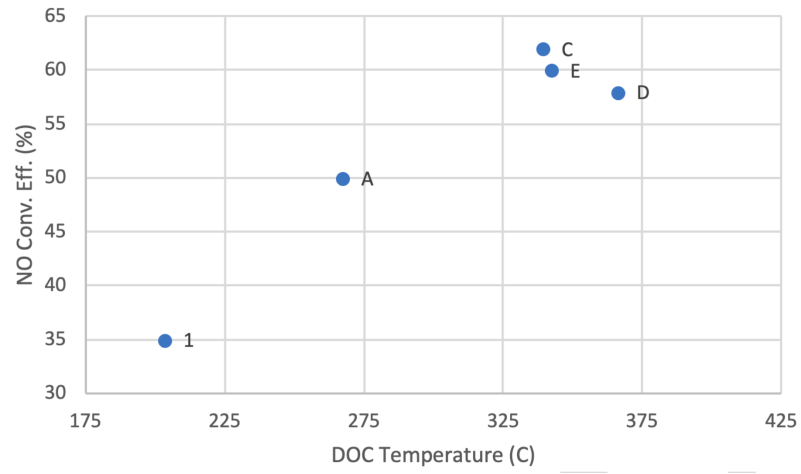
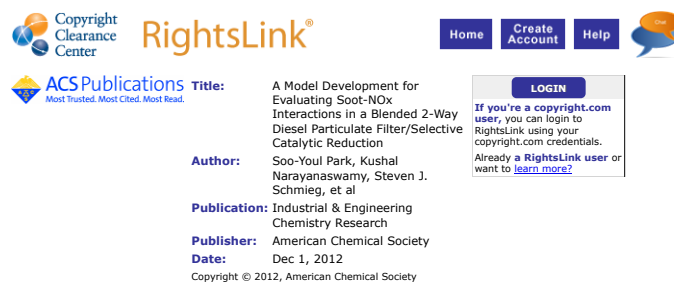


Figure H.17: NO conversion efficiency vs DOC₂ temperature for all the five engine conditions

Appendix I

Letters of Permission

Figure 2.1



The screenshot shows the Copyright Clearance Center RightsLink interface. At the top left is the Copyright Clearance Center logo. To its right is the RightsLink logo. Further right are navigation buttons for Home, Create Account, and Help. Below the Copyright Clearance Center logo is the ACS Publications logo with the tagline "Most Trusted. Most Cited. Most Read." The main content area displays the following information:

Title: A Model Development for Evaluating Soot-NOx Interactions in a Blended 2-Way Diesel Particulate Filter/Selective Catalytic Reduction

Author: Soo-Youl Park, Kushal Narayanaswamy, Steven J. Schmiege, et al

Publication: Industrial & Engineering Chemistry Research

Publisher: American Chemical Society

Date: Dec 1, 2012

Copyright © 2012, American Chemical Society

On the right side of the interface, there is a LOGIN button and a text box that reads: "If you're a copyright.com user, you can login to RightsLink using your copyright.com credentials. Already a RightsLink user or want to [learn more?](#)"

PERMISSION/LICENSE IS GRANTED FOR YOUR ORDER AT NO CHARGE

This type of permission/license, instead of the standard Terms & Conditions, is sent to you because no fee is being charged for your order. Please note the following:

- Permission is granted for your request in both print and electronic formats, and translations.
- If figures and/or tables were requested, they may be adapted or used in part.
- Please print this page for your records and send a copy of it to your publisher/graduate school.
- Appropriate credit for the requested material should be given as follows: "Reprinted (adapted) with permission from (COMPLETE REFERENCE CITATION). Copyright (YEAR) American Chemical Society." Insert appropriate information in place of the capitalized words.
- One-time permission is granted only for the use specified in your request. No additional uses are granted (such as derivative works or other editions). For any other uses, please submit a new request.

BACK

CLOSE WINDOW

Copyright © 2019 Copyright Clearance Center, Inc. All Rights Reserved. [Privacy statement](#). [Terms and Conditions](#).
Comments? We would like to hear from you. E-mail us at customer@copyright.com

ECST paper used for Chapter 3,4 and 5

Rightslink® by Copyright Clearance Center 4/9/19, 3:05 PM

RightsLink®

[Home](#)[Account Info](#)[Help](#)





Title: Development of a 2D Model of a SCR Catalyst on a DPF

Author: Venkata R. Chundru, Boopathi S. Mahadevan, John H. Johnson et al

Publication: Emission Control Science and Technology

Publisher: Springer Nature

Date: Jan 1, 2019

Copyright © 2019, Springer Nature Switzerland AG

Logged in as:
Venkata rajesh chundru
Michigan Technological University

[LOGOUT](#)

Order Completed

Thank you for your order.

This Agreement between Michigan Technological University -- Venkata rajesh chundru ("You") and Springer Nature ("Springer Nature") consists of your license details and the terms and conditions provided by Springer Nature and Copyright Clearance Center.

Your confirmation email will contain your order number for future reference.

[printable details](#)

License Number	4564930077437
License date	Apr 09, 2019
Licensed Content Publisher	Springer Nature
Licensed Content Publication	Emission Control Science and Technology
Licensed Content Title	Development of a 2D Model of a SCR Catalyst on a DPF
Licensed Content Author	Venkata R. Chundru, Boopathi S. Mahadevan, John H. Johnson et al
Licensed Content Date	Jan 1, 2019
Type of Use	Thesis/Dissertation
Requestor type	academic/university or research institute
Format	print and electronic
Portion	full article/chapter
Will you be translating?	no
Circulation/distribution	<501
Author of this Springer Nature content	yes
Title	Venkata Rajesh Chundru
Institution name	Michigan Technological University
Expected presentation date	May 2019
Requestor Location	Michigan Technological University 1400 townsend drive

<https://s100.copyright.com/AppDispatchServlet> Page 1 of 2

Figure 2.6




Title: Interaction of NOx Reduction and Soot Oxidation in a DPF with Cu-Zeolite SCR Coating

Author: E. Tronconi, I. Nova, F. Marchitti et al

Publication: Emission Control Science and Technology

Publisher: Springer Nature

Date: Jan 1, 2015

Copyright © 2015, Springer SIP, AG

Logged in as:
Venkata rajesh chundru
Michigan Technological University

Account # :
3001434324

[LOGOUT](#)

Order Completed

Thank you for your order.

This Agreement between Michigan Technological University -- Venkata rajesh chundru ("You") and Springer Nature ("Springer Nature") consists of your license details and the terms and conditions provided by Springer Nature and Copyright Clearance Center.

Your confirmation email will contain your order number for future reference.

[printable details](#)

License Number	4572050285632
License date	Apr 18, 2019
Licensed Content Publisher	Springer Nature
Licensed Content Publication	Emission Control Science and Technology
Licensed Content Title	Interaction of NOx Reduction and Soot Oxidation in a DPF with Cu-Zeolite SCR Coating
Licensed Content Author	E. Tronconi, I. Nova, F. Marchitti et al
Licensed Content Date	Jan 1, 2015
Licensed Content Volume	1
Licensed Content Issue	2
Type of Use	Thesis/Dissertation
Requestor type	academic/university or research institute
Format	print and electronic
Portion	figures/tables/illustrations
Number of figures/tables/illustrations	2
Will you be translating?	no
Circulation/distribution	<501
Author of this Springer Nature content	no
Title	Venkata Rajesh Chundru
Institution name	Michigan Technological University
Expected presentation date	May 2019
Portions	Figure 14 and Figure 15

Figure 2.7



SPRINGER NATURE

Title: A Study of the Soot Combustion Efficiency of an SCRf® Catalyst vs a CSF During Active Regeneration
Author: Lasitha Cumaranatunge, Andrew Chiffey, Joel Stetina et al
Publication: Emission Control Science and Technology
Publisher: Springer Nature
Date: Jan 1, 2016
 Copyright © 2016, Springer International Publishing Switzerland

Logged in as:
 Venkata rajesh chundru
 Michigan Technological University

Account # :
 3001434324

[LOGOUT](#)

Order Completed

Thank you for your order.


This Agreement between Michigan Technological University -- Venkata rajesh chundru ("You") and Springer Nature ("Springer Nature") consists of your license details and the terms and conditions provided by Springer Nature and Copyright Clearance Center.

Your confirmation email will contain your order number for future reference.

[printable details](#)

License Number	4572050400794
License date	Apr 18, 2019
Licensed Content Publisher	Springer Nature
Licensed Content Publication	Emission Control Science and Technology
Licensed Content Title	A Study of the Soot Combustion Efficiency of an SCRf® Catalyst vs a CSF During Active Regeneration
Licensed Content Author	Lasitha Cumaranatunge, Andrew Chiffey, Joel Stetina et al
Licensed Content Date	Jan 1, 2016
Licensed Content Volume	3
Licensed Content Issue	1
Type of Use	Thesis/Dissertation
Requestor type	academic/university or research institute
Format	print and electronic
Portion	figures/tables/illustrations
Number of figures/tables/illustrations	1
Will you be translating?	no
Circulation/distribution	<501
Author of this Springer Nature content	no
Title	Venkata Rajesh Chundru
Institution name	Michigan Technological University
Expected presentation	May 2019

Figure 2.8

 Copyright Clearance Center

Note: Copyright.com supplies permissions but not the copyrighted content itself.

1 PAYMENT 2 REVIEW 3 CONFIRMATION

Step 3: Order Confirmation

Thank you for your order! A confirmation for your order will be sent to your account email address. If you have questions about your order, you can call us 24 hrs/day, M-F at +1.855.239.3415 Toll Free, or write to us at info@copyright.com. This is not an invoice.

Confirmation Number: 11808566
Order Date: 04/18/2019

If you paid by credit card, your order will be finalized and your card will be charged within 24 hours. If you choose to be invoiced, you can change or cancel your order until the invoice is generated.


Payment Information

Venkata rajesh chundru
 Michigan Technological University
 vrchundr@mtu.edu
 +1 (906) 281-8993
 Payment Method: n/a

Order Details

Philosophical transactions

Order detail ID: 71880308
Order License Id: 4572051339388
ISSN: 1471-2962
Publication Type: e-Journal
Volume:
Issue:
Start page:
Publisher: ROYAL SOCIETY
Author/Editor: Royal Society

Permission Status:  **Granted**
Permission type: Republish or display content
Type of use: Republish in a thesis/dissertation
[View details](#)

Note: This item will be invoiced or charged separately through CCC's **RightsLink** service. [More info](#) **\$ 0.00**

Total order items: 1 **This is not an invoice.** **Order Total: 0.00 USD**

Figure 2.9



RightsLink®

[Home](#)
[Account Info](#)
[Help](#)


Title: An extended Kalman filter for NOx sensor ammonia cross-sensitivity elimination in selective catalytic reduction applications

Conference Proceedings: Proceedings of the 2010 American Control Conference

Author: Ming Feng Hsieh

Publisher: IEEE

Date: June 2010

Copyright © 2010, IEEE

Logged in as:
Venkata rajesh chundru
Michigan Technological
University
Account # :
3001434324

[LOGOUT](#)

Thesis / Dissertation Reuse

The IEEE does not require individuals working on a thesis to obtain a formal reuse license, however, you may print out this statement to be used as a permission grant:

Requirements to be followed when using any portion (e.g., figure, graph, table, or textual material) of an IEEE copyrighted paper in a thesis:

- 1) In the case of textual material (e.g., using short quotes or referring to the work within these papers) users must give full credit to the original source (author, paper, publication) followed by the IEEE copyright line © 2011 IEEE.
- 2) In the case of illustrations or tabular material, we require that the copyright line © [Year of original publication] IEEE appear prominently with each reprinted figure and/or table.
- 3) If a substantial portion of the original paper is to be used, and if you are not the senior author, also obtain the senior author's approval.

Requirements to be followed when using an entire IEEE copyrighted paper in a thesis:

- 1) The following IEEE copyright/ credit notice should be placed prominently in the references: © [year of original publication] IEEE. Reprinted, with permission, from [author names, paper title, IEEE publication title, and month/year of publication]
- 2) Only the accepted version of an IEEE copyrighted paper can be used when posting the paper or your thesis on-line.
- 3) In placing the thesis on the author's university website, please display the following message in a prominent place on the website: In reference to IEEE copyrighted material which is used with permission in this thesis, the IEEE does not endorse any of [university/educational entity's name goes here]'s products or services. Internal or personal use of this material is permitted. If interested in reprinting/republishing IEEE copyrighted material for advertising or promotional purposes or for creating new collective works for resale or redistribution, please go to http://www.ieee.org/publications_standards/publications/rights/rights_link.html to learn how to obtain a License from RightsLink.

If applicable, University Microfilms and/or ProQuest Library, or the Archives of Canada may supply single copies of the dissertation.

[BACK](#)
[CLOSE WINDOW](#)

Copyright © 2019 [Copyright Clearance Center, Inc.](#) All Rights Reserved. [Privacy statement.](#) [Terms and Conditions.](#)

<https://s100.copyright.com/AppDispatchServlet#formTop>

Page 1 of 2

Figure 2.10



RightsLink®

Home

Account
Info

Help



Title: Estimation of automotive urea-based selective catalytic reduction systems during low temperature operations

Conference Proceedings: 2014 American Control Conference

Author: Pingen Chen

Publisher: IEEE

Date: June 2014

Copyright © 2014, IEEE

Logged in as:
Venkata rajesh chundru
Michigan Technological
University
Account #:
3001434324

LOGOUT

Thesis / Dissertation Reuse

The IEEE does not require individuals working on a thesis to obtain a formal reuse license, however, you may print out this statement to be used as a permission grant:

Requirements to be followed when using any portion (e.g., figure, graph, table, or textual material) of an IEEE copyrighted paper in a thesis:

- 1) In the case of textual material (e.g., using short quotes or referring to the work within these papers) users must give full credit to the original source (author, paper, publication) followed by the IEEE copyright line © 2011 IEEE.
- 2) In the case of illustrations or tabular material, we require that the copyright line © [Year of original publication] IEEE appear prominently with each reprinted figure and/or table.
- 3) If a substantial portion of the original paper is to be used, and if you are not the senior author, also obtain the senior author's approval.

Requirements to be followed when using an entire IEEE copyrighted paper in a thesis:

- 1) The following IEEE copyright/ credit notice should be placed prominently in the references: © [year of original publication] IEEE. Reprinted, with permission, from [author names, paper title, IEEE publication title, and month/year of publication]
- 2) Only the accepted version of an IEEE copyrighted paper can be used when posting the paper or your thesis on-line.
- 3) In placing the thesis on the author's university website, please display the following message in a prominent place on the website: In reference to IEEE copyrighted material which is used with permission in this thesis, the IEEE does not endorse any of [university/educational entity's name goes here]'s products or services. Internal or personal use of this material is permitted. If interested in reprinting/republishing IEEE copyrighted material for advertising or promotional purposes or for creating new collective works for resale or redistribution, please go to http://www.ieee.org/publications_standards/publications/rights/rights_link.html to learn how to obtain a License from RightsLink.

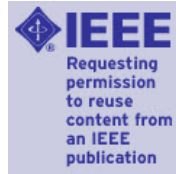
If applicable, University Microfilms and/or ProQuest Library, or the Archives of Canada may supply single copies of the dissertation.

BACK

CLOSE WINDOW

Copyright © 2019 Copyright Clearance Center, Inc. All Rights Reserved. [Privacy statement](#). [Terms and Conditions](#).
Comments? We would like to hear from you. E-mail us at customer@copyright.com

Figure 2.12



Title: Sensor Reduction in Diesel Engine Two-Cell Selective Catalytic Reduction (SCR) Systems for Automotive Applications

Author: Hui Zhang

Publication: Mechatronics, IEEE/ASME Transactions on

Publisher: IEEE

Date: Oct. 2015

Copyright © 2015, IEEE

Logged in as:
Venkata rajesh chundru
Michigan Technological
University
Account # :
3001434324

[LOGOUT](#)

Thesis / Dissertation Reuse

The IEEE does not require individuals working on a thesis to obtain a formal reuse license, however, you may print out this statement to be used as a permission grant:

Requirements to be followed when using any portion (e.g., figure, graph, table, or textual material) of an IEEE copyrighted paper in a thesis:

- 1) In the case of textual material (e.g., using short quotes or referring to the work within these papers) users must give full credit to the original source (author, paper, publication) followed by the IEEE copyright line © 2011 IEEE.
- 2) In the case of illustrations or tabular material, we require that the copyright line © [Year of original publication] IEEE appear prominently with each reprinted figure and/or table.
- 3) If a substantial portion of the original paper is to be used, and if you are not the senior author, also obtain the senior author's approval.

Requirements to be followed when using an entire IEEE copyrighted paper in a thesis:

- 1) The following IEEE copyright/ credit notice should be placed prominently in the references: © [year of original publication] IEEE. Reprinted, with permission, from [author names, paper title, IEEE publication title, and month/year of publication]
- 2) Only the accepted version of an IEEE copyrighted paper can be used when posting the paper or your thesis on-line.
- 3) In placing the thesis on the author's university website, please display the following message in a prominent place on the website: In reference to IEEE copyrighted material which is used with permission in this thesis, the IEEE does not endorse any of [university/educational entity's name goes here]'s products or services. Internal or personal use of this material is permitted. If interested in reprinting/republishing IEEE copyrighted material for advertising or promotional purposes or for creating new collective works for resale or redistribution, please go to http://www.ieee.org/publications_standards/publications/rights/rights_link.html to learn how to obtain a License from RightsLink.

If applicable, University Microfilms and/or ProQuest Library, or the Archives of Canada may supply single copies of the dissertation.

[BACK](#)[CLOSE WINDOW](#)

Copyright © 2019 [Copyright Clearance Center, Inc.](#) All Rights Reserved. [Privacy statement.](#) [Terms and Conditions.](#)
Comments? We would like to hear from you. E-mail us at customer care@copyright.com

Figure 2.13



RightsLink®

Home

Account
Info

Help



Title: Development of a Kalman filter estimator for simulation and control of particulate matter distribution of a diesel catalyzed particulate filter

Author: Boopathi Singalandapuram Mahadevan, John H Johnson, Mahdi Shahbakhti

Publication: International Journal of Engine Research

Publisher: SAGE Publications

Date: 07/17/2018

Copyright © 2018, © SAGE Publications

Logged in as:
Venkata rajesh
chundru
Michigan
Technological
University

Account # :
3001434324

LOGOUT

Gratis Reuse

Permission is granted at no cost for use of content in a Master's Thesis and/or Doctoral Dissertation. If you intend to distribute or sell your Master's Thesis/Doctoral Dissertation to the general public through print or website publication, please return to the previous page and select 'Republish in a Book/Journal' or 'Post on intranet/password-protected website' to complete your request.

BACK

CLOSE WINDOW

Copyright © 2019 Copyright Clearance Center, Inc. All Rights Reserved. [Privacy statement](#). [Terms and Conditions](#). Comments? We would like to hear from you. E-mail us at customer@copyright.com